LA-13635-MS

Approved for public release;
distribution is unlimited.

Structural Health Monitoring Studies of the Alamosa Canyon and I-40 Bridges

Los Alamos
NATIONAL LABORATORY

Los Alamos National Laboratory is operated by the University of California for the United States Department of Energy under contract W-7405-ENG-36.

Cover photos: The Alamosa Canyon Bridge and various activities performed during this study.

An Affirmative Action/Equal Opportunity Employer

This report was prepared as an account of work sponsored by an agency of the United States Government. Neither The Regents of the University of California, the United States Government nor any agency thereof, nor any of their employees, makes any warranty, express or implied, or assumes any legal liability or responsibility for the accuracy, completeness, or usefulness of any information, apparatus, product, or process disclosed, or represents that its use would not infringe privately owned rights. Reference herein to any specific commercial product, process, or service by trade name, trademark, manufacturer, or otherwise, does not necessarily constitute or imply its endorsement, recommendation, or favoring by The Regents of the University of California, the United States Government, or any agency thereof. The views and opinions of authors expressed herein do not necessarily state or reflect those of The Regents of the University of California, the United States Government, or any agency thereof. Los Alamos National Laboratory strongly supports academic freedom and a researcher's right to publish; as an institution, however, the Laboratory does not endorse the viewpoint of a publication or guarantee its technical correctness.

LA-13635-MS

Issued: July 2000

Structural Health Monitoring Studies of the Alamosa Canyon and I-40 Bridges

Charles R. Farrar
*Phillip J. Cornwell**
Scott W. Doebling
Michael B. Prime

Student Participants
Alex Barron, Stanford University
Bethany Carlson, University of California, Berkeley
Randy Goodman, University of Colorado
Gwang-He Heo, University of New Mexico
Marcie Kam, Rose-Hulman Institute of Technology
Erik Straser, Stanford University
Janneane S. Vigil, New Mexico State University

Post-Doctoral Research Associate
Daniel Shevitz

Service Academy Graduate Research Assistant
Lt. Brian Hoerst, USN

**Rose-Hulman Institute of Technology, 5500 Wabash Ave., Terre Haute, IN 47803.*

Los Alamos
NATIONAL LABORATORY
Los Alamos, New Mexico 87545

TABLE OF CONTENTS

LIST OF FIGURES viii

LIST OF TABLES xi

ABSTRACT 1

I. INTRODUCTION 2

II. DESCRIPTION OF THE ALAMOSA CANYON BRIDGE 4

III. PRELIMINARY VIBRATION TESTS PERFORMED ON THE ALAMOSA CANYON BRIDGE 12

A. Forced Vibration Tests 12

1. Roving Hammer Impact Test 12

a. Experimental procedure and equipment 12

b. Results of roving hammer impact test 17

2. Single Excitation Point Impact Test Method 20

a. Experimental procedure and equipment 20

b. Results of the single excitation point impact test 21

B. Ambient Vibration Tests 25

1. Ambient Vibration Test Following the Roving Hammer Impact Test 25

a. Experimental procedure and equipment 25

b. Results 26

2. Ambient Vibration Test Following the Single Excitation Point Test 29

a. Experimental procedure and equipment 29

b. Results 29

C. Lessons Learned from the Preliminary Tests 31

IV. VIBRATION TESTS PERFORMED ON THE ALAMOSA CANYON BRIDGE 31

A. Forced Vibration Tests 31

1. Linearity and Reciprocity Checks 31

a. Experimental procedure and equipment 31

b. Linearity and reciprocity test results 34

2. Three-span test 39

a. Experimental procedure and equipment 39

b. Results from the three-span test 39

B. Vibration Tests Performed to Study Variability of Modal Properties 42

1. Results from Tests to Study Variability Caused by Thermal Effects 42

2. Results from Tests to Study Variability Caused by Vehicle Weight 45

3. Results from Tests to Study Variability Caused by the Excitation Source 46

4. Results from Tests to Study Variability Caused by Data Reduction 46

C. Statistical Analysis Methods 48

1. Monte Carlo Analysis Procedure 48
2. Bootstrap Analysis Procedure 50
3. Test on Simulated Data 52

D. A Statistical Comparison of Impact and Ambient Testing Results 54

1. Description of the Ambient Test 55
2. Description of the Statistical Methods 57
3. Results 58

E. A Comparison of the Monte Carlo and Bootstrap Techniques 61

1. Application to the Alamosa Canyon Bridge 61
2. Summary and Observations 65

F. Tests to Study Damage Identification 66

1. Simulated Damage Study 67
a. Uncertainty bounds on measured parameters from random disturbance 67
b. Simulation of damage in the finite element model 68
c. Comparison of statistics to predicted damage effects 68
2. Stiffening the Structure 75
a. Results from stiffening the structure 76

G. Shaker Tests 79

H. A Modular, Wireless Damage Monitoring System (WiMMS) 84

V. FINITE ELEMENT MODELING OF THE ALAMOSA CANYON BRIDGE 86

VI. APPLICATION OF STATISTICAL METHODS TO I-40 TEST DATA 89

A. The I-40 Bridge Damage Identification Experiment 90

B. Theoretical Development 92

1. Estimation of Random Error in Measured Modal Data 92
2. Monte Carlo Simulation and Application to Modal Parameter Identification 93
3. Damage Identification Using Modal Flexibility Change 93
4. Confidence Intervals on Flexibility Damage Indicator 94
5. Tests of Significant Difference Between Sample Means 94

C. Experimental Results, Statistical Analysis, and Discussion 96

1. Damage Identification Using Measured Flexibility Change 100

D. Conclusions from the I-40 Bridge Tests 101

VII. SUMMARY AND CONCLUSIONS 102

A. Variability Studies 102

B. Statistical Methods 104

C. Damage Assessment of Alamosa Canyon Bridge 104

D. Statistical Damage Assessment of the I-40 Bridge 105

E. Wireless Data Acquisition 106

F. Lessons Learned 106

APPENDIX A: Identifying Modal Properties Using a Rational-Fraction Polynomial Curve-Fitting Algorithm 109

A. The Rational Fraction Polynomial Method 109

B. The Global Rational Polynomial Method (GRFP) 118

APPENDIX B: Identifying Modal Properties Using an Eigensystem Realization Algorithm . 123

APPENDIX C: Estimating Confidence Limits for Frequency Response Functions from Measured Coherence Functions 130

A. Random Error in Gain Factor Estimates 132

B. Random Error in Phase Factor Estimates 135

APPENDIX D: DIAMOND: A Matlab Toolbox for Modal Analysis and Damage Identification 138

A. Experimental Modal Analysis / Statistical Analysis of Modal Data 139

B. Damage Identification 141

C. Finite Element Model Refinement 142

APPENDIX E: The Strain Energy Damage Detection Method 144

A. Theory 145

B. Application 149

APPENDIX F: Data File Summary 150

REFERENCES 155

DISTRIBUTION 161

LIST OF FIGURES

Figure 1. Alamosa Canyon Bridge near Truth or Consequences, New Mexico. 4
Figure 2. Elevation view of the Alamosa Canyon Bridge. 5
Figure 3. Bridge substructure. 5
Figure 4. Cross section of the bridge at the location of the interior cross braces. 6
Figure 5. Photo of interior cross braces. 6
Figure 6. Cross section of the bridge at the end of the span. 7
Figure 7. Photo of the cross bracing at the end of a span. 7
Figure 8. Roller support. 8
Figure 9. Roller connections at the northern-most pier. 8
Figure 10. Half-roller connection. 9
Figure 11. Photo of a half-roller connection at the northern abutment. 9
Figure 12. Deterioration of paint on west exterior girder. 10
Figure 13. Cracks in deck surface near an accelerometer. 10
Figure 14. Debris in expansion joint at the north end of the bridge. 11
Figure 15. Dead cow located underneath an area of the bridge where instrumentation would be mounted. 11
Figure 16. Schematic of the data acquisition equipment. 15
Figure 17. Data acquistion equipment. 15
Figure 18. Generator used to power the data acquisition equipment. 16
Figure 19. The hammer and accelerometer used for the impact test. 17
Figure 20. Measurement and excitation locations for the impact test. The reference accelerometer as located at position 8. 18
Figure 21. An impact being applied to position 2. 18
Figure 22. Typical FRF obtained from the impact test. For this FRF, the impact was applied to position 9 and the reference was located at position 8. 19
Figure 23. First six mode shapes and frequencies. 19
Figure 24. Accelerometer and magnetic mount. 20
Figure 25. Accelerometer locations for the single excitation test. 21
Figure 26. CMIF for span 1. 24
Figure 27. CMIF for span 2. 24
Figure 28. Source of excitation for ambient test one. 25
Figure 29. Ford Taurus used for ambient test two and the van containing the data acquisition equipment. 26
Figure 30. CPS (magnitude only) obtained from Ambient Test One using the accelerometers at point 8 and 11. 27
Figure 31. CPS obtained from Ambient Test Two using the accelerometers at points 8 and 11. 27
Figure 32. New, more compact, data acquisition and analysis equipment and laptop computer. 32
Figure 33. Accelerometer, impact, and thermometer locations. 33
Figure 34. Indoor-outdoor thermometer taped to the exterior girders. 34
Figure 35. Indoor-outdoor thermometer located on the deck of the bridge. 34
Figure 36. PSDs of impact excitations used in the linearity check at driving point A. 35
Figure 37. FRF magnitudes measured at location 6 (impact appied at point B). 36

Figure 38. Coherence functions for the FRFs measured at location 6 for the low and high excitation levels..... 36
Figure 39. FRF magnitudes used to check reciprocity of the structure and the electronics. 37
Figure 40. Coherence functions of the FRFs used to check the reciprocity of the structure and the electronics..... 37
Figure 41. FRF magnitudes to check reciprocity of the structure only..... 38
Figure 42. Coherence functions of the FRFs used to check the reciprocity of the structure only38
Figure 43. Accelerometer locations for the 3-span test..... 39
Figure 44. Typical FRFs and COHs for points on spans one, two and three..... 40
Figure 45. CMIF for data from the three-span test. 41
Figure 46. The first four mode shapes for the three-span test..... 41
Figure 47. Change in the first mode frequency during a 24-hour time period (ACBT3). 43
Figure 48. Change in the first modal frequency during the second 24-hour test (ACBT4)..... 43
Figure 49. Change in the second modal frequency during the second 24-hour test (ACBT4)..... 44
Figure 50. Change in the third modal frequency during the second 24-hour test (ACBT4)..... 44
Figure 51. Flowchart of Monte Carlo analysis procedure..... 50
Figure 52. Flowchart of the bootstrap procedure..... 51
Figure 53. Simulated FRFs. 53
Figure 54. Accelerometer located midway between the I-25 bridge and the Alamosa Canyon Bridge..... 56
Figure 55. PSDs of ground motion induced by trucks on the adjacent Interstate 25 bridge..... 56
Figure 56. Typical cross-power spectrum used to identify modal properties..... 57
Figure 57. Typical 95% confidence bounds on FRF magnitude and phase shown as dotted lines 57
Figure 58. Nine identified modes from impact excitation of the Alamosa Canyon Bridge..... 58
Figure 59. Thirty FRFs measured at Pt. 2..... 61
Figure 60. Average FRF measured at Pt. 2..... 62
Figure 61. Coherence Function corresponding to the average FRF..... 62
Figure 62. Overlay of 11 averaged (30 averages) FRFs measured at Pt. 2 over a 24-hour period. 63
Figure 63. Average of 330 FRFs measured at Pt. 2 during a 24-hour period..... 64
Figure 64. Coherence function corresponding to the average FRF measured during a 24-hour period. 64
Figure 65. Comparison of modal frequency 95% confidence bounds to changes predicted as a result of damage..... 69
Figure 66. Comparison of modes 3 and 7 confidence bounds and predicted change after damage..... 70
Figure 67. Comparison of average mode shape component 95% confidence bounds to changes predicted as a result of damage..... 71
Figure 68. Comparison of modes 3 and 7 curvature confidence bounds and predicted change after damage. 73
Figure 69. Comparison of average mode shape curvature component 95% confidence bounds to changes predicted as a result of damage..... 74
Figure 70. Clamps and plate used to stiffen the structure locally..... 75
Figure 71. Bar plots of the normalized damage indices obtained from the strain energy method..... 78

Figure 72. Bar plots of the changes in flexibility for the three data sets analyzed. 79
Figure 73. 100 lb shaker provided by the University of California at Irvine..... 80
Figure 74. A comparison of the input PSD from the hammer, 30 lb shaker and 100 lb shaker. . 81
Figure 75. A comparison of the PSD for the output signal at the excitation location using the hammer, 30 lb shaker and 100 lb shaker..... 81
Figure 76. CMIF from the 30 lb shaker test..... 82
Figure 77. CMIF from the 100 lb shaker test..... 82
Figure 78. Eccentric mass shaker provided by the University of California at Irvine..... 83
Figure 79. Site master radio modem and the sensor unit installed on a beam. 85
Figure 80. Sensor unit and accelerometers mounted to the bottom of a beam flange. 85
Figure 81. Finite element mesh..... 86
Figure 82. Solid model of the first span..... 87
Figure 83. I-40 Bridges over the Rio Grande River in Albuquerque, New Mexico..... 91
Figure 84. The four levels of damage induced by cutting the I-40 plate girder..... 92
Figure 85. Flowchart of the Monte Carlo method applied to the flexibility damage detection method..... 95
Figure 86. First modal frequency for each damage case..... 96
Figure 87. First modal frequency for first two damage cases..... 96
Figure 88. First mode shape for undamaged case and first damage case. 97
Figure 89. First mode shape for undamaged case and fourth damage case. 97
Figure 90. Third mode shape for undamaged case and fourth damage case..... 98
Figure 91. Comparison of z-statistics for mode shape change comparisons. 99
Figure 92. Comparison of z-statistics for mode shape 1 for each damage case vs. undamaged.. 99
Figure 93. Flexibility change for all 4 damage cases..... 100
Figure 94. Z-statistic values for flexibility change for all 4 damage cases..... 101

LIST OF TABLES

Table 1. Comparison of the frequencies and damping for the roving hammer impact test and the single excitation point impact test using both the rational polynomial and the ERA parameter identification methods. 22
Table 2. Comparison of frequencies and damping for four spans of the Alamosa Canyon Bridge. 23
Table 3. Resonant frequencies identified from ambient vibration response compared with similar quantities identified from roving hammer impact tests for span one. 28
Table 4. Comparison of the single excitation point impact test and the ambient tests for span three of the Alamosa Canyon Bridge. 30
Table 5. Change in Modal Frequencies Resulting from Added Mass of Cars 45
Table 6. Comparison of Two Modal Analyses of Data from Seymour Bridge in Cincinnati, Ohio 47
Table 7. Comparison of the Monte Carlo and bootstrap methods on numerically simulated data..... 54
Table 8. Mean Modal Frequency Comparison 59
Table 9. Mean Modal Damping Ratio Comparison..... 59
Table 10. Relative 95% Uncertainty Level Comparison for Identified Modal Parameters..... 60
Table 11. Comparison of Bootstrap and Monte Carlo Statistical Analysis Results on Data from the Alamosa Canyon Bridge..... 65
Table 12. Uncertainty Bounds on Measured Parameters from Random Disturbances 67
Table 13. Changes in FEM Modal Parameters Resulting fromDamage 68
Table 14. Number of DOF for Each Mode Shape That Undergo Change Resulting from Damage ≥ 95% Confidence Bounds..... 72
Table 15. Number of DOF for Each Mode Shape Curvature That Undergo Change Resulting from Damage ≥ 95% Confidence Bounds..... 74
Table 16. Comparison of Frequencies and Damping for the Stiffened Structure and the Unstiffened Structure..... 76
Table 17. Comparison of Frequency and Damping Obtained from a Hammer Test and the Shaker Tests..... 83
Table 18. FEM Material and Cross-Sectional Properties 87
Table 19. Comparison of Frequencies Obtained Experimentally With Those Obtained from the Finite Element Analysis..... 88
Table 20. Figure Modal Assurance Criteria for the Mode Sshapes Identified from the Finite Element Model Compared With Mode Shapes Identified from Forced Vibration Tests..... 89

STRUCTURAL HEALTH MONITORING STUDIES OF THE ALAMOSA CANYON AND I-40 BRIDGES

by

Charles R. Farrar, Phillip J. Cornwell, Scott W. Doebling, and Michael B. Prime

ABSTRACT

From 1994 to 1997 internal research grants from Los Alamos National Laboratory's Laboratory Direct Research and Development (LDRD) office were used to fund an effort aimed at studying global vibration-based damage detection methods. To support this work, several field tests of the Alamosa Canyon Bridge have been performed to study various aspects of applying vibration–based damage detection methods to a real world in situ structure. This report summarizes the data that has been collected from the various vibration tests performed on the Alamosa Canyon Bridge, analyses of these data, and the results that have been obtained.

Initially, it was the investigators' intent to introduce various types of damage into this bridge and study several vibration-based damage detection methods. The feasibility of continuously monitoring such a structure for the onset of damage was also going to be studied. However, the restrictions that the damage must be relatively benign or repairable made it difficult to take the damage identification portion of the study to completion. Subsequently, this study focused on quantifying the variability in identified modal parameters caused by sources other than damage. These sources include variability in testing procedures, variability in test conditions, and environmental variability. These variabilities must be understood and their influence on identified modal properties quantified before vibration-based damage detection can be applied with unambiguous results. Quantifying the variability in the identified modal parameters led to the development of statistical analysis procedures that can be applied to the experimental modal analysis results. It is the authors' opinion that these statistical analysis procedures represent one of the major contributions of these studies to the vibration-based damage detection field. Another significant contribution that came from this portion of the study was the extension of a strain-energy-based damage detection method originally developed for structures that exhibit beam-bending response to structures that exhibit plate-like bending or bending in two directions.

In addition, based on lessons learned from the Alamosa Canyon Bridge test, data from the I-40 Bridge tests have been re-analyzed using the statistical analysis procedures developed as part of this study. The application of these statistical procedures to the I-40 Bridge test results gives particular insight into how statistical analysis can be used to enhance the vibration-based damage detection process. Finally, data from the Alamosa Canyon and I-40 Bridge tests along with all reports and papers related to these studies have been made available to other researchers at the following site: http://ext.lanl.gov/projects/damage_id/.

I. INTRODUCTION

The interest in the ability to monitor a structure and detect damage at the earliest possible stage is pervasive throughout the civil, mechanical and aerospace engineering communities. Current damage-detection methods are either visual [White, Minor and Derucher (1992)] or localized experimental methods such as acoustic or ultrasonic methods, magnet field methods, radiographs, eddy-current methods and thermal field methods [Doherty (1987)]. All of these experimental techniques require that the vicinity of the damage is known *a priori* and that the portion of the structure being inspected is readily accessible. Subjected to these limitations, these experimental methods can detect damage on or near the surface of the structure. The need for additional global damage detection methods that can be applied to complex structures has led to the development of methods that examine changes in the global dynamic characteristics of the structure.

Damage or fault detection, as determined by changes in the dynamic properties or response of structures, is a subject that has received considerable attention in the recent technical literature. The basic concept is that global modal parameters (notably resonant frequencies, mode shapes, and modal damping) are functions of the physical properties of the structure (mass, damping, and stiffness). Therefore, changes in the physical properties will cause changes in the modal properties. Recent research has focused on developing methods to measure and analyze changes in these global dynamics properties in an effort to detect and locate damage on a local level. These vibration-based damage detection methods can be based on physical models of the structure or can merely apply various pattern recognition algorithms to the measured response data from the structures.

From 1994 to 1997 internal research grants from Los Alamos National Laboratory's Laboratory Direct Research and Development (LDRD) office have been used to fund an effort aimed at studying vibration-based damage detection methods. To support this work, several field tests of the Alamosa Canyon Bridge have been performed to study various aspects of applying vibration–based damage detection methods to a real world in situ structure. This bridge is located adjacent to Interstate 25 (I-25) approximately 16 km (10 miles) north of Truth or Consequences, New Mexico. The New Mexico State Highway and Transportation Department has made the Alamosa Canyon Bridge into a "Bridge Safety Test Site". This test site is intended to provide an actual highway bridge that can be used to study various issues related to bridge structural integrity. Professor Ken White at New Mexico State University and staff from the Alliance for Transportation Research have been instrumental in establishing this bridge as a field test site.

This report will summarize the data that has been collected from the various vibration tests performed on the Alamosa Canyon Bridge, experimental procedures used to obtain these data, analyses of these data, and the results that have been obtained. Data from these tests have been made available to other researchers at the following site: http://ext.lanl.gov/projects/damage_id/.

Initially, it was the investigators' intent to introduce various types of damage into this bridge and study several damage detection methods along with the feasibility of continuously monitoring such a structure. However, the restrictions that the damage to the Alamosa Canyon Bridge must be relatively benign or repairable made it difficult to take the damage identification portion of the study to completion. Subsequently, this study focused on quantifying the variability in identified modal parameters caused by sources other than damage. This variability

must be understood before vibration-based damage detection can be applied with unambiguous results. Quantifying the variability in the identified modal parameters led to the development of statistical analysis procedures that can be applied to the experimental modal analysis results. It is the authors' opinion that these statistical analysis procedures represent one of the major contributions of these studies to the vibration-based damage detection field. The experimental quantification of variability in measured modal parameters from the bridge represents a unique set of data for bridge structures. Another major contribution that came from this portion of the study was the extension of a strain-energy-based damage detection method to structures that exhibit plate-like bending or bending in two directions. The strain energy method of global damage detection was originally developed by Prof. Norris Stubbs at Texas A&M University for structures that exhibit beam-bending response.

In addition, based on lessons learned from the Alamosa Canyon Bridge tests, data from the I-40 Bridge tests were re-analyzed using the statistical analysis procedures developed as part of this study. The application of the statistical procedures to the I-40 Bridge test results gives particular insight into how statistical analysis can be used to enhance the vibration-based damage detection process. The data from the I-40 Bridge tests along with all reports and papers that the authors have produced related to vibration-based damage detection have also been included on the web site http://ext.lanl.gov/projects/damage_id/.

Los Alamos National Laboratory's University of California Interaction Office provided additional funds so that Prof. Gerry Pardoen and students from the University of California, Irvine could participate in the last series of tests. Prof. Pardoen used an electrodynamic shaker and an eccentric mass shaker to excite the structure. These additional excitation sources allowed the LANL staff to compare dynamic properties identified using a variety of excitation techniques including ambient excitation from traffic, impact excitation using an instrumented hammer, random excitation from the electrodynamic shaker, and swept-sine excitation imparted by the eccentric mass shaker.

The final tests performed on the Alamosa Canyon Bridge were done in support of a NSF research grant that was awarded to Prof. Anne Kiremidjian at Stanford University. These tests were done to demonstrate a wireless data acquisition system being developed by Erik Straser at Stanford. It is the authors' opinion that if vibration-based damage detection technology is to be adopted on a wide scale, then it will have to be used in conjunction with a wireless data acquisition system. Otherwise the maintenance associated with the wires will make the system too unreliable for commercial application.

Finally the authors must acknowledge the invaluable assistance provide by numerous undergraduate and graduate students, a post-doctoral research associate, and a service academy graduate research assistant. None of the testing and analyses reported herein could have been completed without their help.

II. DESCRIPTION OF THE ALAMOSA CANYON BRIDGE

The Alamosa Canyon Bridge has seven independent spans with a common pier between successive spans. The bridge, as seen from the arroyo it crosses, is shown in Figure 1. The bridge was constructed around 1937 and was replaced by a new bridge when I-25 was constructed in the early 1960s. Currently the Alamosa Canyon Bridge is at the end of a frontage road and is rarely used. The bridge is aligned primarily in the north-south direction.

A drawing depicting an elevation view of the bridge's northern three spans is shown in Figure 2. Each span consists of a concrete deck supported by six steel beams. The roadway in each span is approximately 7.3 m (24 ft) wide and 15.2 m (50 ft) long. A concrete curb and guardrail are integrally attached to the deck. Expansion joints are located at both ends of each span. Measurements made on the six beams' cross sections indicate they correspond to a $W30 \times 116$ standard wide-flange beam. The substructure of a span is shown in Figure 3. Inspection of the bridge showed that the upper flanges of the beams are imbedded in the concrete. Plans for the bridge do not show shear studs on the top flanges of the girders. Between adjacent beams are four cross braces equally spaced along the length of the span. The cross braces are channel sections ($C12 \times 25$). A cross section of the span at a location showing the interior cross braces is shown in Figure 4 and a photo of this bracing is shown in Figure 5. A view showing the braces at the end of the span is shown in Figure 6 along with a corresponding photo in Figure 7. At the first pier the beams of the northern-most span rest on rollers as shown in Figure 8. A photo of the rollers is shown in Figure 9. At the north abutment the beams are bolted to a half-roller as shown in Figure 10. A photo of the half-roller connection at the northern abutment is shown in Figure 11.

A visual inspection of the bridge revealed that the structure was in generally good condition. Some rust and peeling of paint was observed on the exterior beam, Figure 12, and at the supports. Spalling of the concrete was observed on one of the piers. The concrete deck had numerous cracks on its surface, Figure 13, but inspection of the deck's underside found no corresponding cracks. Expansion joints located at either end of the spans were filled with dirt as shown in Figure 14.

Figure 1. Alamosa Canyon Bridge near Truth or Consequences, New Mexico.

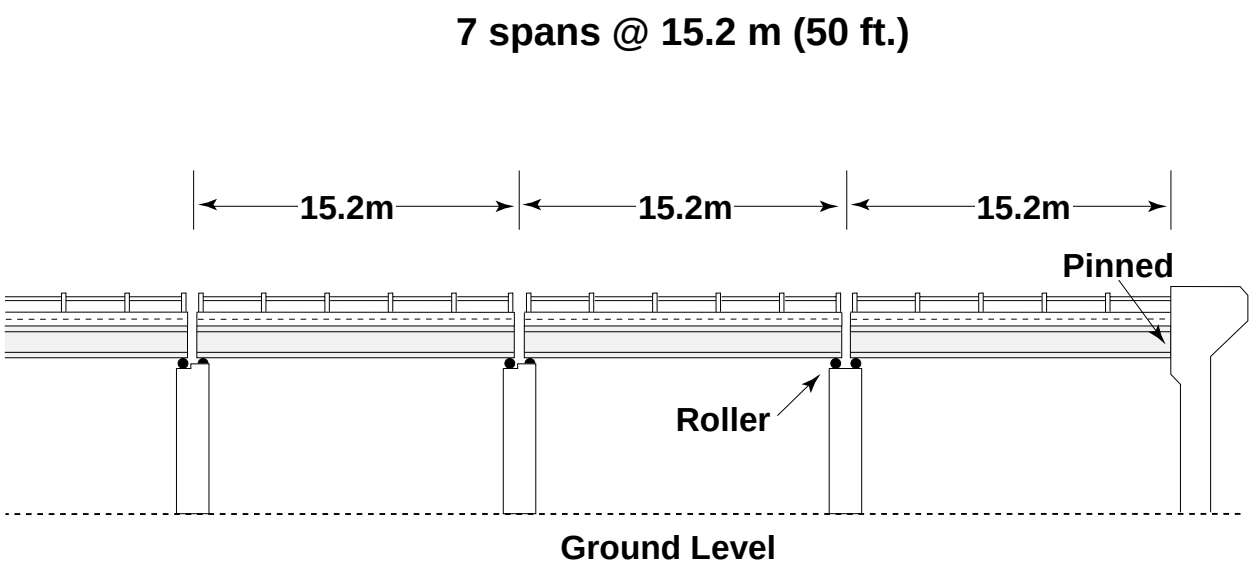

Figure 2. Elevation view of the Alamosa Canyon Bridge.

Figure 3. Bridge substructure.

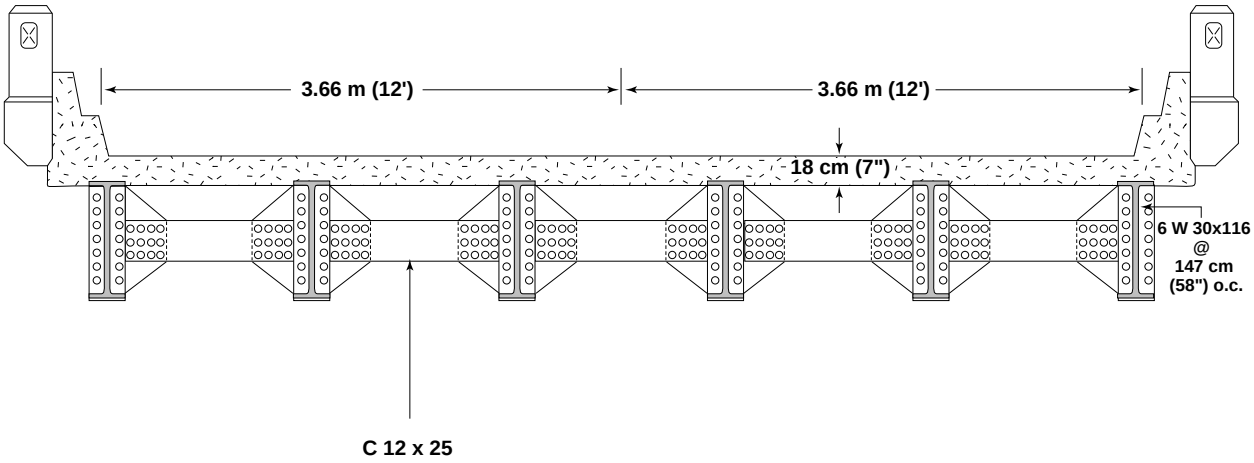

Figure 4. Cross section of the bridge at the location of the interior cross braces.

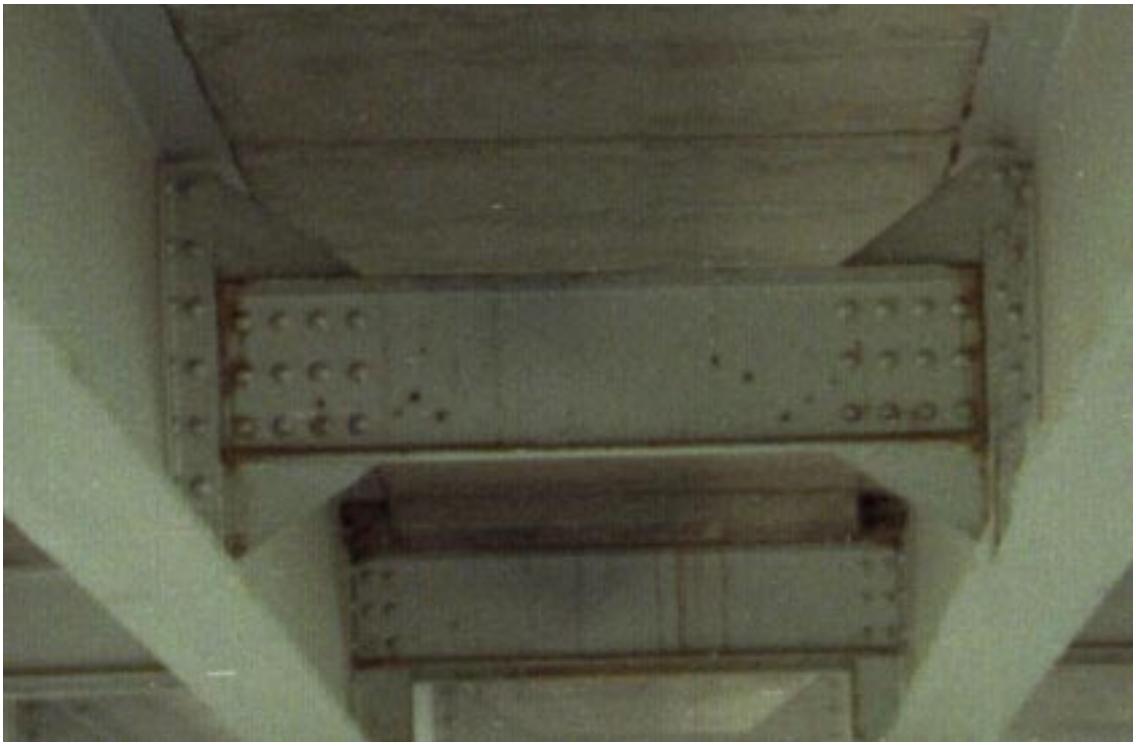

Figure 5. Photo of interior cross braces.

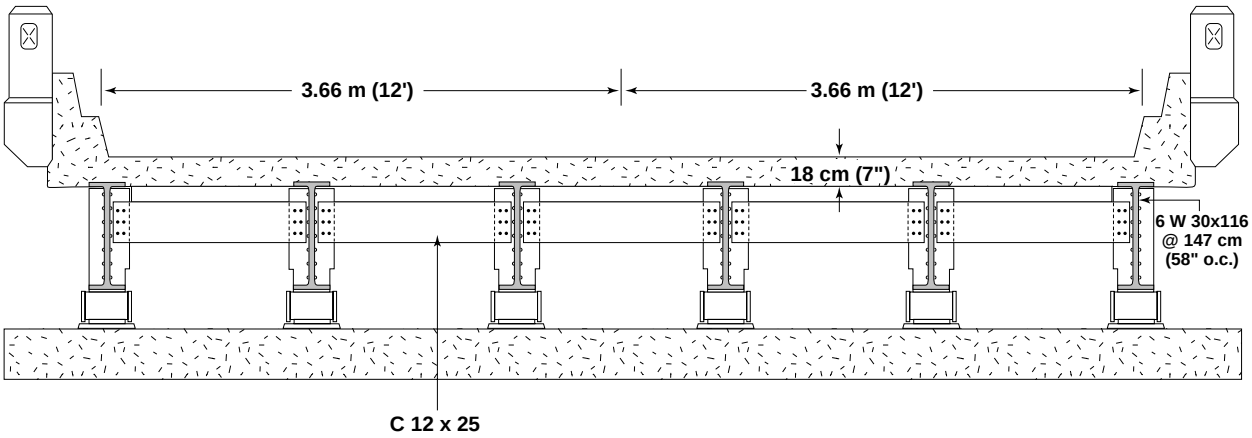

Figure 6. Cross section of the bridge at the end of the span.

Figure 7. Photo of the cross bracing at the end of a span.

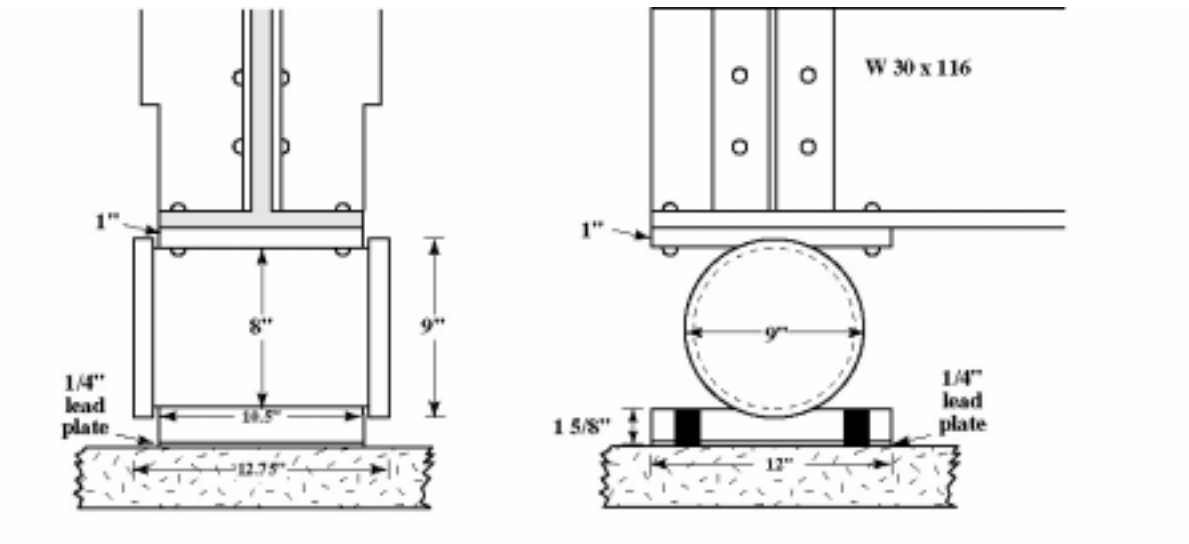

Figure 8. Roller support.

Figure 9. Roller connections at the northern-most pier.

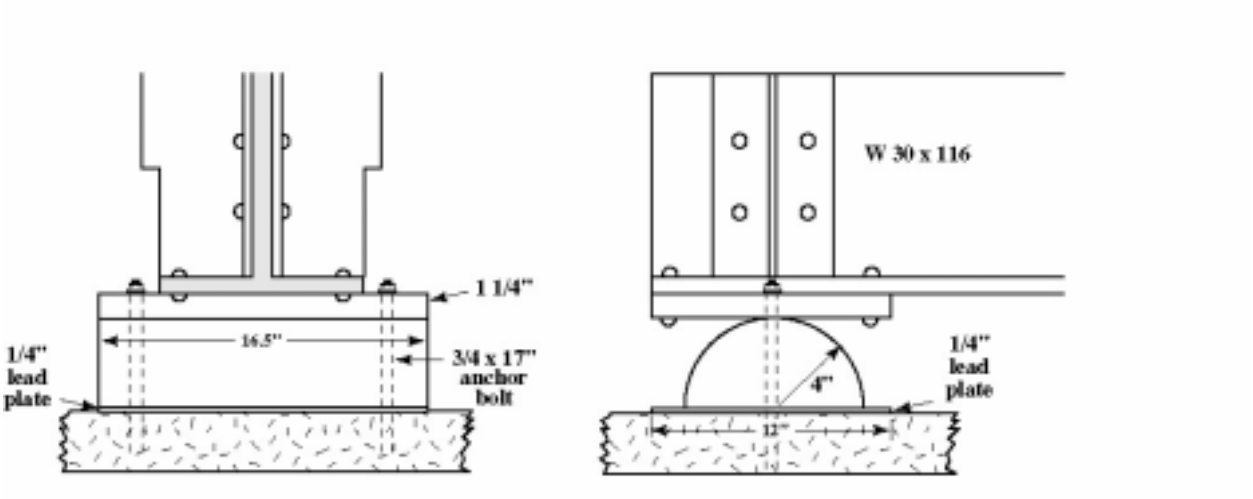

Figure 10. Half-roller connection.

Figure 11. Photo of a half-roller connection at the northern abutment.

Figure 12. Deterioration of paint on west exterior girder.

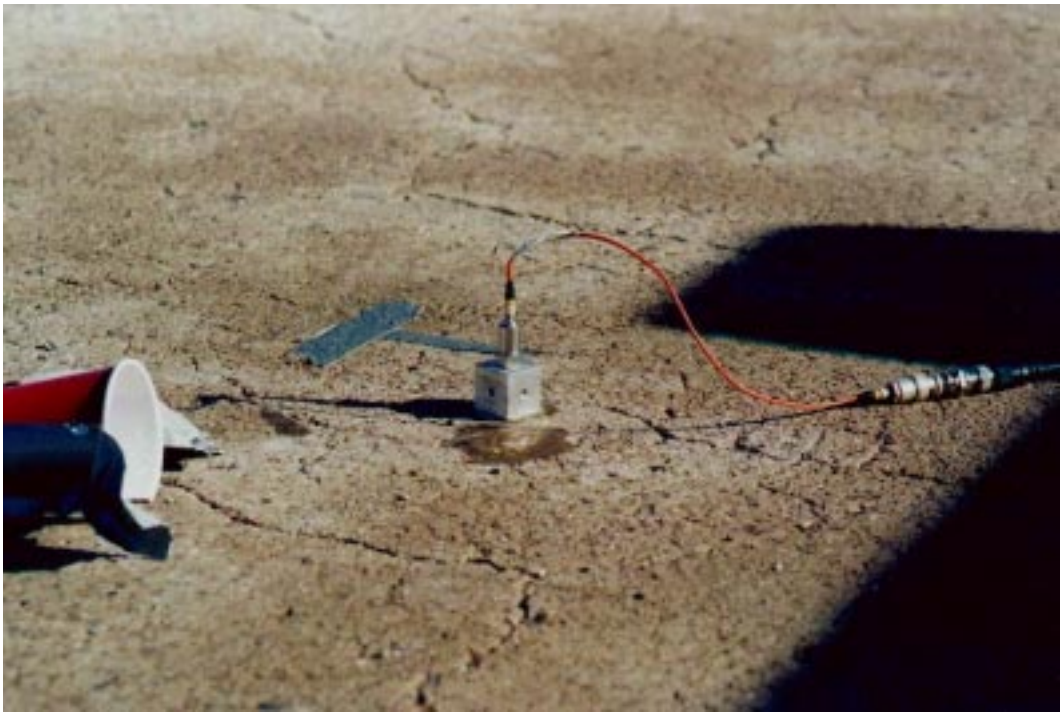

Figure 13. Cracks in deck surface near an accelerometer.

Figure 14. Debris in expansion joint at the north end of the bridge.

Figure 15. Dead cow located underneath an area of the bridge where instrumentation would be mounted.

The arroyo that the bridge spans is dry most of the year. During the summer monsoon season thunderstorms in the vicinity produce enough rain for sustained flow under the center span of the bridge. These storms also produce standing pools of water on the deck of the bridge as some of the drainage spouts located on the edge of the deck are clogged with debris. In addition to variable and somewhat extreme environmental conditions, rattlesnakes, cows (both dead and live), and abundant insect life posed additional difficulties to the testing. The hazard of a dead cow located in the center of the test area is shown in Figure 15.

III. PRELIMINARY VIBRATION TESTS PERFORMED ON THE ALAMOSA CANYON BRIDGE

Preliminary experimental vibration tests were performed on the Alamosa Canyon Bridge on August 29, 1995 and on November 29 through December 1, 1995. The purpose of these tests was to obtain initial estimates of the dynamic characteristics of the bridge (resonant frequencies, mode shapes and damping factors). These data were subsequently used to benchmark a finite element model of the structure.

A. Forced Vibration Tests

The experimental procedures and test equipment used in the initial tests are summarized in the following sections. The reader will notice an evolution in the test procedures and equipment used to conduct the tests reflecting lessons learned during each test sequence and upgrades made to the data acquisition system.

1. Roving Hammer Impact Test

A roving hammer impact test was performed on August 29, 1995. This test has the advantage that it requires only two data acquisition channels. This test will be called ACBT1. A single accelerometer was located at one reference location and the hammer was used to impact the bridge at numerous additional locations. The weather was warm, approximately 35 °C (95 °F), sunny, and there was negligible wind. These measurements were intended to identify the structure's resonant frequencies, modal damping, and the corresponding mode shapes. Excitation from traffic on the adjacent bridges could be felt during the impact testing of the bridge, but no attempt was made to characterize the input from the adjacent bridges.

a. Experimental procedure and equipment

The data acquisition system used in this forced vibration test consisted of many components. A Hewlett Packard 9000 Series 370 workstation with a 300-megabyte hard disk was used to monitor the data acquisition system. This computer was the platform for Vista®, a commercial data-acquisition/signal-analysis software package from Hewlett Packard. HP 35652A input modules provided power to the accelerometer and force transducer and performed analog-to-digital conversion of the accelerometer signals. An HP 35651A signal-processing module performed the needed fast Fourier transform calculations. The system is shown schematically in Figure 16 and a photograph of the data acquisition modules is shown in Figure 17. All of the data

acquisition equipment was located in a van positioned just off the north end of the bridge. A 3500 watt GENERAC Model R-3500 XL AC generator shown in Figure 18 was used to power this system.

The system samples the analog signal from the accelerometer at 262 kHz (regardless of the frequency range being analyzed). The signals are first passed through an analog antialiasing filter. The signals are then digitized and passed through a digital antialiasing filter with the cutoff frequency based upon the Nyquist frequency for the specified sampling parameters. The signal is then decimated based on the particular sampling parameters. A voltage overload test is performed on each measurement channel prior to the digital filtering and decimating process. Hence, inputs that will subsequently be decimated can cause overloads.

The data acquisition system was set up to measure acceleration and force time histories and to calculate power spectra, cross-power spectra, frequency response functions and coherence functions. For a continuous time series, x(t), defined on the interval from 0 to T, the Fourier Spectrum (Fourier Transform), X(f) is defined as

$$X(f) = \int_0^T x(t) e^{i2\pi ft} dt \,, \tag{1}$$

where $i = \sqrt{-1}$, and f = cyclic frequency (Hz). This function is complex and the magnitude is typically plotted in engineering units (EU), such as m/s^2 or g's, versus frequency. The power spectrum is defined as

$$\left| X(f) \right|^2 = X(f) X^*(f) \,, \tag{2}$$

where * denotes complex conjugate. The power spectrum is a real-valued frequency domain function and has the units of (EU)^2.

The power spectral density (autospectral density), $G_{xx}(f)$ is defined as

$$G_{xx}(f) = \frac{2}{T} E\left[\left| X(f) \right|^2 \right], \tag{3}$$

where E[ ] indicates an ensemble average for a specific f over n samples of X(f). This function will often be referred to by the abbreviation PSD. Again, this is a real valued frequency domain function and has the units of $(EU)^2$/Hz.

The cross-power spectrum (cross-spectral density), $G_{xy}(f)$, relating two time histories, x(t) and y(t), is defined as

$$G_{xy}(f) = \frac{2}{T} E\left[X^*(f)Y(f)\right]. \tag{4}$$

The abbreviation CPS will be used to denote cross-power spectrum.

For a linear system the frequency response function (transfer function), H(f), which relates an input, X(f), to a response, Y(f), is defined as

$$H(f) = \frac{Y(f)}{X(f)} = \frac{G_{xy}(f)}{G_{xx}(f)}. \tag{5}$$

This function is abbreviated as FRF throughout this report.

The coherence function, $\gamma_{xy}^2(\omega)$ is used to quantify the linear relationship between the input and the output and is defined to be

$$\gamma_{xy}^2(\omega) = \frac{\left|G_{xy}(\omega)\right|^2}{G_{xx}(\omega)G_{yy}(\omega)}. \tag{6}$$

This function is abbreviated COH throughout this report. In actual dynamic testing discrete time series are measured. The reader is referred to Bendat and Piersol (1980) for discrete representations of the functions listed in Eqs. 1-6.

For ACBT1 the sampling parameters were specified that calculated the FRFs from a 16-s time window discretized with 2048 samples. The FRFs were calculated for a frequency range of 0 to 50 Hz and at a frequency resolution of 0.0625 Hz. A force window was used on the signal from the hammer's force transducer and an exponential window on the signal from the accelerometer. These windows are described in McConnell (1995). AC coupling was specified to minimize DC offsets. The AC coupling filter had been tested when this system was used to test the I-40 Bridge across the Rio Grande in Albuquerque, New Mexico, (Farrar, et al., 1994) and it

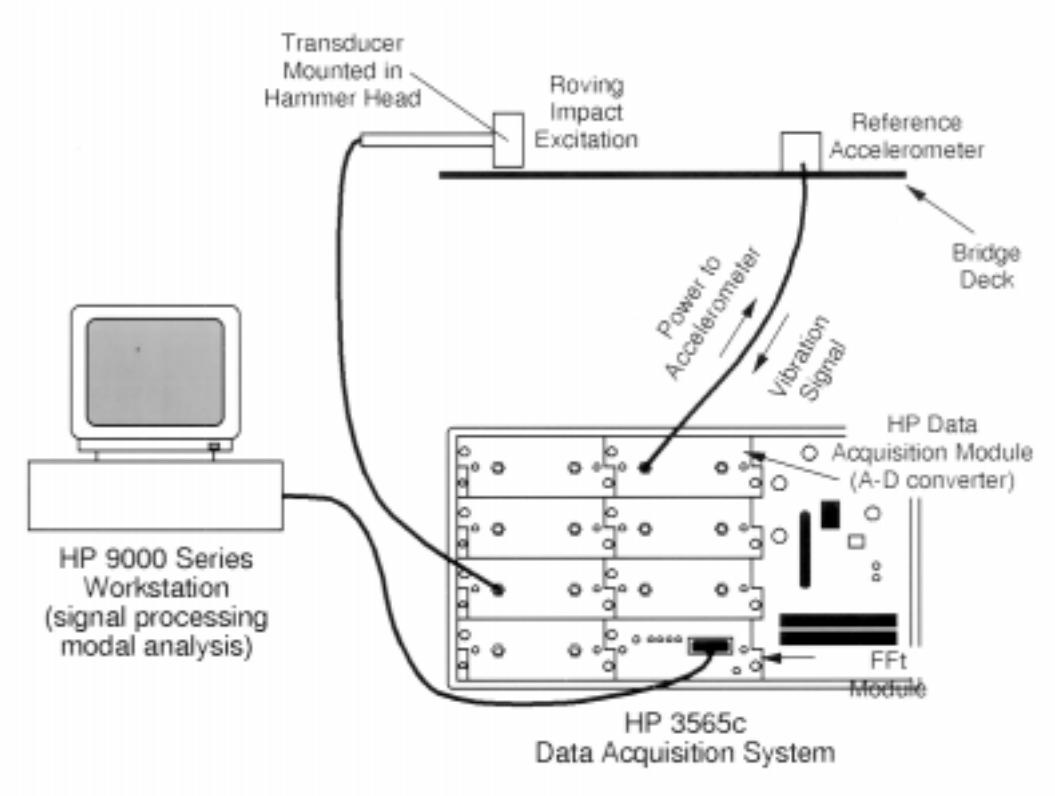

Figure 16. Schematic of the data acquisition equipment.

Figure 17. Data acquistion equipment.

Figure 18. Generator used to power the data acquisition equipment.

was determined that the filter did not attenuate the signal at frequencies above 2 Hz. Therefore, it was concluded that the AC coupling filter would not adversely affect the data in the frequency range of interest. The dynamic ranges for the data acquisition from the accelerometer and the hammer were set at 0.5 and 1 volt peak respectively. Time samples that overloaded these ranges were rejected.

A PCB model 086B50 impact sledge hammer was used to strike the bridge in specified locations. The hammer weighed approximately 53 N (12 lbs) and had a 7.6-cm-diam (3-in.-diam) steel head. A 0.61-m-length (2-ft-length) of MicroDot cable was attached to the hammer. The MicroDot cable was then connected to a long, approximately 30 m (100 ft), RG-58 coaxial cable that was connected to an input module. The hammer tip was one that had been manufactured locally at Los Alamos National Laboratory and was softer than the one designated as "super-soft" by the manufacturer. The custom made tip was used to broaden the impulse that was imparted to structure in an effort to better excite the lower frequency modes of the structure. The hammer and the accelerometer mounting system are shown in Figure 19. To demonstrate the softness of the tip, it was deformed between two fingers as shown in Figure 19.

A PCB model 393C integrated circuit piezoelectric accelerometer was used for the forced vibration measurements. This accelerometer has a nominal sensitivity of 1 V/g, a specified frequency range of 0.01–800 Hz, and an amplitude range of ± 2 g. A MicroDot cable was used to connect the accelerometer to the input module. A 7.6 cm (3 in.) square aluminum mounting block for the accelerometer was attached to the top surface of the bridge with dental cement as shown in Figure 19. The accelerometer was connected to the aluminum block with a 10-32 stud.

A total of 30 impact points were marked on the surface of the bridge as shown in Figure 20. During the impacts the reference accelerometer was located at position 8. Each point was struck

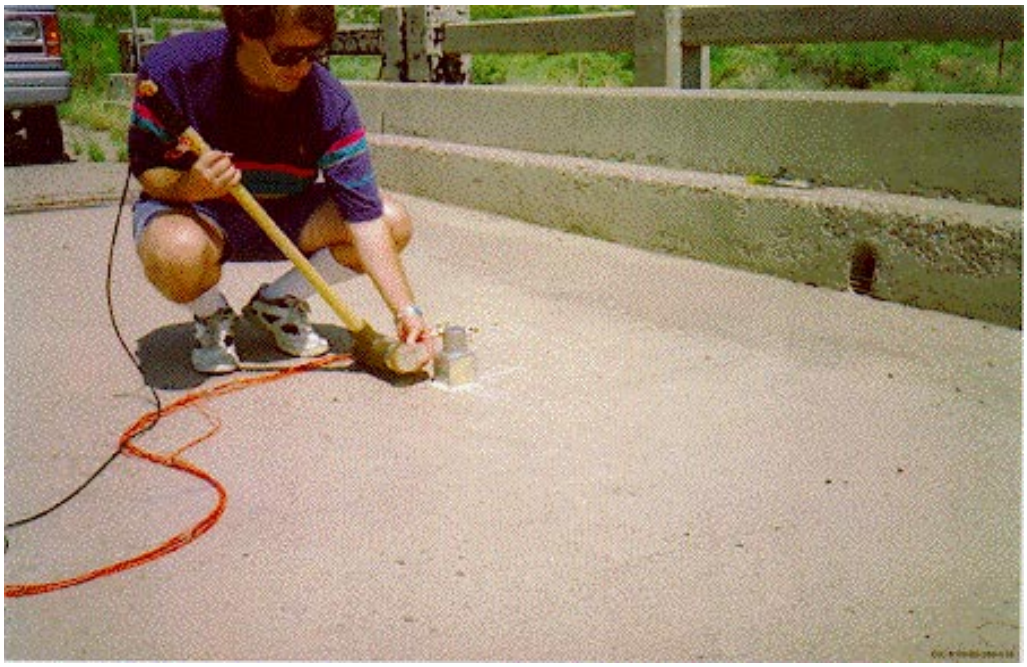

Figure 19. The hammer and accelerometer used for the impact test.

using the impact hammer and both the input force and acceleration were recorded by the data acquisition system. An impact being applied to position 2 with the accelerometer at position 8 is shown in Figure 21. The time histories obtained were subsequently transformed into the frequency domain so that estimates of the PSDs and FRFs could be calculated. These frequency domain functions were used to estimate the dynamic properties (resonant frequencies, mode shapes and modal damping values) of the structure. Ten impacts were applied at each location and the results averaged. With these sampling parameters and the overload reject specified, data were acquired over a time period of approximately three hours. The overload reject option ensured that signals exceeding the specified voltage range were not saved.

b. Results of roving hammer impact test

In this test, the FRFs relating the measured input, that is, the force applied by the hammer, to the measured acceleration responses, were analyzed to estimate the dynamic properties of the structure. Figure 22 shows a typical FRF obtained. The FRF shown in Figure 22 was determined when the hammer was used at location 9 and the accelerometer was located at position 8. A rational-fraction polynomial global curve-fitting algorithm in a commercial modal analysis software package (Structural Measurements Systems, 1987) was used to fit the FRFs and obtain estimates of the bridge's resonant frequencies, mode shapes and modal damping values. A complete description of this experimental modal analysis method is presented in Appendix A. Figure 23 shows the first six modes and associated frequencies of the undamaged bridge. It is clear from this figure that the modes observed are more characteristic of a plate rather than a beam. This feature distinguishes this bridge test from the previous I-40 Bridge test (Farrar et al., 1994). It should be noted that the first bending mode in Figure 23 is not symmetric about the longitudinal axis of the bridge. This result, which will be further discussed in Section IV.B.1, was one of the first indications that environmental effects were influencing the dynamic properties of the bridge.

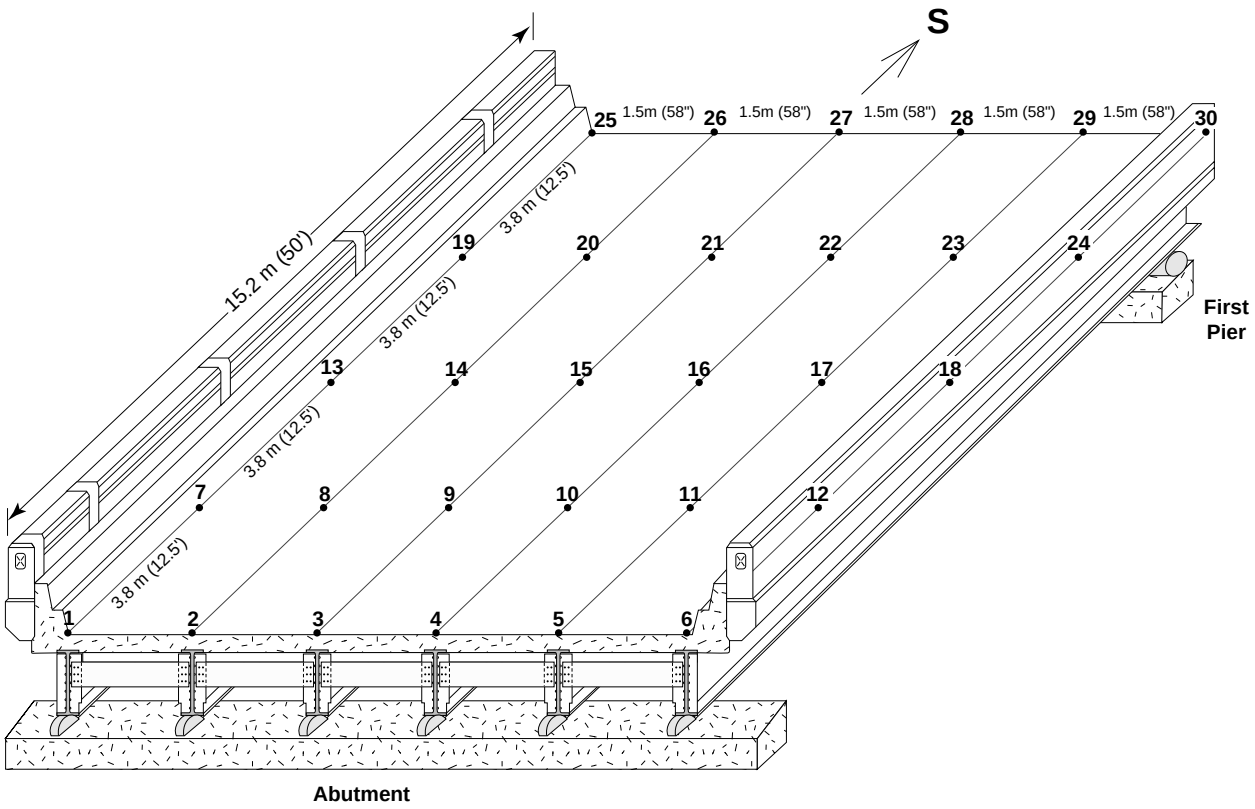

Figure 20. Measurement and excitation locations for the impact test. The reference accelerometer as located at position 8.

Figure 21. An impact being applied to position 2.

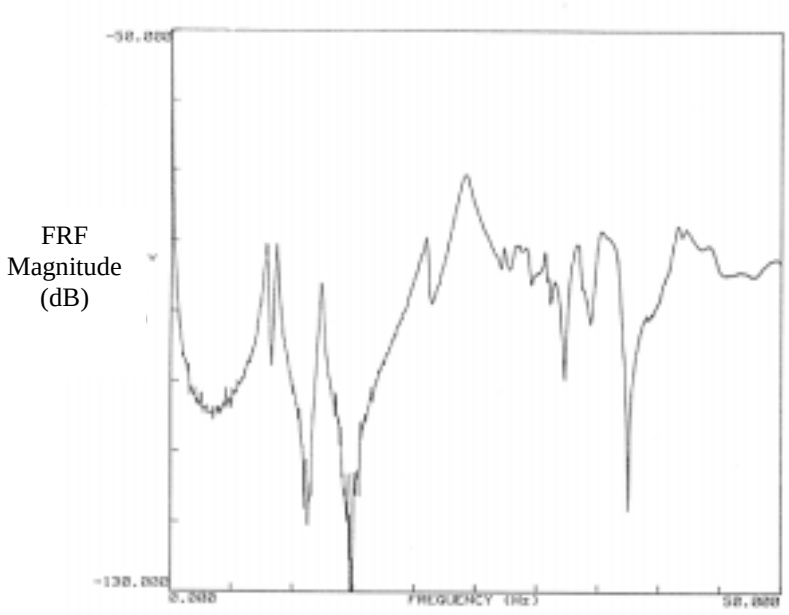

Figure 22. Typical FRF obtained from the impact test. For this FRF, the impact was applied to position 9 and the reference was located at position 8.

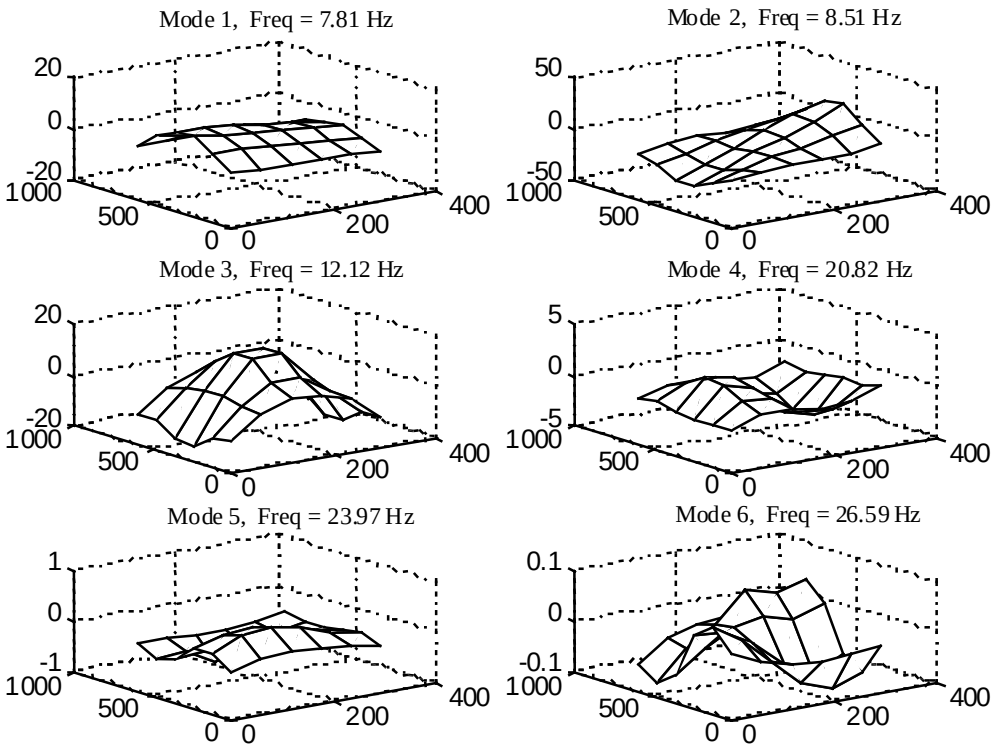

Figure 23. First six mode shapes and frequencies.

2. Single Excitation Point Impact Test Method

One problem with the roving hammer impact tests was the time required to take the data. Using 10 averages of impact applied at 30 locations data acquisition took approximately three hours. As an alternative to the roving hammer impact test a single excitation point test was performed on the bridge on 11/29/95–12/01/95 (ACBT2). This type of test allows for quicker data acquisition, but requires many more accelerometer channels and a longer setup time. A hammer was used to impact the bridge at one location and accelerometers were located at numerous additional locations on the bridge. During these tests the weather was warm, approximately 20°C (65–70°F), sunny, and there was negligible wind. These measurements were intended to confirm the frequencies and mode shapes determined from data acquired during the previous roving hammer impact tests and to examine the variability introduced into estimates of dynamic properties by using various parameter identification techniques. Also, several spans were tested in addition to the one span tested in the roving hammer impact test. Excitation from traffic on the adjacent bridges could be felt during the impact testing of the bridge, but no attempt was made to characterize the input from the adjacent bridges.

a. Experimental procedure and equipment

The data acquisition system, hammer, and system parameters used for the single excitation point test were identical to those used for the roving hammer impact test. The primary difference was that instead of a single accelerometer on the deck, a total of 28 PCB model no. 336C integrated circuit piezoelectric accelerometers were attached to the bottom of the longitudinal I-beams using PCB model 080A27 magnetic mounts as shown in Figure 24. These accelerometers had a nominal sensitivity of 1 V/g, a specified frequency range of 1–2000 Hz, and an amplitude range of ± 4 g. The grid of accelerometer locations is shown in Figure 25. A total of four spans were tested using this grid of accelerometers. The spans tested were spans one, two, three and six where span one refers to the northern most span of the bridge.

Figure 24. Accelerometer and magnetic mount.

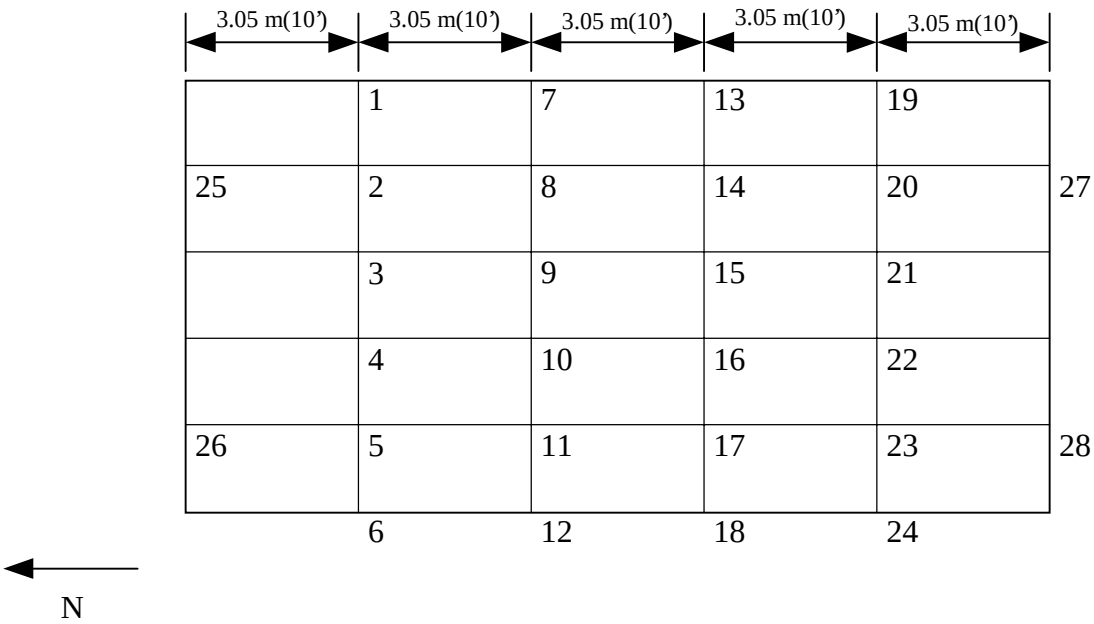

Figure 25. Accelerometer locations for the single excitation test.

The impact location was on the surface of the deck at location 8 in the roving hammer impact test (Figure 20) which was approximately 2.5 feet south of point 2 in Figure 25. Unfortunately an accelerometer was not placed on the deck at the driving point so it was not possible to obtain mass normalized mode shapes.

b. Results of the single excitation point impact test

As in the roving hammer impact test the FRFs were used to determine the dynamic properties of the structure. In addition to using the SMS rational polynomial global curve-fitting algorithm the ERA time domain method was also used to identify the modes and frequencies. A complete discussion of the ERA method is presented in Appendix B. The ERA method was used because it has been shown [James, Carne, and Lauffer (1995)] that it can also be applied to ambient data in the form of cross correlation functions to identify the frequencies, damping and mode shapes. The ERA procedure is based upon the formation of a Hankel matrix containing the measured discrete-time impulse response data, computed using the inverse fast Fourier transform of the measured FRFs. The shift in this matrix from one time step to the next is then used to estimate a discrete-time state space model for the structure. This data set contained 28 responses and 1 reference.

The model resulting from the ERA analysis always contains a large number of computational modes, that is, modes identified by the ERA analysis that do not correspond to physical modes. Thus, it is necessary to apply some discrimination procedures to select the modes that are physically meaningful. There are three indicators developed specifically for use with ERA: Extended Modal Amplitude Coherence (EMAC), Modal Phase Colinearity (MPC) and Consistent Mode Indicator (CMI), which is the product of EMAC and MPC [Pappa, Elliott, and Schenk (1993)]. EMAC is a measure of how accurately a particular mode projects forward (in

time) onto the impulse response data. MPC is a measure of how colinear the phases of the components of a particular complex mode are. If the phases are perfectly linear (i.e. either in phase or 180 degrees out of phase with each other), this mode is exactly proportionately damped, and can then be completely represented by a corresponding real mode shape. Thus, EMAC is a temporal quality measure and MPC is a spatial quality measure. Typically, values of EMAC = 0.7, MPC = 0.7 and CMI = 0.5, are used as initial values for "filtering" the ERA results.

A comparison of the frequencies and damping of the first six modes from the roving hammer impact test and the single excitation point test for span one are shown in **Table 1**. From this table it can be seen that the maximum difference between frequencies identified by the two parameter identification techniques is approximately 1.2%. The maximum difference between frequencies identified from data collected during the roving hammer impact test and the single excitation point test is approximately 3.6%. Although the ambient temperature of the bridge was not measured during either one of these tests, this difference is assumed to be a result of natural variations in the frequencies of the bridge caused by changing environmental conditions. This result helped motivate a third Alamosa Canyon Bridge test to be discussed in Section IV.B.1 where data was taken over a 24 hour period to specifically examine the influence of changing environmental conditions on the identified dynamic properties of the bridge. It can also be seen from **Table 1** that the damping values vary significantly between the two tests as well as between the two identification methods. This result is not unexpected because damping values typically have the greatest uncertainty associated with them. However, with the exception of the damping value identified for Mode 4 using the ERA method, the general trends regarding relative magnitudes of the modal damping values are consistent between the various experimental modal analysis procedures.

Table 1. Comparison of the frequencies and damping for the roving hammer impact test and the single excitation point impact test using both the rational polynomial and the ERA parameter identification methods.

Mode	**Frequency – Hz (Damping – %)**		
	Roving Hammer	**Single Excitation Point**	
	Rational Polynomial	**Rational Polynomial**	**ERA**
1	7.81 (1.8)	7.66 (2.5)	7.73 (2.5)
2	8.51 (1.1)	8.20 (1.6)	8.30 (1.8)
3	12.1 (1.0)	11.8 (1.2)	11.8 (1.4)
4	20.8 (2.0)	20.4 (3.6)	20.4 (1.2)
5	24.0 (2.5)	23.4 (3.1)	23.5 (3.1)
6	26.6 (1.7)	26.1 (2.1)	26.2 (2.0)

In addition to retesting span one with the single excitation point impact test method, several additional spans were also tested. According to the drawings the spans were identical in design and should therefore have almost identical frequencies and modes. A comparison of the frequencies and damping for spans one, two, three and six are shown in Table 2. The rational polynomial method was used to identify the frequencies and modes in this table. It is immediately apparent from Table 2 that some of the additional spans appear to have additional modes. The numbering scheme used for span one was used in **Table 2** with the additional modes identified from tests on spans 2, 3 and 6 being designated by letters. Complex Mode Indicator Functions (CMIFs) for spans one and two are shown in Figure 26 and Figure 27. The CMIF is a measure of the maximum singular values of the FRF matrix at each frequency bin. The CMIF produces a peak at each modal frequency proportional to the overall magnitude of the frequency response at that bin across all measured degrees of freedom. This proportionality is advantageous because it allows the user to get a feel for the contribution of each mode to the response of the structure. When using the global rational polynomial curve fitting method, the CMIF was used to help determine the frequency bins used for the fitting of each mode. Clearly from Figure 26 and Figure 27 there are additional peaks in the CMIF for span two compared to the CMIF for span one. The CMIFs for spans three and six were similar to that of span two. Modes 2 and 2a of span two looked almost identical. These results from spans two, three and six motivated a future test discussed in Section IV.A.2, where spans one, two and three were all instrumented at the same time in an attempt to gain a better understanding of the dynamics of the structure. The frequencies of the low frequency modes are typically greater for span one than for the other spans. This result could be a consequence of span one being adjacent to the abutment.

Table 2. Comparison of frequencies and damping for four spans of the Alamosa Canyon Bridge.

	Frequencies – Hz (Damping – %)			
Mode	**Span 1**	**Span 2**	**Span 3**	**Span 6**
1	7.81 (1.8)	7.02 (2.9)	7.07 (3.5)	7.02 (3.0)
2	8.51 (1.1)	8.07 (0.8)	8.19 (1.9)	7.91 (2.2)
2a	–	9.10 (3.0)	9.17 (5.0)	9.27 (0.9)
3	12.1 (1.0)	11.9 (1.1)	12.0 (1.3)	11.5 (0.9)
3a	–	12.5 (1.9)	12.6 (1.2)	12.4 (1.2)
4	20.8 (2.0)	19.9 (1.4)	21.4 (1.4)	21.1 (3.6)
5	24.0 (2.5)	23.9 (2.3)	24.1 (3.9)	24.0 (2.8)
5a	–	–	–	25.9 (3.3)
6	26.6 (1.7)	26.9 (1.8)	26.7 (2.7)	27.9 (2.9)

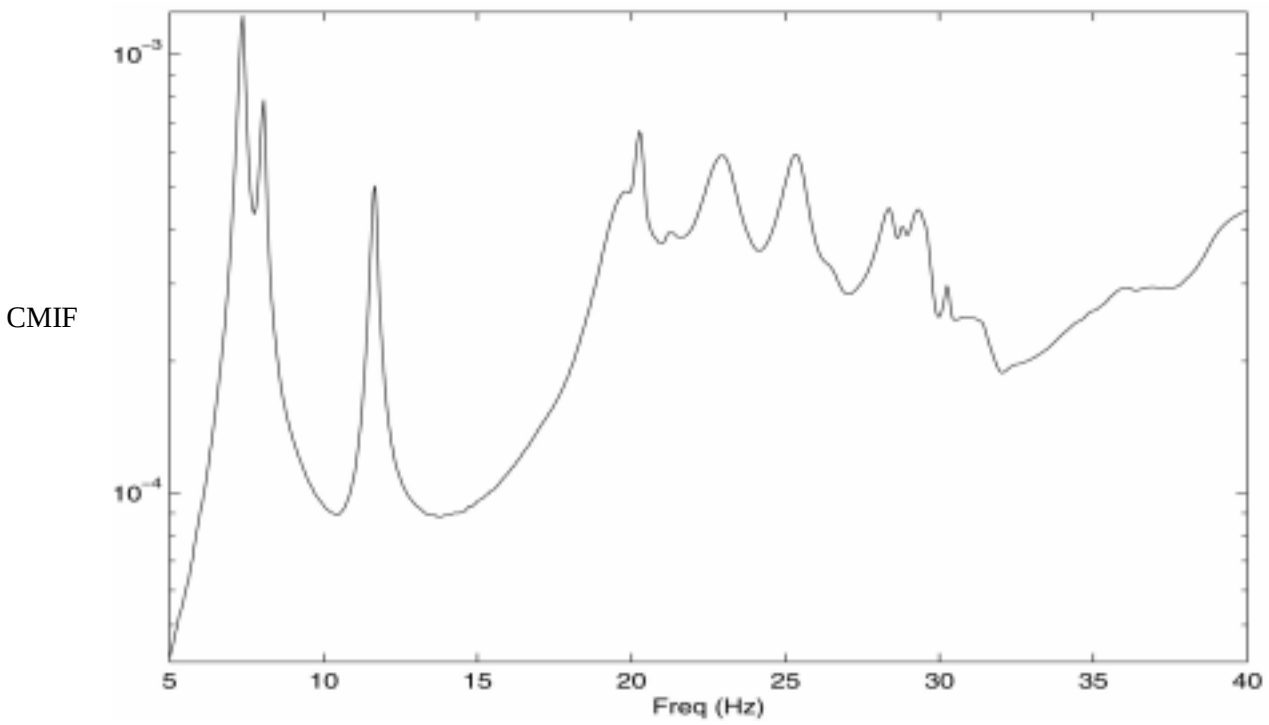

Figure 26. CMIF for span 1.

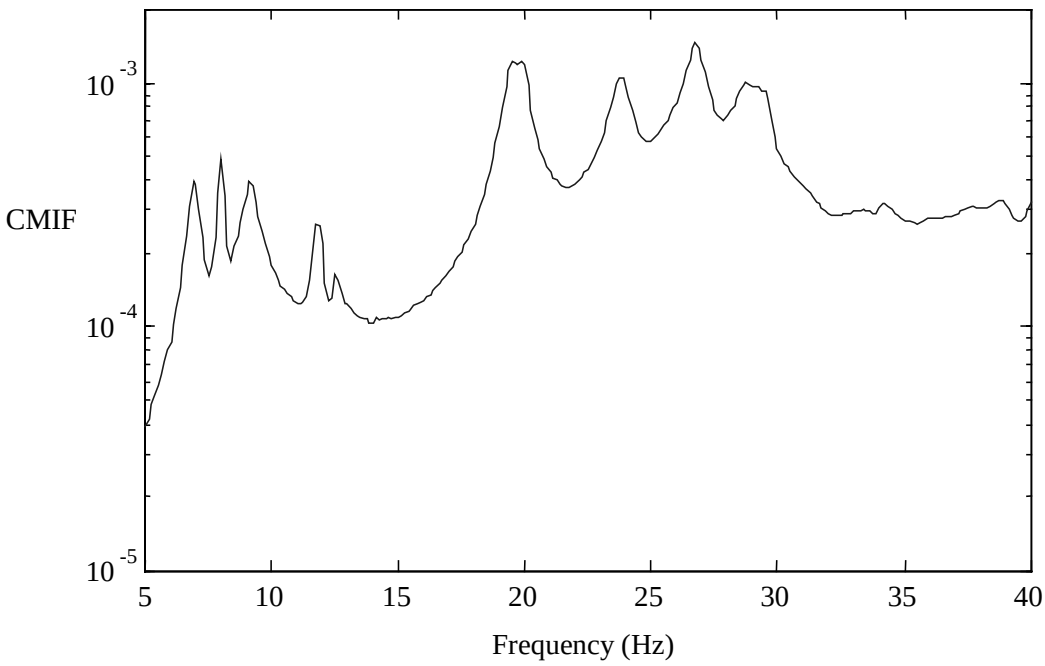

Figure 27. CMIF for span 2.

B. Ambient Vibration Tests

1. Ambient Vibration Test Following the Roving Hammer Impact Test

Following the roving hammer impact tests on 8/29/95 (ACBT1), two sets of data were taken using ambient vibrations from different sources. The first ambient vibration source was provided by the traffic on the adjacent bridge that was transmitted through the ground to the piers and abutment of the bridge being tested. This test will be referred to as Ambient Test One. The adjacent bridge with a truck about to drive over it is shown in Figure 28. The distance between the two bridges is approximately 22.9 m (75 feet). The second ambient vibration source was provided by driving a Ford Taurus sedan over the bridge, and the test using this source will be referred to as Ambient Test Two. The Ford Taurus and the van containing the instrumentation are shown in Figure 29. During all ambient tests, no attempt was made to characterize the input to the bridge.

a. Experimental procedure and equipment

The data acquisition system, cabling and generator used for the ambient vibration tests were identical to those used for the forced vibration test. PCB model no. 336C integrated circuit piezoelectric accelerometers were used for the ambient vibration measurements. MicroDot cables were used to connect the accelerometers to the input modules. A total of four accelerometers were used for the two ambient vibration tests done on 8/29/95. These accelerometers were located on the concrete deck at positions 8, 11, 20, and 23 in Figure 20.

Figure 28. Source of excitation for ambient test one.

Figure 29. Ford Taurus used for ambient test two and the van containing the data acquisition equipment.

The data acquisition system was set up to measure acceleration time histories and calculate cross-power spectra (CPS). The CPS were calculated with the accelerometer at location 8 specified as the reference channel. Sampling parameters were specified that calculated the CPS from 8-s time windows discretized with 2048 samples. The CPS were calculated for a frequency range of 0 to 100 Hz with a frequency resolution of 0.125 Hz. Hanning windows were applied to the time signals to minimize leakage and AC coupling was specified to minimize DC offsets.

b. Results

Typically in modal vibration testing, FRFs relating a measured input, usually force, to a measured response such as acceleration are used to estimate the dynamic properties of a structure (as in the forced vibration test described earlier). However, when a bridge is subjected to traffic excitation, it is difficult, if not impossible, to measure the input to the structure. The extension of system identification methods to ambient vibration cases where an input cannot be measured has received considerably less attention in the technical literature.

From the definition of the CPS it is evident that two measured responses will be correlated only at the resonant frequencies of the structure. Therefore, the CPS will show peaks corresponding to the resonant frequencies. A typical cross power spectrum between position 8 and position 23 using the two different sources of ambient vibration, traffic on the adjacent bridge and driving the Ford Taurus over the bridge, is shown in Figure 30 and Figure 31 respectively.

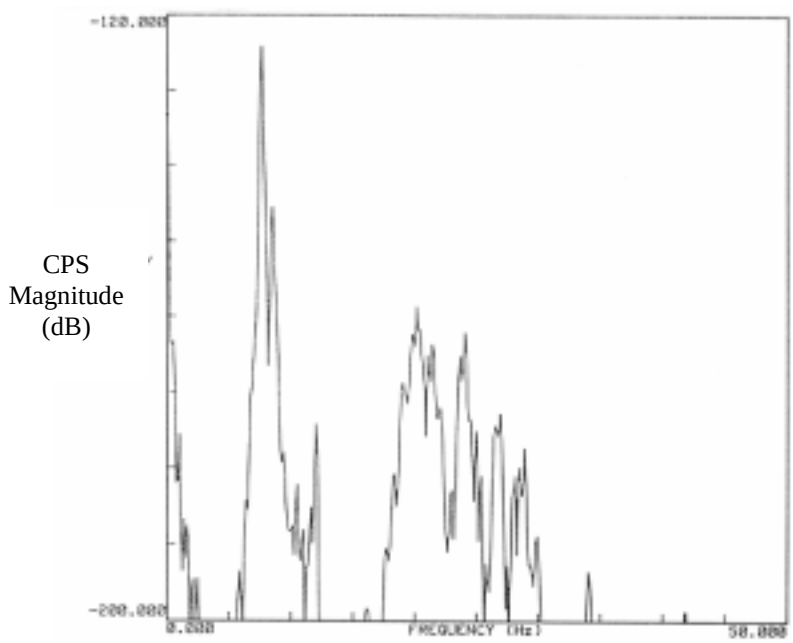

Figure 30. CPS (magnitude only) obtained from Ambient Test One using the accelerometers at point 8 and 11. The accelerometer at point 8 was used as the reference.

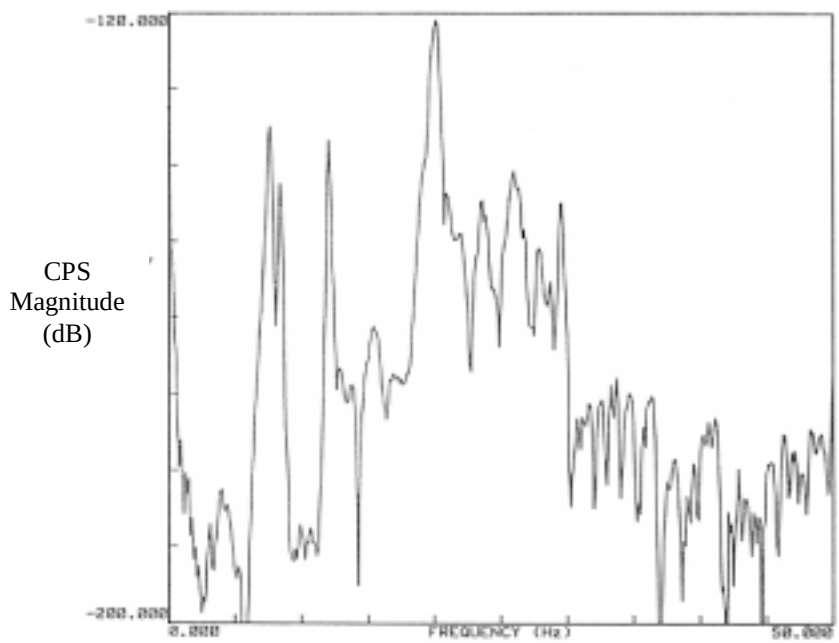

Figure 31. CPS obtained from Ambient Test Two using the accelerometers at points 8 and 11. The accelerometer at point 8 was used as the reference.

The resonant frequencies can be estimated using visual inspection to locate peaks in the CPS. Mode shapes are estimated from the relative magnitudes of these peaks (relative phase information must be obtained from either the CPS or FRF) and modal damping values can be obtained by applying the half power bandwidth (HPBW) method to these peaks. This method has been used in numerous previous investigations, McLamore, et al. (1971) for example. Drawbacks of this method that have been previously identified by Abdel-Ghaffar and Housner (1978) are the need for very high frequency resolution (the necessary resolution has been quantified by Bendat and Piersol, (1980)) around the resonance to adequately define the half-power points and the difficulties in identifying closely spaced modes. This method of obtaining the frequencies and mode shapes will be referred to as the "peak picking" method.

Because only four accelerometers were used it was difficult to compare the mode shapes obtained from the ambient test with those from the impact test. The first six frequencies were easily compared however. **Table 3** provides a comparison of the resonant frequencies determined from the two ambient vibration tests with those determined during the roving hammer impact tests.

Table 3. Resonant frequencies identified from ambient vibration response compared with similar quantities identified from roving hammer impact tests for span one.

Mode	**Frequencies – Hz (Damping – %)**		
	Impact Test–rational polynomial method	**Ambient Test 1–complex exponential method (Traffic on the adjacent bridge)**	**Ambient Test 2–complex exponential method (Car driving on bridge)**
1	7.8 (1.8)	7.7 (1.1)	7.7 (2.1)
2	8.5 (1.1)	8.6 (1.8)	8.5 (2.0)
3	12.1 (1.0)	12.2 (0.76)	12.1 (0.92)
4	20.8 (2.0)	20.2 (1.2)	20.3 (1.3)
5	24.0 (2.5)	24.1 (0.56)	24.0 (1.1)
6	26.6 (1.7)	26.5 (0.64)	26.1 (0.64)

Values reported for the ambient measurement are the average obtained by applying the complex exponential curve-fit procedure to the three CPS measured during each test. Details of the complex exponential curve-fit procedure can be found in Maia and Silva (1997). Application of this curve-fit procedure to ambient data can be found in Farrar et al. (1994) and Farrar and James (1997). From this table it is evident that the differences between the resonant frequencies measured during the ambient vibration test and those measured during the forced vibration test are less than 2.5%. Because the hammer test and the ambient tests were performed at different times during the day, this difference in frequency could simply be the variation of the natural frequency of the structure as a function of the temperature. This hypothesis was investigated in detail during subsequent tests. Magnitude and phase information showed that the modes identified from the ambient tests were the same as those found in the impact test to the extent that this limited number of measurement points could provide comparative data.

2. Ambient Vibration Test Following the Single Excitation Point Test

Following the single excitation point tests done at the end of November 1995, ambient data was taken for span three using the same two excitation sources discussed earlier.

a. Experimental procedure and equipment

The data acquisition system, cabling and generator used for the ambient vibration tests were identical to those used for the single excitation point impact tests discussed earlier. The primary difference between this ambient test and the previous one was that 28 accelerometers were used in the configuration shown in Figure 25 rather than just using four as discussed earlier. The data acquisition system was set up to measure acceleration time histories and to calculate cross-power spectra (CPS) using the accelerometer at location 2 in Figure 25 as the reference channel. Sampling parameters were specified that calculated the CPS from 8-s time windows discretized with 2048 samples. The CPS were calculated for a frequency range of 0 to 100 Hz with a frequency resolution of 0.125 Hz. Hanning windows were applied to the time signals to minimize leakage and AC coupling was specified to minimize DC offsets.

b. Results

The frequencies for the structure using the ambient data were initially determined using the peak picking method as discussed earlier. To circumvent the drawbacks of the peak picking method, an ambient vibration system identification method developed at SNL was applied to the measured response data obtained from the Alamosa Canyon Bridge. James, Carne, and Lauffer (1995), have shown that for an input, which is not measured but assumed to be white noise, the cross-correlation function between two response measurements (the inverse Fourier transform of the CPS) is the sum of decaying sinusoids and these decaying sinusoids have the same damped resonant frequencies and damping ratios as the modes of the system. Therefore, the cross-correlation functions will have the same form as the system's impulse response function, and, hence, time domain curve-fitting algorithms such as the polyreference method (Vold and Rocklin, 1982), complex exponential method (Ewins, 1985) or the ERA method (Juang and Pappa, 1985) can be applied to these functions to obtain the resonant frequencies and modal damping exhibited by the structure. These curve-fitting methods have the ability to identify closely spaced modes and, in general, provide a more accurate method for estimating damping than the HPBW method. Mode shapes are determined from magnitudes and phases in the CPS at the identified resonant frequencies.

A comparison of the ambient results to those obtained using the single excitation point impact test method is shown in Table 4. The same mode numbering scheme used for **Table 2** was also used for **Table 4**. Visual inspections of the mode shapes were used to correlate the modes identified from the ambient data to the corresponding modes identified from the hammer test. Using traffic on the adjacent bridge as the excitation source resulted in time responses of considerably smaller amplitude. Therefore, the signal to noise ratio was larger for this data. Both of the ambient tests resulted in additional peaks in the CPS that were identified as modes even though these did not appear in the single excitation point impact tests. A difficulty when analyzing ambient response data is that one cannot always distinguish between peaks in the CPS caused by the modal response of the structure or peaks resulting from the frequency content of

the input. When comparing identified frequencies from the hammer test and the ambient tests, the largest difference seen was approximately 3%. A 2.3% difference in frequencies was observed when the peak-picking method was applied to data obtained during tests using the different ambient excitation sources. This error is comparable to that obtained from tests of span 1 using similar sources of excitation as summarized in **Table 3**. A similar difference was seen when results from the peak-picking method and the ERA method are compared using the same data. It is important to note, however, that the ERA method was unable to identify some of the modes identified by applying either the peak-picking method to the ambient data or the rational polynomial method to the hammer data. The variations in the frequencies between the various tests summarized in **Table 4** could be a result of the data being taken at different times during the day.

Table 4. Comparison of the single excitation point impact test and the ambient tests for span three of the Alamosa Canyon Bridge.

	Frequencies – Hz (Damping – %)				
		Ambient Test 1 (Traffic on the adjacent bridge)		**Ambient Test 2 (Car driving on bridge)**	
Mode	**Hammer**	**Peak Pick**	**ERA**	**Peak Pick**	**ERA**
1	7.07 (3.5)	7.00	6.95 (2.9)	7.00	7.06 (3.2)
2	8.19 (1.9)	8.00	–	8.00	8.05 (3.5)
2a	9.17 (5.0)	9.00	9.45 (2.1)	9.00	–
3	12.0 (1.3)	12.0	12.1 (1.4)	11.8	11.8 (1.7)
3a	12.6 (1.2)	12.6	12.7 (1.4)	12.4	12.4 (1.6)
4	21.4 (1.4)	21.6	21.8 (0.9)	21.1	21.2 (2.1)
5	24.1 (3.9)	23.9	25.0 (0.9)	24.6	23.9 (2.4)
5a	–	24.2	–	–	24.6 (1.6)
5b	–	24.8	–	–	25.4 (2.4)
5c	–	25.5	–	–	–

C. Lessons Learned from the Preliminary Tests

A number of valuable lessons were learned from the first two Alamosa Canyon tests that helped in the planning of subsequent tests.

1. A driving point measurement needs to be taken so that mass normalized modes can be determined.
2. The environmental variability of the modal properties of the structure clearly need further study. To quantify the variability, data should be taken at different times during the day and the corresponding temperature distribution across the bridge needs to be measured.
3. The test-to-test random variability needs to be statistically quantified to determine if the observed variability is just caused by random experimental error or is there some systematic experimental error that needs to be considered.
4. The data needs to be analyzed while still in the field to verify that it is adequate.

IV. VIBRATION TESTS PERFORMED ON THE ALAMOSA CANYON BRIDGE

Based on the findings of the preliminary experimental vibration tests performed on the Alamosa Canyon Bridge, a series of tests were performed to examine the variability of the bridge modal properties and to apply statistical techniques to the data in an attempt to quantify the variability in these properties. These tests were performed from July 29, 1996 to Aug. 3, 1996 (ACBT3) and from July 21, 1997 to July 23, 1997 (ACBT4). A small shaker was available for the test in July 1997 so the previously discussed hammer and ambient results can be compared to those obtained using the shaker.

A. Forced Vibration Tests

1. Linearity and Reciprocity Checks

Almost all modal analysis algorithms are developed based on the assumption that the structure will exhibit time-invariant response, linearity and reciprocity. A structure is said to be linear if the FRFs obtained are independent of the input magnitude. Reciprocity means that the measured FRF for a force at location j and a response at location i should correspond directly with the measured FRF for a force at location i and response at location j. Therefore, before any tests were performed to investigate the temporal variability of modal parameters, tests were first conducted to check the validity of the assumptions regarding linearity and reciprocity.

a. Experimental procedure and equipment

New, more compact, data acquisition and analysis equipment (Figure 32) was purchased for the vibration tests performed in July of 1996 and July of 1997. The data acquisition system consisted of a Toshiba TECRA 700 laptop computer, four Hewlett Packard (HP) 35652A input modules that provide power to the accelerometers and perform analog to digital conversion of the accelerometer signals, an HP 35651A signal processing module that performs the needed fast Fourier transform calculations, and a commercial data acquisition/signal analysis software package produced by HP. The same 3500 watt GENERAC Model R-3500 XL AC generator was used to power this system.

Figure 32. New, more compact, data acquisition and analysis equipment and laptop computer.

The data acquisition system was set up to measure acceleration and force time histories and to calculate power spectra, cross-power spectra, FRFs and coherence functions. Sampling parameters were specified that calculated the FRFs from a 16-s time window discretized with 2048 samples, The FRFs were calculated for a frequency range of 0 to 50 Hz at a frequency resolution of 0.0625 Hz. A force window was applied to the signal from the hammer's force transducer and exponential windows were applied to the signal from the accelerometers. AC coupling was specified to minimize DC offsets.

A PCB model 086B50 impact sledge hammer was used to provide the excitation source. The hammer weighed approximately 53.4 N (12 lbs) and had a 7.6-cm-diam (3-in.-diam) steel head. The sensor in the hammer had a nominal sensitivity of 0.73 mV/lb and a peak amplitude range of 5000 lbs. A hammer tip specially manufactured at Los Alamos National Laboratory was used to broaden the time duration of the impact and, hence, better excite the low frequency response of the bridge.

A Wilcoxon Research model 736T accelerometer was used to make the driving point acceleration response measurement adjacent to the hammer impact point. This accelerometer has a nominal sensitivity of 100 mV/g, a specified frequency range of 5–15,000 Hz, and a peak amplitude range of 50 g. Two 2.54-cm-sq (1-in.-sq) aluminum blocks were attached to the top surface of the bridge using epoxy in order to mount the driving point accelerometers.

PCB model 336C piezoelectric accelerometers were used for the vibration measurements. These accelerometers have a nominal sensitivity of 1 V/g, a specified frequency range of 1–2000 Hz, and an amplitude range of ± 4 g. All accelerometers were mounted to the bottom flange of the steel girders using PCB model 080A05 magnetic mounts.

A total of 31 acceleration measurements were made on the concrete deck and on the girders below the bridge as shown in Figure 33. Five accelerometers were spaced along the length of

each girder. Because of the limited number of data channels measurements were not made on the girders at the abutment or at the pier. From the preliminary vibration tests it was known that these points have very small displacement so when plotting the mode shapes it was assumed that the mode shape amplitudes at the ends were zero. Two excitation points were located on the top of the concrete deck. Point A was used as the primary excitation location. Point B was used to perform a reciprocity check. The force-input and acceleration-response time histories obtained from each impact were subsequently transformed into the frequency domain so that estimates of the PSDs, FRFs, and coherence functions could be calculated. Thirty averages were typically used for these estimates. With the sampling parameters listed above and the overload reject specified, data acquisition for a specific test usually occurred over a time period of approximately 30–45 minutes.

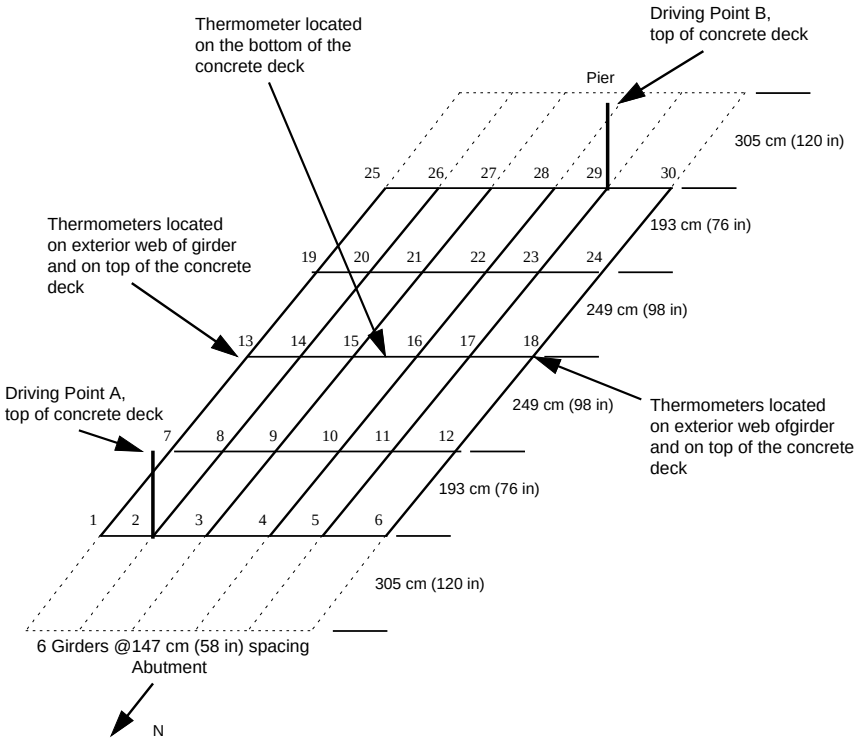

Figure 33. Accelerometer, impact, and thermometer locations.

Five indoor-outdoor digital-readout thermometers were located across the center of the span. Two thermometers were positioned such that their outdoor sensor was taped to the outside web surface at midheight of the exterior girders (Figure 34). The indoor readings from these two thermometers were made on the inside, bottom flange of the exterior girders. A third thermometer was taped to the underside of the concrete deck at the middle of the span. The outside sensor for this thermometer was located adjacent to the indoor sensor yielding almost identical temperature readings. The two remaining thermometers were located on the topside of the bridge (Figure 35). The outside sensors were taped to the bridge deck immediately adjacent to the concrete curbs. The indoor sensor was located on the top of the guardrail. All sensors were shaded from direct sun light either by the bridge itself or by shades made from duct tape and plastic cups. All temperature readings were made by visual inspection of the thermometers.

Figure 34. Indoor-outdoor thermometer taped to the exterior girders.

Figure 35. Indoor-outdoor thermometer located on the deck of the bridge.

b. Linearity and reciprocity test results

Ideally a linearity check should be performed over the expected range of operating loads, but this linearity test was limited to what could be obtained using the instrumented hammer. Measurements were made using two impact levels, whose PSD amplitudes were different by a factor of approximately 5. Figure 36 shows an overlay of the input PSDs and Figure 37 shows

the corresponding overlay of FRF magnitudes when these inputs were applied at Pt. A and response measurements were made at location 6 (see Figure 33). These tests were performed sequentially between 4:00 and 6:00 AM when temperature gradients across the bridge were negligible. Figure 37 shows that the structure was exhibiting linear response in the range of 5 to 25 Hz. Above 30 Hz there is a noticeable difference in the two measurements suggesting the possibility that nonlinearities were excited in this frequency range or that signal-to-noise ratios were poor thus providing the appearance of nonlinear response. This frequency range also corresponds to lower coherence in the measurements as shown in Figure 38. In general the coherence functions for these measurements were greater than 0.9 across the entire spectrum. The coherence was observed to improve for the higher magnitude input.

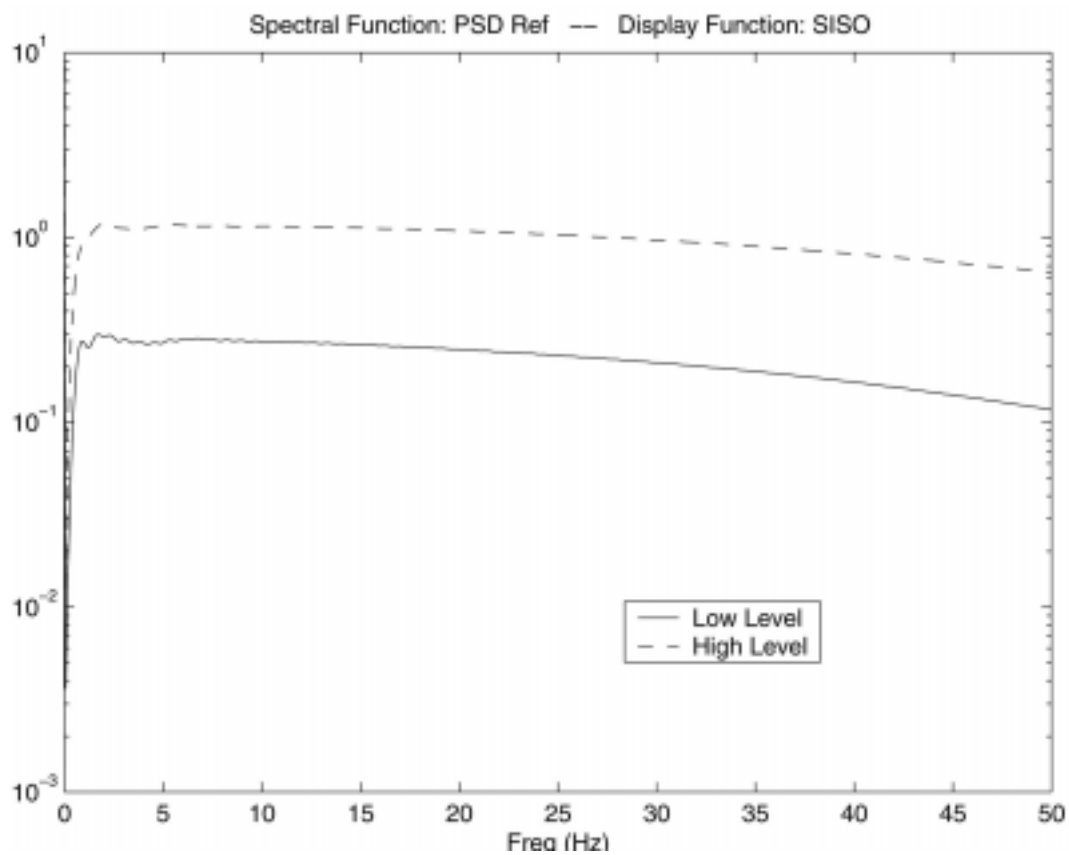

Figure 36. PSDs of impact excitations used in the linearity check at driving point A.

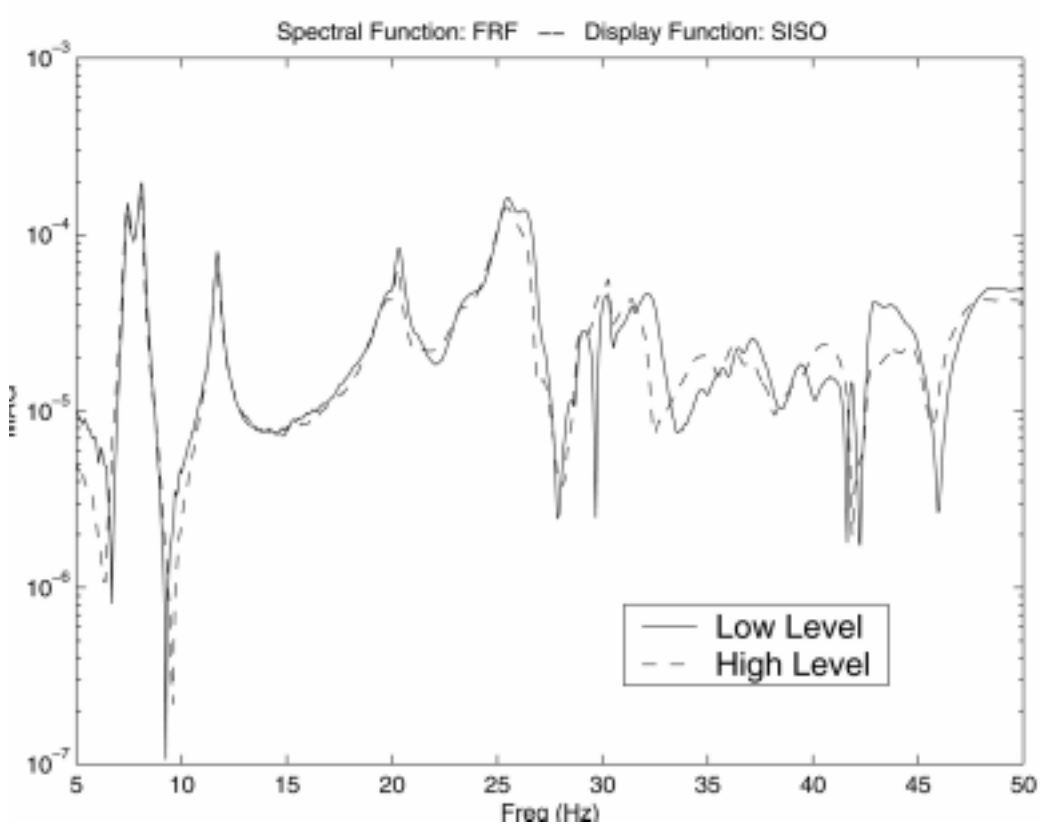

Figure 37. FRF magnitudes measured at location 6 (impact appied at point B).

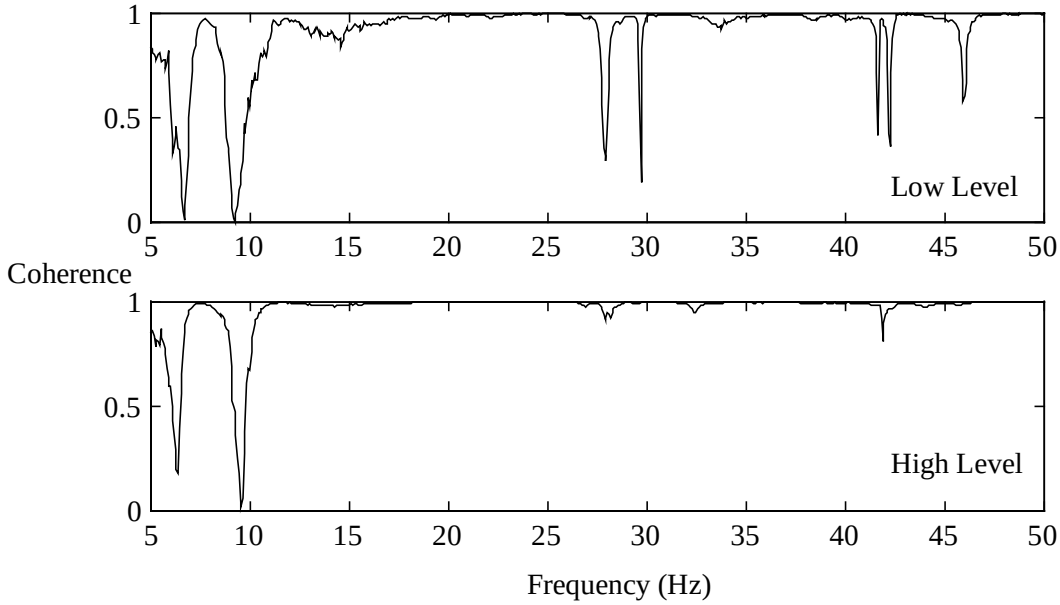

Figure 38. Coherence functions for the FRFs measured at location 6 for the low and high excitation levels.

Figure 39 shows the FRF magnitudes for an impact applied at pt. A (see Figure 33) and a response measured at Point B. Also shown in this figure is the FRF magnitude for an impact applied at pt. B and a response measured at Point A. Coherence plots corresponding to the reciprocity results shown in Figure 39 are shown in Figure 40. These figures demonstrate the reciprocity of the entire system, including the structure and the data acquisition system. A plot of the FRF magnitudes when the accelerometers at pts. A and B have been switched is shown in Figure 41 and the corresponding coherence functions in Figure 42. By switching the accelerometers the reciprocity being measured is that of the structure alone. From Figure 39 and Figure 41 it is evident that the structure itself is exhibiting reciprocity in the 5 to 25 Hz region. Above thirty Hz one could not make this claim. Also, when Figure 39 is compared to Figure 41 it is evident that the electronics of the data acquisition system are contributing to the loss of reciprocity, particularly at the third natural frequency near 11.5 Hz.

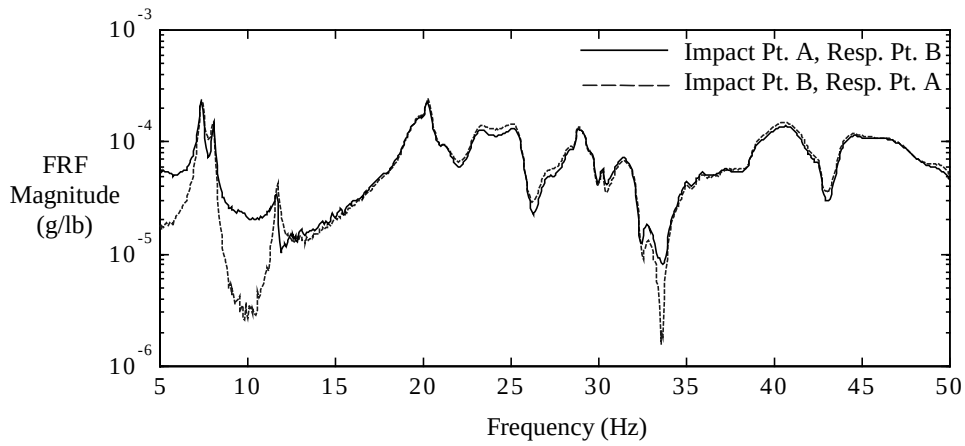

Figure 39. FRF magnitudes used to check reciprocity of the structure and the electronics.

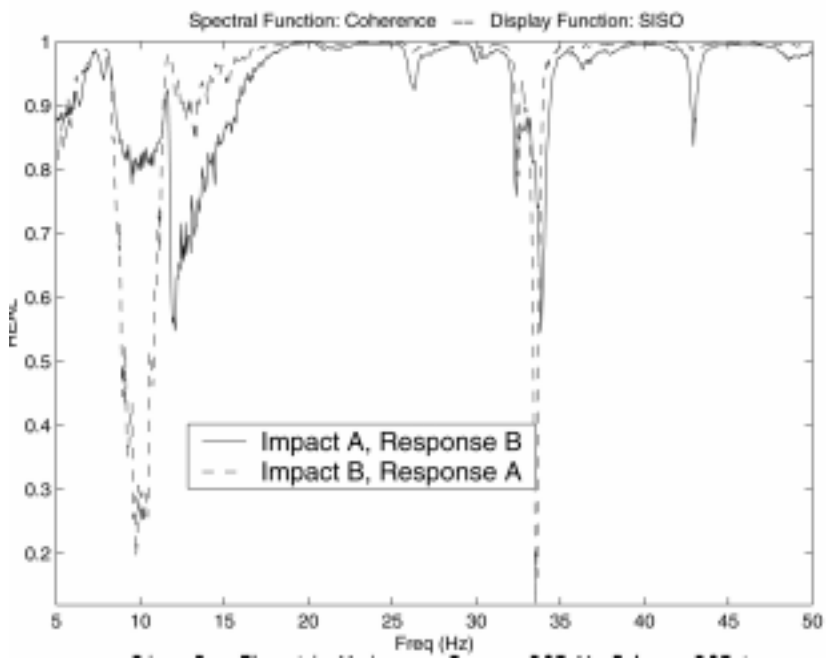

Figure 40. Coherence functions of the FRFs used to check the reciprocity of the structure and the electronics.

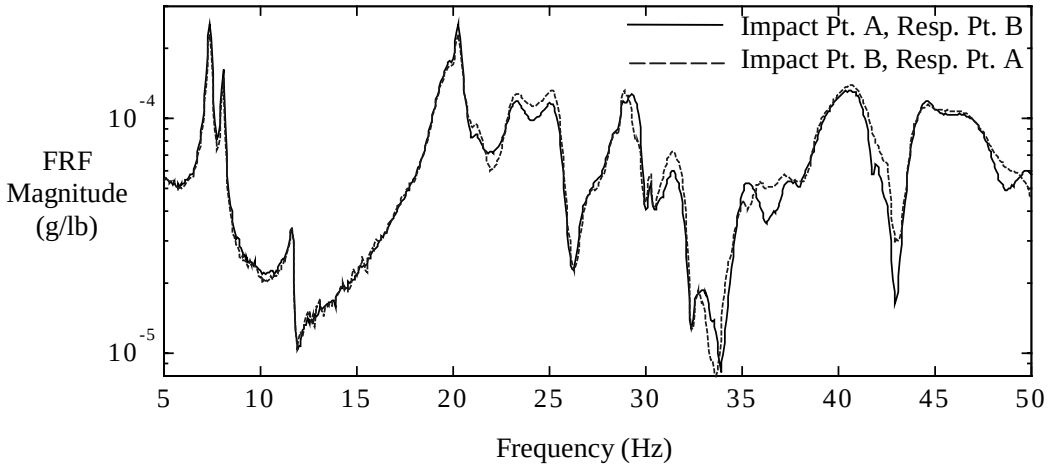

Figure 41. FRF magnitudes to check reciprocity of the structure only.

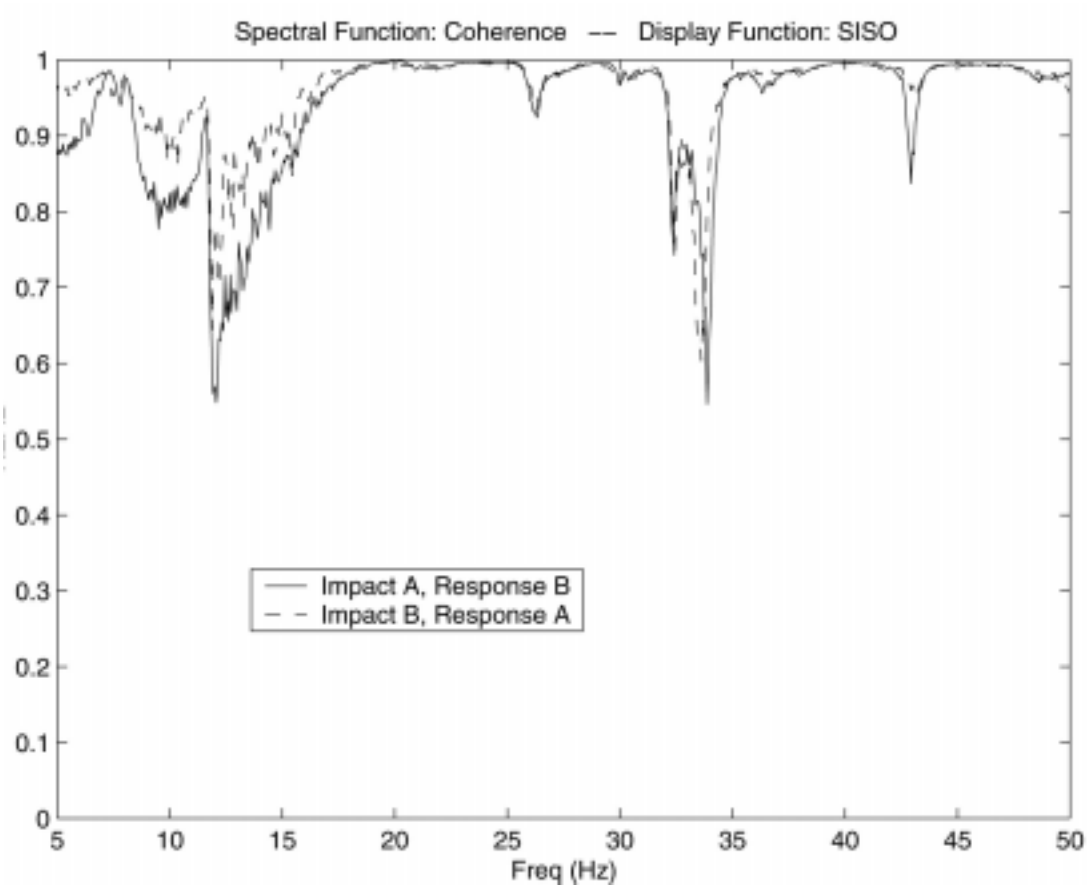

Figure 42. Coherence functions of the FRFs used to check the reciprocity of the structure only.

2. Three-Span Test

The preliminary tests indicated that the span adjacent to the northern abutment (span 1) and the interior spans had significant differences in their FRFs, such as additional modes for the interior spans. To explore possible dynamic coupling between the spans, a three-span test was done. One purpose of this test was to determine if the additional modes could be caused by the interactions of adjacent spans.

a. Experimental procedure and equipment

The same equipment was used for the three-span test as previously described for the linearity and reciprocity test. A total of 31 acceleration measurements were made on the concrete deck and on the girders below the bridge for the first three spans as shown in Figure 43. The accelerometers were mounted to the bottom of the 2nd and 5th girders using magnetic mounts and were approximately spaced at a distance of 3.8 m (12.5 ft). The impact was applied to point 1 in Figure 43. Thirty averages were used when determining the FRFs and COHs.

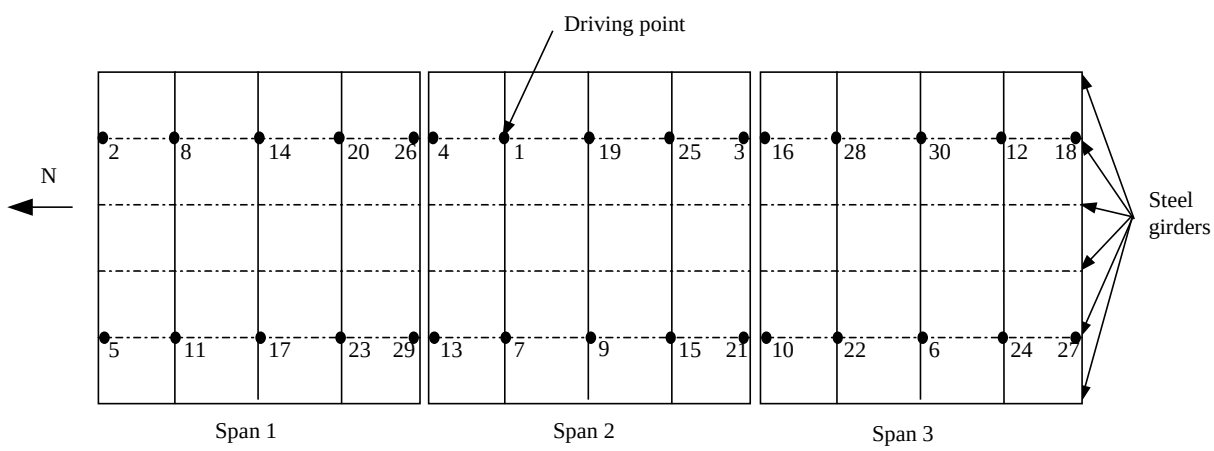

Figure 43. Accelerometer locations for the 3-span test.

b. Results from the three-span test

The magnitudes of FRFs and coherence between points 20 on span one, 25 on span two, and 12 on span three and the driving point are shown in Figure 44. From this figure it is clear that the coherence is better for spans two and three than for span one. The magnitude of the FRFs are also significantly larger for span two and span three than for span one. It is expected that the magnitude of the FRF for the point on span two would be larger because the driving point was on span two, but one would expect the magnitude to be approximately the same for the points on span one and span three. This expectation did not turn out to be the case. A possible explanation is that between spans one and two both spans have a roller connection sitting on the pier whereas span two has a pinned connection at the pier between spans two and three. Clearly, the pinned connection is better coupled to the pier and can transfer more energy to the pier and subsequently to span three. Also, three peaks around 8 Hz can be seen in the FRFs for the points on spans two and three but not for the FRF for the point on span one. This observation is consistent with the results obtained from the preliminary tests.

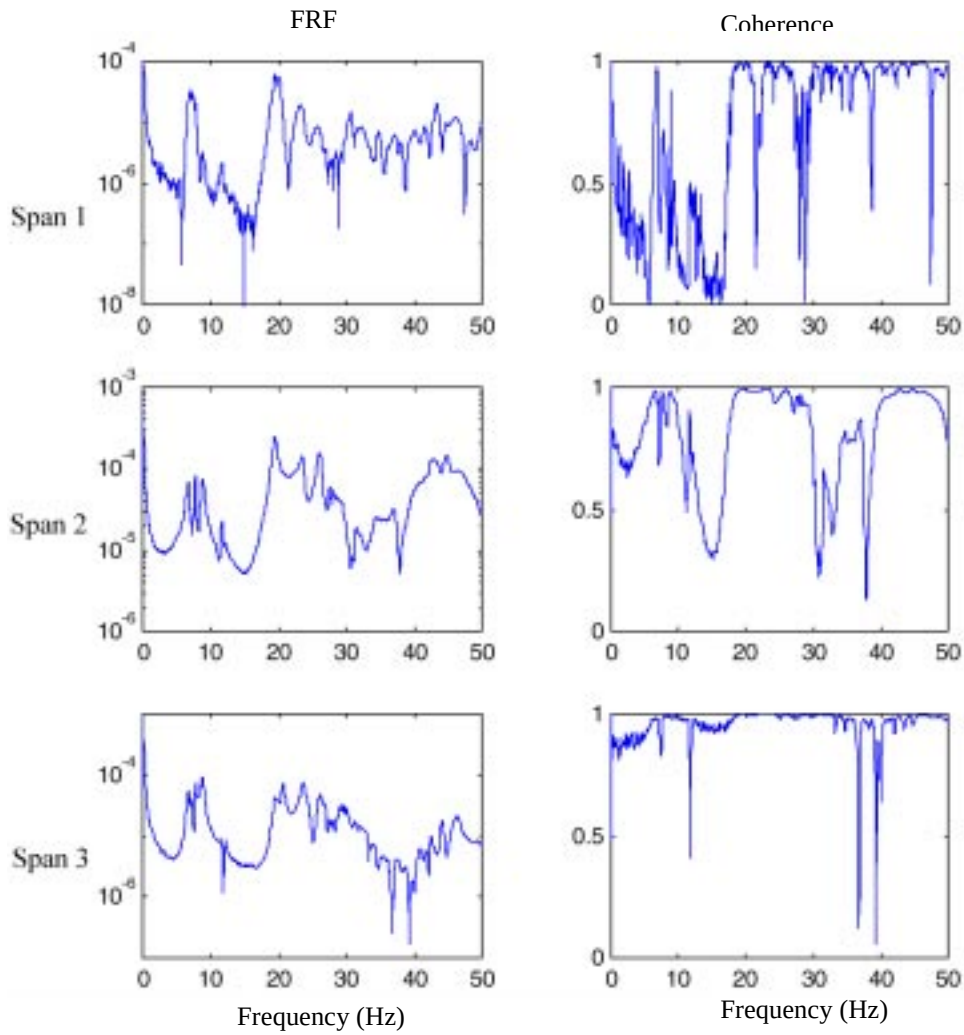

Figure 44. Typical FRFs and COHs for points on spans one, two and three.

The frequencies, damping and modes of the structure were determined using a rational-fraction polynomial global curve fitting algorithm in the modal analysis and damage identification package, DIAMOND, described in Appendix D. The cursor bands for the rational polynomial method were determined by visually inspecting the CMIF. The CMIF for the three-span data is shown in Figure 45. From this figure it appears that four modes exist between 7 and 9 Hz. These first four modes are shown in Figure 46. From Figure 46 it is evident that spans two and three seem to be coupled together well and act in conjunction with each other whereas span 1 seems to be only weakly coupled to span two.

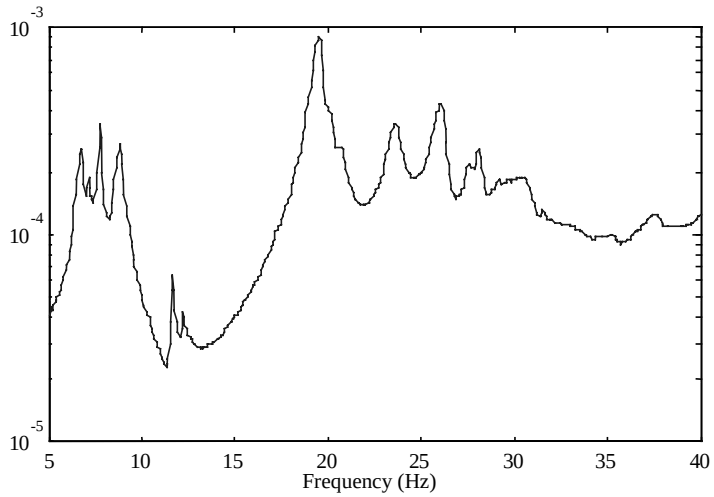

Figure 45. CMIF for data from the three-span test.

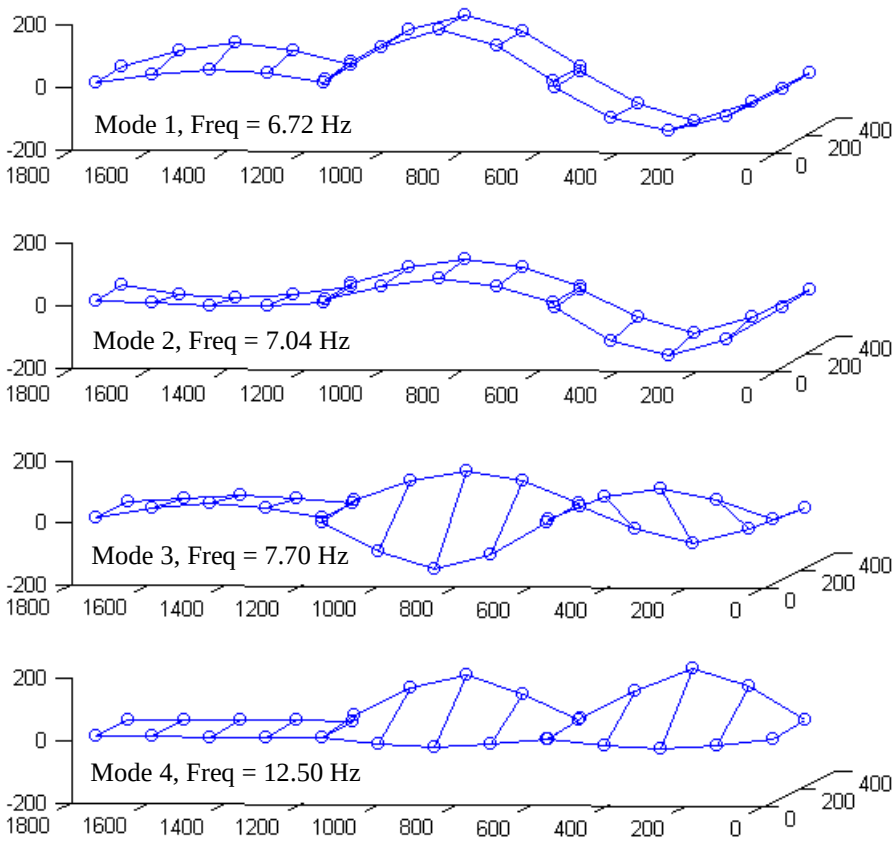

Figure 46. The first four mode shapes for the three-span test.

B. Vibration Tests Performed to Study Variability of Modal Properties

Recent advances in wireless, remotely monitored data acquisition systems coupled with the development of vibration-based damage detection algorithms make the possibility of a self-monitoring bridge appear to be within the capabilities of current or near-future technology. However, before such a system can be relied upon to perform this monitoring, the variability of the dynamic properties that are the basis for the damage detection algorithm must be understood and quantified. The variability must be quantified so that changes in vibration response resulting from damage can be discriminated from changes resulting from such variability.

In the preliminary tests it was observed that slightly different frequencies were obtained from the roving hammer impact test and from the single excitation point test. For this reason, tests were performed specifically designed to examine the variability in modal parameters of the first span of the bridge caused by environmental effects.

1. Results from Tests to Study Variability Caused by Thermal Effects

Following the 1996 test, experimental modal analyses were performed on data measured at two hour increments over a 24-hour time period to investigate the change in the modal properties as a function of time. The changes were assumed to be primarily caused by changes in the temperature of the structure. For this reason the temperature was measured at several locations on the structure throughout the test. The equipment and procedure were identical to that described earlier in Section IV.A.1.a. After the data were obtained, the ERA method was used to determine the frequencies, damping and modes.

Statistical uncertainty bounds on the measured frequency response function magnitude and phase were computed based on the measured coherence functions, assuming that the errors were distributed independently at each frequency line in a Gaussian manner, according to the method developed by Bendat and Piersol (1980) and presented in Appendix C. Monte Carlo analyses were then performed, using the previously determined uncertainty bounds on the FRFs, to establish statistical uncertainty bounds on the identified modal parameters (frequencies, damping ratios, and mode shapes). The procedure used is discussed in more detail in Section IV.C. The basic idea of a Monte Carlo analysis is the repeated simulation of randomly varied input data, in this case the FRFs with perturbations based on the estimated mean and standard deviation values, and compilation of statistics on the output data, in this case the ERA results.

Figure 47 shows the first mode frequencies along with their 95% confidence limits determined by Monte Carlo analysis of the data obtained during the 1996 test (ACBT3) plotted as a function of the measurement completion time. Also plotted on Figure 47 is the difference in temperature between the two thermometer readings made on the concrete deck (east—west). This figure clearly shows that the changes in modal frequencies are related to the temperature differentials across the deck. The first mode frequency varies approximately 5% during this 24-hour time period. Similar variations and correlation with deck temperature differentials were observed for the other modes of the structure.

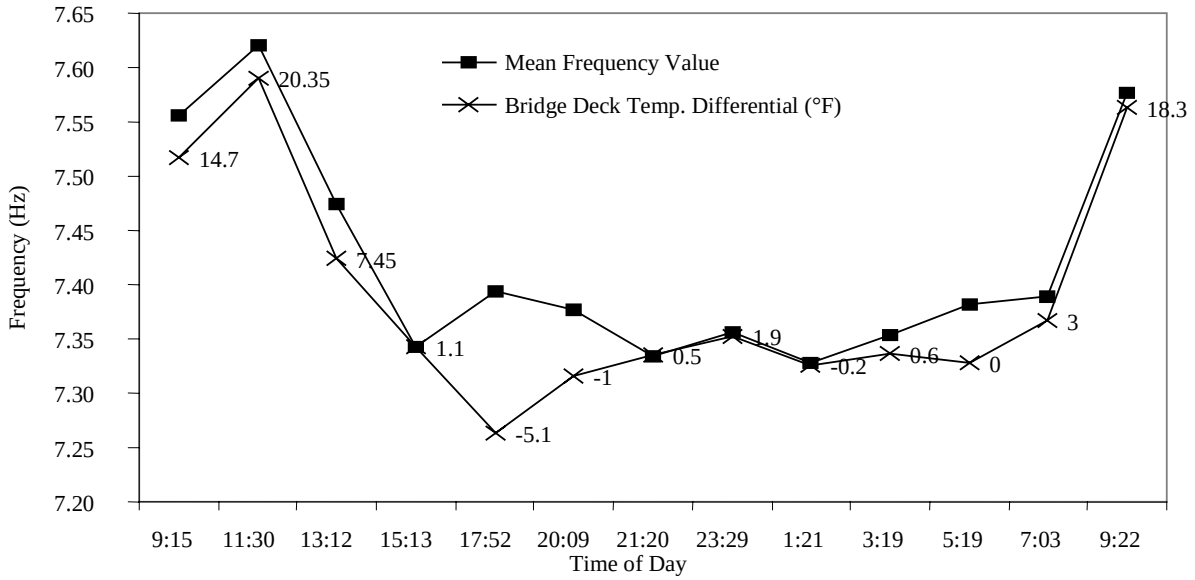

Figure 47. Change in the first mode frequency during a 24-hour time period (ACBT3).

To confirm the observation that the changes in modal frequency of this structure are related to the temperature differential across the deck, a second set of 24-hour data was taken during the July, 1997 test (ACBT4). Data were taken every two hours over an approximate 24-hour period. Note that it rained heavily before the second twenty-four hour test was started and this moisture could change the effective mass of the deck as well as equilibrate the temperature distribution. The results from this test for the first three modes are shown in Figure 48–Figure 50.

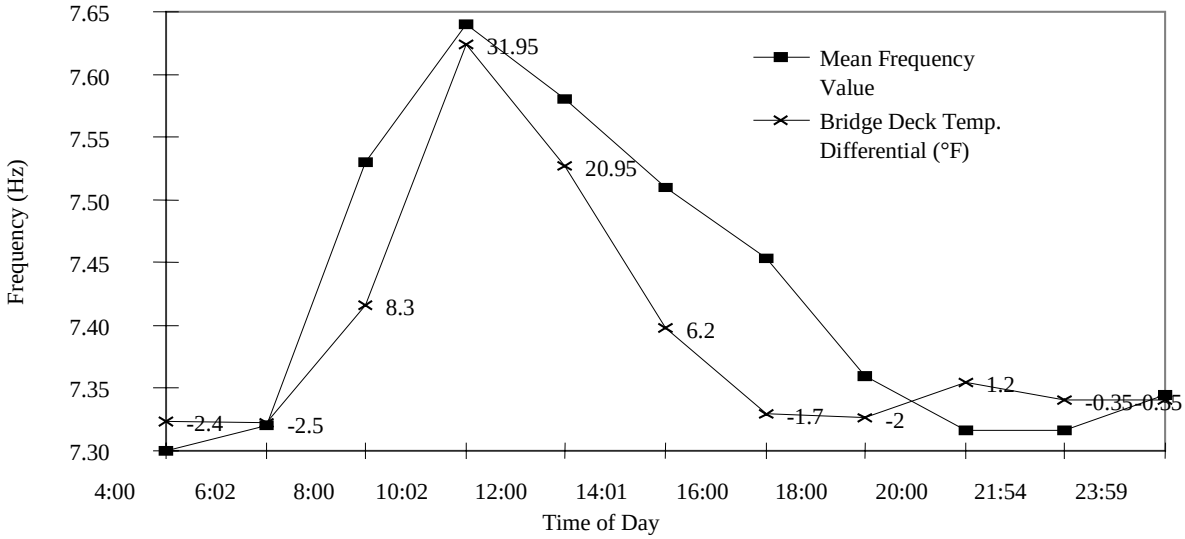

Figure 48. Change in the first modal frequency during the second 24-hour test (ACBT4).

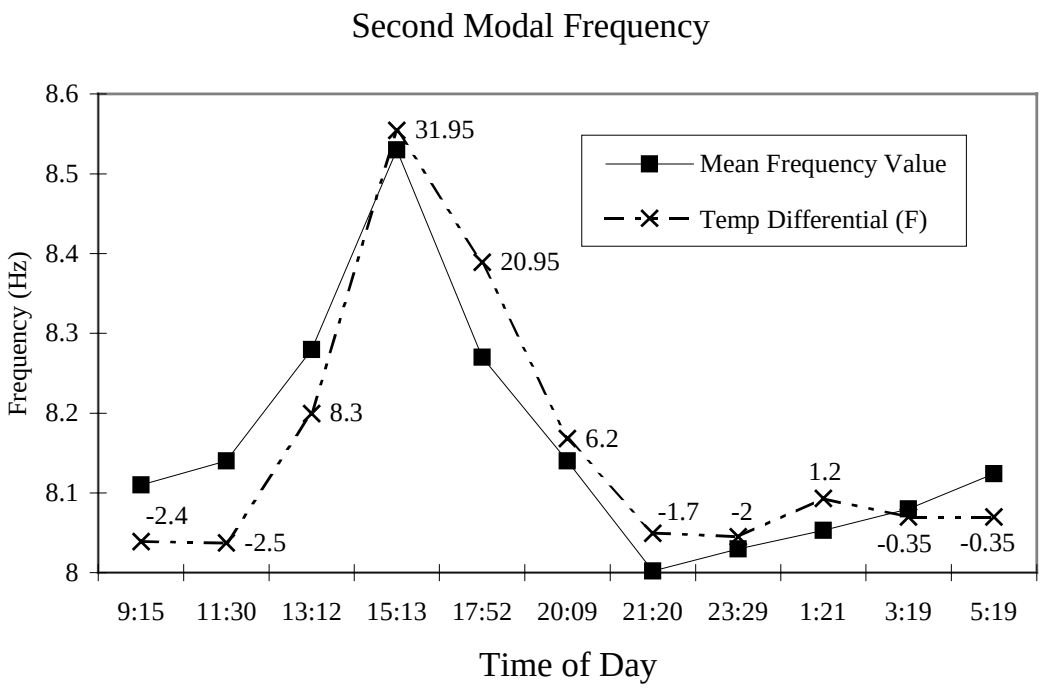

Figure 49. Change in the second modal frequency during the second 24-hour test (ACBT4).

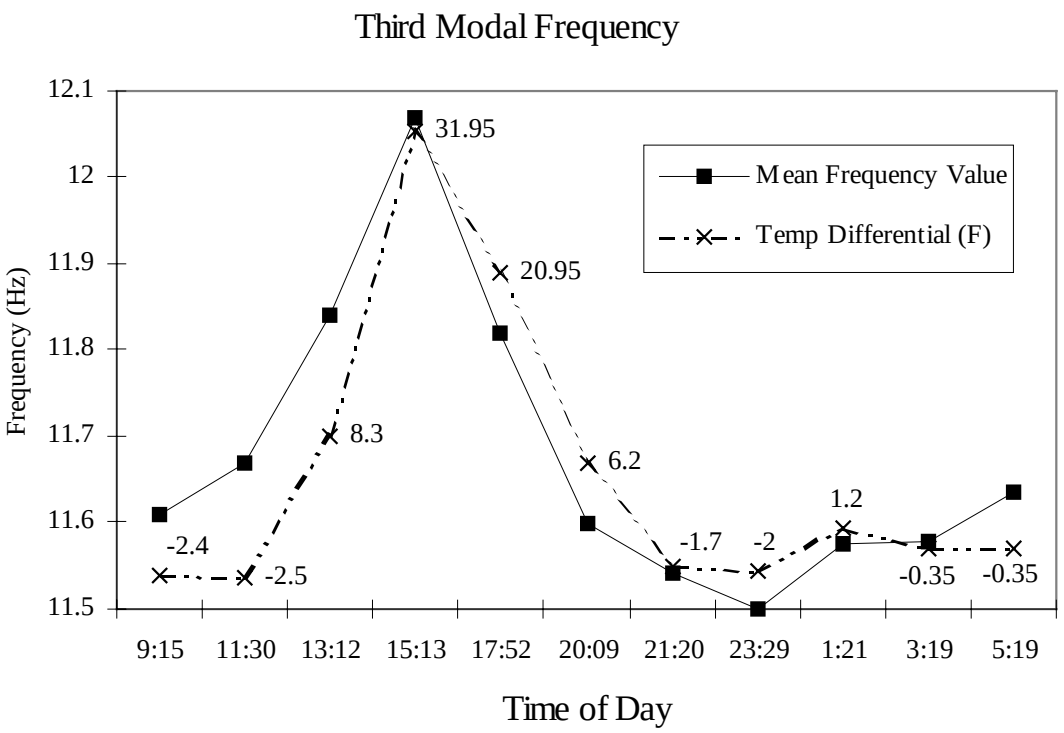

Figure 50. Change in the third modal frequency during the second 24-hour test (ACBT4).

2. Results from Tests to Study Variability Caused by Vehicle Weight

An impact modal test was performed on span one with four cars parked on the bridge and compared to impact tests without cars. The ERA method was used to determine resonant frequencies from this data. For one span the concrete deck and reinforcing steel weighs approximately 525 kN (118 kips) and the steel girders, cross bracing and gusset plates weigh 178 kN (40 kips) yielding a total span weight of 703 kN (158 kips). The four cars that were placed on the bridge weighed approximately 99 kN (22 kips). Assuming the parked cars have no other effects on the dynamics of the structure other than the addition of mass, they should lower the frequencies by a value proportional to the square root of the mass ratios, in this case approximately 6.4%. This result was not observed in the measured modal frequencies when they were compared to the frequencies from a test performed at a similar time of the day (again, to minimize thermal effects) as shown in **Table 5**. The reasons for this result are not understood at this time. This result is assumed to be caused by the vehicles and their suspension systems forming a more complex dynamic system where the change in mass is not sufficient to account for the change in dynamic property and/or the deflections produced by the vehicles causing a change in the boundary conditions.

Table 5. Change in modal frequencies resulting from added mass of cars

Mode	Measured Modal Frequency, No Cars (Hz)	Predicted Drop in Modal Frequency, Resulting from Car Mass (Hz)	Measured Modal Frequency Change Resulting from Car Mass (Hz)
1	7.38	6.91	7.43
2	8.04	7.53	8.03
3	11.5	10.8	11.5
4	19.5	18.3	19.8
5	23.4	21.9	23.4
6	25.2	23.6	25.6

The Alamosa Canyon Bridge was rated for 133 kN (30 kips). In theory two vehicles, one from each direction, could be on the span at one time adding 266 kN (60 kips) to the weight of the structure. Based on the added mass alone, these vehicles could theoretically reduce the measured resonant frequencies 19% from those measured when no vehicles are on the bridge. However, because the measured frequencies did not decrease when vehicles were placed on the span it is difficult to predict what the changes in frequencies might be.

3. Results from Tests to Study Variability Caused by the Excitation Source

A drawback of previous comparisons between excitation sources described in Section III is that no consideration was made for the environmental variability and its impact on identified dynamic properties of the bridge as discussed in Section IV.B.1. Therefore, subsequent tests were performed to compare the effects of using different excitation sources when identifying dynamic properties of the bridge. Only two excitation sources were used in these tests: hammer impact and ambient. A comparison of these excitation sources and the statistics associated with the results obtained from these tests is presented in Section IV.D. Comparisons of the ambient test results were made to impact test results from data measured at the same time of day to minimize the differences that can be attributed to thermal effects. Other excitation methods that could be investigated to complete this study include random and swept sine excitations using an electrodynamic or hydraulic shaker, repeatable controlled impact from a drop hammer, and step relaxation methods.

4. Results from Tests to Study Variability Caused by Data Reduction

Variability can be introduced in the data reduction process based on the parameter identification algorithms employed and the analyst that is applying them. Specific analyses were not performed on the Alamosa Canyon Bridge data to investigate the variability resulting from different analysts using different parameter identification algorithms. However, a study has been performed at the University of Cincinnati Infrastructure Institute (UCII). In this study data from a test of the Seymour Bridge in Cincinnati, Ohio, a three-span, two-lane highway overpass were analyzed independently by researchers from both UCII and Los Alamos National Laboratory [Catbas et al. (1997)]. The results of this study are summarized in **Table 6**. The researcher from Los Alamos National Laboratory used the ERA method and the one from the University of Cincinnati used the Complex Mode Indicator Function method. The results correlated reasonably well in the first 24 Hz range when both analysts identified corresponding modes. However, some modes identified by one analyst were missed by the other. Although the correspondence for the modes identified by both analysts were at most 1.6% different, this difference is larger than the changes in modal properties calculated by analyst #1 caused by the damage described in [Catbas et al. (1997)].

Table 6. Comparison of two modal analyses of data from Seymour Bridge in Cincinnati, Ohio

Mode	Frequency (Hz) (Analyst #1)*	Frequency (Hz) Analyst #2)**	% Difference	% Change from damage
1	7.14	7.19	0.70	0.14
2	8.06	8.12	0.74	0.00
3	8.52	–	–	0.47
4	11.44	11.62	1.6	–0.95
5	–	12.43	–	–
6	12.67	12.70	0.24	–0.31
7	15.12	15.09	–0.2	–2.89
8	16.27	16.23	–0.25	0.00
9	20.3	20.31	0.049	–0.78
10	–	21.79	–	–
11	21.92	22.11	0.86	–3.22
12	24.03	24.08	0.21	–0.12

* Analyst #1: F. Necati Catbas, Graduate Student, University of Cincinnati

** Analyst #2: Scott. W. Doebling, Technical Staff Member, Los Alamos National Laboratory

It is the authors' opinion that, in general, variability introduced by the data reduction process will be significantly smaller than the variability caused by environmental effects, particularly for the forced-vibration tests. Reduction of ambient vibration data is not as well documented or standardized as that for forced vibration data, hence, it is assumed that more variability will be introduced in the associated data reduction process. The statistical analysis methods summarized in Doebling, Farrar and Goodman (1997) and presented in the following section can be used to quantify the variability introduced by different data reduction algorithms and the variability introduced by a particular analyst.

C. Statistical Analysis Methods

The purpose of this section is to introduce the Monte Carlo and the bootstrap analysis procedures. As a result of the variability tests it became apparent that an important element of any experimental procedure is the ability to quantify the uncertainty in the test results that can be attributed to either random or bias (systematic) variability. However, relatively few studies have been reported that develop methods to quantify the uncertainty in estimated modal parameters. In Section IV.D the Monte Carlo technique will be used to compare impact and ambient tests and in Section IV.E both methods will be applied to data from the Alamosa Canyon Bridge and the results compared.

1. Monte Carlo Analysis Procedure

The first step in the Monte Carlo Analysis procedure is to establish uncertainly bounds on the measured frequency response function (FRF) magnitude and phase. The procedure developed by Bendat and Piersol (1980) for a randomly excited single-input/output model is employed for this estimate. The procedure assumes the variability is random and distributed in a Gaussian manner. A further assumption is made that the record lengths are long enough such that resolution bias errors are negligible. The analysis presented by Bendat and Piersol (1980) leads to the following relations for the confidence interval, σ_μ, on the magnitude and phase for the FRFs at each frequency value, ω,

$$\begin{aligned} \sigma_\mu\left(\left|H(\omega)\right|\right) &= \frac{\sqrt{1-\gamma^2(\omega)}}{\left|\gamma(\omega)\right|\sqrt{2n_d}}\left|H(\omega)\right| \\ \sigma_\mu\left(\angle H(\omega)\right) &= \frac{\sqrt{1-\gamma^2(\omega)}}{\left|\gamma(\omega)\right|\sqrt{2n_d}} \end{aligned} \tag{7}$$

where $\left|H(\omega)\right|$ and $\angle H(\omega)$ are the magnitude and phase angle of the measured FRF, respectively, $\gamma^2(\omega)$ is the coherence function, n_d is the number of measurement averages, and $\sigma_\mu(\bullet)$ is the value of the 68% uncertainty bound. These uncertainty bounds represent a statistical distribution of the FRF based on a realistic level of random noise on the measurement. Once the 68% uncertainty bounds are known, 95% uncertainty bounds can be computed.

It should be noted that the formulae in Eq. (7) are estimates of the confidence intervals on the mean of the magnitude and phase, NOT estimates of the standard deviation of the magnitude and phase, assuming that the magnitude and phase themselves are Gaussian-distributed random variables. As derived in Bevington and Robinson (1992), the relationship between the estimate of the population standard deviation, σ, and the confidence interval on the mean estimate, σ_μ, is given as

$$\sigma_\mu = \frac{\sigma}{\sqrt{n_d}} \tag{8}$$

Thus, the estimates of the standard deviations of the FRF magnitude and phase are

$$\sigma\left(\left|\hat{H}_{xy}(\omega)\right|\right) = \frac{\sqrt{1-\gamma_{xy}^2(\omega)}}{\left|\gamma_{xy}(\omega)\right|\sqrt{2}}\left|\hat{H}_{xy}(\omega)\right|$$
$$\sigma\left(\angle\hat{H}_{xy}(\omega)\right) = \sin^{-1}\left(\frac{\sqrt{1-\gamma_{xy}^2(\omega)}}{\left|\gamma_{xy}(\omega)\right|\sqrt{2}}\right) \tag{9}$$

It is noted by comparing Equations (9) and (7) that they differ by the factor $\sqrt{n_d}$ as described in Equation (8). For the phase, this factor is applied to the operand of the arcsin function because the relationship of Equation (8) is applied to the relative error terms, from which the standard deviation estimates of Equations (9) are derived. A complete derivation of these standard deviation formulas is shown in Appendix C.

Statistical uncertainty bounds on the identified modal parameters (frequencies, damping ratios, and mode shapes) can be estimated using the previously determined uncertainty bounds on the FRFs via a Monte Carlo analysis [Press et al., (1992)]. The basic idea of a Monte Carlo analysis is the repeated simulation of random input data, in this case the FRF with estimated mean and standard deviation values, and compilation of statistics on the output data, either rational polynomial curve fit or ERA results. For this analysis, the procedure is summarized as:

1. Measure the averaged FRF and coherence functions for each degree of freedom (DOF).

2. At each frequency interval add random Gaussian noise to the magnitude and phase of the mean FRF for all measurements. This noise is based on the mean values of the FRFs obtained from the ensemble averages made during the measurement process and standard deviation values calculated from Eq. (9).

3. Run the randomly perturbed set of FRFs through the ERA identification procedure or apply the rational polynomial curve fit and identify the standard modal properties (resonant frequency, modal damping, mode shape amplitudes and phases).

4. Steps 1, 2, and 3 are repeated and the mean and standard deviation for the identified modal properties are calculated at the end of each iteration. The process is repeated until the means and standard deviations converge (typically less than 100 iterations).

A flowchart of the procedure for a Monte Carlo Analysis is shown in Figure 51.

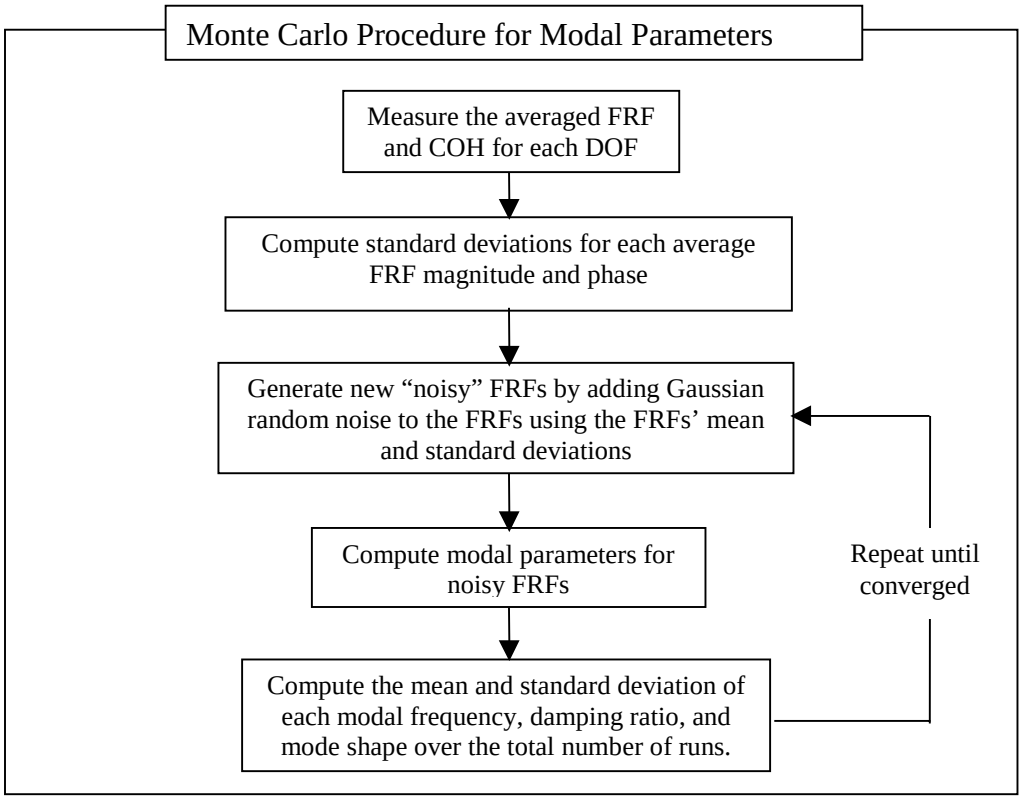

Figure 51. Flowchart of Monte Carlo analysis procedure.

Tracking the convergence determines the sufficient sample size to provide significant confidence on the statistical estimates. Ninety-five percent confidence limits for each modal parameter are established based on the mean and standard deviation values calculated from the Monte Carlo simulations along with the assumption of the Gaussian distribution on the variations in these parameters. Note that this procedure does not require storage of individual FRF measurements that make up the ensemble averages at each DOF.

2. Bootstrap Analysis Procedure

The bootstrap analysis procedure [Efron and Tibshirani (1993)] randomly selects individual FRF measurements at each DOF to form the ensemble average. Because the FRFs for a particular DOF are selected at random and "with replacement," a single FRF sample may be used more than once in the ensemble average while others may not be included. This process results in ensemble averages that are based on random weighting of the sample FRFs.

In application, the same sequence of randomly selected sample FRFs is used for each DOF. This selection procedure preserves the temporal variations in measured inputs and responses across all DOFs. As an example, assume that a large truck on an adjacent bridge applies a significant unmeasured input into the bridge that is being testing during a particular FRF measurement. The selection process described above will assure that all DOFs include this measurement with equal weighting. Such a weighting scheme is important when attempting to accurately assess the variations of modal parameters using global curve-fitting algorithms

(algorithms that estimate modal parameter by fitting all FRFs simultaneously). This selection process should still accurately account for variations that are a function of spatial location such as a particularly noisy sensor.

Once the randomly weighted ensemble averages are formed for each DOF, the rational polynomial parameter estimation procedure is applied and the modal parameters are identified. This procedure is repeated numerous times to form a histogram of the identified modal parameters.

The percentile interval method discussed in Efron and Tibshirani (1993) is then used to establish the 95 percent confidence limits on the identified modal parameters. The values of the parameters are placed in an ordered list. Values of the parameters corresponding to the upper and lower 2.5 percentile are used to define the 95 percent confidence limits.

In summary, the steps used to implement the bootstrap procedure are:

1. Measure and store *N* FRF samples at each DOF.
2. At each DOF randomly select *N* FRFs, with replacement, and form an ensemble average. The same random sequence of FRFs is used at each DOF.
3. Apply a curve-fit procedure to these ensemble averages to determine the modal parameters (resonant frequencies, modal damping, mode shape amplitudes and phases).
4. Repeat steps 1–3 and form a histogram for each modal parameter. Calculate the mean value of each modal parameter.
5. Place the parameters into an ordered list and estimate the 95 percent confidence limits from the values corresponding to the upper and lower 2.5 percentiles.

A flowchart of the bootstrap procedure is shown in Figure 52.

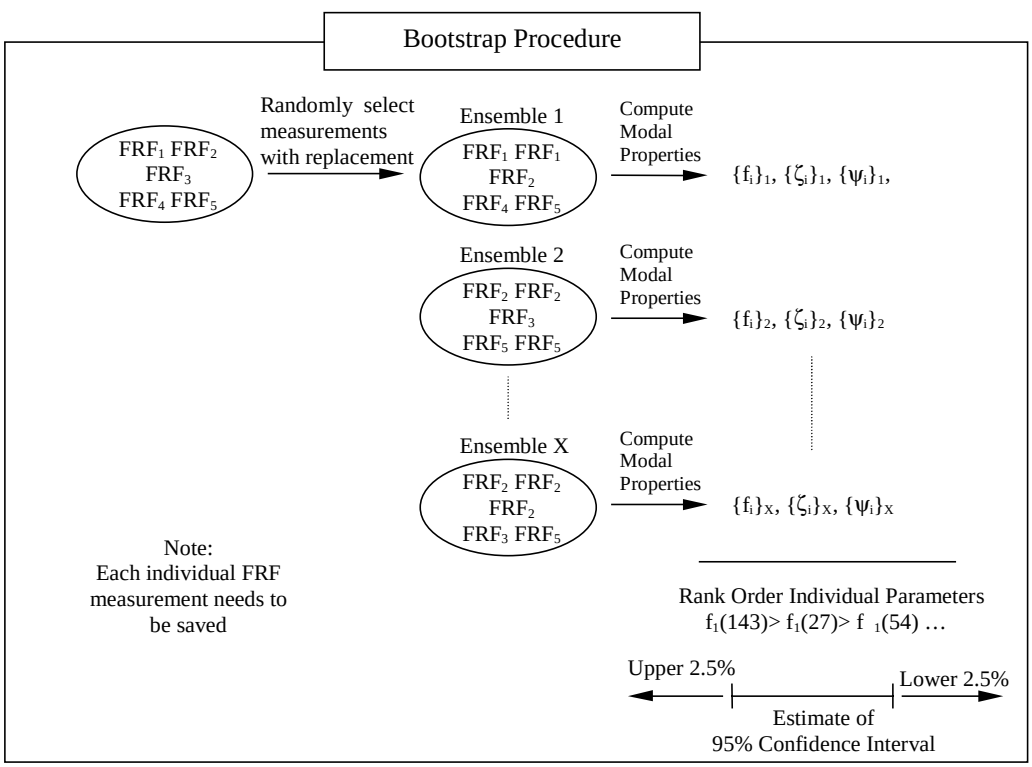

Figure 52. Flowchart of the bootstrap procedure.

Note that no assumption on the distribution of the identified parameters, no assumption about the form of the input or response, and no assumption about the number of inputs or responses are made in this analysis. The bootstrap method does require each individual FRF to be stored for each measurement DOF. As with the Monte Carlo method, no quantitative method was employed to determine the number of iterations needed for the bootstrap method to converge. Rather, various numbers of iterations were tried until there was no significant change in the confidence limits calculated for the various parameters. Typically, approximately 100 iterations were required for convergence.

Finally, it should be noted that both the Monte Carlo and the bootstrap procedures will not account for bias or systematic errors introduced by procedures to estimate the FRFs (for example, those introduced by windowing functions) or for bias errors introduced during the parameter estimation procedure. Also, neither method allows one to "extrapolate" beyond the measured data variability.

3. Test on Simulated Data

To test the two statistical analysis procedures, a set of 30 randomly perturbed FRFs were generated for a single degree of freedom system. This idealized system has a mean resonant frequency and damping ratio of 5.0 Hz and 1%, respectively. A standard deviation of 0.01 Hz was assigned to the resonant frequency and a standard deviation of 0.1% was assigned to the damping value. A unit modal mass was assigned to this system. The generated FRFs, $H(i\omega)$, were defined at 0.03125 Hz increments and have the form

$$H(i\omega) = \frac{C}{i\omega - \lambda} + \frac{C^*}{i\omega - \lambda^*} \tag{10}$$

where

$i = \sqrt{-1}$

ω = cyclic frequency

$C = \dfrac{1}{2iM\omega_d}$ = residue

M = the system modal mass

$\omega_d = \omega_n\sqrt{1-\zeta^2}$ = damped natural frequency

ω_n = system natural frequency

ζ = system damping ratio

$\lambda = \zeta\omega_n + \omega_d i$ = pole

* *denotes complex conjugate.*

Note that the standard deviation on the resonant frequency is smaller than one frequency interval, which was consistent with observations in the Alamosa Canyon Bridge data. An

alternate case was studied where the standard deviation of the resonant frequency was 0.1 Hz. However, the example reported is considered more severe. Care must be taken in generating variations in damping such that negative damping values are not specified. Prior to performing the statistical analyses, the rational polynomial curve-fitting algorithm was applied to each of the 30 generated FRFs. The curve-fitting algorithm predicted the specified parameters almost exactly, hence it can be concluded that for this simulated data no bias error is being introduced by this algorithm. Further studies are needed to determine if this statement will still hold for multi degree-of-freedom systems with closely spaced modes. It should be noted, however, that there is no guarantee that the FRFs will preserve the original distributions of the natural frequency and damping.

Figure 53 shows an overlay of the 30 FRF magnitudes generated for this system. The variations in the FRFs can only be seen when the plot is expanded around the resonant frequency. Coherence functions were not generated for the implementation of the Monte Carlo procedure. Instead, the 30 FRFs were used to generate a mean and standard deviation for the real and imaginary part at each frequency. The Monte Carlo procedure then generated perturbed FRFs based on these statistics and the assumption of an independent Gaussian distribution at each frequency value.

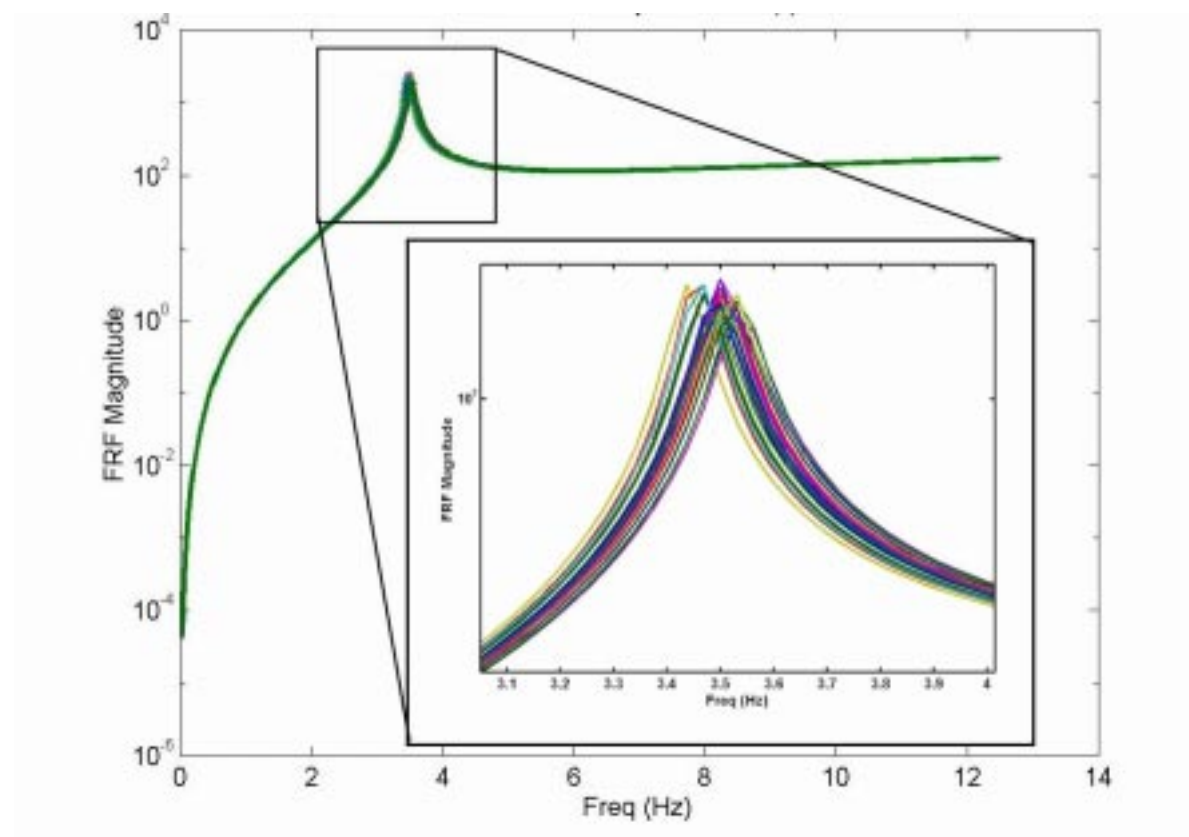

Figure 53. Simulated FRFs.

Table 7 summarizes the results of applying the Monte Carlo and bootstrap statistical analysis methods to the numerically generated data. This example shows that for a case where the variations in the measured data are consistent with the assumptions that the Monte Carlo method is based upon, the procedure accurately predicts the uncertainty in the parameters identified from the simulated data. Similarly, the bootstrap analysis also predicts the correct uncertainty in the modal parameters.

Table 7. Comparison of the Monte Carlo and bootstrap methods on numerically simulated data

Method (Iteration)	ω_{mean} (Hz)	ω 95% Confidence Intervals (Hz)	ζ_{mean} (%)	ζ 95% Confidence Intervals
Population "True" Value	5.00	0.0200	1.00	0.200
BS (100)	5.00	0.0211	0.968	0.218
BS (500)	5.00	0.0217	0.986	0.231
BS (1000)	5.00	0.0220	0.992	0.235
MC (100)	5.00	0.0225	0.989	0.270
MC (500)	5.00	0.0221	0.994	0.262
MC (1000)	5.00	0.0219	0.992	0.242

BS = Bootstrap, MC = Monte Carlo

Once there was confidence that the statistical analysis procedures were working correctly, these methods were applied to data from the Alamosa Canyon Bridge tests.

D. A Statistical Comparison of Impact and Ambient Testing Results

Ambient excitation is the most practical type of excitation for testing of large civil engineering structures and for an automated, vibration-based health monitoring system designed to assess the deterioration of bridges. Also, an automated health monitoring system for a bridge would undoubtedly use ambient excitation so that the data could be taken periodically and possibly remotely, without taking the bridge out of service. Ambient excitation is widely used as is evident by the large number of papers at the 1996 International Modal Analysis Conference, over 15, that discuss such testing procedures. However, comparisons of ambient results with those obtained using other more traditional forced vibration methods, especially impact

excitation are much rarer [Kong, Zhong and Lee (1996), Farrar et al. (1994)] and are often done in a laboratory setting. To gain confidence in the data reduction techniques required when using ambient data and in the subsequent results it is desirable, when possible, to compare the results with those obtained using more traditional excitation sources. In this section the modal properties of the Alamosa Canyon Bridge obtained using ambient data are compared to those obtained from a more traditional impact vibration test.

As discussed earlier there are challenges to performing modal identification on ambient excitation data. Because it is not possible to measure the input force when using ambient excitation, the identified mode shapes will not be mass normalized, which is a problem for damage detection techniques that require mass-normalized modes, such as flexibility based damage methods [Toksoy and Aktan (1994)]. Also, because the spectra and spatial locations of the input forces cannot be dictated, some vibration modes may not be well excited and therefore may not be identifiable from the data. Finally, when analyzing ambient response data one cannot always distinguish between peaks in the spectra caused by the modal response of the structure or peaks resulting from the frequency content of the input.

When analyzing the results of a modal test, it is important to understand the statistical uncertainty of the results arising from random errors such as electrical noise, slight variations in testing conditions, environmental effects (such as temperature and wind), etc. In this section, the Monte Carlo analysis procedure was used to compute uncertainty bounds on the identified modal frequencies and damping ratios based on the actual level of measured random noise as quantified by the coherence function. The mean values and the uncertainty bounds for both the modal frequencies and modal damping ratios will be compared for the ambient and hammer impact data sets. The results will demonstrate the relative level of confidence that should be placed in the ambient results as compared to the impact hammer test results.

1. Description of the Ambient Test

All of the results in this section are from measurements made on span one of the bridge, which is located at the far north end. The first source of ambient excitation tried was from trucks driving over the bridge, but unfortunately the dominant dynamics was that of the suspension of the trucks. Therefore, the ambient vibration forces were provided by tractor-trailer trucks descending the hill on the highway next to the bridge. As the trucks passed over expansion joints and onto the Interstate 25 Bridge, they induced sufficient ground motions to vibrate the Alamosa Canyon Bridge via its piers and abutments. An accelerometer mounted to an aluminum block in the ground midway between the Interstate 25 Bridge and the Alamosa Canyon Bridge (Figure 54) was used to monitor the level of vibration induced in the ground from the excitation sources. The PSD of the ground motion induced by the trucks (in units of g^2/Hz) is shown in Figure 55 and a typical average CPS used to identify the modal parameters is shown in Figure 56. The accelerometer locations (see Figure 33) and data acquisition hardware were identical to that used in ACBT4. Thirty averages were taken for the ambient tests over a period of approximately 1.5 hours. The accelerometer at location 9 on the sensor diagram of Figure 33 was used as the reference for the CPS computations.

Figure 54. Accelerometer located midway between the I-25 Bridge and the Alamosa Canyon Bridge.

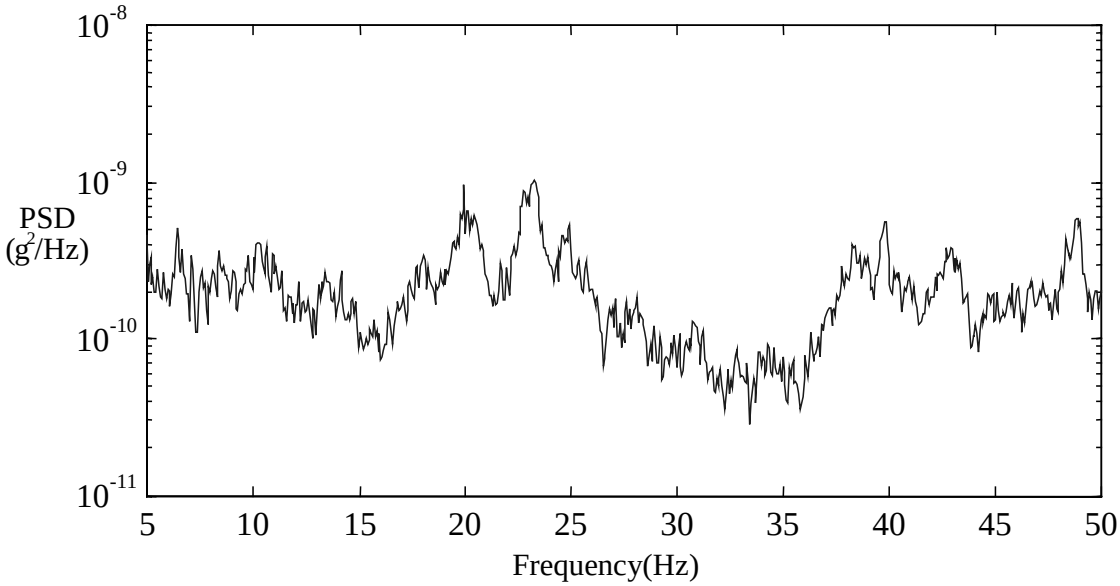

Figure 55. PSDs of ground motion induced by trucks on the adjacent Interstate 25 Bridge.

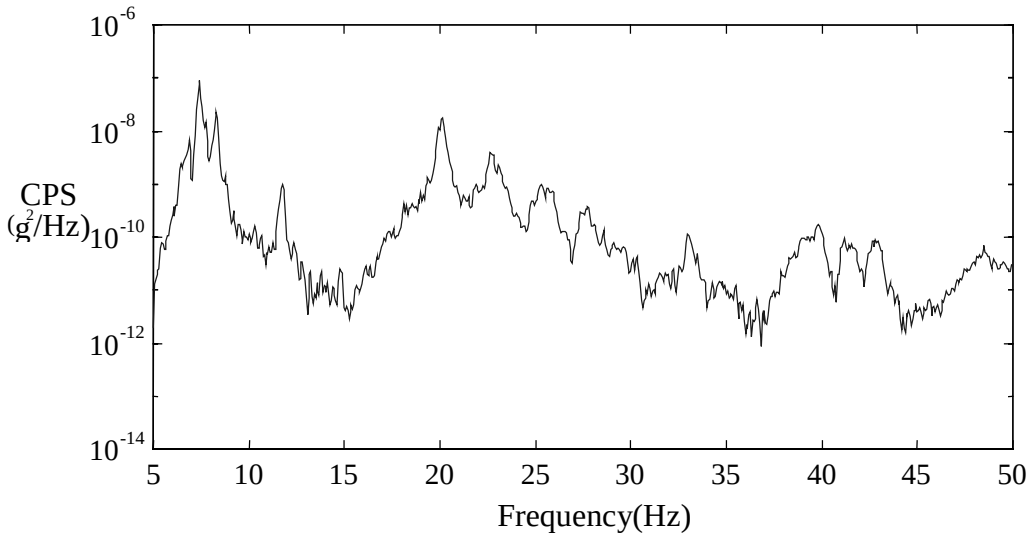

Figure 56. Typical cross-power spectrum used to identify modal properties.

It is known that the dynamic response of this structure exhibits a significant amount of sensitivity to environmental conditions, as shown in Section IV.B. The ambient excitation data set used in this analysis was taken within one hour of the same time of day with approximately the same environmental conditions as the single excitation point impact test. Thus it is assumed that the actual dynamic response of the bridge was approximately the same between the impact hammer test and the ambient test. However, it is probable that a slight difference exists between the two data sets caused by environmental variability.

2. Description of the Statistical Methods

The statistical methods used to compare the ambient and the hammer tests were discussed in detail in Section IV.C. Typical 95% uncertainty bounds on the FRF magnitude and phase for the impact excitation data set are shown in Figure 57. The ERA method was used to determine the modal properties from both the ambient and hammer test data. For this study, the convergence took about 100 runs.

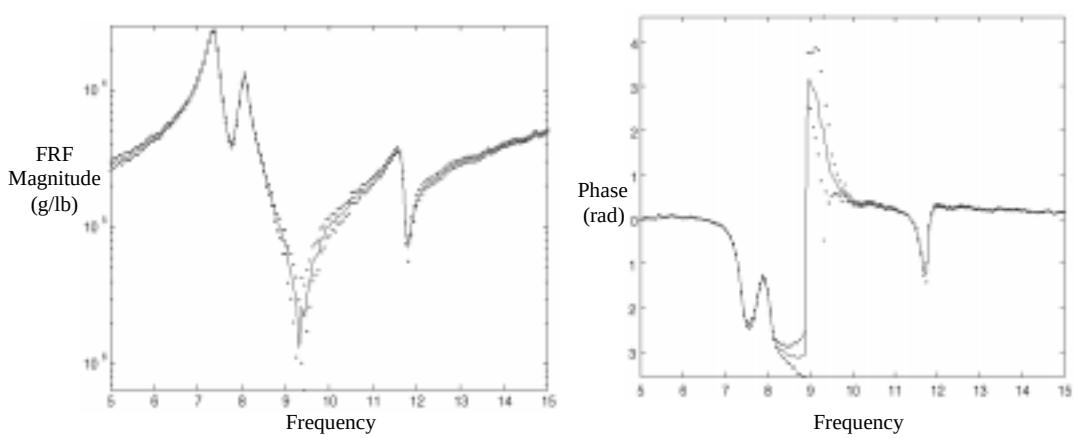

Figure 57. Typical 95% confidence bounds on FRF magnitude and phase shown as dotted lines.

3. Results

A total of nine modes were identified from the impact excitation tests. These modes are shown in Figure 58. A comparison of the mean modal frequencies for these modes is shown in **Table 8**. The percent differences between the hammer test and the ambient test range from 0.03% (mode 9) to 3.19% (mode 5), but most are in the vicinity of 1%. It should be noted that mode 7 was not identified in the ambient data set. Presumably, that mode was not sufficiently excited by the ambient excitation forces possibly because the power spectrum of the ground motion induced by trucks shows relative low magnitudes at this frequency.

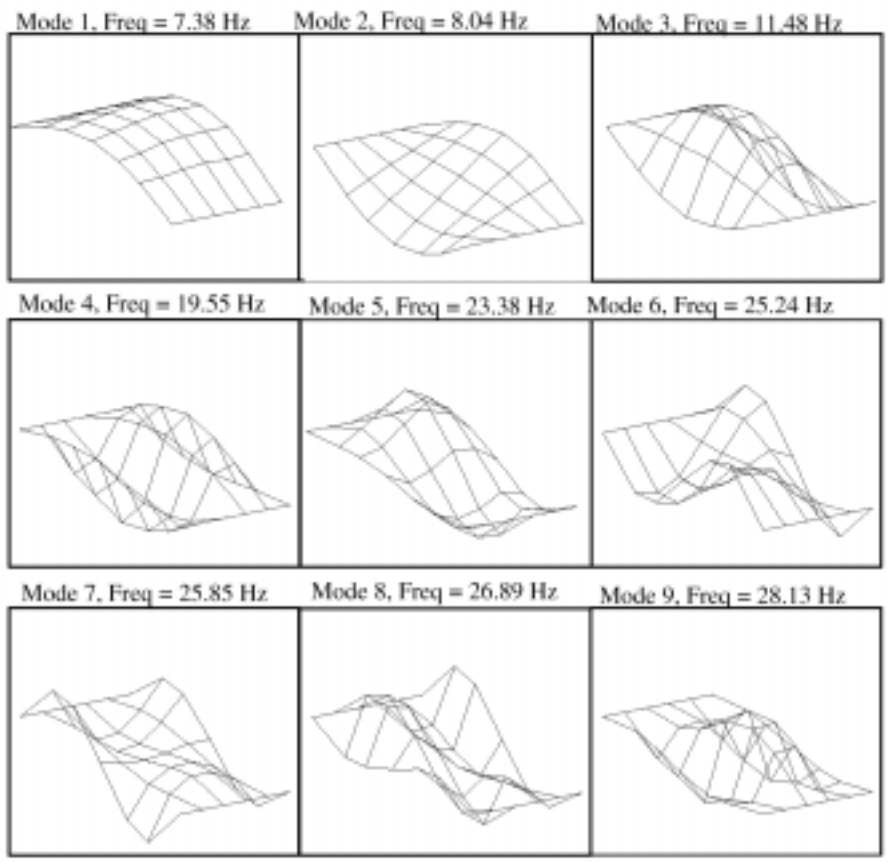

Figure 58. Nine identified modes from impact excitation of the Alamosa Canyon Bridge.

Table 8. Mean Modal Frequency Comparison			
Mode	**Hammer Data (Hz)**	**Ambient Data (Hz)**	**% Difference**
1	7.38	7.46	1.1%
2	8.04	8.01	–0.37%
3	11.5	11.5	0.0 %
4	19.5	19.9	2.1%
5	23.4	22.6	–3.4%
6	25.2	25.6	1.6%
7	25.8	(Missed)	N/A
8	26.9	27.2	1.1%
9	28.1	28.1	0.0%

A comparison of the mean modal damping ratios for the 9 identified modes is shown in **Table 9**. These values have percent differences ranging from 18% (mode 1) to 109% (mode 5). Overall the errors in the damping ratios are on the order of 50%, with the modes from the hammer impact test typically having the higher damping ratio. It is typically thought that damping levels increase with increasing excitation force level, so that the damping ratios from the hammer data should be higher than the damping ratios from the ambient data. Except for mode 5, this trend is observed.

Table 9. Mean Modal Damping Ratio Comparison			
Mode	**Hammer Data**	**Ambient Data**	**% Diff**
1	1.5%	1.3%	–13%
2	1.2%	0.58%	–52%
3	1.1%	0.68%	–38%
4	2.2%	1.1%	–50%
5	0.96%	2.0%	110%
6	2.3%	1.1%	–52%
7	0.64%	(Missed)	N/A
8	1.9%	0.93%	–51%
9	0.92%	0.75%	–18%

A comparison of the relative levels of uncertainty between the modal frequencies and damping ratios is shown in **Table 10**. Columns 2 and 3 are the 95% uncertainty bounds (2 standard deviations) on the hammer and ambient data modal frequencies, respectively, calculated using the Monte Carlo method. In **Table 10** the 95% uncertainty bounds are stated as a percent of the mean value. With the exception of mode 9, the 95% uncertainty bounds on the measured modal frequencies are smaller than the percent differences presented in **Table 8**. Thus, it can be stated that the frequency differences observed in **Table 8** are statistically significant, and are not attributable merely to random variability. It is possible that these frequency differences are a result of the fact that these data sets were acquired on different days, albeit under similar environmental conditions, but with different test durations (30–40 minutes for impact, 1–1.5 hours for ambient).

Table 10. Relative 95% Uncertainty Level Comparison for Identified Modal Parameters.

Mode	**Hammer Freq. 2σ**	**Ambient Freq. 2σ**	**Hammer Damp. 2σ**	**Ambient Damp. 2σ**
1	0.12%	1.0%	7.8%	51%
2	0.13%	0.31%	12%	54%
3	0.16%	0.12%	12%	16%
4	0.44%	0.45%	22%	51%
5	0.61%	1.4%	90%	88%
6	0.68%	0.66%	23%	62%
7	0.55%	N/A	110%	N/A
8	0.30%	0.15%	19%	16%
9	0.10%	0.14%	10%	19%

Columns 4 and 5 in **Table 10** are the 95% uncertainty bounds on the identified modal damping ratios calculated using the Monte Carlo method. With the exception of modes 3 and 8, the uncertainties on the ambient modal damping ratios are significantly larger than the percent differences between the hammer and ambient modal damping ratios from column 4 of **Table 9**. Thus, it can be stated for all of the modes (except 3 and 8) that the differences between modal damping ratios observed in **Table 9** are most likely the results of random variations in the structural response measurements as well as the modal identification software, and not actual differences in the response of the structure. For modes 3 and 8, the uncertainty levels in the damping ratios are much less than the difference between the hammer and ambient modal damping ratios, indicating that for those two modes, there is a significant difference in the damping response of the structure between the two types of excitation.

E. A Comparison of the Monte Carlo and Bootstrap Techniques

To the authors' knowledge, attempts to compare different statistical methods on similar experimental modal analysis data sets have not been published. In this section, two different methods will be applied for determining confidence intervals to modal data obtained from the Alamosa Canyon Bridge.

1. Application to the Alamosa Canyon Bridge

Two sets of FRFs were investigated for the Alamosa Canyon Bridge. The first set of data consisted of 30 averages made early in the morning before the sun hit the bridge. These measurements were made over a 30-minute time interval. Air temperatures remained nearly constant during the time of the test. Traffic on the adjacent bridges was light during this period. Therefore, it was assumed that variability in the FRF measurements made during this test were the result of random error sources. Figure 59 shows an overlay of the thirty FRF magnitudes measured at location 2 (see Figure 33) during this test. Figure 60 shows the average FRF for location 2. Figure 61 shows the corresponding coherence function that was used to generate the standard deviations associated with these measurements.

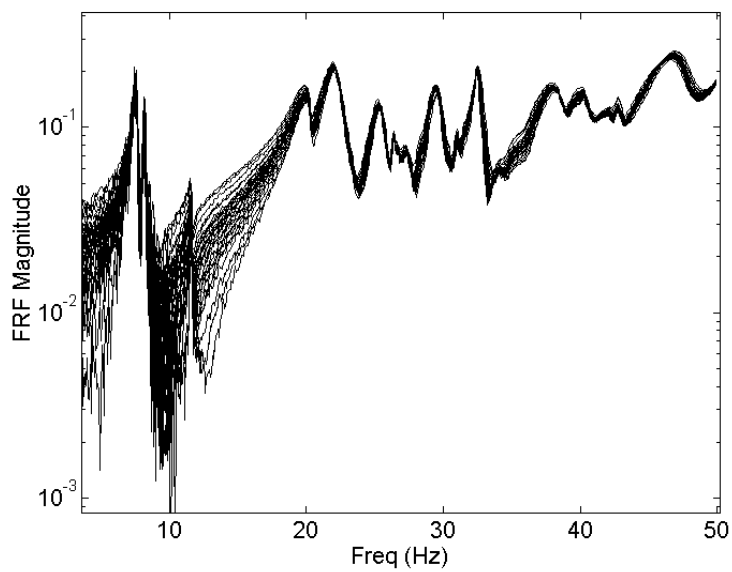

Figure 59. Thirty FRFs measured at Pt. 2.

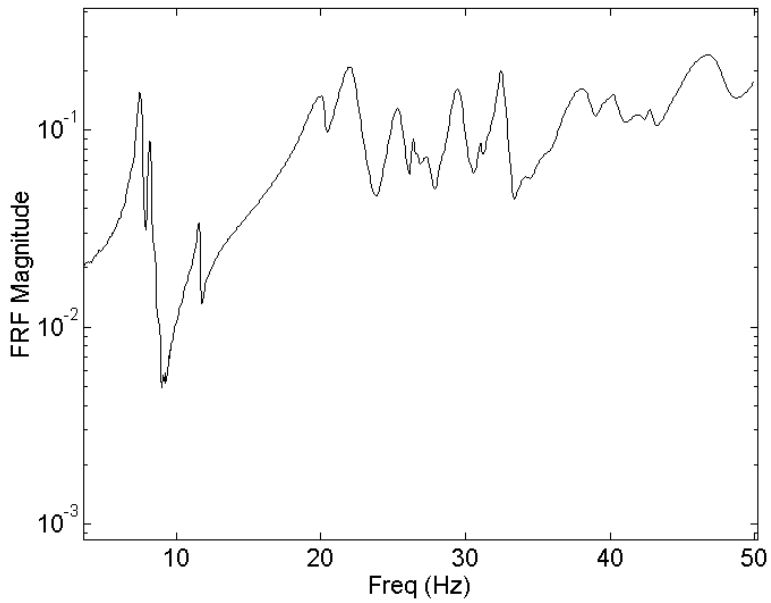

Figure 60. Average FRF measured at Pt. 2.

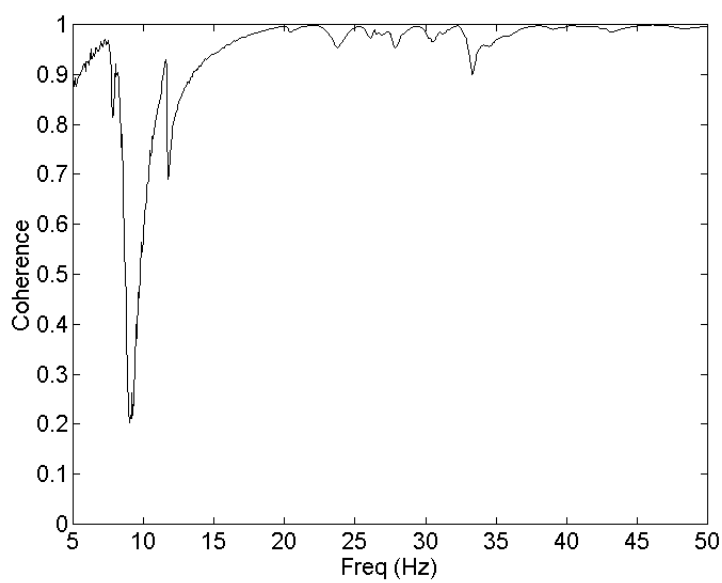

Figure 61. Coherence Function corresponding to the average FRF.

The second set of data corresponds to measurements made at two-hour increments over a 24-hour period. Eleven FRFs, each of which are the average of 30 measurements made at the two-hour increments, were analyzed. These 11 FRFs were analyzed by the bootstrap procedure. Then the 11 FRFs were averaged along with their corresponding coherence functions to form the data for the Monte Carlo analysis. Therefore, at each DOF, the FRFs and coherence used in the Monte Carlo analysis were based on 330 measurements made over a 24-hour time period. Figure 62 shows an overlay of the 11 averaged FRFs for DOF 2. Figure 63 shows the mean FRF for this same DOF and Figure 64 shows the corresponding mean coherence function.

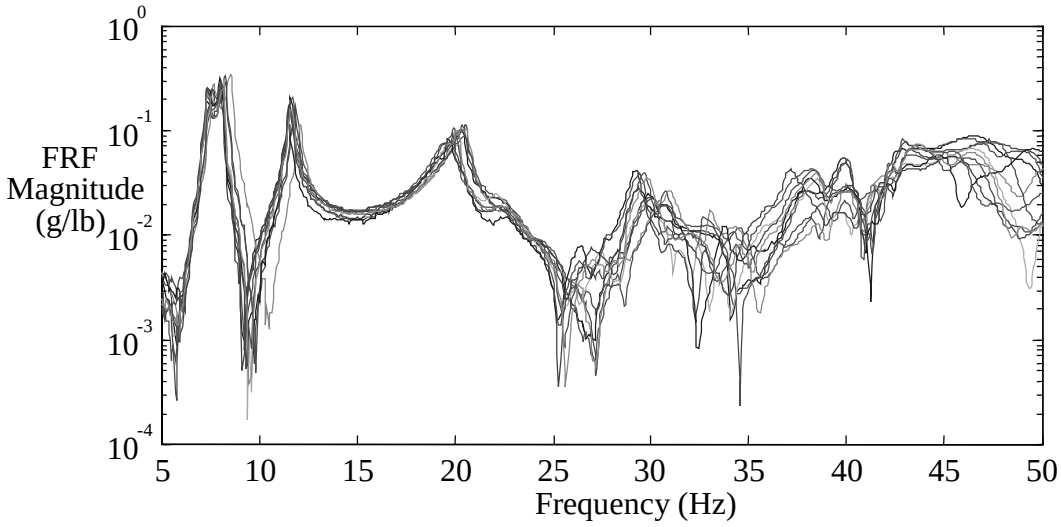

Figure 62. Overlay of 11 averaged (30 averages) FRFs measured at Pt. 2 over a 24-hour period.

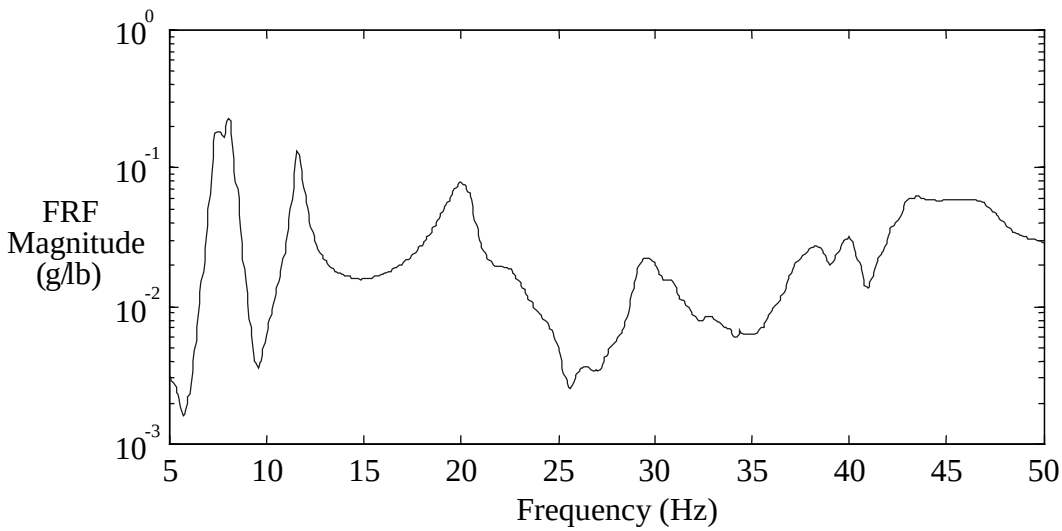

Figure 63. Average of 330 FRFs measured at Pt. 2 during a 24-hour period.

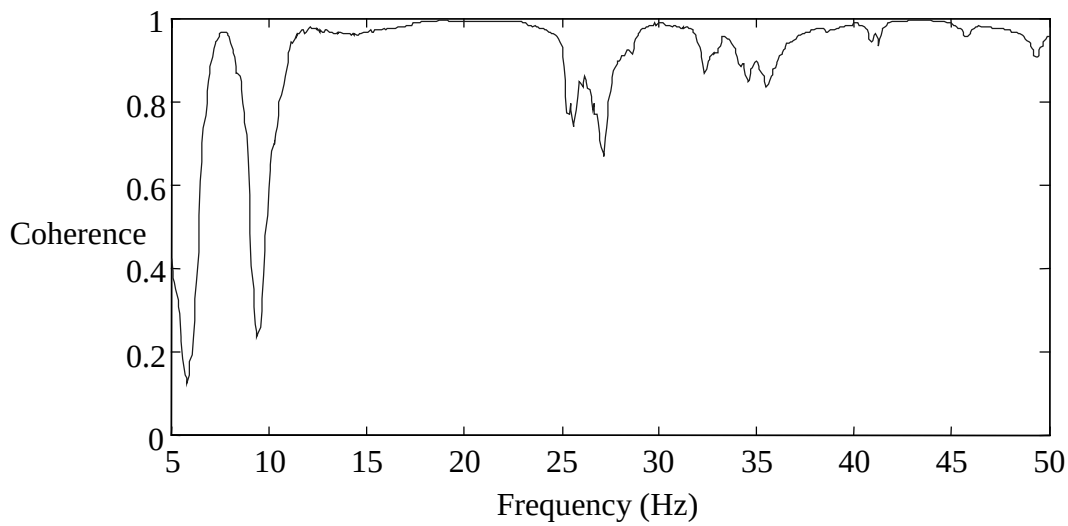

Figure 64. Coherence function corresponding to the average FRF measured during a 24-hour period.

From the results presented in Section IV.B it was known that temperature variations during the day produce up to 5% changes in the resonant frequencies of this bridge. These temperature changes represent a systematic error source inherent in these data. Recall that the Monte Carlo procedure assumes that the error source is random while the bootstrap procedure makes no underlying assumption about the error source. **Table 11** summarizes the results from the statistical analyses of the two Alamosa Canyon Bridge data sets.

Table 11. Comparison of bootstrap and Monte Carlo statistical analysis results on data from the Alamosa Canyon Bridge

	Mean (Bootstrap)	**95% Confidence Interval (Bootstrap)**	**Mean (Monte Carlo)**	**95% Confidence Interval (Monte Carlo)**
Individual test (30 averages)				
1st Mode Freq.	7.30 Hz	0.00323 Hz	7.30 Hz	0.00408 Hz
2nd Mode Freq.	8.05 Hz	0.00412 Hz	8.09 Hz	0.0205 Hz
3rd Mode Freq.	11.6 Hz	0.00219 Hz	11.6 Hz	0.00924 Hz
1st Mode Damp.	1.7 %	0.038 %	1.6 %	0.047 %
2nd Mode Damp.	1.4 %	0.048 %	1.1 %	0.16 %
3rd Mode Damp.	0.983 %	0.017 %	0.94 %	0.043 %
Results from 11 tests (30 averages each) over a 24-hour period				
1st Mode Freq.	7.34 Hz	0.0768 Hz	7.32 Hz	0.0070 Hz
2nd Mode Freq.	7.96 Hz	0.113 Hz	8.08 Hz	0.0331 Hz
3rd Mode Freq.	11.6 Hz	0.0621 Hz	11.5 Hz	0.0188 Hz
1st Mode Damp.	2.4 %	0.84 %	2.2 %	0.083 %
2nd Mode Damp.	2.3 %	0.94 %	1.6 %	0.25 %
3rd Mode Damp.	1.5 %	0.64 %	1.3 %	0.086 %

2. Summary and Observations

Two methods, Monte Carlo simulation and bootstrap analysis have been presented for evaluating the statistical variations in modal parameters identified from measured FRF data. The variability in these parameters arises from environmental effects such as thermal gradients, changing service conditions such as traffic loads, and from variability associated with the measurement and data reduction process. Note that some of these processes produce random errors while others produce bias (systematic) errors.

Before vibration-based damage identification procedures can be routinely applied to a bridge, particularly in a remote monitoring mode, the effects of these variability sources on the modal-based parameters used by the damage identification algorithm must be quantified. Such quantification may require measurements to be made at different times of the year, during different weather conditions, and when the bridge is experiencing different service conditions. Based on the results of such tests, it is conceivable that bounds can be developed for the base parameters that are monitored by the damage identification system. Damage must cause changes in these parameters that are outside these bounds for a definitive statement to be made regarding the onset of damage in the bridge.

F. Tests to Study Damage Identification

Damage identification using changes in measured modal parameters is a topic that has received considerable attention in the literature in recent years. The majority of existing methods use the following three modal parameters as basic building blocks for damage identification: modal frequency, mode shape, and mode shape curvature. Frequency and mode shape are used in flexibility analysis (see Toksoy and Aktan (1994)) and model correlation approaches (see Hemez and Farhat (1995), Zimmerman and Kaouk (1994), and Doebling (1996)). Mode shape curvature is used primarily in discretized strain energy methods (see Stubbs, et al. (1995)).

Each of these basic parameters has positive and negative attributes for use in damage identification. The modal frequency has the advantage of ease and accuracy of measurement, but does not provide spatial information regarding the damage location and the lower frequencies typically measured in a vibration tests are not very sensitive to damage. Mode shapes have the advantage of providing spatial information regarding the damage location, but require more sensors to measure and are more mathematically involved to extract from the data. The mode shape curvature offers spatial specificity along with high sensitivity to damage, but can be subject to numerical estimation difficulties resulting from the need for differentiation of mode shape approximations.

One characteristic of the basic modal damage indicators that is often overlooked is the statistical uncertainty inherent in the measurements caused by random variation in the signal. This uncertainty describes the amount by which one would expect the estimated value to change from one measurement to the next as a result of electrical noise, slight variations in testing conditions, environmental effects (such as temperature and wind), etc. Once the uncertainty bounds for each of the basic indicators has been defined, any change within that bound can be classified as “statistically insignificant,” i.e. it can be attributed to the random variations. Thus, the statistical uncertainty on the damage indicators must be defined so that the analyst can determine whether an observed change in the indicator is large enough to be exclusively indicative of damage, or whether it can be attributed to the natural variations in the measurements.

The tests that took place between July 19, 1996 to Aug. 3, 1996 (ACBT3) included a series of tests with various levels of attempted damage. Unfortunately, the permitted alterations in the bridge did not cause a significant change in the measured modal properties. Specifically, the bolts that held one of the channel-section cross members to the girders were removed. Unfortunately, even with the bolts removed, no relative motion could be induced at the interface under the loading of the modal excitation because of metal sleeves that had been inserted into the bolt holes. For this reason, the damage cases presented in Section IV.F.1 are results from simulated stiffness reduction using a correlated FEM. The finite element model is discussed in Section V. During the test in 1997 an attempt to stiffen the structure was made by clamping a steel plate to the bottom of the eastern most I-beam. The results from this test will be presented in Section IV.F.2.

1. Simulated Damage Study

In this section, modal measurements from the Alamosa Canyon Bridge are analyzed to determine the 95% statistical uncertainty bounds on the modal frequencies, mode shapes, and mode shape curvatures. These uncertainty bounds are based on the propagation of standard values for the random error on the frequency response function (FRF) estimates through the modal identification procedure to the modal parameters.

Changes in the modal frequencies, mode shapes, and mode shape curvatures that are expected as a result of damage are computed using a correlated finite element model (FEM). These predicted changes are compared to the 95% confidence bounds computed from the experimental data, to determine which changes can be classified as statistically significant. A comparison is made of the overall statistical significance of the three indicators. The results indicate that although frequency is not very sensitive to damage, it has such low uncertainty bounds that it is a good indicator for the existence (not location) of the damage case considered. Also, particular components of the mode shape, and especially the mode shape curvature, can be statistically significant indicators of the location damage. However, the overall average values of the mode shape and mode shape curvature changes are typically not statistically significant.

a. Uncertainty bounds on measured parameters from random disturbance

The statistical methods used to put confidence bounds on modal quantities were discussed in Section IV.D. The 95% uncertainty bounds on the modal frequencies, mode shapes, and mode shape curvatures resulting from random disturbances and noise, as computed by the Monte Carlo analysis, are presented in **Table 12**. It is observed from these results that the uncertainty bounds on the modal frequencies are much smaller than on the mode shapes, with the mode shape curvatures having the largest uncertainties. (The definition of the "average" errors for mode shape and mode shape curvature is presented in section V.E.3.)

Table 12. Uncertainty Bounds on Measured Parameters from Random Disturbances

Mode #	Error on Modal Freq.	Avg. Error on Mode Shape	Avg. Error on Mode Shape Curvature
1	0.06%	1.7%	560%
2	0.73%	45%	5200%
3	0.06%	1.7%	6.8%
4	0.24%	24%	13%
5	0.50%	160%	640%
6	0.06%	5.6%	37%
7	0.09%	3.6%	34%
8	0.11%	5.5%	9.5%
9	0.19%	160%	37%

b. Simulation of damage in the finite element model

The finite element model is discussed in detail in Section V. The damage case that was simulated for the Alamosa Canyon Bridge was the complete failure of the bolted connection of two cross members at an interior girder. The damage was simulated by 99% reduction in the modulus of elasticity of the cross members on either side of the connection. Thus, their ability to carry loads is lost, but their mass is still contained in the model, as would be the case in an actual connection failure. The changes in the FEM modal frequencies, mode shapes, and mode shape curvatures as a result of damage are presented in **Table 13**. It is observed in this table that the relative change of mode shapes is larger than that of frequencies and the relative change of mode shape curvatures is typically the largest.

Table 13. Changes in FEM Modal Parameters Resulting from Damage

Mode Number	Change in Modal Freq.	Avg. Change in Mode Shape	Avg. Change in Mode Shape Curvature
1	0.00%	0.03%	4.6%
2	0.02%	0.16%	2.4%
3	0.27%	0.87%	5.8%
4	1.11%	3.9%	3.5%
5	0.00%	0.07%	8.1%
6	0.03%	0.25%	1.8%
7	0.24%	1.5%	24%
8	0.76%	5.4%	6.5%
9	1.2%	21%	4.8%

c. Comparison of statistics to predicted damage effects

A comparison of the estimated 95% confidence bounds determined by the Monte Carlo method and the predicted changes as a result of damage for the modal frequencies are shown in Figure 65. The modal frequencies of modes 3, 4, 7, 8, and 9 undergo a change that is significantly larger than the corresponding 95% confidence bounds. The relative magnitudes of the changes indicate that the frequency changes of these modes could be used with confidence in a damage identification analysis. It should be noted from the y-axis scale of Figure 65 that the overall changes in frequency as a result of damage are quite small (< 1.2%), but as a consequence of the extremely low uncertainty bounds on the modal frequencies (many less than 0.2%), these small changes can be considered to be statistically significant.

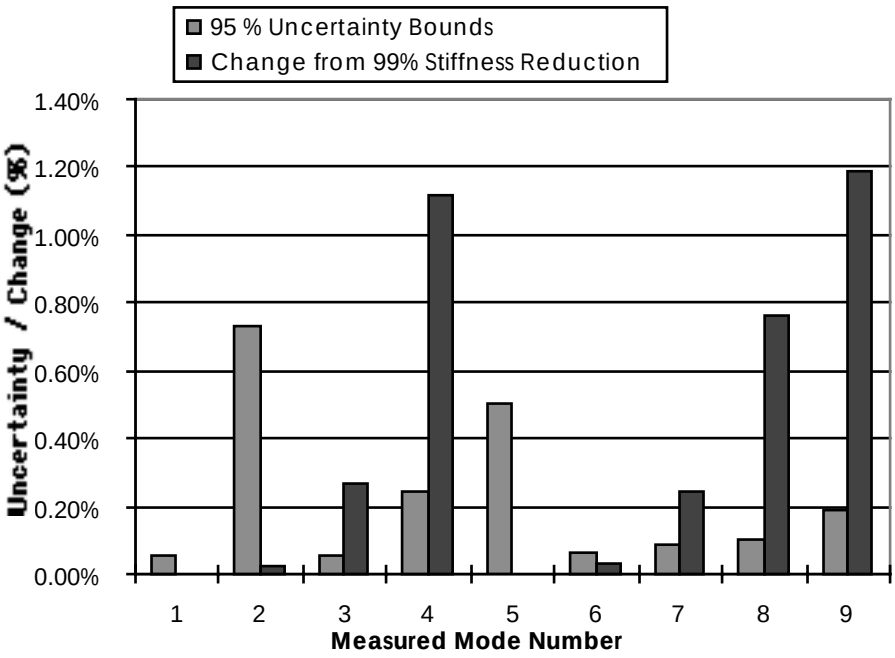

Figure 65. Comparison of modal frequency 95% confidence bounds to changes predicted as a result of damage.

One method for comparison of the confidence bounds on the mode shape components to the predicted change as a result of damage is a direct, component-by-component comparison. Such a comparison for modes 3 and 7 is shown in Figure 66. Modes 3 and 7 were chosen for illustration purposes because mode 3 was found to be sensitive to damage and mode 7 was not as determined by a visual inspection of the modes. These plots show the mean values of the undamaged mode shape components in a solid line (with 95% confidence bounds at the measurement locations as determined by the Monte Carlo method), with the predicted mode shape after damage represented by a dashed line. These mode shape components represent a "slice" of each of these mode shapes taken along one girder of the bridge. This slice of mode shape 3 contains 3 components that have a predicted change from damage that is greater than the 95% confidence bounds. Thus, the change in these 3 components can be used with confidence in a damage identification algorithm. However, none of the components of this slice of mode shape 7 have a change that is greater than the 95% bound, so these components of this mode shape have an insignificant change as a result of damage, and should not be used in a damage identification analysis.

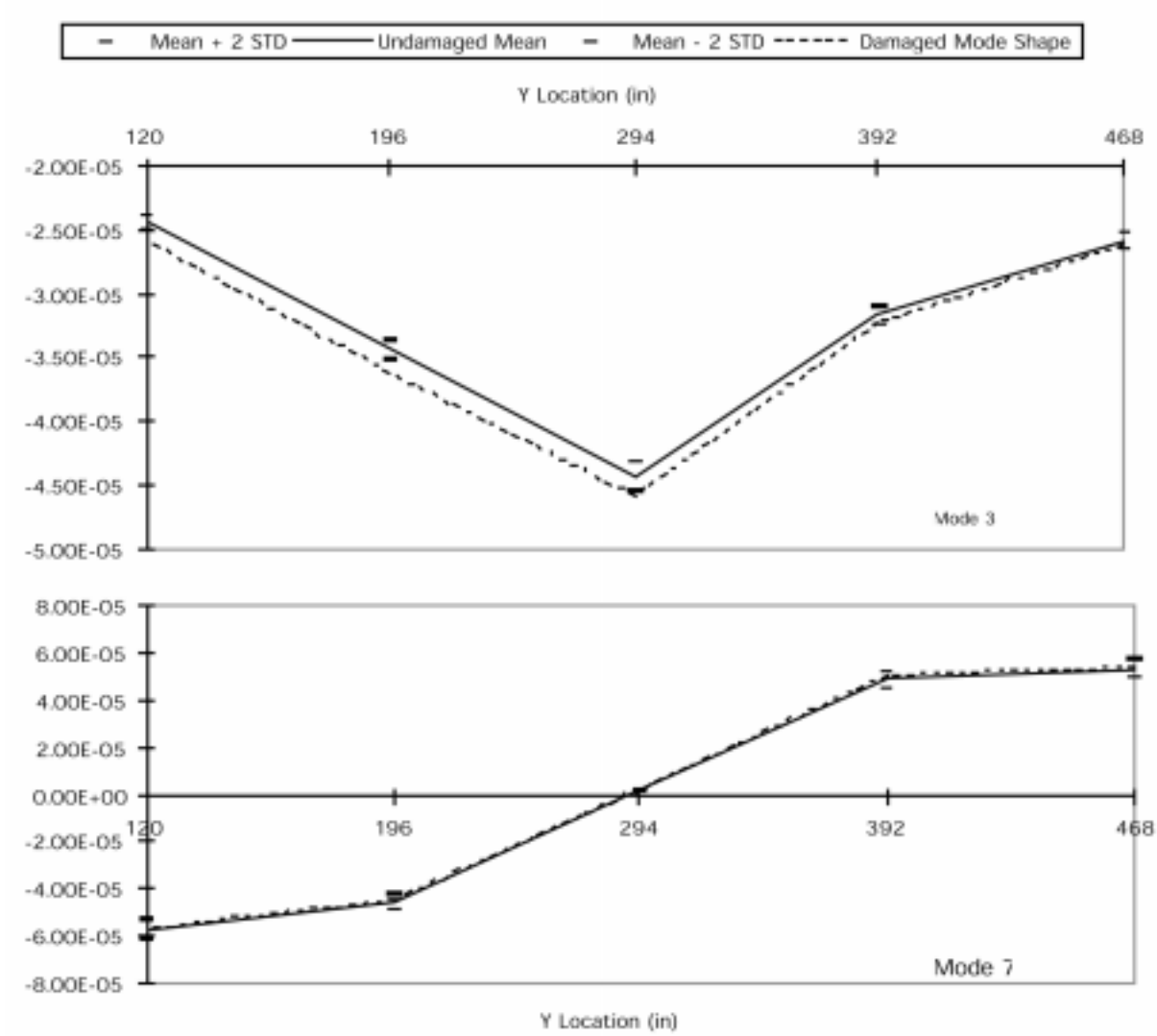

Figure 66. Comparison of modes 3 and 7 confidence bounds and predicted change after damage.

An "average" of the component-by-component mode shape comparison shown above was computed to give an overall measure of the mode shape change and corresponding 95% confidence bound for each mode shape. The average mode shape change for mode j as a result of damage, $\overline{\Delta\phi}_j$, was defined as

$$\overline{\Delta\phi}_j = \frac{\sum_i \phi_{ij}^d - \phi_{ij}^u}{\sum_i \left|\phi_{ij}^u\right|} \tag{11}$$

where ϕ_{ij} is the jth mode shape measured at the ith DOF, and the superscripts u and d refer to modes from the undamaged and damaged structure, respectively. A corresponding average 95% confidence bound for the jth mode, $\overline{\sigma}_j$, was defined as

$$\overline{\sigma}_j = \frac{2\sum_j \sigma(\hat{\phi}_{ij})}{\sum_j \left|\mu(\hat{\phi}_{ij})\right|} \tag{12}$$

where $\sigma(\hat{\phi}_{ij})$ and $\mu(\hat{\phi}_{ij})$ are the standard deviation and mean of the jth identified mode shape at the ith DOF, $\hat{\phi}_{ij}$.

A comparison of the average 95% confidence bounds and the predicted changes as a result of damage for the mode shapes are shown (on a semilog scale) in Figure 67. Although many of the mode shapes undergo a significant (> 5%) average change, none of the mode shapes undergo an average change over all degrees of freedom that is larger than the 95% confidence bounds caused by random variations in the measurements. Mode 8 is the only mode whose average change is near statistical significance. This figure only indicates the average change over all of the mode shape components, however, when in fact several of the mode shapes undergo a large localized change at particular DOF. The total number of DOF where the mode shape components undergo a change equal to or greater than the 95% confidence bounds is shown in **Table 14**. Mode 8 has the component with the largest change. It is interesting to note that although mode shapes 3, 7, and 8 have average changes that are less than the average 95% uncertainty bound, they have 9, 5, and 6 individual components (out of 30 total) that undergo a significant change, respectively.

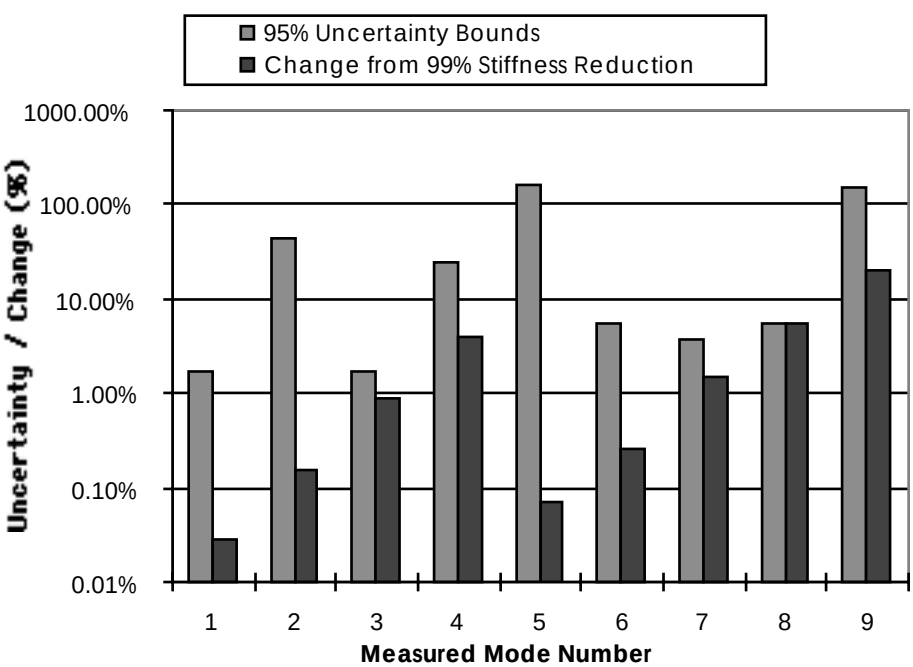

Figure 67. Comparison of average mode shape component 95% confidence bounds to changes predicted as a result of damage.

Table 14. Number of DOF for each mode shape that undergo change resulting from damage ≥ 95% confidence bounds.		
Mode Number	**Number of Mode Shape Components with Change > 95% Bound**	**Maximum Ratio of Component Change to 95% Bound**
1	0	0.069
2	0	0.016
3	9	2.521
4	0	0.982
5	0	0.002
6	1	1.048
7	5	2.955
8	6	5.431
9	1	1.361

The statistical significance of changes to the mode shape curvature can be evaluated in a manner analogous to the analysis of the mode shapes. The most basic method is a direct, component-by-component comparison, as shown in Figure 68 for modes 3 and 7. In this case, mode 3 shows only slight changes in some of its curvature components, whereas mode 7 shows a large change in two of its curvature components. It should be noted that the curvatures shown in Figure 68 are the curvatures in the east-west direction of the sensor configuration, which is parallel to the cross-members and perpendicular to the girders. Therefore, the curvatures of Figure 68 are not the second derivatives of the mode shapes shown in Figure 66 along the y-axis, but rather along the transverse direction.

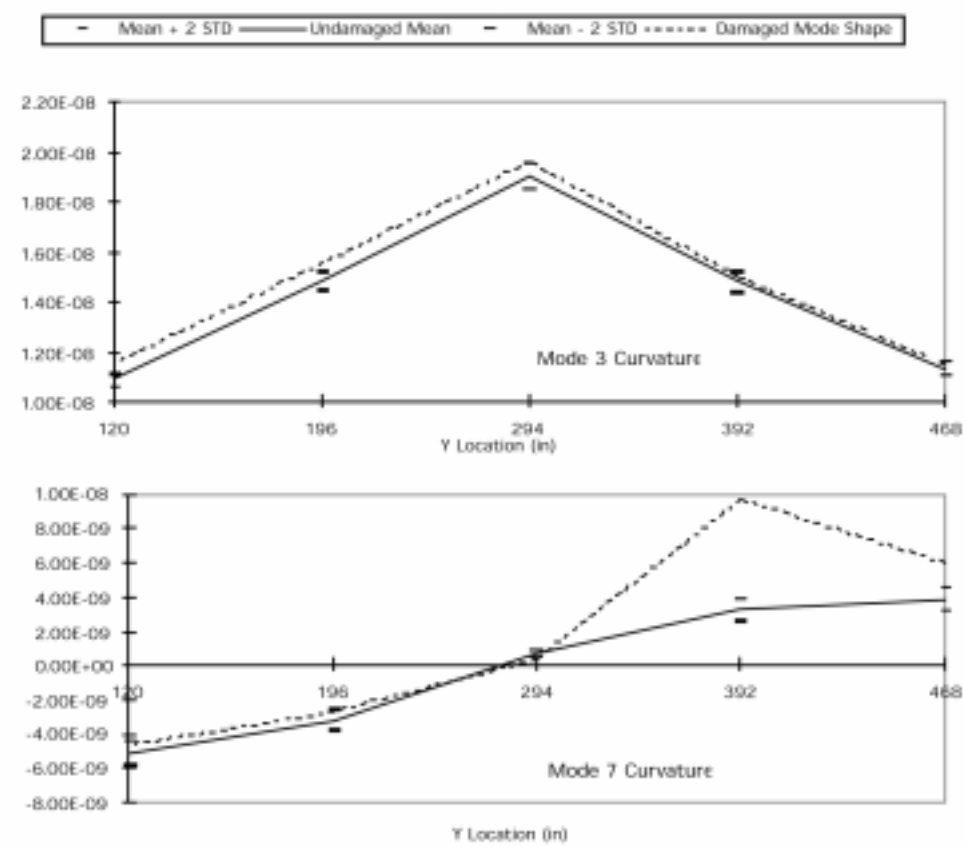

Figure 68. Comparison of modes 3 and 7 curvature confidence bounds and predicted change after damage.

Indicators that show the average uncertainty and change in curvature after damage were defined analogous to those defined for mode shapes in Eq. (10) and Eq. (11). A comparison of the average 95% confidence bounds and the predicted changes as a result of damage for the mode shape curvature components for each mode are shown in Figure 69. Although many of the mode shape curvatures undergo a significant (> 5%) average change, none of the mode shape curvatures undergoes an average change over all degrees of freedom that is larger than the 95% confidence bounds caused by random variations in the measurements. Modes 3, 7 and 8 are the only modes whose average curvature change is near statistical significance. This figure only indicates the average change over all of the mode shape curvature components, however, when in fact several of the mode shapes undergo a large localized curvature change at particular DOF. The total number of DOF where the mode shape components undergo a change equal to or greater than the 95% confidence bounds is shown in Table 15. Mode 7 has the individual component with the largest curvature change. It is interesting to note that although mode shape curvatures 3, 6, 7, 8 have average changes that are less than the average 95% uncertainty bound, they have 7, 3, 9 and 8 individual components that undergo a significant change, respectively. In summary, the statistical analysis of the mode shape curvature changes shows that over all their components, they generally do not exhibit a change larger than the 95% uncertainty bounds. However, individual components of certain mode shape curvatures exhibit changes that are much larger than the 95% uncertainty bounds, as shown for mode 7 in Figure 68. These local

statistically significant changes provide the spatial information necessary to locate damage. Therefore, individual components of the mode shape curvatures can be used for damage identification, but the analyst should compare the measured changes in curvature to the computed 95% uncertainty bounds to determine whether the observed changes in curvature are statistically significant.

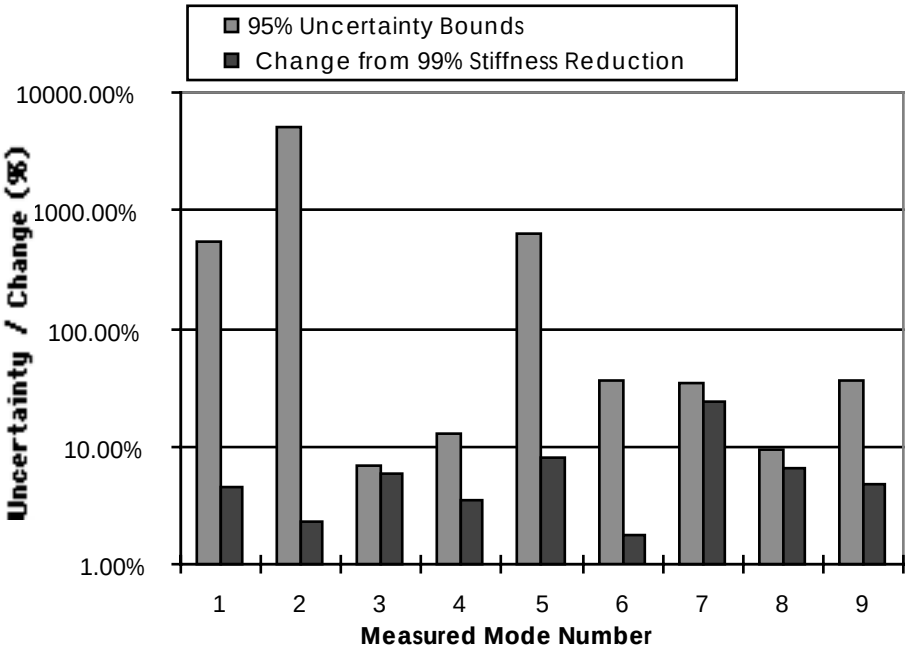

Figure 69. Comparison of average mode shape curvature component 95% confidence bounds to changes predicted as a result of damage.

Table 15. Number of DOF for Each Mode Shape Curvature That Undergo Change Resulting from Damage ≥ 95% Confidence Bounds.

Mode Number	Number of Mode Curv. Components with Change > 95% Bound	Maximum ratio of Component Change to 95% Bound
1	0	0.21
2	0	0.011
3	7	2.6
4	0	0.86
5	0	0.87
6	3	2.1
7	9	9.9
8	8	5.2
9	0	0.90

2. Stiffening the Structure

As discussed earlier, the first attempt to introduce a change to the structure by removing the nuts on the bolted connections that hold the channel-section cross members to the girders was unsuccessful. Even with the bolts removed, no relative motion could be induced at the interface under the loading of the modal excitation because of metal sleeves that had been inserted into the bolt holes. A second attempt to modify the structure was made during the test performed in July 1997. In this test an attempt to stiffen the structure was made by clamping a steel plate to the bottom of the eastern most I-beam. The clamps and plate can be seen in Figure 70.

Figure 70. Clamps and plate used to stiffen the structure locally.

The procedure for taking data for the stiffened bridge was identical to that discussed in Section IV.A.1. The primary purpose of this test was to determine if the slight stiffening of the structure caused by the steel plate could be identified. Two of the data sets that were obtained as part of the 24-hour test were used as representative of the unstiffened structure. These two tests will be referred to as Time 6 and Time 7 (corresponding to the 6th and 7th of the data sets taken during the 24-hour test) throughout the remainder of this section. The two data sets chosen for comparison were performed at temperatures similar to those experienced during the stiffened test.

a. Results from stiffening the structure

The frequencies and damping of the stiffened structure as compared to those obtained from several of the data sets taken during the 24-hour test are shown in **Table 16** along with the "average" temperature of the deck during each test. "Time 10" was included for comparison because it had an average temperature significantly lower than the others. The average temperature was obtained by averaging the thermometer readings taken at the start and at the conclusion of each test from the thermometers located on the top and bottom surfaces of the bridge. For some reason the temperature on the bottom of the bridge was higher for the stiffened test than for any of the tests taken during the 24-hour test. During the stiffened test the deck also experienced a larger negative temperature differential than it did during any of the times during the 24-hour test. From **Table 16** the frequencies of the stiffened structure fall into the range of frequencies caused by temperature effects only about half the time. This could be explained by the fact that the temperature difference between the east and west sides of the bridge was so large and, as shown in Section IV.B.1, this temperature differential seems to correlate well with changes in the frequencies.

Table 16. Comparison of Frequencies and Damping for the Stiffened Structure and the Unstiffened Structure

Mode	Frequency–Hz (Damping–%)			
	Time 7	Time 6	Time 10	Stiffened Test
1	7.44 (1.9)	7.49 (1.9)	7.32 (1.5)	7.39 (1.7)
2	7.99 (1.2)	8.12 (1.1)	8.09 (1.2)	8.21 (1.3)
3	11.5 (0.93)	11.6 (0.92)	11.6 (1.1)	11.6 (1.2)
4	20.0 (2.2)	20.0 (2.4)	20.1 (1.8)	19.7 (1.1)
5	22.2 (3.1)	22.0 (2.9)	23.5 (3.2)	22.5 (3.0)
6	25.1 (2.1)	25.4 (2.0)	25.3 (2.1)	25.4 (2.0)
	Average Temperature (°F)			
	Time 7	Time 6	Time 10	Stiffened Test
Average Top	102	109	74.5	98.4
Average Bottom	90.4	89.9	71.5	99.4
Bridge Deck Temp. Differential	6.2	–1.7	–0.35	–17

The data from the stiffened test and from Time 6 and Time 7 were analyzed in DIAMOND using two damage detection methods to determine if the stiffened location could be identified. The two damage detection methods used were the flexibility method [Farrar and Jauregui (1996)] and the 2-D strain energy method. The 2-D strain energy method is discussed in detail in Appendix E. Unfortunately, there were not data available for the unstiffened structure that had the same deck temperature differential as that observed during the stiffened test. A total of three analyses were performed as listed below using both the flexibility method and the strain energy method:

Case 1:	Undamaged data: from Time 7 Damaged Data: from stiffened test
Case 2:	Undamaged data: from Time 6 Damaged Data: from stiffened test
Case 3:	Undamaged data: from Time 7 Damaged Data: from Time 6

The purpose of the third analysis listed above was to see if there was any difference between the comparison of the stiffened structure to the unstiffened structure and that obtained by comparing two sets of data from the unstiffened structure taken at two different times during the day.

In the 2-D strain energy algorithm the first six modes were used and the damage index was determined after dividing the structure into a twenty by twenty grid. A spline interpolation was used to determine the intermediate points required for the calculations of the curvatures of the mode shapes. These curvature calculations were performed by numerically differentiating the mode shapes. The results from all three cases listed above looked very similar, with the normalized damage index appearing to be essentially random. Bar plots of the normalized damage indices for the three cases are shown in Figure 71. The stiffening plates were centered on a longitudinal coordinate of approximately 250 on the axis ranging from 100 to 500 in Figure 71. In this figure the “U” and “D” indicate which data sets were designated as undamaged and damaged in the algorithm. Therefore, in this case the strain energy method was not sensitive enough to determine any changes in the structure caused by addition of the steel plate.

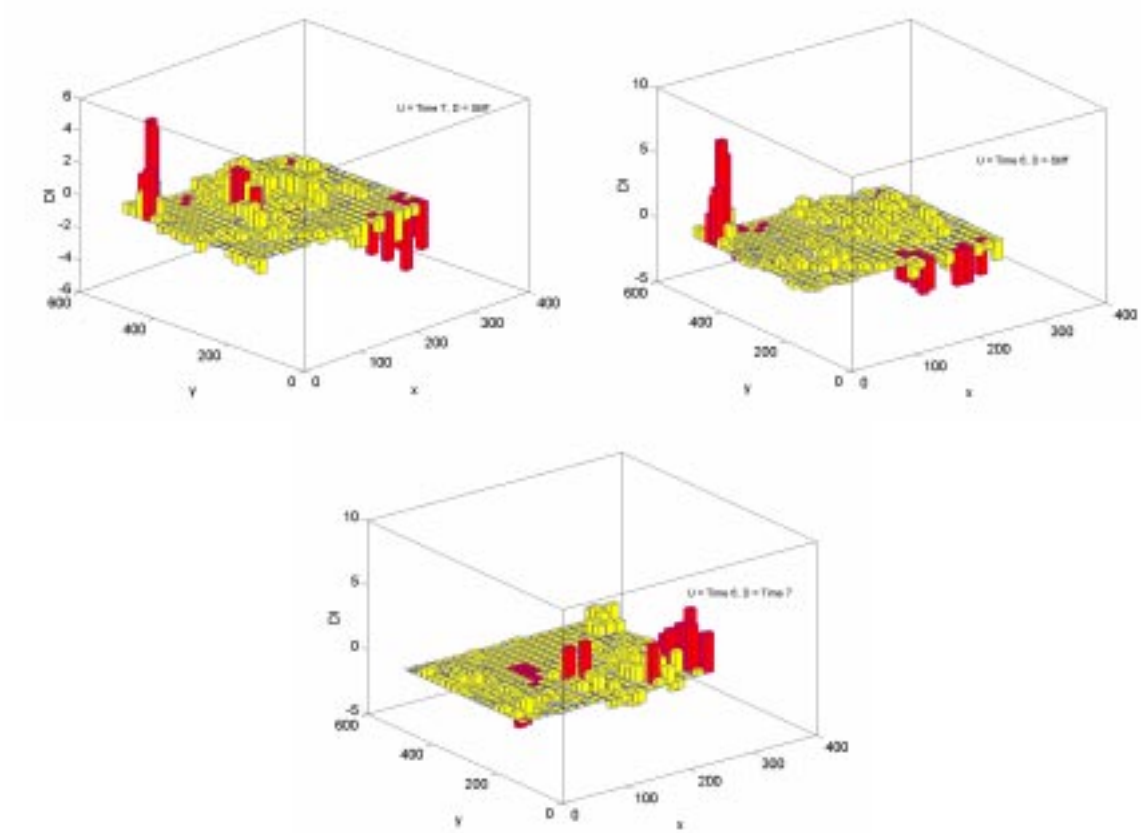

Figure 71. Bar plots of the normalized damage indices obtained from the strain energy method.

The second damage detection method used on the data was the flexibility method. Six modes were used in the algorithm. Contour plots of the flexibility changes are shown in Figure 72. In all three cases a flexibility change was observed in various areas of the structure, but unfortunately, these flexibility changes were not at the location of the stiffening. The magnitudes in the change of flexibility between the two unstiffened cases, Time 6 and Time 7, were very similar to those obtained by comparing Time 6 and Time 7 to the stiffened test. In all three cases the changes in flexibility were very small, that is, on the order of 10^{-12}. Therefore, the flexibility method also failed to locate the stiffened region of the structure.

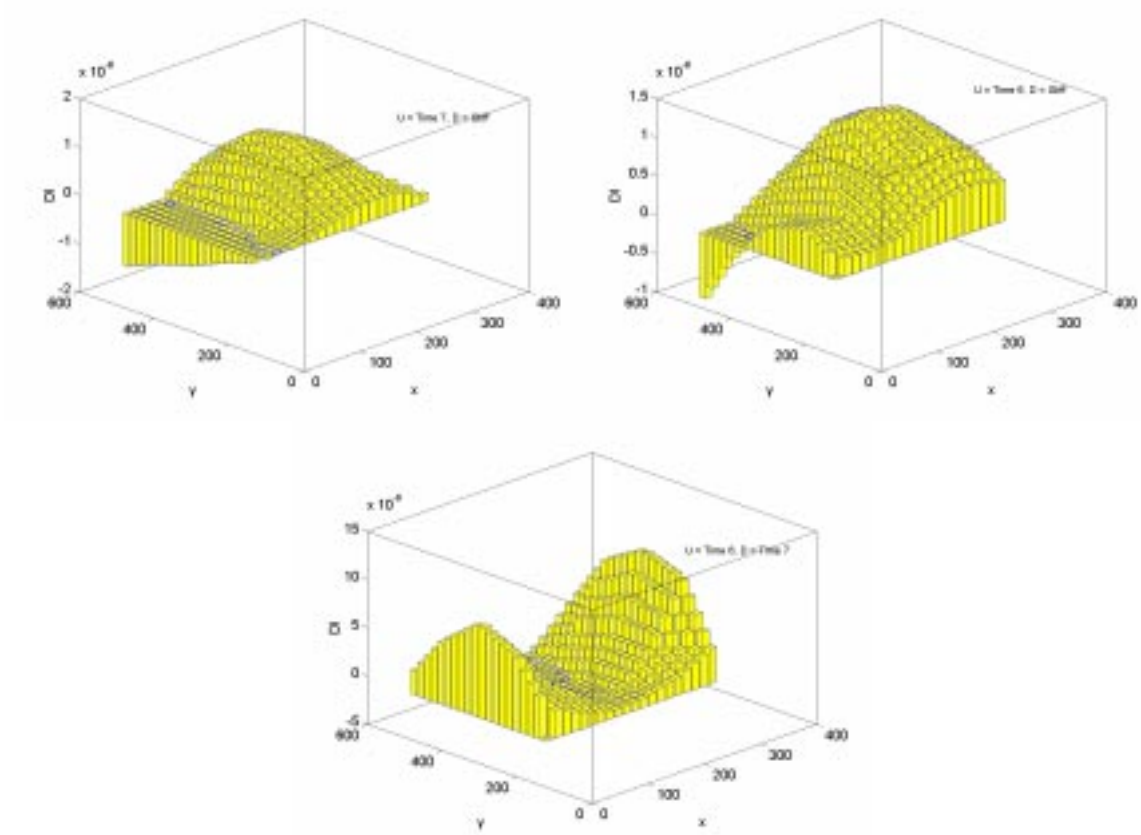

Figure 72. Bar plots of the changes in flexibility for the three data sets analyzed.

In conclusion, both damage identification methods failed in locating the stiffened region of the structure and are clearly not sensitive enough to detect changes at the level introduced by the stiffening.

G. Shaker Tests

Los Alamos National Laboratory's University of California Interaction office provided additional funds so that Professor Gerry Pardoen and students from the University of California Irvine could participate in the series of tests done in July 1997. Professor Pardoen used 30 lb and 100 lb shakers to excite the structure in a direction perpendicular to the bridge deck. The 100 lb shaker is shown in Figure 73.

Figure 73. 100 lb shaker provided by the University of California at Irvine.

The shaker was located at the same point the impact has been applied in previous tests, that is, at point A in Figure 33. The input spectrum from the 30 lb and 100 lb shakers was significantly noisier than that obtained when using the instrumented sledge hammer. This is clearly shown in Figure 74 where PSDs for the input signals are compared for the two shaker tests and for a hammer test. Unfortunately, the calibration factors for the accelerometers located on the shakers were not recorded. These transducers were provided by the researchers from UC Irvine. The output PSDs at point A in Figure 33, that is from the accelerometer located on the top of the deck, are shown in Figure 75 for the hammer and the two shaker tests. The hammer test chosen for comparison was one that was taken at a similar average temperature to the shaker tests. Clearly the PSDs from the shaker tests are much noisier even though the same number of averages were used for all the tests.

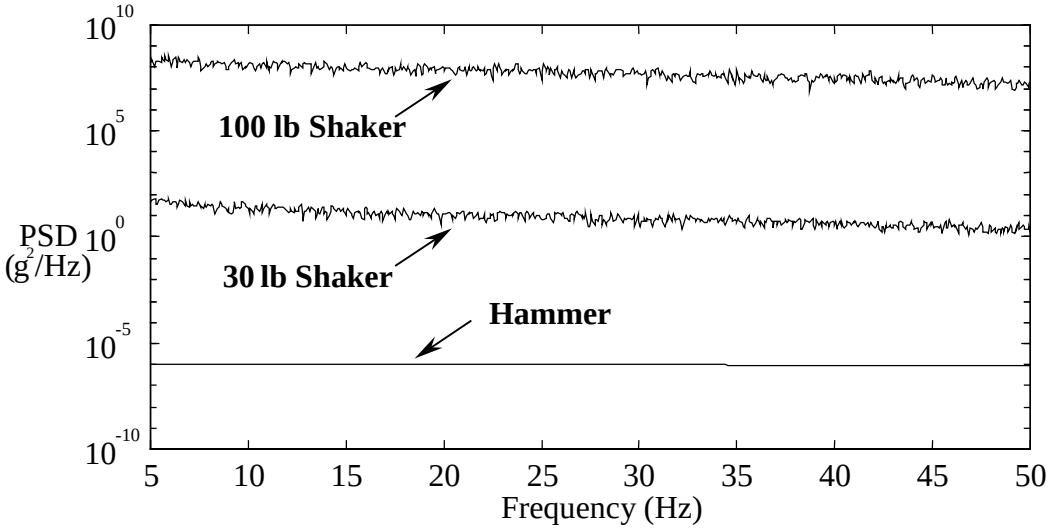

Figure 74. A comparison of the input PSD from the hammer, 30 lb shaker and 100 lb shaker.

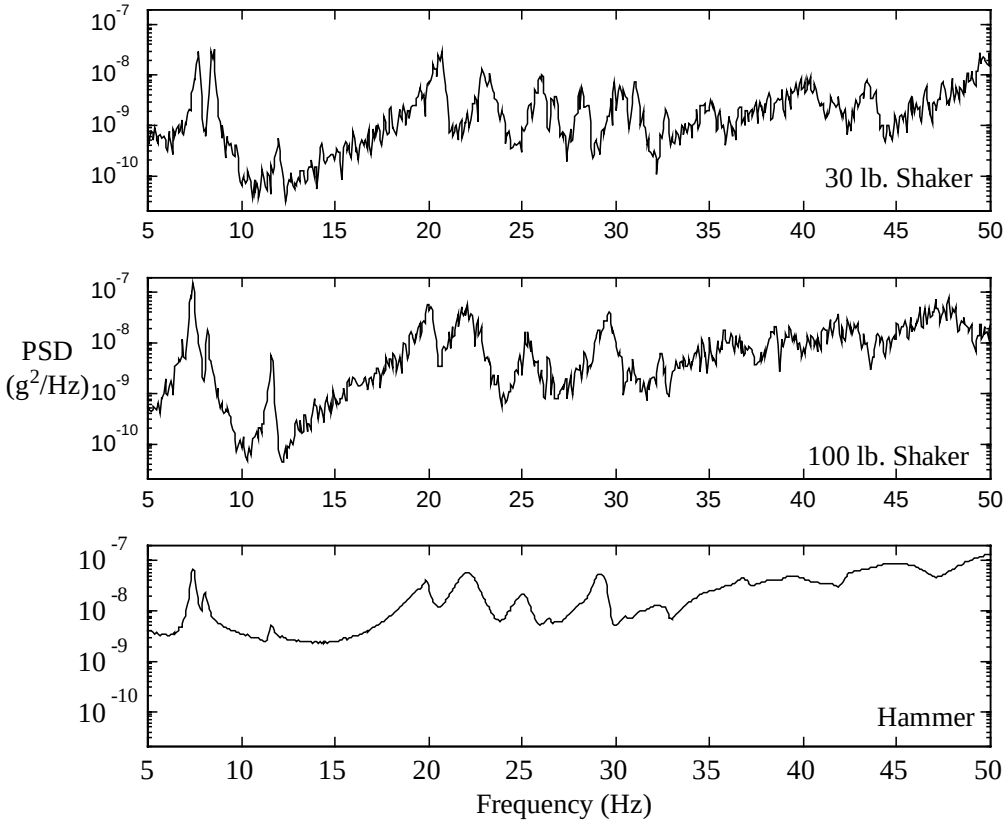

Figure 75. A comparison of the PSD for the output signal at the excitation location using the hammer, 30 lb shaker and 100 lb shaker.

The first step in the analysis of the shaker data was to determine the CMIFs. The CMIFs of the 30 pound and the 100 pound shaker tests are shown in Figure 76 and Figure 77 respectively. As expected from looking at the PSDs, the CMIFs from the shaker tests appear to be much noisier. Clearly there are also more peaks in the CMIFs from the shaker tests than there were in the CMIF for a hammer test as shown in Figure 26. The CMIF was used to set the frequency bands for a global rational polynomial curve fit. A comparison of the frequencies and damping obtained from the shaker tests to those obtained from a hammer test is shown in **Table 17**. Almost all of the modes from the hammer test were also identified from the shaker tests except that the fifth mode from the shaker test was not identified using the 30lb shaker. A number of additional modes were identified from the shaker tests, but it is not clear if these were physical modes because the FRFs looked so noisy.

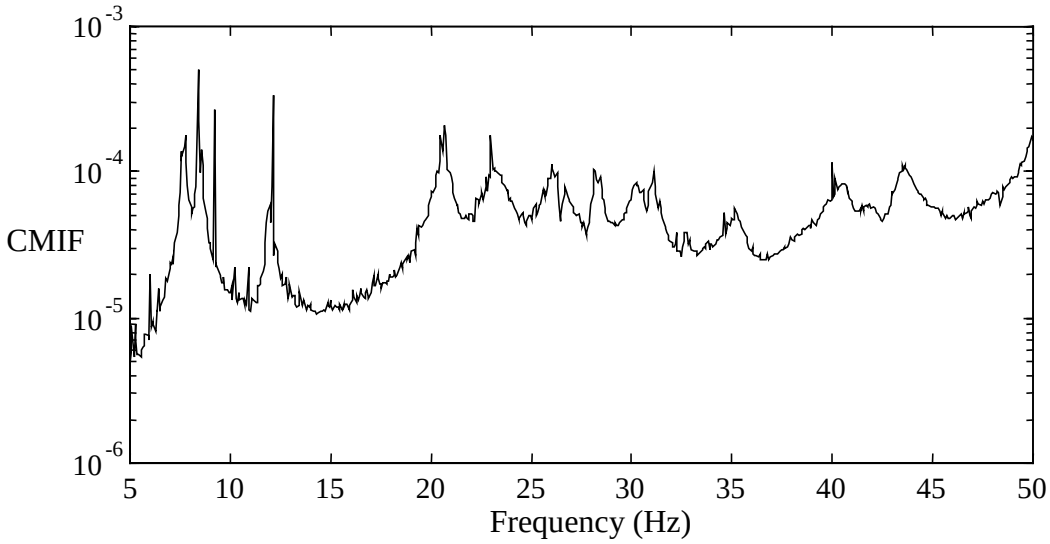

Figure 76. CMIF from the 30 lb shaker test.

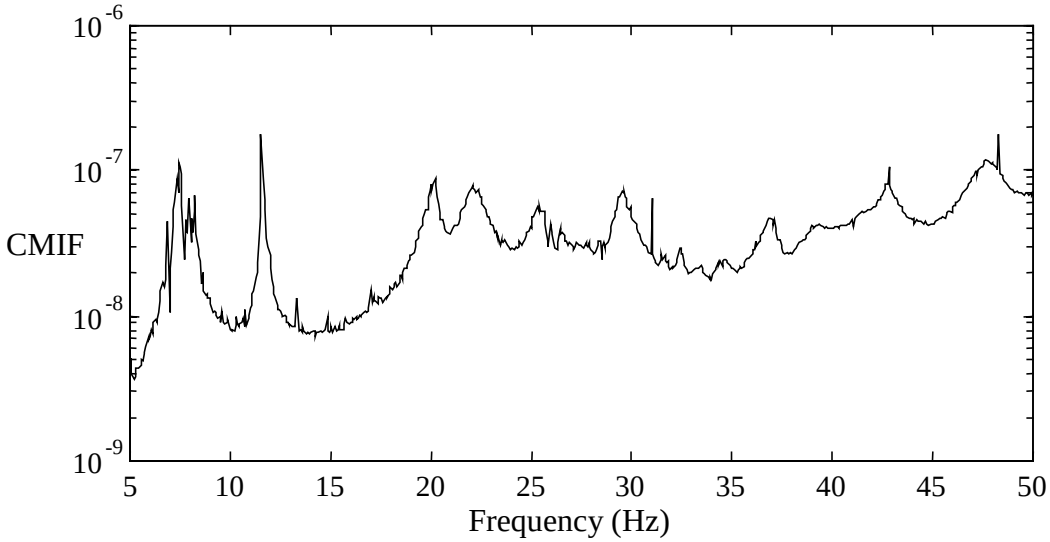

Figure 77. CMIF from the 100 lb shaker test.

Table 17. Comparison of Frequency and Damping Obtained from a Hammer Test and the Shaker Tests

Mode	Hammer Test		30 lb Shaker Test		100 lb Shaker Test	
	Frequency (Hz)	Damping (%)	Frequency (Hz)	Damping (%)	Frequency (Hz)	Damping (%)
1	7.44	1.9	7.70	1.1	7.33	0.89
1a	–	–	–	–	7.58	1.2
2	7.99	1.2	8.40	0.12	7.93	0.00
2a	–	–	9.18	0.00	–	–
3	11.5	0.93	12.1	0.08	11.6	0.21
4	20.0	2.2	20.5	0.10	20.1	1.2
4a	–	–	20.7	0.42	–	–
5	22.2	3.1	Not identified	Not identified	22.1	1.5
6	25.1	2.1	26.2	0.65	25.1	0.27
6a	–	–	–	–	–	–
7	25.3	0.46	26.6	0.47	25.4	0.73
7a	–	–	–	–	25.5	0.20

In an attempt to excite the lateral modes of the structure, an eccentric mass shaker was used to provide a swept-sine excitation to the structure in a direction parallel to the deck as shown in Figure 78. Unfortunately the eccentric mass shaker had a maximum frequency of just over 5 Hz which was lower than any of the modes of the bridge. Because it was not possible to significantly excite any of the lateral modes of the bridge, no useful data was obtained from these tests.

Figure 78. Eccentric mass shaker provided by the University of California at Irvine.

H. A Modular, Wireless Damage Monitoring System (WiMMS)

If vibration-based damage detection technology is to be adopted on a wide scale, it is the authors' opinion that it will have to be used in conjunction with a wireless data acquisition system. Otherwise the maintenance associated with wires will make the system too unreliable for commercial application. Such a system was developed by Eric Straser as part of his Ph.D. requirements at Stanford University [Straser (1998)]. The Alamosa Canyon Bridge was selected as the structure to perform a validation experiment and to provide a proof of concept of his design. The validation experiments were intended to (1) demonstrate the performance and problems of the system in a side-by-side comparison with a conventional monitoring system, and (2) verify the postulated benefits of the WiMMS in testing efficiency and immunity to the field environment.

The Alamosa Canyon Bridge was selected as the ideal structure because it is a full-scale structure in the field and its dynamic characteristics are well documented by previous experimental modal tests. The field test of the structure was performed in December 1997. The two systems used for the testing included a conventional instrumentation system and a wireless system. The conventional system was the one used in all the previous tests of the bridge consisting of a wired monitoring system with a centralized data acquisition system.

The wireless, modular monitoring system (WiMMS) consisted of five "sensor units" and a "site master" in the form of a receiver and a laptop PC. The sensor unit performs the data acquisition and then transmits the data to the site master via a digital wireless modem. A photo of the sensor unit installed on the flange of an interior girder and a photo of the site master radio modem are shown in Figure 79. The accelerometer used with each sensor unit was attached via epoxy to the underside of the flange as shown in Figure 80. The accelerometer on the right was used with the traditional data acquisition system and the one on the left was used with the WiMMS. The installation time and disassembly time for the WiMMS were both on the order of 30 minutes. By comparison, it took over 2.5 hours to install the traditional system and approximately 4 hours to disassemble it.

Side-by-side comparisons of the two systems were made for both ambient excitation and impact excitation caused by an instrumented sledge hammer. In general the tests went smoothly and the WiMMS performed well in the hostile New Mexico winter. A more detailed discussion of this test and the wireless, modular monitoring system can be found in Straser (1998). The primary results of this test are listed below.

1. It was demonstrated that a system of modular, wireless units could be installed in a fraction of the time of a standard, cable instrumentation system.
2. It was shown that a system can be designed for both an ambient excitation, periodic monitoring case as well as having the dynamic range to monitor an earthquake scenario. This is critical, as it is hard to envision a building owner or manager installing two separate systems for structural monitoring.
3. The basic process of triggering, acquiring data from multiple units, transmitting the data wirelessly, and archiving the data for later use worked well.

Site Master Ratio modem **Sensor Unit**

Figure 79. Site master radio modem and the sensor unit installed on a beam.

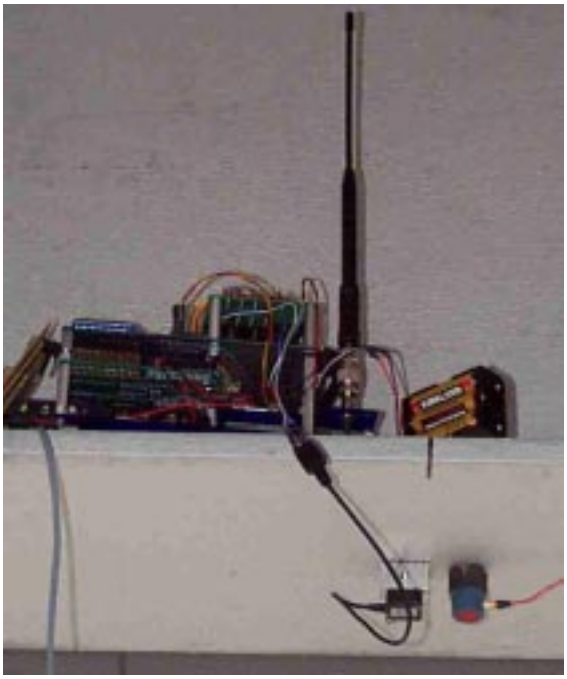

Figure 80. Sensor unit and accelerometers mounted to the bottom of a beam flange.

4. A side-by-side comparison of data taken from both the conventional system and the WiMMS concluded that some signal processing difficulties caused by impedance loading of the accelerometers and the lack of an antialiasing filter. A choice of a different accelerometer, among the many available on the commercial market can eliminate this problem. Another solution involves implementing a buffer amplifier in series with the current sensor and including a single pole 80 Hz antialiasing filter.

V. FINITE ELEMENT MODELING OF THE ALAMOSA CANYON BRIDGE

Detailed finite element analyses (FEA) were performed in conjunction with the experimental modal analyses. All calculations, mesh generation, vibration analysis, and post-processing were performed using the solid modeling program IDEAS. When benchmarked against measured dynamic properties of the structure, this numerical model can be used to study the effects of different damage scenarios on the dynamic response of the bridge as discussed in Section IV.F.1.

Because the Alamosa Canyon Bridge consists of seven spans that are coupled only through the interaction of their expansion joints and the bridge piers, they were treated as independent so that only one span needed to be modeled. The finite element model of one span of the Alamosa Canyon Bridge consisted of 612 thin shell elements for the bridge deck and 318 linear beam elements for the girders, cross members, and curbs. The beam elements were offset from the shell elements used to model the deck. The full model had 666 nodes. The finite element mesh used is shown in Figure 81 and a solid model representation of the span is shown in Figure 82.

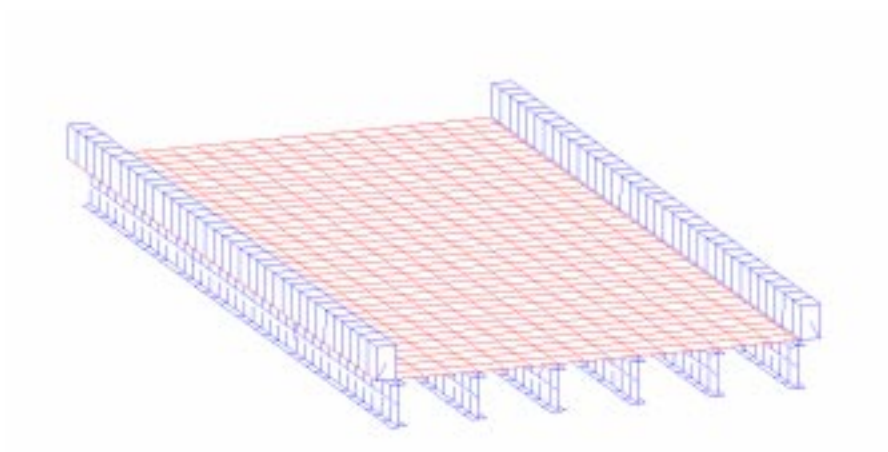

Figure 81. Finite element mesh.

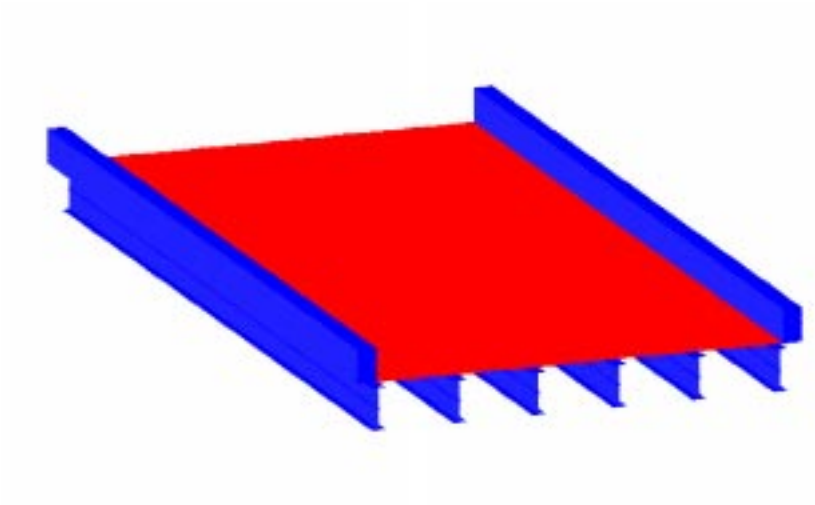

Figure 82. Solid model of the first span.

The finite element model was correlated with the measured modal frequencies from span 1 (far north end of the bridge). The final material and cross-sectional properties obtained for the model are shown in **Table 18**. The boundary conditions of the bridge were pinned-roller connections.

Table 18. FEM material and cross-sectional properties

Name	**Value**
Modulus of Elasticity, Steel	30×10^6 psi
Density, Steel	7.32×10^{-4} $lb_f\ s^2/in^4$
Modulus of Elasticity, Concrete	3.012×10^6 psi
Density, Concrete	1.903×10^{-4} $lb_f\ s^2/in^4$
Cross Section, Girder	Wide Flange, W30X116
Cross Section, Cross Members	Channel, C12X25
Cross Section, Curb	Rectangle, 14×24

The calculated resonant frequencies are compared to the measured resonant frequencies in Table 19. From this table it can be see that the magnitude of the average percent error between the calculated frequencies and the measured frequencies is 3.7%.

Table 19. Comparison of Frequencies Obtained Experimentally With Those Obtained From the Finite Element Analysis

Mode Number	Experiment Frequency (Hz)	Finite Element Analysis Frequency (Hz)	Percent Difference
1	7.81	7.34	–6.0
2	8.51	8.15	–4.2
3	12.1	11.5	–5.0
4	20.8	21.1	1.4
5	24.0	23.1	–3.8
6	26.6	27.0	1.5

A modal assurance criteria (MAC), sometimes referred to as a modal correlation coefficient was calculated to quantify the correlation between analytical and measured mode shapes. The MAC makes use of the orthogonality properties of mode shapes to compare the analytical and experimental mode shapes. If the modes are identical, a scalar value of one is calculated by the MAC. If the modes are orthogonal and dissimilar, a value of zero is calculated. The MAC that compares modes i and j has the form

$$\mathrm{MAC}(i, j) = \frac{\left|\sum_{k=1}^{n} (\phi_j)_k (\phi_i)_k^*\right|^2}{\left(\sum_{k=1}^{n} (\phi_j)_k (\phi_j)_k^*\right)\left(\sum_{k=1}^{n} (\phi_i)_k (\phi_i)_k^*\right)} \tag{13}$$

where $(\phi)_k$ is an element of the mode-shape vector and the asterisk denotes complex conjugate. The value of the MAC does not actually quantify the correlation between modes. Ewins (1985) points out that, in practice, correlated modes will yield a value greater than 0.9, and uncorrelated modes will yield a value less than 0.05.

Table 20 shows a comparison of the measured mode shapes to the mode shape data obtained from the finite element analysis. Table 20 shows that similar mode shapes are being identified for the first six modes. The primary source of error in this finite element model are the concrete material properties (modulus and mass density), the constraints of the girders to the abutments and piers, effects of concrete cracking, the torsional properties of the beam element representing the curb and the bond between the concrete deck and the girders.

Table 20. Figure Modal Assurance Criteria for the Mode Sshapes Identified from the Finite Element Model Compared With Mode Shapes Identified from Forced Vibration Tests

Mode/Test	1/Meas	2/Meas	3/Meas	4/Meas	5/Meas	6/Meas
1/FEM	0.93	0.041	0.068	0.0012	0.0009	0.0001
2/FEM	0.048	0.93	0.0022	0.17	0.0023	0.0018
3/FEM	0.013	0.0089	0.96	0.0002	0.0036	0.0069
4/FEM	0.0007	0.036	0.0004	0.94	0.0033	0.0036
5/FEM	0.010	0.0019	0.0088	0.0061	0.83	0.15
6/FEM	0.0006	0.0027	0.0004	0.0014	0.09	0.77

VI. APPLICATION OF STATISTICAL METHODS TO I-40 TEST DATA

The damage identification experiments on the I-40 Bridge over the Rio Grande River in Albuquerque, New Mexico, described in Farrar, et al. (1994), produced what is to date one of the most studied data sets in the field of vibration-based damage identification. A number of different researchers have analyzed these damage cases, including: Stubbs, et al. (1995), Jauregui and Farrar (1996), Farrar and Jauregui (1996) Alvin (1995), Simmermacher, et al. (1995), James, et al. (1994), and Mayes (1995).

However, one aspect of these data sets that has not been examined is the statistical significance of the damage identification results. Characterization of the statistical confidence on the damage identification results is important in order to be able to state that the observed changes are statistically significant, and therefore most likely not the result of random variability in the measurements. Previously, very little has been published on the application of statistical confidence to damage identification. The exception is the work of Mazurek (1997), who used the measured confidence intervals on the damage indicator as an inverse-weighting criteria for damage identification.

Based on the lessons learned from the Alamosa Canyon Bridge tests, data from the I-40 Bridge test were re-analyzed using the statistical methods discussed in Section IV.C. and first presented in Doebling and Farrar (1998). This study was motivated by previous damage identification analyses of the I-40 data sets that raised questions about false positive indications caused by test-to-test random variations rather than statistically significant changes caused by the actual damage. For example, Farrar and Jauregui (1996) applied 5 different damage identification techniques to the I-40 data sets, and 3 of them successfully identified the damage at the lowest level damage case. However, when they attempted to simulate the lowest level of damage from the I-40 tests using a finite element model, they were unable to get the same level of conclusive damage indication as from the experimental result. Of course, this result could be an effect of the inability to properly model the dynamic effects of the damage case, but

regardless it raises the question of whether the observed indicators in this lowest level of damage are just a result of random variations.

In another study, Alvin (1995) showed that the three lowest level damage cases from the I-40 tests did not differ significantly from his finite element model than the undamaged case did. Thus, he concluded that the three lower level damage cases did not produce significant enough changes in the modal properties to enable detection of the damage. Simmermacher (1996) applied a finite element model updating procedure to the I-40 Bridge data and also performed a study of the effects of noise on the damage detection process by adding noise to the modal vectors. The sensitivity of the various measurement locations to damage was studied. It was found that the locations at the center of the middle span were the most sensitive to noise and one of these locations corresponded to the point where damage was introduced. Subsequent applications of the minimum rank perturbation (MRPT) method using the noisy modes revealed that the addition of noise actually enhanced the damage detection process because the damage was located at a point very susceptible to the influence of noise.

The purpose of this section is to explore the issue of the statistical significance of the changes in the modal parameters and damage indicators between the various damage cases in the I-40 experiments. The emphasis is on very simple ways to determine the statistical significance of the changes from case to case. The approach demonstrated in this paper uses Monte Carlo analysis to compute statistical confidence intervals on the mode shape components and damage indication parameters (in this case modal flexibility components). Then a statistical difference test is employed to associate a confidence level with the statement that the means between the two sample sets are significantly different. This statistical difference test is applied to the individual flexibility components to determine if the flexibility change at that particular degree of freedom (DOF) should be considered to be statistically significant or not. These difference statistics indicate the relative significance of the changes in a particular parameter relative to changes in other parameters.

It should be noted, however, that the results of this analysis can only discriminate whether the observed changes are statistically significant, not whether the source of the observed changes is structural damage. For example, a systematic error in the testing procedure or a change in the structural boundary conditions can both lead to a statistically significant change in measured structural flexibility, which the analyst may falsely conclude is the result of structural damage. The exception is when a change of larger significance is isolated at one particular DOF or set of spatially close DOF. Discriminating between changes resulting from damage and changes resulting from other systematic errors or unknown effects is beyond the scope of this study. The only statement that can be made from this result is whether or not the observed changes at each DOF are statistically significant.

A. The I-40 Bridge Damage Identification Experiment

The research described in this section uses data from a series of modal tests of a section of a highway bridge. The bridge was located along Interstate Highway 40 across the Rio Grande River in Albuquerque, New Mexico and is shown in Figure 83. A series of modal tests was performed on this bridge after it had been closed to traffic prior to demolition in 1993. The bridge was constructed of a concrete deck approximately 13.3 m wide and 17.8 cm thick,

supported by two steel plate girders, each 3.05 m high, and three steel stringers. The section of the bridge that was instrumented for this series of modal tests consisted of three spans with a combined length of about 130 m. The instrumentation consisted of 13 accelerometers mounted to each of the two plate girders along the length of the three spans, for a total of 26 response measurements. The excitation system consisted of a 9863 kg reaction mass supported by three air springs moved by a 9.79 kN hydraulic actuator. The actuator system was placed on the deck directly over one of the plate girders in the middle of the span closest to the abutment. Full details of the modal testing of this bridge can be found in Farrar, et al. (1994).

Figure 83. I-40 Bridges over the Rio Grande River in Albuquerque, New Mexico.

The damage that was introduced was intended to simulate fatigue cracking that has been observed in plate-girder bridges. Four levels of damage were introduced by making various torch cuts in the web and flange of the girder, as shown in Figure 84. The first level of damage, designated E-1, consisted of a 61-cm-long (2 ft), 10-mm-wide (3/8-in.) cut through the web centered at mid-height of the web. Next, this cut was continued to the bottom of the web to produce a second level of damage designated E-2. For the third level of damage, E-3, the flange was then cut halfway in from either side directly below the cut in the web. Finally, the flange was cut completely through for damage case E-4 leaving the top 1.22 m of the web and the top flange to carry the load at this location. After this damage case this span of the bridge was

sagging about 2 cm at the damage location. This damage location is at DOF 20 in the modal data sets.

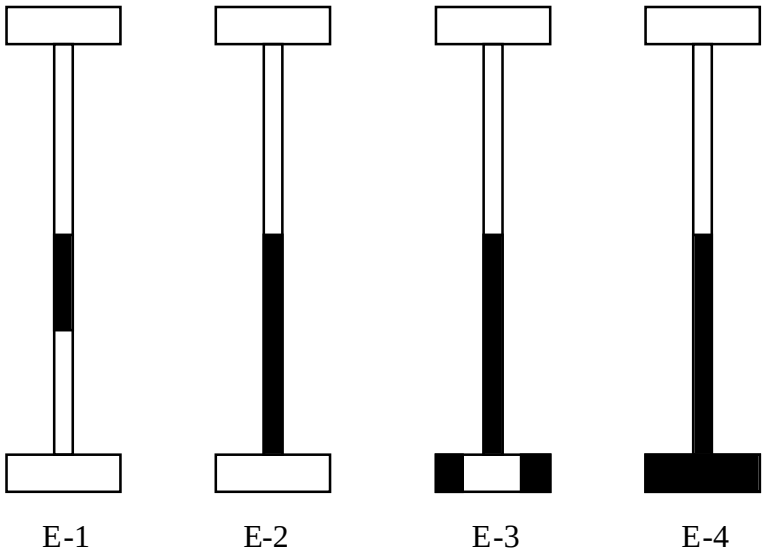

Figure 84. The four levels of damage induced by cutting the I-40 plate girder.

B. Theoretical Development

The analysis of damage identification considering the statistical significance of the damage indicators requires the determination of statistical confidence intervals. These intervals are determined by first computing confidence intervals on the measured modal data. Next, the statistics are propagated (via Monte Carlo simulations) to the identified modal parameters and then to the damage indicators. The method used for the results stated in this section is the Rational Polynomial curve fit as described in Appendix A.

1. Estimation of Random Error in Measured Modal Data

The first step in this analysis is the determination of random errors on measured FRF data in the form of statistical confidence intervals. Measured data contain errors caused by many sources that result in measured spectral function estimates that are not equal to the actual spectral functions of the structure. The errors that are present in the measured modal data can be divided into two basic categories, as described in Bendat and Piersol (1980) and Allemang (1995): bias (systematic) errors and random errors. Bias errors cause the mean of the function estimate not to converge to the actual value of the function as more averages are taken. The random errors on these data are quantified in the form of a standard deviation associated with the mean of the FRF estimate magnitude and phase at each frequency line for each measurement DOF as discussed in Section IV.C.

After the mean and the standard deviation of the estimate have been computed, they are usually expressed in association with a statistical confidence level that is defined by the assumed distribution of the estimate. For a normal distribution, plus and minus one standard deviation is the confidence interval for a 68% confidence level and plus or minus two standard deviations is the confidence interval for (approximately) a 95% confidence level. Thus, given the mean, μ, and the standard deviation, σ, of an estimate, and assuming that the distribution is Gaussian, there is a 68% probability that the next value measured, v, will fall into the range

$$\mu - \sigma < v < \mu + \sigma. \tag{14}$$

Likewise, there is a 95% probability that the next value measured, v, will fall into the range

$$\mu - 2\sigma < v < \mu + 2\sigma. \tag{15}$$

2. Monte Carlo Simulation and Application to Modal Parameter Identification

The next step in the analysis is the estimation of confidence intervals on the measured modal parameter, e.g. the modal frequencies and mode shape components. The approach used to characterize errors on identified modal parameters given the distribution of the errors on the data is Monte Carlo simulation as discussed in Section IV.C.

3. Damage Identification Using Modal Flexibility Change

The vibration-based damage identification method used in this research idealizes the change in the dynamically measured flexibility matrix as an estimate of the change in the static behavior of the structure. Because the flexibility matrix is defined as the inverse of the static stiffness matrix, the flexibility matrix [G] relates the applied static force {u} and resulting structural displacement {F} as

$$\{u\} = [G]\{F\}. \tag{16}$$

Thus, each column of the flexibility matrix represents the displacement pattern of the structure associated with a unit force applied at the associated DOF.

The measured flexibility matrix is estimated from the mass-normalized measured mode shapes [Φ] and squared modal frequencies [Λ] as

$$[G] \approx [\Phi][\Lambda]^{-1}[\Phi]^{T}. \tag{17}$$

The formulation of the flexibility matrix in Eq. (17) is approximate because only the first few modes of the structure (typically the lowest-frequency modes) are measured. The synthesis of the complete static flexibility matrix would require the measurement of all of the mode shapes and frequencies.

For this particular study, the difference in the diagonal values of the flexibility matrices before and after damage is used as an indicator of damage, in a manner similar to that presented by Robinson, et al. (1996). The change in the diagonal components represents the change in local flexibility at a point; i.e. the change in the point displacement observed by applying a unit load at that same point. This technique is sometimes referred to as the "multi-point flexibility change" technique.

4. Confidence Intervals on Flexibility Damage Indicator

A Monte Carlo procedure similar to that used to estimate the confidence intervals on the identified modal parameters is used to estimate the confidence intervals on the values of the flexibility change used as the damage indicator. Specifically, the confidence intervals on the mode shapes and modal frequencies are used to define a normal probability distribution on each component used to compute the flexibility. Then uncertain values of the modal parameters are computed repeatedly and the diagonal values of the flexibility matrix are computed each time for each damage case. After a sufficient number of runs a statistical distribution is formed on the flexibility change parameters and a mean and confidence intervals are computed. The number of runs is determined using convergence of the mean and standard deviations as well as the skewness and kurtosis of the distribution, as discussed in Doebling and Farrar (1997). Skewness characterizes the degree of asymmetry of a distribution about its mean and kurtosis is a measure of the relative peakedness or flatness of a distribution. The damage indicator (in this case the diagonal values of the flexibility change) now has statistical confidence intervals associated with it. A flowchart of the this procedure is shown in Figure 85.

5. Tests of Significant Difference Between Sample Means

To assess whether the observed change between the undamaged and damaged flexibility coefficients is statistically significant, a statistical test known as the t-test is used. As described by Freund (1992), given two population samples of size n_1 and n_2 with sample means $\overline{x}_1$ and $\overline{x}_2$ and sample standard deviations S_1 and S_2, a test statistic z can be defined as

$$z = \frac{\overline{x}_1 - \overline{x}_2 - \delta}{\sqrt{\frac{S_1^2}{n_1} - \frac{S_2^2}{n_2}}} \tag{18}$$

to describe the hypothesis $\overline{x}_1 - \overline{x}_2 = \delta$, i.e. that the two sample means differ by an arbitrary value δ. This formulation assumes that n_1 and n_2 are large enough to invoke the central limit theorem and thus assume normal distributions in the populations.

Using this statistical approach, the objective is to test the hypothesis that one sample mean is statistically larger than the other, written as

$$\left|\overline{x}_1 - \overline{x}_2\right| > \delta. \tag{19}$$

Solving for z in Eq. (18) with $\delta = 0$, it can then be stated that Eq. (19) is true to approximately the 95% confidence level if $|z| \geq 2$. Also, it can be stated that larger values of z indicate more confidence that the difference in the sample means is statistically significant. We can thus define parameter changes that have larger values of z as being "more significant changes".

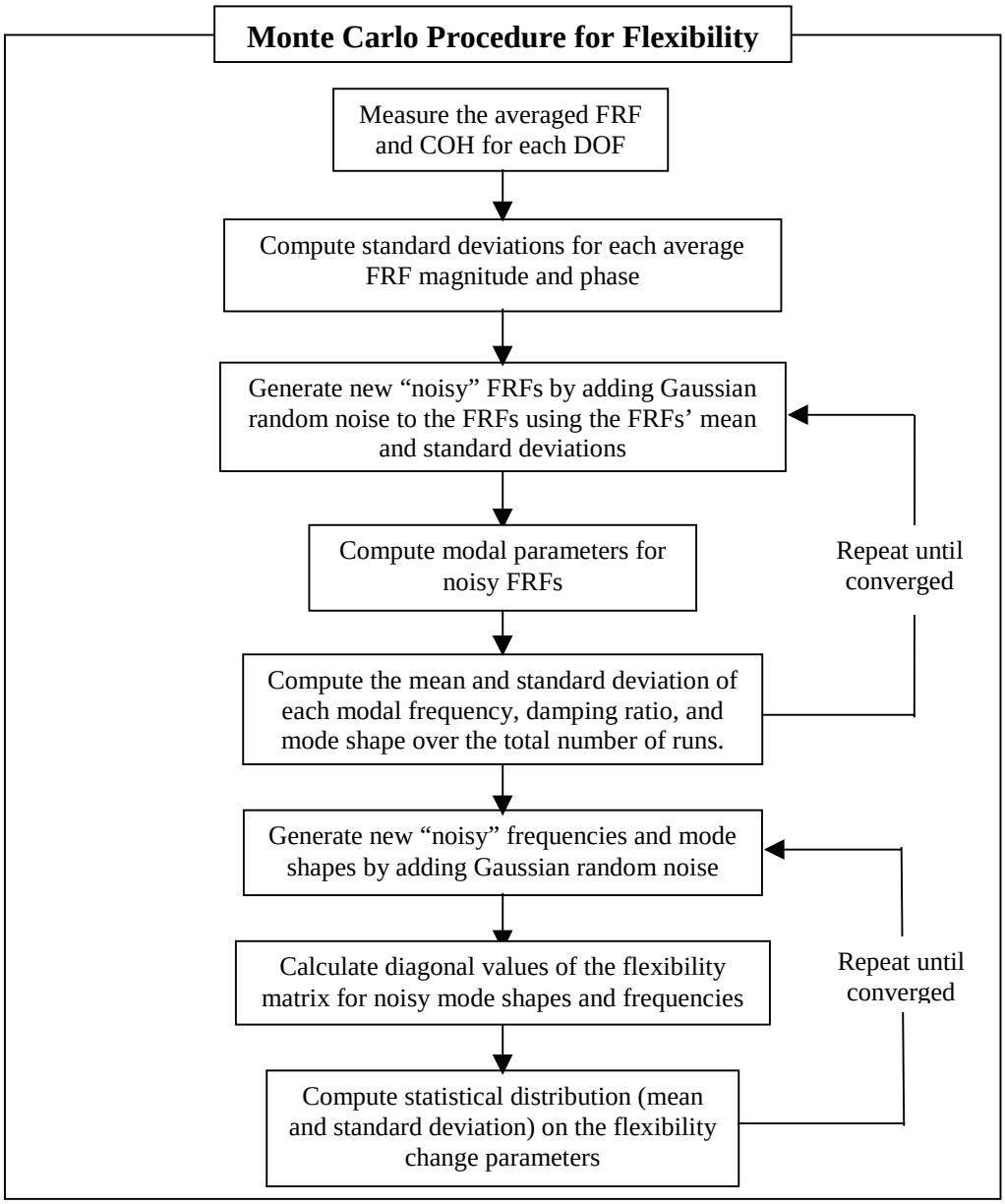

Figure 85. Flowchart of the Monte Carlo method applied to the flexibility damage detection method.

C. Experimental Results, Statistical Analysis, and Discussion

The most basic sets of results from the identification of the modal parameters using the Monte Carlo estimation technique described above are the confidence intervals on the identified modal frequencies, modal damping ratios, and mode shape components for each damage case. A comparison of the first modal frequency for each damage case with 2σ confidence intervals is shown in Figure 86. As shown in this figure, the 2σ confidence intervals are so small relative to the change from case to case that the –2σ and +2σ markers are barely distinguishable from each other. A close up of Figure 86 showing only the undamaged case and the first two damage cases is shown in Figure 87. In this figure, the confidence intervals are distinguishable, but it is still obvious that the change from case to case is much greater than the confidence interval for each case. These results indicate that the changes in modal frequency from one damage case to the next tend to be statistically significant with respect to the level of uncertainty arising from experimental repeatability.

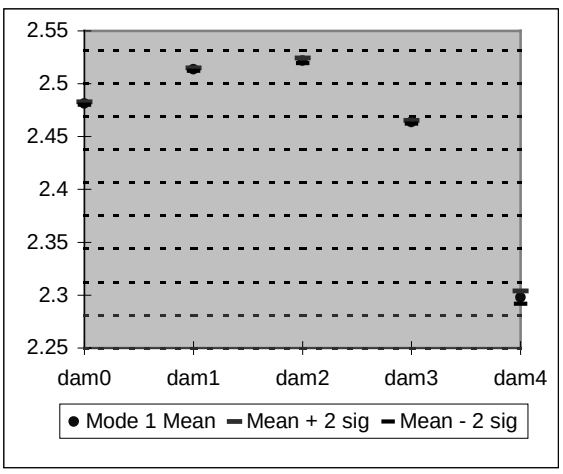

Figure 86. First modal frequency for each damage case.

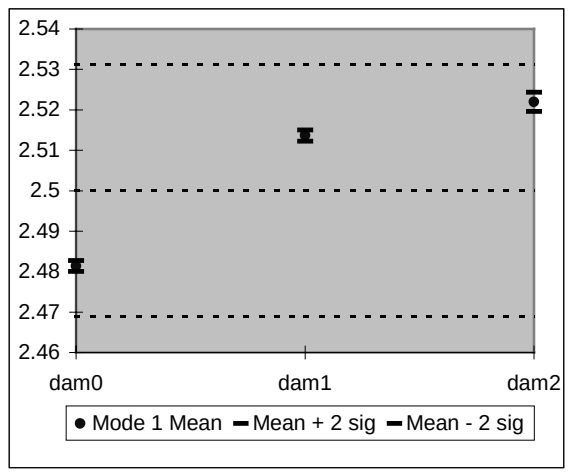

Figure 87. First modal frequency for first two damage cases.

A comparison of the first mode shape (plotted against DOF number) for the undamaged and first damage cases (including 2σ confidence intervals) is shown in Figure 88. This figure demonstrates that there is a slight shift in this mode shape after the first damage state is applied. The confidence intervals at some degrees of freedom clearly overlap, while the confidence intervals at other degrees of freedom do not overlap. In contrast to Figure 88, a comparison of the first mode shape for the undamaged and fourth damage cases is shown in Figure 89. This figure demonstrates that there is a major shift in this mode shape after the fourth damage state is applied. Thus it is clear that there is a significant change in some components of mode shape 1 for damage case 4, but the result is not as conclusive for damage case 1.

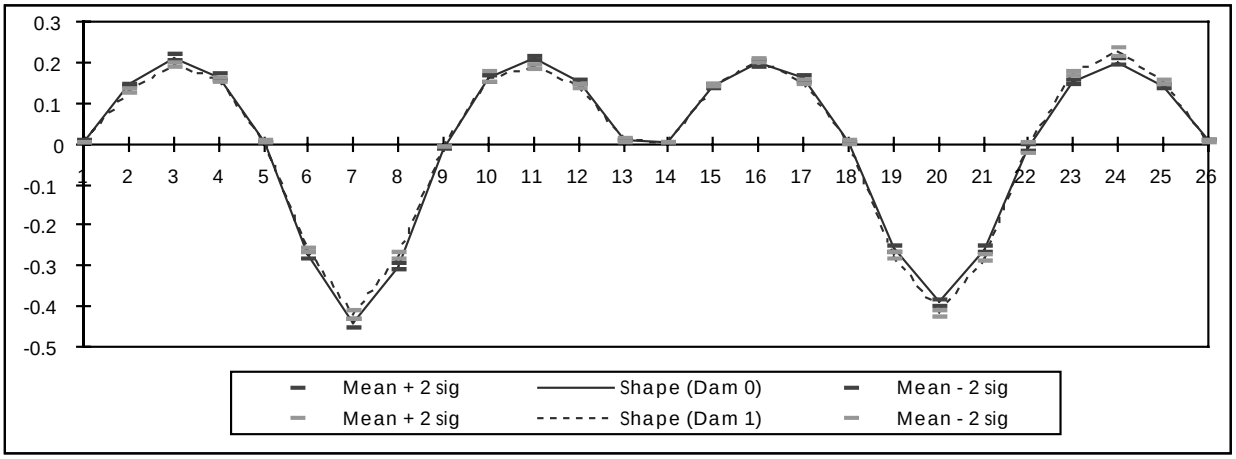

Figure 88. First mode shape for undamaged case and first damage case.

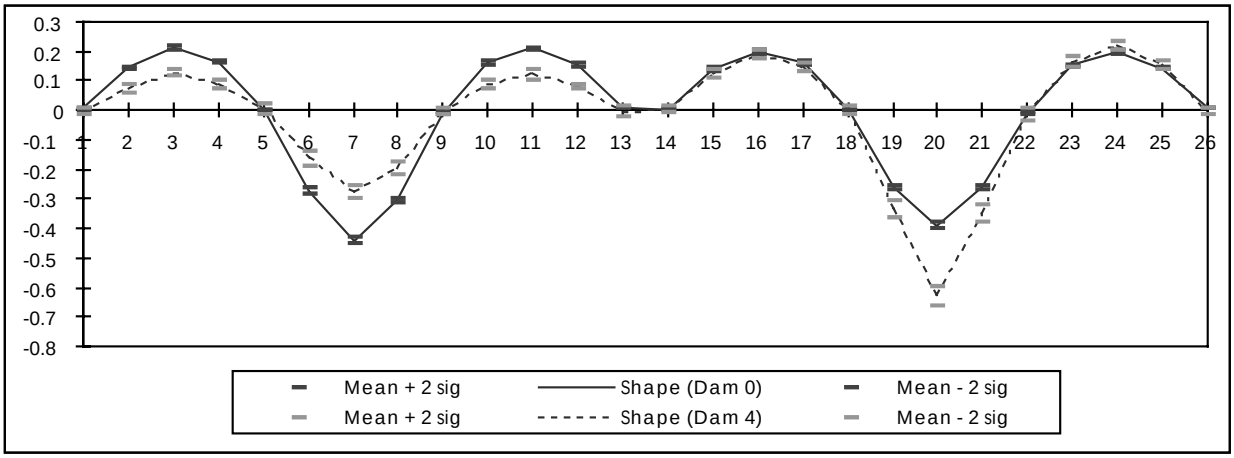

Figure 89. First mode shape for undamaged case and fourth damage case.

A similar comparison of the third mode shape for the undamaged and fourth damage cases is shown in Figure 90. This figure demonstrates that there is a very slight shift in this mode shape even after the fourth damage state is applied. The confidence intervals at almost all degrees of freedom clearly overlap. Upon close inspection of this mode shape, it is apparent that it has a node at DOF 20, which is the location where the damage is applied. Thus it is logical that this mode is insensitive to damage at DOF 20 for all four damage cases.

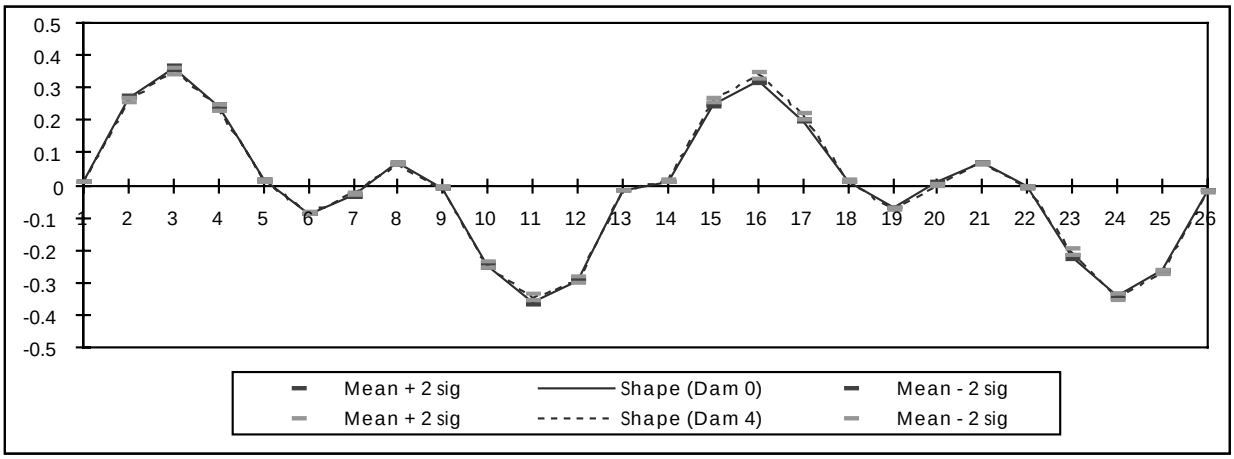

Figure 90. Third mode shape for undamaged case and fourth damage case.

The previous three comparisons give an idea of the statistical significance of the changes of these mode shapes as a result of damage, but in a purely qualitative manner. To compare the relative level of statistical significance of the changes in these mode shapes after damage in a more quantitative manner, the z-statistics for $\delta = 0$ were computed using Eq. (18). The values of these z-statistics are shown in Figure 91. The three lines represent the z-statistic values of the differences between each of the mode shape pairs in Figure 88, Figure 89, and Figure 90. As discussed in the theory section, the z-statistics give a measure of statistical significance of the change of each mode shape component. It is clear from this plot that the only mode shape component that has a significantly larger change than the other components is at DOF 20 for the comparison of the undamaged first mode to the first mode after damage case 4. It can be seen in this plot that the change of mode 1 from undamaged to damage case 1 and the change of mode 3 from undamaged to damage case 4 are of about equal significance. Noting that mode three is almost totally insensitive to the damage, it is logical to assume that the changes in mode shape 3 (as well as mode shape 1 for damage case 1) do not result from damage, but rather from some other change in the experimental conditions.

Another comparison of z-statistics, Figure 92, shows the statistical significance of the changes in mode shape 1 for each damage case. This comparison would seem to support the assertion that the fourth damage case is the only one that demonstrates significant change in its modal properties as a result of damage. However, the real measure of the statistical significance of the changes must be made with respect to the damage indicator function and not with respect to the raw modal properties. Such a comparison follows in the next section.

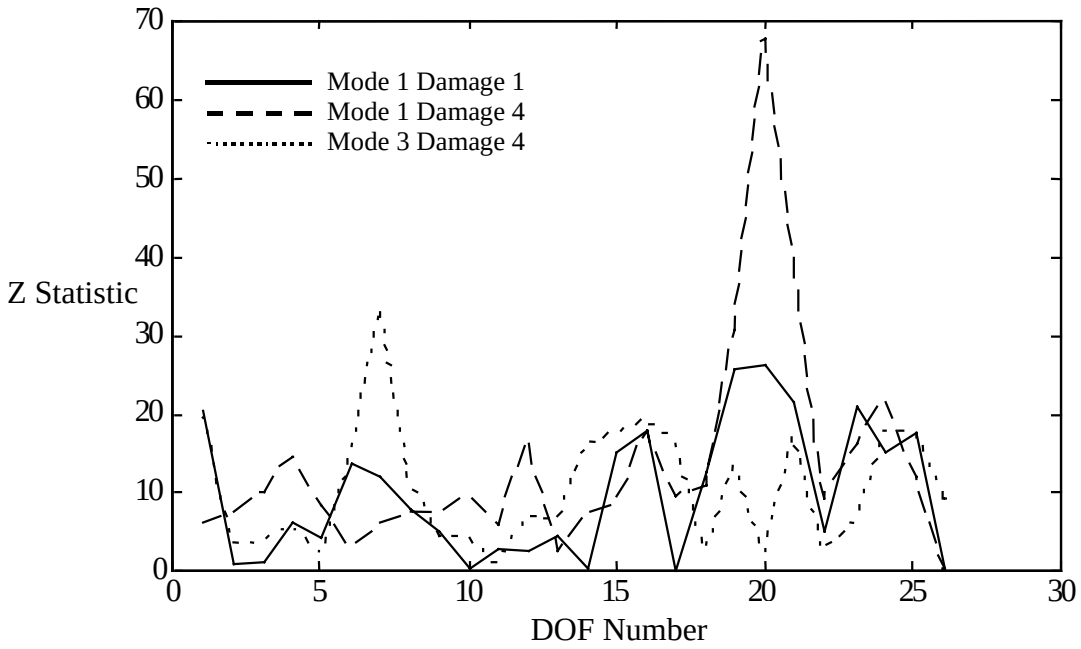

Figure 91. Comparison of z-statistics for mode shape change comparisons.

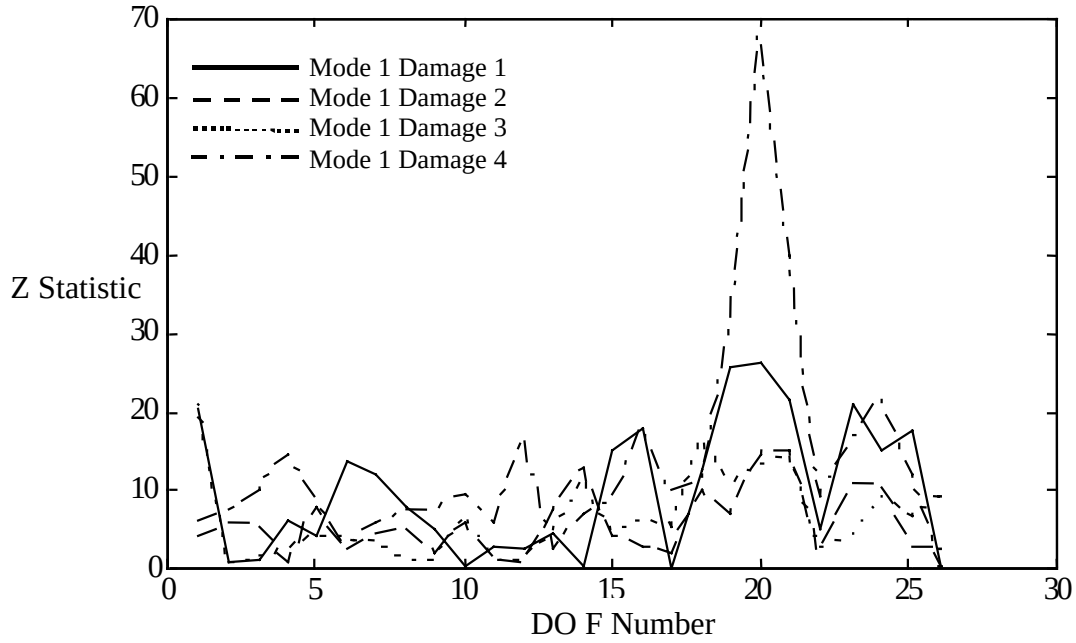

Figure 92. Comparison of z-statistics for mode shape 1 for each damage case vs. undamaged.

1. Damage Identification Using Measured Flexibility Change

The change in the measured flexibility parameters is used as an indicator of structural damage for the I-40 test results. The changes in the point-flexibility (diagonal values of the flexibility matrix) are shown for each damage case in Figure 93. According to these computations, the largest change in flexibility for each of the damage cases occurs at DOF 20, which is the known location of the damage. The second largest change is at DOF 7, which is the symmetric location across the span from the damage location. However, as mentioned in the introduction, other researchers have found reason to believe that this fact is mere coincidence and that damage is not actually being detected until the final damage case.

To study the statistical significance of the flexibility changes presented in Figure 93 it is necessary to compute statistical confidence intervals on the measured flexibility from the undamaged case and each damage case. The estimation of these intervals is accomplished by means of a Monte Carlo analysis.

The z-statistics of Eq. (18) with $\delta = 0$ are again used, this time to determine the relative significance of the changes in the measured flexibility components. A chart showing the z-statistic values for the changes in the flexibility components is presented in Figure 94. Upon examination of these values, the first observation that is apparent is that each damage case demonstrates a significant change from the undamaged case, as proven by the values of z which are much larger than 2 (in fact, are on the order of 10 and 20). However, this result alone only demonstrates that the changes in the structural flexibility are statistically significant with respect to the measurement repeatability, not that the identification of the damage location is statistically significant.

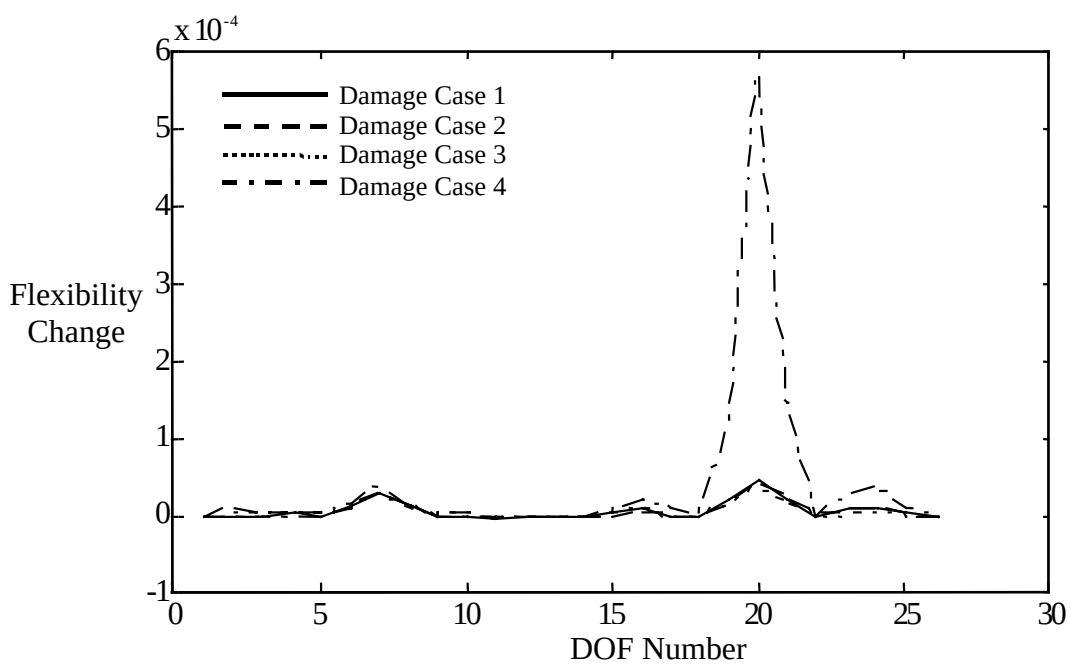

Figure 93. Flexibility change for all 4 damage cases.

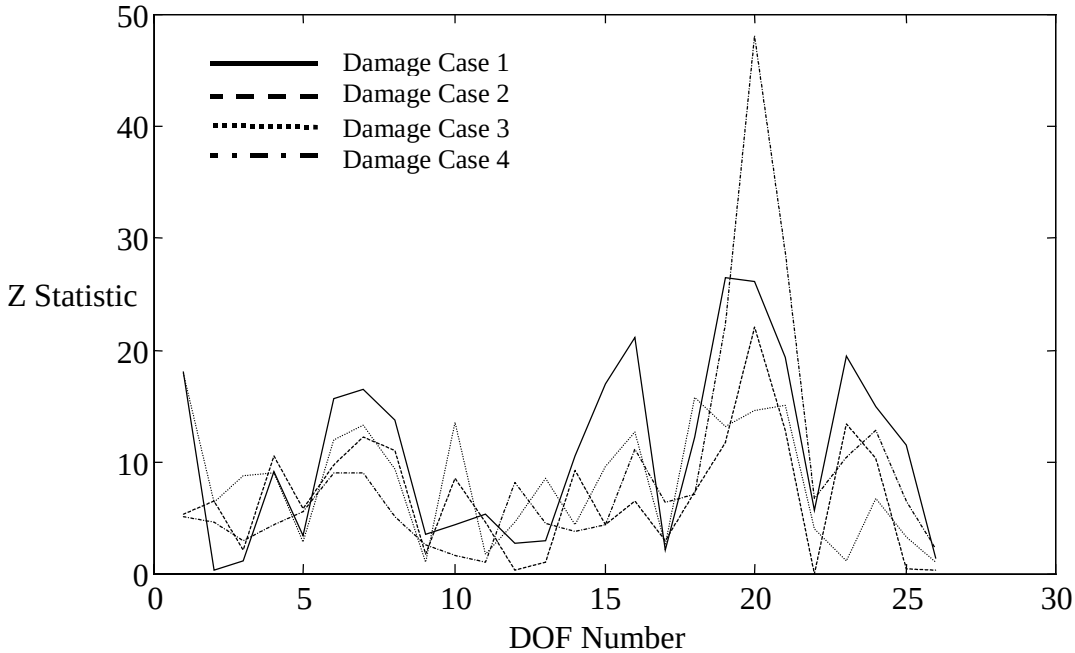

Figure 94. Z-statistic values for flexibility change for all 4 damage cases.

The second observation that is apparent from examination of Figure 94 is that until damage case 4, there is not a single particular flexibility component that is noticeably larger than the others, implying that there is no localized damage. To illustrate this point, consider damage case 1. If the changes in flexibility for damage case 1 were caused by localized damage, then one would expect to see a more significant change at one particular flexibility component. The changes in flexibility of approximately equal significance at several locations on the bridge indicate that variability other than localized damage is present in this data set. Thus, it can be stated that all four of the damage cases in the I-40 experiment show statistically significant changes in measured flexibility. However, it cannot be stated that these changes conclusively localize the damage until the fourth and final damage case.

D. Conclusions from the I-40 Bridge Tests

The statistical significance of vibration-based damage identification parameters was studied via application to the data from tests performed on the Interstate 40 highway bridge in Albuquerque, New Mexico. A test of statistical significance was applied to the mean and confidence interval estimates of the modal properties and the corresponding indicators of damage in the form of the change in the measured flexibility matrix. Previously presented deterministic results indicate that damage is detectable in all of the damage cases from these data sets. The results of this study indicate that the changes in both the modal properties and the damage indicators are statistically significant for all of the damage cases. However, these changes are distributed spatially for the first three damage cases and do not localize the damage until the fourth and final damage case. Perhaps an approach to consider for future studies of this type is the generation of a “damage

noise floor" by computing damage indicators between multiple undamaged data sets. This approach would produce a baseline value for the damage indicator at each DOF that could be expected as a result of test-to-test variations. The damage indicators computed using subsequent data sets could then be compared to the damage noise floor to quantify the statistical significance of the structural damage.

VII. SUMMARY AND CONCLUSIONS

This report summarized the data that have been collected from the various vibration tests performed on the Alamosa Canyon Bridge over a period of three years, experimental procedures used to obtain these data, analyses of these data, and the results that have been obtained. Data from these tests have been made available to other researchers at the following site: http://ext.lanl.gov/projects/damage_id/.

This study focused on quantifying the variability in identified modal parameters caused by sources other than damage. Quantifying the variability in the identified modal parameters led to the development of statistical analysis procedures that can be applied to experimental modal analysis results. Vibration-based global damage detection methods applied to bridge structures were also studied during this investigation. A major contribution that came from this portion of the study was the extension of a strain-energy-based damage detection method to structures that exhibit plate-like bending or bending in two directions. Based on lessons learned from the Alamosa Canyon Bridge tests, data from the I-40 Bridge tests were re-analyzed using the statistical analysis procedures developed as part of this study. The application of the statistical procedures to the I-40 Bridge test results gave particular insight into how statistical analysis can be used to enhance the vibration-based damage detection process. The final tests performed on the Alamosa Canyon Bridge were done to demonstrate a wireless data acquisition system being developed by Erik Straser at Stanford. A brief summary of conclusions from the various portions of this study is presented below along with a summary of general lessons learned regarding dynamic testing of bridges for the purpose of condition monitoring.

A. Variability Studies

Before vibration-based damage identification procedures can be routinely applied to a bridge, particularly in a remote monitoring mode, the effects of variability sources on the modal-based parameters used by the damage identification algorithm must be quantified. Such quantification may require measurements to be made at different times of the year, during different weather conditions, and when the bridge is experiencing different service conditions. During the various Alamosa Canyon Bridge tests the following sources of variability were studied:

1. Variability caused by thermal effects.
2. Variability caused by vehicle weight.
3. Variability caused by excitation source.
4. Variability caused by the data reduction process.

To investigate the variability caused by thermal effects modal tests were performed at two hour increments over a 24-hour time period. During these tests temperature measurements were made at various locations on the bridge. The modal frequencies were found to vary approximately 5% during this 24-hour time period. These changes were found to be related to the temperature differentials across the deck. Similar variations and correlation with deck temperature differentials were observed when the tests were repeated a year later.

To investigate the variability caused by vehicle weight, modal tests were performed with four cars parked on the bridge and the results were compared to those obtained from modal tests without cars on the deck. Assuming the parked cars have no effects on the dynamics of the structure other than the addition of mass, they should lower the frequencies by a value proportional to the square root of the mass ratios, in this case approximately 6.4%. This result was not observed in the measured modal frequencies when they were compared to the frequencies from a test performed at a similar time of the day (again, to minimize thermal effects). The reasons for this result are not understood at this time. This result is assumed to be caused by the vehicles and their suspension systems forming a more complex dynamic system where the change in mass is not sufficient to account for the change in dynamic property and/or the deflections produced by the vehicles causing a change in the boundary conditions.

To investigate the variability caused by excitation source tests were performed using roving hammer impact excitation, single point impact excitation, ambient excitation from traffic on an adjacent bridge, ambient excitation from a single car driven over the bridge, and from electrodynamic shakers. In general, the differences in modal parameters identified during tests conducted using the various excitation sources were difficult to distinguish from the variability caused by environmental effects. However, there did appear to be statistically significant differences in the damping that were correlated to the excitation amplitude. In some cases, modes identified by impact excitation could not be identified from ambient excitation test data. It is assumed that the ambient excitation did not have sufficient energy content at the frequencies associated with these modes.

To investigate the variability caused by data reduction methods three different modal parameter identification techniques were applied to various data sets measured during this study. The parameter techniques were the Global Rational Polynomial Method, the Eigensystem Realization Algorithm, and the “peak picking” method. In addition, a data set from a bridge test performed by investigators from the University of Cincinnati was analyzed independently by researchers at Los Alamos and the University of Cincinnati. In general, these studies showed that the changes in frequencies and mode shapes found using the various methods were relatively small but could be on the same order as the changes produced by damage. It is important to note, however, that the ERA method was unable to identify some of the modes identified by the other methods.

Based on the results of the variability tests, it is conceivable that bounds can be developed for the base parameters that could be monitored by a damage identification system. These bounds can potentially account for the types of variability investigated in this study. Damage must cause changes in these parameters that are outside these bounds for a definitive statement to be made regarding the onset of damage in the bridge.

B. Statistical Methods

As a result of the variability tests it became apparent that an important element of any experimental procedure is the ability to quantify the uncertainty in the test results that can be attributed to either random or bias (systematic) variability. Two methods, Monte Carlo simulation and bootstrap analysis have been presented for evaluating the statistical variations in modal parameters identified from measured FRF data. The variability in these parameters arises from environmental effects such as thermal gradients, changing service conditions such as traffic loads, and from variability associated with the measurement and data reduction process. Note that some of these processes produce random errors while others produce bias (systematic) errors. The Monte Carlo procedure assumes that the error source is random while the bootstrap procedure makes no underlying assumption about the error source. The Monte Carlo method, as used in this study, was applied to averaged FRF data where the uncertainty bounds on these data were estimated using the measured coherence function. The bootstrap procedure requires individual FRF measurements to be stored for the analysis of uncertainty bounds.

Since the time of the original statistical analyses on the Alamosa Canyon Bridge data, further investigation of the statistics of parametric regression has yielded new insights about the results presented above. First, the procedure described in this report for performing the bootstrap analysis is unnecessarily complicated, and actually reduces the apparent variance in the data by means of averaging. When performing the bootstrap analysis, it is not actually necessary to take a number of samples and then average them prior to performing the modal curve fit. When this averaging is performed, the actual results then reflect the distribution of the averaged population, rather than the distribution of the sample population. Another way to perform the bootstrap would be simply to select one sample from the population each time (with replacement) until a converged set of parameters is attained.

C. Damage Assessment of Alamosa Canyon Bridge

A series of tests were performed where an attempt was made to introduce damage into the bridge. In the first test, the bolts that held one of the channel-section cross members to the girders were removed. Unfortunately, this alteration in the bridge did not cause a significant change in the measured modal properties. Even with the bolts removed, no relative motion could be induced at the interface under the loading of the modal excitation because of metal sleeves that had been inserted into the bolt holes. For this reason, the damage cases studied are results from simulated stiffness reduction using a correlated finite element model. Vibration measurements from the Alamosa Canyon Bridge were then analyzed to determine the 95% statistical uncertainty bounds on the modal frequencies, mode shapes, and mode shape curvatures of the undamaged structure using the Monte Carlo method. Changes in the modal frequencies, mode shapes, and mode shape curvatures that are expected as a result of removing a cross member were computed using the correlated finite element model. These predicted changes were compared to the 95% confidence bounds to determine which changes can be classified as statistically significant. Finally, a comparison was made of the overall statistical significance of the three indicators.

A second damage detection study was conducted during the test in 1997. In this study an attempt to stiffen the structure was made by clamping a steel plate to the bottom of the eastern most I-beam. The results of both damage detection studies are listed below.

1. The results of the first damage detection study indicate that although frequency is not very sensitive to damage, it has such low uncertainty bounds that it is a good indicator for the existence (not location) of the damage case considered. Also, particular components of the mode shape, and especially the mode shape curvature, can be statistically significant indicators of the location damage.
2. Because the bridge exhibited plate-like dynamic behavior, a previously developed 1-D strain energy method was extended to account for the two-dimensional curvature associated with plate-like structures. Numerical simulation and laboratory experiments on small-scale structures were used to verify the ability of this method to detect damage.
3. In the test where the structure was stiffened, both the flexibility damage detection method and the 2-D strain energy damage detection methods failed to locate the stiffened region of the structure. The changes in flexibility and strain energy were on the same order as that observed between two data sets taken at different times during the day and, therefore, when the bridge was subjected to different environmental conditions.

D. Statistical Damage Assessment of the I-40 Bridge

Using statistical methods developed as part of the Alamosa Canyon Bridge study, the statistical significance of vibration-based damage identification parameters was studied by applying these methods to the data from tests performed on the Interstate 40 highway bridge in Albuquerque, New Mexico. Monte Carlo methods were used to estimate statistical confidence intervals on the identified resonant frequencies and mode shape amplitudes. A test of statistical significance was applied to the mean and confidence interval estimates of the modal properties and the corresponding indicators of damage in the form of the change in the measured flexibility matrix. Previously presented deterministic results indicate that damage is detectable in all of the damage cases from these data sets. The results of this study indicate that the changes in both the modal properties and the damage indicators are statistically significant for all of the damage cases. However, these changes are distributed spatially for the first three damage cases and do not localize the damage until the fourth and final damage case.

One limitation of the I-40 data set is that no measurements were made that would allow one to quantify environmental variability or test-to-test repeatability. An approach to consider for future studies of this type is the generation of a “damage noise floor” by computing damage indicators between multiple undamaged data sets accounting for environmental and operational variability. This approach would produce a baseline value for the damage indicator at each DOF that could be expected as a result of test-to-test variations. The damage indicators computed using subsequent data sets could then be compared to the damage noise floor to quantify the statistical significance of the structural damage.

E. Wireless Data Acquisition

Side-by-side comparisons of a wireless data acquisition system developed at Stanford University and a conventional wired data acquisition system were made for both ambient excitation and impact excitation caused by an instrumented sledge hammer. The primary results of this test are listed below.

1. It was demonstrated that a system of modular, wireless units could be installed in a fraction of the time of a standard, cable instrumentation system.
2. It was shown that a system can be designed for both ambient excitation and periodic monitoring case as well as having the dynamic range to monitor an earthquake scenario.
3. The basic process of triggering, acquiring data from multiple units, transmitting the data wirelessly, and archiving the data for later use worked well.
4. A side-by-side comparison of data taken from both the conventional system and the wireless system concluded that some signal processing difficulties were caused by impedance loading of the accelerometers and the lack of an antialiasing filter. A choice of a different accelerometer, among the many available on the commercial market can eliminate this problem. Another solution involves implementing a buffer amplifier in series with the current sensor and including a single pole 80 Hz antialiasing filter.

If vibration-based damage detection technology is to be adopted on a wide scale, it is the authors' opinion that it will have to be used in conjunction with a wireless data acquisition system. Otherwise the maintenance associated with wires will make the system too unreliable for commercial application. These test results indicate that wireless data acquisition systems are feasible with current technology.

F. Lessons Learned

Based on the experience gained from all the Alamosa Canyon Bridge tests and the I-40 Bridge test many lessons have been learned regarding modal testing of large civil engineering infrastructure for the purpose of condition monitoring. The series of tests conducted on the I-40 Bridge and the Alamosa Canyon Bridge reflect an evolution in the authors' understanding of appropriate test procedures, data reduction methods and bridge dynamic characteristics. As an example, environmental variability and statistical means of characterizing this variability were not considered at all during the I-40 Bridge test but became a focus of the Alamosa Canyon Bridge tests. For the benefit of other researchers a summary of the lessons that have been learned during this series of tests is presented below.

1. Need to define "damage."

It is not currently economically practical to instrument a bridge for all possible damage scenarios. It is therefore necessary to prioritize and select various damage scenarios that are to be monitored. Instrumentation can then be designed with the specific damage in mind. For example,

32 channels of commercially available data acquisition were used during these tests. By current standards, these structures would be considered reasonably well instrumented. However, this limited amount of data acquisition proved insufficient to characterize the dynamic properties of a single interior span of the Alamosa Canyon Bridge because of coupling between adjacent spans. When the instrumentation was placed on three adjacent spans, the dynamic coupling was better understood, but it is questionable whether the resulting coarse instrumentation would be adequate to detect damage.

2. Perform thorough pre-test visual inspection and measurements.

Damage identification is not practical or meaningful without some comparison to an initial state of the structure. Documentation of that initial state along with initial measurements are a necessary part of bridge health monitoring.

3. Perform linearity, stationarity and reciprocity checks.

Almost all linear modal parameter ID methods assume the data is stationary and that the structure will exhibit linearity and reciprocity. If these assumptions are not verified then one can have no confidence in any subsequent results that are dependent on these assumptions.

4. Perform environmental, operational and testing procedure sensitivity studies.

In order to distinguish damage from test-to-test repeatability it is necessary to have a good understanding of the variability in parameters caused by changing environmental and operational conditions and by the testing and data reduction procedures. These variations need to be quantified for the particular structure being monitored. Because these variations can occur over time scales varying from daily to seasonal, this characterization may be quite time consuming and difficult.

5. Perform false-positive damage ID studies.

Two dangers with the remote monitoring of a bridge are false positives and false negatives. To minimize false positives, it is necessary to establish the threshold level at which damage can be detected. It is very important to be confident that we are not predicting damage when none is present. Too many false positive indications will be the demise of this technology as it will be expensive to shut the bridge down and look for the nonexistent damage and public and funding agencies will lose confidence with each false-positive indication. Needless to say, false-negative results are even worse, but harder to quantify.

6. Use numerical models to gain insight into response of the bridge and the sensitivity of that response to various parameters.

Testing of structure is very expensive. Finite element models can help plan the test of a large structure to maximize its effectiveness. In the study of damage detection, finite element models can provide a great deal of information with regard to the threshold levels of damage identification because various damage scenarios can be modeled. It is important to note, however, that the finite element model should be correlated to experimental data because there is always significant uncertainty in the material properties and boundary conditions.

7. Develop ambient vibration system identification procedures. Compare ambient results with forced vibration results (if possible).

Because it is difficult to get access to a bridge without traffic to perform a forced vibration test, and even if access is available forcing large structures is quite difficult, it will be necessary to use ambient excitation if a monitoring system is to be practical. Therefore, it is important that the engineering community is confident in the results obtained from ambient excitation. This confidence can only be gained by studies comparing ambient and forced excitation studies for a structure similar to the ones discussed in this paper.

8. Develop statistical analysis procedures for measured results.

Statistical analysis is the only way to quantify that changes being measured are distinguishable from test-to-test variability. Two methods that were used in this study are Monte Carlo simulation and the bootstrap method.

9. Be prepared for changes to the structure and testing procedures that are beyond the researchers' control.

The only thing that one can be confident of in a field test is that it will not go exactly as planned. There will always be unexpected problems (transducers that stop working, changing weather conditions, rattlesnakes, dead cow, etc.) that will require the investigators to develop fall-back testing procedures on short notice.

10. Be open-minded!

It is important to not focus on just one method of data analysis and to perform comparative studies. Similarly, data should be shared with other researchers to provide independent analyses. Finally, researchers need to be willing to "hang out the dirty laundry", that is, explain what went wrong as well as what went right so others can benefit and hopefully avoid similar mistakes or problems.

APPENDIX A:

IDENTIFYING MODAL PROPERTIES USING A RATIONAL-FRACTION POLYNOMIAL CURVE-FITTING ALGORITHM

The Rational Fraction Polynomial Method (RFP) is a SISO method that first appeared in 1982 [Richardson and Formenti (1982)] and is now one of the most popular and widely used MDOF frequency response domain methods. This method was extended to analyze globally a set of FRFs, using one single input reference and multiple outputs making it a SIMO method. This extension is called the Global Rational Fraction Polynomial Method (GRFP); although mentioned in Richardson and Formenti (1982), this method was developed further in Richardson and Formenti (1985) and Richardson (1986). The following discussion closely follows that given by an excellent text edited by Maia and Silva (1997). The Rational Polynomial Method will first be discussed in detail followed by how it can be extended to be the GRFP method.

A. The Rational Fraction Polynomial Method

The FRF, in terms of receptance, which is the displacement response divided by the force excitation, for a linear system with *N* DOF and modal damping can be given by the partial fraction form:

$$\alpha(\omega) = \sum_{r=1}^{N} \frac{A_r + i\omega B_r}{\omega_r^2 - \omega^2 + 2i\xi_r\omega_r\omega} \qquad \text{(A-1)}$$

where A_r and B_r are constants. Equation A-1 can be written in rational polynomial form, that is as a ratio of two polynomials in $i\omega$ as shown below,

$$\alpha(\omega) = \frac{\sum_{k=0}^{2N-1} a_k (i\omega)^k}{\sum_{k=0}^{2N} b_k (i\omega)^k}. \qquad \text{(A-2)}$$

Our primary goal is to estimate the values of the coefficients a_k and b_k such that the error between the analytical FRF and the measured FRF is minimized. The values of the coefficients

are then used to estimate the poles and residues of the system, which are then used to determine the resonant frequencies, modal damping, and mode shapes of the system. An error function between the analytical FRF $\alpha(\omega)$ and the experimental values $\tilde{\alpha}(\omega)$ at each frequency ω_j is defined as

$$e_j = \frac{\sum_{k=0}^{2N-1} a_k (i\omega)^k}{\sum_{k=0}^{2N} b_k (i\omega)^k} - \tilde{\alpha}(\omega_j)\,. \tag{A-3}$$

Defining a modified error function $e'_j = e_j \sum_{k=0}^{2N} b_k (i\omega_j)^k$ and making $b_{2N} = 1$, gives

$$e'_j = \sum_{k=0}^{2N-1} a_k (i\omega)^k - \tilde{\alpha}(\omega_j)\left[\sum_{k=0}^{2N-1} b_k (i\omega)^k - (i\omega)^{2N}\right]. \tag{A-4}$$

This formulation leads to a linear system of equations, avoiding the necessity of initial estimates for the modal parameters. A squared error criterion, J, is defined as

$$J = \{E^*\}^T \{E\} \tag{A-5}$$

where

$$\{E\} = \begin{Bmatrix} e'_1 \\ e'_2 \\ \vdots \\ e'_L \end{Bmatrix} \tag{A-6}$$

where * denotes a complex conjugate and L is the number of frequency values that form the specified frequency range to be analyzed. The error can be written in matrix form as

$$\underset{(L\times 1)}{\{E\}} = \underset{(L\times 2N)}{[P]}\,\underset{(2N\times 1)}{\{a\}} - \underset{(L\times 2N)}{[T]}\,\underset{(2N\times 1)}{\{b\}} - \underset{(L\times 1)}{\{W\}} \tag{A-7}$$

where

$$[P] = \begin{bmatrix} 1 & i\omega_1 & (i\omega_1)^2 & \cdots & (i\omega_1)^{2N-1} \\ 1 & i\omega_2 & (i\omega_2)^2 & \cdots & (i\omega_2)^{2N-1} \\ \vdots & \vdots & \vdots & \ddots & \vdots \\ 1 & i\omega_L & (i\omega_L)^2 & \cdots & (i\omega_L)^{2N-1} \end{bmatrix}$$

$$[T] = \begin{bmatrix} \tilde{\alpha}(\omega_1) & \tilde{\alpha}(\omega_1)(i\omega_1) & \cdots & \tilde{\alpha}(\omega_1)(i\omega_1)^{2N-1} \\ \tilde{\alpha}(\omega_2) & \tilde{\alpha}(\omega_2)(i\omega_2) & \cdots & \tilde{\alpha}(\omega_2)(i\omega_2)^{2N-1} \\ \vdots & \vdots & \ddots & \vdots \\ \tilde{\alpha}(\omega_L) & \tilde{\alpha}(\omega_L)(i\omega_L) & \cdots & \tilde{\alpha}(\omega_L)(i\omega_L)^{2N-1} \end{bmatrix}$$

$$\{W\} = \begin{Bmatrix} \tilde{\alpha}(\omega_1)(i\omega_1)^{2N} \\ \tilde{\alpha}(\omega_2)(i\omega_2)^{2N} \\ \vdots \\ \tilde{\alpha}(\omega_L)(i\omega_L)^{2N} \end{Bmatrix},\ \{a\} = \begin{Bmatrix} a_0 \\ a_1 \\ \vdots \\ a_{2N-1} \end{Bmatrix},\ \text{and}\ \{b\} = \begin{Bmatrix} b_0 \\ b_1 \\ \vdots \\ b_{2N-1} \end{Bmatrix}.$$

Substituting Eq. A-7 into A-5 and after some manipulations gives the squared error criteria as

$$\begin{aligned} J = {} & \{a\}^T \operatorname{Re}\left([P^*]^T [P]\right)\{a\} + \{b\}^T \operatorname{Re}\left([T^*]^T [T]\right)\{b\} + \{W^*\}^T \{W\} \\ & - 2\{a\}^T \operatorname{Re}\left([P^*]^T [T]\right)\{b\} - 2\{a\}^T \operatorname{Re}\left([P^*]^T \{W\}\right) + 2\{b\}^T \operatorname{Re}\left([T^*]^T \{W\}\right) \end{aligned}. \tag{A-8}$$

The values of {a} and {b} that will yield a minimum value of J can be determined by setting the partial derivatives of Eq. A-8 with respect to {a} and {b} equal to zero yielding

$$\begin{aligned} \frac{\partial J}{\partial \{a\}} &= 2\operatorname{Re}\left([P^*]^T [P]\right)\{a\} - 2\operatorname{Re}\left([P^*]^T [T]\right)\{b\} - 2\operatorname{Re}\left([P^*]^T \{W\}\right) = \{0\} \\ \frac{\partial J}{\partial \{b\}} &= 2\operatorname{Re}\left([T^*]^T [T]\right)\{b\} - 2\operatorname{Re}\left([T^*]^T [P]\right)\{a\} + 2\operatorname{Re}\left([T^*]^T \{W\}\right) = \{0\} \end{aligned} \tag{A-9}$$

or, in matrix form

$$\begin{bmatrix} [Y] & [X] \\ [X]^T & [Z] \end{bmatrix} \begin{Bmatrix} \{a\} \\ \{b\} \end{Bmatrix} = \begin{Bmatrix} \{G\} \\ \{F\} \end{Bmatrix} \tag{A-10}$$

where

$$\begin{aligned} [Y] &= \mathrm{Re}\left(\left[P^*\right]^T [P]\right) \\ [X] &= -\mathrm{Re}\left(\left[P^*\right]^T [T]\right) \\ [Z] &= \mathrm{Re}\left(\left[T^*\right]^T [T]\right) \quad . \\ \{G\} &= \mathrm{Re}\left(\left[P^*\right]^T \{W\}\right) \\ \{F\} &= -\mathrm{Re}\left(\left[T^*\right]^T \{W\}\right) \end{aligned} \tag{A-11}$$

Eq. A-10 contains the normal equations of the least-squares problem. It was found by Richardson and Formenti (1982) that the numerical problems (ill-conditioning) encountered in the resolution of Eq. A-10 could be overcome if matrices [Y] and [Z] were each an identity matrix. So, instead of $[Y]=\mathrm{Re}([P^*]^T[P])$ and $[Z]=\mathrm{Re}([T^*]^T[T])$, these matrices will have to be the product of two orthonormal matrices. So, [P] must be replaced by

$$[P] = \begin{bmatrix} \varphi_{1,0} & \varphi_{1,1} & \cdots & \varphi_{1,2N-1} \\ \varphi_{2,0} & \varphi_{2,1} & \cdots & \varphi_{2,2N-1} \\ \vdots & \vdots & \ddots & \vdots \\ \varphi_{L,0} & \varphi_{L,1} & \cdots & \varphi_{L,2N-1} \end{bmatrix} = [\vartheta] \tag{A-12}$$

where $\varphi_{j,i}$ means a polynomial of order i evaluated at frequency ω_j. Likewise, [T] will now be given by

$$
\begin{aligned}
[T] &= \begin{bmatrix} \tilde{\alpha}(\omega_1)\theta_{1,0} & \tilde{\alpha}(\omega_1)\theta_{1,1} & \cdots & \tilde{\alpha}(\omega_1)\theta_{1,2N-1} \\ \tilde{\alpha}(\omega_2)\theta_{2,0} & \tilde{\alpha}(\omega_2)\theta_{2,1} & \cdots & \tilde{\alpha}(\omega_2)\theta_{2,2N-1} \\ \vdots & \vdots & \ddots & \vdots \\ \tilde{\alpha}(\omega_L)\theta_{L,0} & \tilde{\alpha}(\omega_L)\theta_{L,1} & \cdots & \tilde{\alpha}(\omega_L)\theta_{L,2N-1} \end{bmatrix} \\
&= \begin{bmatrix} \tilde{\alpha}(\omega_1) & 0 & \cdots & 0 \\ 0 & \tilde{\alpha}(\omega_2) & \cdots & 0 \\ \vdots & \vdots & \ddots & \vdots \\ 0 & 0 & \cdots & \tilde{\alpha}(\omega_L) \end{bmatrix} \begin{bmatrix} \theta_{1,0} & \theta_{1,1} & \cdots & \theta_{1,2N-1} \\ \theta_{2,0} & \theta_{2,1} & \cdots & \theta_{2,2N-1} \\ \vdots & \vdots & \ddots & \vdots \\ \theta_{L,0} & \theta_{L,1} & \cdots & \theta_{L,2N-1} \end{bmatrix} \qquad \text{(A-13)} \\
&= \begin{bmatrix} \text{‘}\tilde{\alpha}\text{‘} \end{bmatrix} [\Theta]
\end{aligned}
$$

and

$$
\{W\} = \begin{Bmatrix} \tilde{\alpha}(\omega_1)\theta_{1,2N} \\ \tilde{\alpha}(\omega_2)\theta_{2,2N} \\ \vdots \\ \tilde{\alpha}(\omega_L)\theta_{2,2N} \end{Bmatrix} . \qquad \text{(A-14)}
$$

It is now necessary to find complex functions φ and θ such that $\mathrm{Re}([P^*]^T[P])$ and $\mathrm{Re}([T^*]^T[T])$ are unit matrices. This is possible if φ and θ are complex orthonormal polynomials. The FRF is then written in terms of these polynomials, with e_k and d_k as the unknowns instead of a_k and b_k as shown below

$$
\alpha(\omega) = \frac{\sum_{k=0}^{2N-1} c_k \varphi_k}{\sum_{k=0}^{2N} d_k \theta_k} . \qquad \text{(A-15)}
$$

After finding {c} and {d}, {a} and {b} can be recovered to calculate the modal parameters.

<u>Calculation of orthogonal polynomials φ and θ</u>

As explained before, it is necessary to have

$$\mathrm{Re}\left(\left[\vartheta^{*}\right]^{T}\left[\vartheta\right]\right)=\left[I\right]$$
$$\mathrm{Re}\left(\left[\Theta^{*}\right]^{T}\left[\tilde{\alpha}^{*}_{\epsilon}\right]\left[\tilde{\alpha}_{\epsilon}\right]\left[\Theta\right]\right)=\left[I\right] \quad . \tag{A-16}$$

From Maia and Silva (1997) the polynomials j must be calculated using a unit weighting function and q must be calculated using a weighting function given by $[\tilde{\alpha}^{2}]$. Each polynomial can be regarded as a linear combination of real and imaginary orthogonal polynomials, the real ones being even functions and the odd ones being odd functions. If we want to take advantage of the fact we can use even and odd functions it is necessary to consider both positive and negative frequencies. If there are L points to be fitted, the orthogonal property will be

$$\mathrm{Re}\left(\sum_{j=-L}^{L}\varphi^{*}_{j,k}\varphi_{j,k}\right)=\begin{cases}0 & k\neq i\\ 0 & k=i\,.\end{cases} \tag{A-17}$$

Writing φ as Re(φ) + i Im(φ), it follows that

$$\sum_{j=-L}^{L}\left(\mathrm{Re}(\varphi_{j,k})\,\mathrm{Re}(\varphi_{j,i})+\mathrm{Im}(\varphi_{j,k})\,\mathrm{Im}(\varphi_{j,i})\right)=\begin{cases}0 & k\neq i\\ 1 & k=i\,.\end{cases} \tag{A-18}$$

In fact, the FRF is only defined for positive frequencies and so Eq. A-18 must be transformed so that only the positive functions for points 1 to L are considered. Extracting the half-functions, negative and positive, from A-18 we obtain

$$\begin{aligned}&\sum_{j=-L}^{-1}\left(\mathrm{Re}(\varphi^{-}_{j,k})\,\mathrm{Re}(\varphi^{-}_{j,i})+\mathrm{Im}(\varphi^{-}_{j,k})\,\mathrm{Im}(\varphi^{-}_{j,i})\right)\\ &+\sum_{j=1}^{L}\left(\mathrm{Re}(\varphi^{+}_{j,k})\,\mathrm{Re}(\varphi^{+}_{j,i})+\mathrm{Im}(\varphi^{+}_{j,k})\,\mathrm{Im}(\varphi^{+}_{j,i})\right)=\begin{cases}0 & k\neq i\\ 1 & k=i\,.\end{cases}\end{aligned} \tag{A-19}$$

According to the definition of even and odd functions $\mathrm{Re}(\varphi^{-}) = \mathrm{Re}(\varphi^{+})$ and $\mathrm{Im}(\varphi^{-})=-\mathrm{Im}(\varphi^{+})$, and therefore,

$$2\sum_{j=1}^{L}\left(\mathrm{Re}(\varphi^{+}_{j,k})\,\mathrm{Re}(\varphi^{+}_{j,i})+\mathrm{Im}(\varphi^{+}_{j,k})\,\mathrm{Im}(\varphi^{+}_{j,i})\right)=\begin{cases}0 & k\neq i\\ 1 & k=i\end{cases} \tag{A-20}$$

or

$$\mathrm{Re}\left(\sum_{j=1}^{L}\left(\varphi_{j,k}^{+}\right)^{*}\left(\varphi_{j,i}^{+}\right)\right)=\begin{cases}0 & k\neq i\\ 0.5 & k=i\end{cases}. \tag{A-21}$$

For polynomials θ^{+} (corresponding to polynomials θ_k in Eq. A-15) everything is similar except there will be a weighting function so that

$$\mathrm{Re}\left(\sum_{j=1}^{L}\left(\theta_{j,k}^{+}\right)^{*}\left(\theta_{j,i}^{+}\right)\left|\tilde{\alpha}(\omega_j)\right|^{2}\right)=\begin{cases}0 & k\neq i\\ 0.5 & k=i\end{cases}. \tag{A-22}$$

The problem now is to generate φ^{+} and θ^{+} automatically so that they satisfy A-21 and A-22. Out of the many types of orthogonal polynomials, the Forsythe type is chosen because of its computational advantages. The Forsythe recursion formulas can be used very conveniently as they are easy to program. The formulas for the general case (not only the positive half-functions) will be presented first using a common notation of γ for either φ or θ. Let q_j be the weighting function and m the degree of the polynomial. The recursive formulas are given by

$$\begin{aligned}
\gamma_0(\omega) &= 1\\
\gamma_1(\omega) &= (\omega-u_1)\gamma_0(\omega)\\
\gamma_2(\omega) &= (\omega-u_2)\gamma_1(\omega)-v_1\gamma_0(\omega)\\
&\vdots\\
\gamma_k(\omega) &= (\omega-u_k)\gamma_{k-1}(\omega)-v_{k-1}\gamma_{k-2}(\omega)\\
&\vdots\\
\gamma_m(\omega) &= (\omega-u_m)\gamma_{m-1}(\omega)-v_{m-1}\gamma_{m-2}(\omega)
\end{aligned} \tag{A-23}$$

where

$$u_k=\frac{\sum_{j=1}^{L}\omega_j\left(\gamma_{k-1}(\omega_j)\right)^2 q_j}{D_{k-1}} \tag{A-24}$$

$$v_k=\frac{\sum_{j=1}^{L}\omega_j\gamma_k(\omega_j)\gamma_{k-1}(\omega_j)q_j}{D_{k-1}} \tag{A-25}$$

$$D_k=\sum_{j=1}^{L}\left(\gamma_k(\omega_j)\right)^2 q_j\,. \tag{A-26}$$

If in Eqs. A-24, A-25 and A-26, the summation is extended from –L to +L, it is easily recognized that u_k is an odd function and v_k an even function of ω and so u_k will be zero and the summation in v_k and D_k will be twice the summation from j=1 to L. The expressions therefore become

$$\begin{aligned}
\gamma_0^+(\omega) &= 1 \\
\gamma_1^+(\omega) &= \omega\gamma_0^+(\omega) \\
\gamma_2^+(\omega) &= \omega\gamma_1^+(\omega) - v_1^+\gamma_0^+(\omega) \\
&\vdots \\
\gamma_k^+(\omega) &= \omega\gamma_{k-1}^+(\omega) - v_{k-1}^+\gamma_{k-2}^+(\omega) \\
&\vdots \\
\gamma_m^+(\omega) &= \omega\gamma_{m-1}^+(\omega) - v_{m-1}^+\gamma_{k-2}^+(\omega)
\end{aligned} \tag{A-27}$$

with

$$v_k^+ = \frac{2\sum_{j=1}^{L}\omega_j\gamma_k^+(\omega_j)\gamma_{k-1}^+(\omega_j)q_j}{D_{k-1}^+} \tag{A-28}$$

$$D_k^+ = 2\sum_{j=1}^{L}\left(\gamma_k^+(\omega_j)\right)^2 q_j\ . \tag{A-29}$$

These equations represent a major simplification and are the reason the half-functions, defined for positive and negative frequencies, have been considered.

After calculating all the polynomials γ_k^+, they must be normalized by dividing by $\sqrt{D_k^+}$, and to obtain the complex polynomials, they must be multiplied by i^k. To multiply the resulting polynomials γ_k^+ by i^k produces the same result as calculating them for iω, instead of ω, in Eqs. A-27, A-28 and A-29. To avoid further numerical problems, the frequency range of interest is scaled by dividing all the frequencies by their maximum value in the considered interval, so that the maximum frequency value is 1.

Applying Eq. A-27, polynomials $\varphi^+(\omega_j)$ and $\theta^+(\omega_j)$ can be calculated by making $q_j = 1$ or $q_j = \left|\tilde{\alpha}(\omega_j)\right|^2$, respectively. Knowing $\varphi^+(\omega_j)$ and $\theta^+(\omega_j)$, it is possible to calculate the new [P]

and [T] matrices, given by Eqs. A-12 and A-13., where φ and θ must be understood as φ^+ and θ^+. Eq. A-10 becomes

$$\begin{bmatrix} \begin{bmatrix} \text{‘0.5} \end{bmatrix} & [X] \\ [X]^T & \begin{bmatrix} \text{‘0.5} \end{bmatrix} \end{bmatrix} \begin{Bmatrix} \{c\} \\ \{d\} \end{Bmatrix} = \begin{Bmatrix} \{G\} \\ \{0\} \end{Bmatrix} \tag{A-29}$$

with [X] and [G] defined as before in Eq. A-11, but with [P] and [T] now in terms of φ^+ and θ^+ and {F} equal zero from Eq. A-22. Multiplying both sides by 2 gives

$$\begin{bmatrix} [I] & [X'] \\ [X']^T & [I] \end{bmatrix} \begin{Bmatrix} \{c\} \\ \{d\} \end{Bmatrix} = \begin{Bmatrix} \{G'\} \\ \{0\} \end{Bmatrix} \tag{A-30}$$

where [X’] = 2[X] and {G’} = 2{G}. Solving Eq. A-30 gives

$$\{d\} = -\left[[I] - [X']^T [X']\right]^{-1} [X']^T \{G'\} \tag{A-31}$$

$$\{c\} = \{G'\} - [X']\{d\} \ . \tag{A-32}$$

<u>Calculation of modal parameters</u>

Having calculated {c} and {d} from Eqs. A-31 and A-32 we now return to Eq. A-15 (where φ and θ must be replaced with $\varphi^+$and θ^+), with the FRF expressed in terms of the coefficients {c} and {d} and orthogonal polynomial $\varphi^+$and θ^+. In order to calculate the modal parameters Eq. A-15 must be written in terms of coefficients {a} and {b} as in Eq. A-2. If the coefficients of polynomials $\varphi^+$and θ^+ have been stored, it is possible to find linear transformations relationships between {a} and {c} and between {b} and {d} in the following form

$$\underset{(2N\times1)}{\{a\}} = \underset{(2N\times2N)}{[T_{ac}]} \underset{(2N\times1)}{\{c\}} \tag{A-33}$$

$$\underset{(2N\times1)}{\{b\}} = \underset{(2N\times2N)}{[T_{bd}]} \underset{(2N\times1)}{\{d\}} + \underset{(2N\times1)}{\{R\}} \ . \tag{A-34}$$

Knowing {b}, these values can be introduced into a complex polynomial solve routine to calculate the roots, which are directly related to the resonant frequencies and damping ratios.

B. The Global Rational Polynomial Method (GRFP)

This method is an extension of the RFP method to analyze globally a set of FRFs, using one single input reference. In the previous discussion only a single FRF was used when identifying the modal parameters. If other FRFs measured on the same structure are also considered, one might expect (theoretically) exactly the same results for the resonant frequencies and damping ratios, as these are characteristic properties of the structure, but different modal constants and phase angles. The former are called 'global' properties and the latter 'local' properties. Using several FRFs to calculated the global properties implies overspecification of the number of equations in relation to the number of unknowns, and so we shall make use again of a least squares procedure. Knowing the global properties, the local ones can be calculated from each FRF.

As seen in the RFP method, the coefficients b_k are the ones which yield the global properties of the system. These are related to coefficients d_k through the transformation relationships given by Eq. A-34, where $[T_{bd}]$ and $\{R\}$ are direct functions of the orthogonal polynomial coefficients. Taking $\{d\}$ from Eq. A-34 and substituting into Eq. A-31 gives

$$\left[[I]-[X']^T[X']\right][T_{bd}]^{-1}\{\{b\}-\{R\}\}=-[X']^T\{G'\} \qquad \text{(A-35)}$$

or

$$[U_G]\{b\}=\{V_G\} \qquad \text{(A-36)}$$

where

$$\underset{(2N\times 2N)}{[U_B]}=\left[[I]-[X']^T[X']\right][T_{bd}]^{-1} \qquad \text{(A-37)}$$

$$\underset{(2N\times 1)}{\{V_G\}}=[U_G]\{R\}-[X']^T\{G'\}\,. \qquad \text{(A-38)}$$

For each FRF there is an equation of the form shown in (A-36). Considering a total of p FRFs,

$$\underset{((2N\times p)\times 2N)}{\begin{bmatrix} [U_G]_1 \\ [U_G]_2 \\ \vdots \\ [U_G]_p \end{bmatrix}} \underset{(2N\times 1)}{\{b\}} = \underset{((2N\times p)\times 1)}{\begin{Bmatrix} \{V_G\}_1 \\ \{V_G\}_2 \\ \vdots \\ \{V_G\}_p \end{Bmatrix}} \tag{A-39}$$

or

$$[U_T]\{b\}\{V_T\} \; . \tag{A-40}$$

Solving Eq. A-40 in a least squares sense gives

$$\{b\} = \left([U_T]^T [U_T]\right)^{-1} [U_T]^T \{V_T\} \; . \tag{A-41}$$

With {b}, a polynomial solver can be used to find the roots and eventually to calculate the natural frequencies and damping ratios.

<u>Calculation of local properties</u>

To calculate {a}, there are two options: either to use Eq. A-33 with {c} given by Eq. A-32, using {d} calculated for each FRF, or, once the resonant frequencies and damping ratios have been calculated, to curve fit each FRF again but now only calculate {a} and then the modal constants.

The second option seems to be much more rational and consistent with the global curve-fitting philosophy, and will be explained next. Eq. A-2 can be rewritten for each measured frequency as

$$\alpha(\omega_j) = \sum_{k=0}^{2N-1} \left(\frac{(i\omega_j)^k}{\sum_{k=0}^{2N} b_k (i\omega_j)^k} \right) a_k \tag{A-42}$$

or simply

$$\alpha(\omega_j) = \sum_{k=0}^{2N-1} t_{jk} a_k \ . \tag{A-43}$$

The error between the analytical and experimental values at each frequency ω_j, is

$$e_j = \alpha(\omega_j) - \tilde{\alpha}(\omega_j) = \sum_{k=0}^{2N-1} t_{jk} a_k - \tilde{\alpha}(\omega_j) \ . \tag{A-44}$$

For all L measured frequencies, the error vector is given by

$$\underset{(L\times 1)}{\{E\}} = \underset{(L\times 2N)}{[T_G]} \underset{2N\times 1}{\{a\}} - \underset{(L\times 1)}{\{\tilde{\alpha}\}} \tag{A-45}$$

where

$$[T_G] = \begin{bmatrix} t_{1,0} & t_{1,1} & \cdots & t_{1,2N-1} \\ t_{2,0} & t_{2,1} & \cdots & t_{2,2N-1} \\ \vdots & \vdots & \ddots & \vdots \\ t_{L,0} & t_{L,1} & \cdots & t_{L,2N-1} \end{bmatrix} . \tag{A-46}$$

The squared error J is

$$J = \{E^*\}^T \{E\} = \{a\}^T [T_G^*]^T [T_G] \{a\} - \{\tilde{\alpha}^*\}^T [T_G] \{a\} - \{a\}^T [T_G^*]^T \{\tilde{\alpha}\} + \{\tilde{\alpha}^*\}^T \{\tilde{\alpha}\} \ . \tag{A-47}$$

Minimizing J by taking its derivative with respect to {a} and setting it equal to zero, and after some algebraic manipulation, it follows that

$$\mathrm{Re}\left(\left[T_G^*\right]^T\left[T_G\right]\right)\{a\} = \mathrm{Re}\left(\left[T_G^*\right]^T\{\tilde{\alpha}\}\right) \ . \qquad \text{(A-48)}$$

Solving for {a} gives

$$\{a\} = \mathrm{Re}\left(\left[T_G^*\right]^T\left[T_G\right]\right)^{-1}\mathrm{Re}\left(\left[T_G^*\right]^T\{\tilde{\alpha}\}\right) \ . \qquad \text{(A-49)}$$

However, once again, some numerical problems may be encountered in the inversion although these may again be avoided by using orthogonal polynomials replacing that term by the unit matrix. This means, following what has been done for the RFP method, changing Eq. A-42 or A-43 into

$$\alpha(\omega_j) = \sum_{k=0}^{2N-1}\left(\frac{\varphi_{j,k}^{+}}{g_j}\right)c_k = \sum_{k=0}^{2N-1} z_{j,k}c_k \qquad \text{(A-50)}$$

where g_j is the denominator of (A-42), which is known, as the coefficients b_k have already been calculated, and $\varphi_{j,k}^{+}$ is the half-positive orthogonal polynomial defined in Eq. A-27, A-28 and A-29 as γ+ and for $q_j = \left|1/g_j\right|^2$. For all L measured points Eq. A-50 can be written as

$$\{\alpha(\omega)\}[Z_G]\{c\} \qquad \text{(A-51)}$$

where $[Z_G]$ can be expressed as $\left[\text{‘}1/g_{\text{،}}\right]\left[\vartheta^+\right]$, $\left[\vartheta^+\right]$ being the matrix composed by $\varphi_{j,k}^{+}$. Thus, to have $\mathrm{Re}\left(\left[T_G^*\right]^T\left[T_G\right]\right) = [I]$ means to have

$$\mathrm{Re}\left(\left[\vartheta^{+*}\right]^T\left[\text{‘}(1/g)_{\text{،}}^*\right]\left[\text{‘}1/g_{\text{،}}\right]\left[\vartheta^+\right]\right) = [I] \ . \qquad \text{(A-52)}$$

Similarly it was found in Eq. A-22, we have to generate orthogonal polynomials with respect to a weighting function $\left|1/g_j\right|^2$ and the orthogonality condition is (using the positive half functions)

$$\mathrm{Re}\left(\sum_{j=1}^{L}\left(\varphi_{j,k}^{+}\right)^{*}\left(\varphi_{j,k}^{+}\right)\left|1/g_j\right|^2\right)=\begin{cases}0 & k\neq i\\ 0.5 & k=i\end{cases}. \qquad \text{(A-53)}$$

Hence, Eq. A-48 becomes

$$\left[\text{‘}0.5\text{،}\right]\{c\}=\mathrm{Re}\left(\left[Z_G^{*}\right]^{T}\{\tilde{\alpha}\}\right)\ \Rightarrow\ \{c\}=2\,\mathrm{Re}\left(\left[Z_G^{*}\right]^{T}\{\tilde{\alpha}\}\right)\ . \qquad \text{(A-54)}$$

{a} can be calculated using a transformation as in Eq. A-33, from which the local modal parameters can be evaluated.

APPENDIX B:

IDENTIFYING MODAL PROPERTIES USING AN EIGENSYSTEM REALIZATION ALGORITHM

The Eigensystem Realization Algorithm (ERA) is a multi-input multi-output method developed by Juang and Pappa (1985). The following discussion closely follows that given by an excellent text edited by Maia and Silva (1997), The equation of motion for an *N* degree of freedom system is

$$[M]\{\ddot{x}\}+[C]\{\dot{x}\}+[K]\{x\}=\{f(x(t),t)\} \tag{B-1}$$

where

$$\begin{aligned}
[M] &= N\times N \text{ mass matrix}\\
[C] &= N\times N \text{ damping matrix}\\
[K] &= N\times N \text{ stiffness matrix}\\
\{\ddot{x}(t)\} &= N\times 1 \text{ acceleration vector}\\
\{\dot{x}(t)\} &= N\times 1 \text{ velocity vector}\\
\{x(t)\} &= N\times 1 \text{ displacement vector}\\
\{f(x(t),t)\} &= N\times 1 \text{ applied force vector}
\end{aligned}$$

Defining

$$\underset{2N\times 1}{\{u(t)\}}=\begin{Bmatrix}\{x(t)\}\\ \{\dot{x}(t)\}\end{Bmatrix} \tag{B-2}$$

$$\underset{N\times 1}{\{f(t)\}}=\underset{N\times q}{[F]}\underset{q\times 1}{\{\delta(t)\}} \tag{B-3}$$

where $\{\delta(t)\}$is the input vector at q locations and [F] is a matrix of input coefficients. Equation (B-1) can be written in state space form as

$$\underset{2N\times 1}{\{\dot{u}(t)\}}=\underset{2N\times 2N}{[A']}\underset{2N\times 1}{\{u(t)\}}+\underset{2N\times q}{[B']}\underset{q\times 1}{\{\delta(t)\}} \tag{B-4}$$

where

$$[A']=\begin{bmatrix}[0] & [I]\\ -[M]^{-1}[K] & -[M]^{-1}[C]\end{bmatrix} \tag{B-5}$$

$$[B'] = \begin{bmatrix} [0] \\ [M]^{-1}[F] \end{bmatrix} . \tag{B-6}$$

It is possible to relate {u(t)} to the measured responses at p physical coordinates {x(t)} through a transformation matrix [R]:

$$\underset{p\times 1}{\{x(t)\}} = \underset{p\times 2N}{[R]}\underset{2N\times 1}{\{u(t)\}} . \tag{B-7}$$

The solution of Eq. B-4 to an input $\{\delta(t)\}$ is given by

$$\{u(t)\} = e^{[A'](t-t_0)}\{u(t_0)\} + \int_{t_0}^{t} e^{[A'](t-\tau)}[B']\{\delta(t)\}d\tau \tag{B-8}$$

for any time t after an initial time t_0. To give a discrete representation of Eq. B-8, several equally spaced time intervals, 0, Δt, …, $k\Delta t$ are considered. We can then take $t = (k+1)\,\Delta t$ and $t_0 = k\Delta t$:

$$\{u((k+1)\Delta t\} = e^{[A']\Delta t}\{u(k\Delta t)\} + \int_{k\Delta t}^{(k+1)\Delta t} e^{[A']((k+1)\Delta t-\tau)}[B']\{\delta(\tau)\}d\tau . \tag{B-9}$$

Assuming that the input $\{\delta(t)\}$ is constant during the time interval $k\Delta t \le \tau \le (k+1)\Delta t$, the input can be designated $\{\delta(k\Delta\tau)\}$, and making the change of variable $\tau' = (k+1)\Delta t - \tau$, Eq. B-9 can be written as

$$\{u((k+1)\Delta t\} = e^{[A']\Delta t}\{u(k\Delta t)\} - \int_{0}^{\Delta t} e^{[A']\tau'}d\tau'[B']\{\delta(k\Delta t)\} . \tag{B-10}$$

By defining some new quantities Eq. B-10 can be written as

$$\{u(k+1)\} = [A]\{u(k)\} + [B]\{\delta(k)\} \qquad \text{for } k = 0, 1, 2, ... \tag{B-11}$$

where

$$\{u(k+1)\} = \{u((k+1)\Delta t)\} \tag{B-12}$$

$$[A] = e^{[A']\Delta t} \tag{B-13}$$

$$[B] = -\int_{0}^{\Delta t} e^{[A']\tau'}d\tau'[B'] \tag{B-14}$$

$$\{\delta(k)\} = \{\delta(k\Delta t)\} . \tag{B-15}$$

Equation B-7 becomes

$$\{x(k)\} = [R]\{u(k)\} . \tag{B-16}$$

Let us consider the response to an impulse at k = 0, that is, $\{\delta(0)\} = \{1, 0, \ldots, 0\}^T$ and $\{\delta(k)\} = \{0\}$ for k >0. Substituting these expressions into Eq. B-11 gives

$$\{u(1)\} = [A]\{u(0)\} + \{B\} \tag{B-17}$$

and from Eq. B-16

$$\{x(1)\} = [R]\{u(1)\} \ . \tag{B-18}$$

Substituting Eq. B-17 into Eq. B-18 and for simplicity letting {u(0)} = {0} gives

$$\underset{p\times 1}{\{x(1)\}} = \underset{p\times 2N}{[R]}\,\underset{2N\times 1}{\{B\}} \ . \tag{B-19}$$

For all other time intervals, $\{\delta(k)\} = \{0\}$ so from Eq. B-11

$$\{u(2)\} = [A]\{u(1)\} = [A]\{B\} \ .$$

Substituting this into B-16 gives

$$\{x(2)\} = [R]\{u(2)\} = [R][A]\{B\} \ . \tag{B-20}$$

Similarly

$$\{x(3)\} = [R]\{u(3)\} = [R][A]\{u(2)\} = [R][A]^2\{B\} \tag{B-21}$$

and, in general,

$$\underset{p\times 1}{\{x(k)\}} = \underset{p\times 2N}{[R]}\,\underset{2N\times 2N}{[A]}^{\,k-1}\,\underset{2N\times 1}{\{B\}} \ . \tag{B-22}$$

If we consider the impulses at all the q input locations, it follows that

$$\underset{p\times q}{[X(k)]} = \underset{p\times 2N}{[R]}\,\underset{2N\times 2N}{[A]}^{\,k-1}\,\underset{2N\times q}{[B]} \tag{B-23}$$

where the matrices [X(k)] are usually called the Markov parameters. These are used to form the generalized Hankel matrices given by:

$$\underset{pr\times qs}{[H(k-1)]} = \begin{bmatrix} [X(k)] & [X(k+1)] & \cdots & [X(k+j)] \\ [X(k+1)] & [X(k+2)] & \cdots & [X(k+j+1)] \\ \vdots & \vdots & \ddots & \vdots \\ [X(k+i)] & [X(k+i+1)] & \cdots & [X(k+i+j)] \end{bmatrix} \tag{B-24}$$

where i = 1, …, r-1 and j = 1, …., s-1, with r and s as integers. If there is an initial state response measurement, [H(k-1)] is simply replaced by [H(k)]. In Eq. B-24 k will be greater than or equal to 1. Substituting B-23 into B-24 gives

$$[H(k)] = [Q][A]^K[W] \qquad k \geq 0 \tag{B-25}$$

where

$$\underset{pr\times 2N}{[Q]} = \begin{bmatrix} [R] \\ [R][A] \\ \vdots \\ [R][A]^{r-1} \end{bmatrix} \tag{B-26}$$

$$\underset{2N\times qs}{[W]} = \begin{bmatrix} [B] & [A][B] & \cdots & [A]^{s-1}[B] \end{bmatrix} . \tag{B-27}$$

[Q] and [W] are called the observability and controllability matrices, respectively. It should be noted that [H(k)] is a known matrix of the responses. One of the advantages of this formulation is that in [H(k)] we may only include good responses. The objective is to reconstruct Eq. B-23 from the experimental data. This process is known as realization and implies the determination of matrices [R], [A], and [B]. There are an infinite number of sets of these three matrices satisfying Eq. B-23. The objective is to obtain a minimum realization, that is, the realization corresponding to the minimum order of the state-space formulation that can still represent the dynamic behavior of the structure.

The first step is to look for a matrix [H]′ such that

$$\underset{2N\times qs}{[W]}\,\underset{qs\times qr}{[H]'}\,\underset{pr\times 2N}{[Q]} = \underset{2N\times 2N}{[I]} . \tag{B-28}$$

Pre- and post-multiplying Eq. B-28 by [Q] and [W] respectively gives

$$[Q][W][H]'[Q][W] = [Q][W] . \tag{B-29}$$

But, from B-25 it is clear that

$$[Q][W] = [H(0)] \tag{B-30}$$

which when substituted into Eq. B-29 gives

$$[H(0)][H]'[H(0)] = [H(0)] . \tag{B-31}$$

Therefore, [H]′ is the pseudo-inverse of [H(0)], that is,

$$[H]' = [H(0)]^{+} . \tag{B-32}$$

The pseudo-inverse of [H(0)] can be calculated via Singular Value Decomposition (SVD)

$$\underset{pr\times qs}{[H(0)]} = \underset{pr\times pr}{[U]}\,\underset{pr\times ps}{[\Sigma]}\,\underset{ps\times qs}{[V]^{T}} . \tag{B-33}$$

Matrix [H(0)] has 2N non-zero singular values (rank = 2N), equivalent to the order of the state-space system. [H(0)] can therefore be recomputed using on the first 2N columns of [U] and [V]

$$\underset{pr\times qs}{[H(0)]} = \underset{pr\times 2N}{[U_{2N}]}\underset{2N\times 2N}{[\Sigma_{2N}]}\underset{2N\times qs}{[V_{2N}]^{T}} \tag{B-34}$$

with

$$[U_{2N}]^{T}[U_{2N}] = [V_{2N}]^{T}[V_{2N}] = [I] . \tag{B-35}$$

Matrix [H]′ (=$[H(0)]^{+}$) is therefore given by

$$[H]' = [V_{2N}][\Sigma_{2N}]^{-1}[U_{2N}]^{T} . \tag{B-36}$$

To obtain the desired realization, we start from Eq. B-23, which for $k \geq 0$ can be written as

$$[X(k+1)] = [R][A]^{k}[B] \tag{B-37}$$

and use the identity

$$\underset{p\times q}{[X(k+1)]} = \underset{p\times pr}{[E_p]^{T}}\,\underset{pr\times qs}{[H(k)]}\underset{qs\times q}{[E_q]} \tag{B-38}$$

where

$$\underset{p\times pr}{[E_p]^{T}} = \begin{bmatrix} \underset{p\times p}{[I]} & \underset{p\times p}{[0]} & \cdots & \underset{p\times p}{[0]} \end{bmatrix} \tag{B-39}$$

$$\underset{qs\times q}{[E_q]} = \begin{bmatrix} [I] \\ [0] \\ \vdots \\ [0] \end{bmatrix} \tag{B-40}$$

where [I] is the identity matrix of appropriate dimension. Using B-25, B-28, B-30, B-34, B-35 and B-36, it is possible to show that

$$[X(k+1)] = \left[[E_p]^T [U_{2N}][\Sigma_{2N}]^{1/2}\right]\left[[\Sigma_{2N}]^{-1/2}[U_{2N}]^T\left[[Q][A]^k[W]\right][V_{2N}][\Sigma_{2N}]^{1/2}\right]\left[[\Sigma_{2N}]^{1/2}[V_{2N}]^T[E_q]\right] \tag{B-41}$$

Similarities between B-37 and B-41 are already apparent. Some modifications need to be made however in Eq. B-41 in the second block of matrices. After some mathematical manipulation it can be shown that

$$[X(k+1)] = \left[[E_p]^T [U_{2N}][\Sigma_{2N}]^{1/2}\right]\left[[\Sigma_{2N}]^{-1/2}[U_{2N}]^T[H(1)][V_{2N}][\Sigma_{2N}]^{1/2}\right]^k\left[[\Sigma_{2N}]^{1/2}[V_{2N}]^T[E_q]\right] . \tag{B-42}$$

Comparing Eqs. B-42 and B-37 it is clear that the desired realization has been achieved, where

$$\begin{aligned} [R] &= [E_p]^T [U_{2N}][\Sigma_{2N}]^{1/2} \\ [A] &= [\Sigma_{2N}]^{-1/2}[U_{2N}]^T[H(1)][V_{2N}][\Sigma_{2N}]^{1/2} \\ [B] &= [\Sigma_{2N}]^{1/2}[V_{2N}]^T[E_q] \end{aligned} \tag{B-43}$$

In order to determine the modal parameters of the system, we must solve an eigenproblem based on the 'realized' matrix [A], of the form

$$[A]\{\psi_u\} = \lambda\{\psi_u\} . \tag{B-44}$$

To obtain the mode shapes in terms of the physical coordinates of the system, the transformation given by Eq. B-7 is used

$$\underset{p\times 1}{\{\psi_x\}} = \underset{p\times 2N}{[R]}\underset{2N\times 1}{\{\psi_u\}} . \tag{B-45}$$

The modal parameters are easily calculated from the eigenproblem results. In summary, the necessary steps to perform an analysis with ERA are as follows:

1. choice of measured data to construct the matrix [H(0)];
2. calculation of SVD of [H(0)], to calculate $[U_{2N}]$, $[V_{2N}]$, and $[\Sigma_{2N}]$ and to recalculate [H(0)] based on the value of the rank found (order of the system);
3. construction of matrix [H(1)] and calculation of the 'realized' matrices [R], [A], and [B], using Eq. B-43; and
4. calculation of eigenvalues and eigenvectors of matrix [A] and the eigenvectors corresponding to the physical coordinates (Eqs. B-44 and A45) and calculation of the modal parameters.

This method requires checks on the calculated modes, to distinguish between genuine and computational modes, as the results from the SVD, in some cases, may not be correct because of noise or nonlinearities. The first check is known as the Modal Amplitude Coherence and is defined as the coherence between each modal amplitude history and an ideal one, formed by extrapolating the initial value of the history to other points, using the identified eigenvalues.

Another check is the Modal Phase Collinearity, for lightly damped structures, where real mode behavior is expected. This indicator measures the strength of the linear functional relationship between the real and imaginary parts of the mode shape, for each mode. Modal reduction is then possible, by truncating the modes with low accuracy indicators. The final model can be assessed by comparing the initial free responses with the ones calculated by Eq. B-42. Additional discussion of ERA can be found in Juang (1987) and Juang and Pappa (1986).

APPENDIX C:

ESTIMATING CONFIDENCE LIMITS FOR FREQUENCY RESPONSE FUNCTIONS FROM MEASURED COHERENCE FUNCTIONS

An important element of any experimental procedure is to quantify the uncertainty in the test that can be attributed to either random or bias (systematic) variability. Uncertainty bounds on measured frequency response function (FRF) magnitude and phase is a necessary first step in trying to quantify the uncertainly of estimated modal parameters. The following discussion for the estimate of uncertainty for a randomly excited single-input/output model closely follows that by Bendat and Piersol (1980).

Consider the single-input/output model of Figure C1 where

X(f) = Fourier transform of measured input single x(t) , assumed noise free
Y(f) = Fourier transform of measured output signal y(t) = v(t) + n(t)
V(f) = Fourier transform of computed output signal v(t)
N(f) = Fourier transform of computed output noise n(t)
$H_{xy}(f)$ = Frequency response function of optimum constant parameter linear system estimating y(t) from x(t)

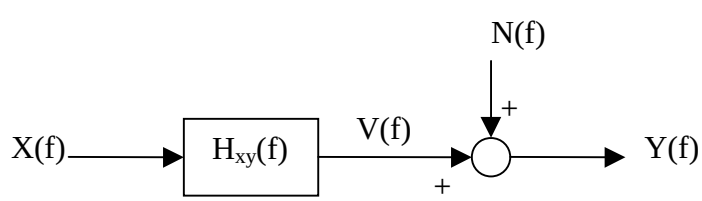

Figure C-1. Single-input/output model.

Assume that x(t) and y(t) are the only records available for analysis and that they are representative members of a zero mean value Gaussian random processes. Data can be either stationary random data or transient random data. For definiteness here, stationary data will be assumed and spectral results will be expressed using one-sided spectra. Normalized error formulas are the same for one-sided or two sided spectra. In the following discussion a hat (^) symbol over a quantity denotes an estimate of this quantity.

When noise is present in output measurements the optimum frequency response function estimate is

$$\hat{H}_{xy}(f) = \frac{\hat{G}_{xy}(f)}{\hat{G}_{xx}(f)} \tag{C-1}$$

where $\hat{G}_{xx}(f)$ and $\hat{G}_{xy}(f)$ are "smooth" estimates of the input autospectral density function and input/output cross-spectral density function, respectively. The associated coherence function estimate is

$$\hat{\gamma}^2_{xy}(f) = \frac{\left|\hat{G}_{xy}(f)\right|^2}{\hat{G}_{xx}(f)\hat{G}_{yy}(f)} \tag{C-2}$$

where $\hat{G}_{yy}(f)$ is a "smooth" estimate of the output autospectral density function. The coherent output spectrum estimate is

$$\hat{G}_{vv}(f) = \left|\hat{H}_{xy}(f)\right|^2 \hat{G}_{xx}(f) = \hat{\gamma}^2_{xy}(f)\hat{G}_{yy}(f). \tag{C-3}$$

The noise output spectrum estimate is

$$\hat{G}_{nn}(f) = \left[1 - \hat{\gamma}^2_{xy}(f)\right]\hat{G}_{yy}(f). \tag{C-4}$$

The coherent output spectrum estimate is a computed quantity that is not measured. The measured quantity is $\hat{G}_{yy}(f)$ which can be shown to be

$$\hat{G}_{yy}(f) = \hat{G}_{vv}(f) + \hat{G}_{nn}(f) \tag{C-5}$$

because v(t) and n(t) are uncorrelated so that $G_{vn}(f) = 0$ when $\hat{H}_{xy}(f)$ is computed from Eq. C-1.

In polar form, the frequency response function can be expressed as

$$\hat{H}_{xy}(f) = \left|\hat{H}_{xy}(f)\right| e^{-j\hat{\phi}_{xy}(f)} \tag{C-6}$$

where

$$\left|\hat{H}_{xy}(f)\right| = \frac{\left|\hat{G}_{xy}(f)\right|}{\hat{G}_{xx}(f)} = \text{system gain factor estimate} \tag{C-7}$$

$$\hat{\phi}_{xy}(f) = \tan^{-1}\left(\frac{\hat{Q}_{xy}(f)}{\hat{C}_{xy}(f)}\right) = \text{ system phase factor estimate}. \tag{C-8}$$

This quantity $\hat{\phi}_{xy}(f)$ is the same as the angle $\hat{\theta}_{xy}(f)$ in $\hat{G}_{xy}(f)$ as shown in Figure C2.

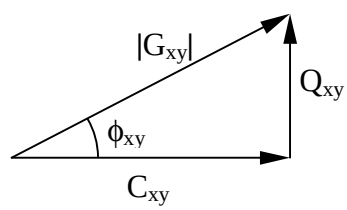

Figure C-2. Illustration of angle definition.

This is also the phase that would be assigned to $\hat{\gamma}_{xy}(f)$ when $\hat{\gamma}_{xy}(f)$ is defined as the complex-valued function given by

$$\hat{\gamma}_{xy}(f) = \left|\hat{\gamma}_{xy}(f)\right| e^{-j\hat{\phi}_{xy}(f)} = +\sqrt{\hat{\gamma}^2_{xy}(f)}\, e^{-j\hat{\phi}_{xy}(f)}. \tag{C-9}$$

Note that all of the above "smooth" estimates can be computed from the original computed "smooth" estimates of $\hat{G}_{xx}(f)$, $\hat{G}_{yy}(f)$, and $\hat{G}_{xy}(f)$.

A. Random Error in Gain Factor Estimates

Random error formulas for all of these quantities will be derived in terms of the unknown true coherence function $\gamma^2_{xy}(f)$ and the number of independent averages n_d. To apply these results to evaluate measured data, one should use the computed coherence function estimate $\hat{\gamma}^2_{xy}(f)$ with an appropriate number of independent averages n_d. This will give practical results, particularly if the resulting random errors are less than 20%. Bias errors will not be discussed in this appendix.

To establish random error in gain factor estimates one can start with the equation

$$G_{vv} = \left|H_{xy}\right|^2 G_{xx} . \tag{C-10}$$

Taking differential increments of both sides yields

$$\Delta G_{vv} \approx \left|H_{xy}\right|^2 \Delta G_{xx} + G_{xx} \Delta \left|H_{xy}\right|^2 \tag{C-11}$$

where

$$\begin{aligned} \Delta G_{vv} &= \hat{G}_{vv} - G_{vv} \\ \Delta G_{xx} &= \hat{G}_{xx} - G_{xx} \\ \Delta \left|H_{xy}\right|^2 &= \left|\hat{H}_{xy}\right|^2 - \left|H_{xy}\right|^2 \end{aligned} \tag{C-12}$$

and, assuming unbiased estimates

$$\begin{aligned} \mathrm{Var}\left[\hat{G}_{vv}\right] &= E\left[\Delta G_{vv} \Delta G_{vv}\right] \\ \mathrm{Var}\left[\hat{G}_{xx}\right] &= E\left[\Delta G_{xx} \Delta G_{xx}\right] \\ \mathrm{Var}\left[\left|\hat{H}_{xy}\right|^2\right] &= E\left[\Delta \left|H_{xy}\right|^2 \Delta \left|H_{xy}\right|^2\right] \end{aligned} \tag{C-13}$$

Also, because $\left|G_{xv}\right|^2 = G_{xx} G_{vv}$

$$\mathrm{Cov}\left(\hat{G}_{xx}, \hat{G}_{vv}\right) = E\left[\Delta G_{xx} \Delta G_{yy}\right] = \frac{G_{xx} G_{vv}}{n_d} . \tag{C-14}$$

Solving Eq. C-11 for $G_{xx} \Delta \left|H_{xy}\right|^2$ gives

$$G_{xx} \Delta \left|H_{xy}\right|^2 \approx \Delta G_{vv} - \left|H_{xy}\right|^2 \Delta G_{xx} . \tag{C-15}$$

Squaring both sides and taking expected values yields

$$G_{xx}^2 \mathrm{Var}\left[\left|\hat{H}_{xy}\right|^2\right] \approx \mathrm{Var}\left[\hat{G}_{vv}\right] - 2\left|\hat{H}_{xy}\right|^2 \mathrm{Cov}(\hat{G}_{xx}, \hat{G}_{vv}) + \left|\hat{H}_{xy}\right|^4 \mathrm{Var}\left[\hat{G}_{xx}\right] . \tag{C-16}$$

To simplify Eq. C-16 we need an expression for $\mathrm{Var}\left[\hat{G}_{vv}\right]$ and $\mathrm{Var}\left[\hat{G}_{xx}\right]$. From Eq. C-5, assuming $\hat{G}_{vv}(f)$ and $\hat{G}_{nn}(f)$ are statistically independent, it follows that

$$\mathrm{Var}\left[\hat{G}_{yy}\right] = \mathrm{Var}\left[\hat{G}_{vv}\right] + \mathrm{Var}\left[\hat{G}_{nn}\right] \tag{C-17}$$

where the corresponding variance errors of "smooth" estimates of all of the above "raw" estimates will be reduced by a factor of n_d when averages are taken over n_d statistically independent "raw" quantities. To be specific

$$\mathrm{Var}\left[G_{yy}\right] = \frac{G_{yy}^2}{n_d}, \quad \mathrm{Var}\left[G_{nn}\right] = \frac{G_{nn}^2}{n_d}, \quad \mathrm{Var}\left[G_{xx}\right] = \frac{G_{xx}^2}{n_d} \ . \tag{C-18}$$

By substituting Eq. C-18 into Eq. C-17 and using $G_{nn} = (1-\gamma_{xy}^2)G_{yy}$ and $G_{vv} = \gamma_{xy}^2 G_{yy}$ we get after some manipulation

$$\mathrm{Var}\left[\hat{G}_{vv}\right] = \frac{G_{yy}^2 - G_{nn}^2}{n_d} = \frac{\left(2-\gamma_{xy}^2\right)G_{vv}^2}{\gamma_{xy}^2 n_d} \ . \tag{C-19}$$

Substituting Eqs. C-14, C-18, and C-19 into C-16 gives

$$G_{xx}^2 \mathrm{Var}\left[\left|\hat{H}_{xy}\right|^2\right] \approx \frac{\left(2-\gamma_{xy}^2\right)G_{vv}^2}{\gamma_{xy}^2 n_d} - 2\left|\hat{H}_{xy}\right|^2 \frac{G_{xx}G_{vv}}{n_d} + \left|\hat{H}_{xy}\right|^4 \frac{G_{xx}^2}{n_d} \ . \tag{C-20}$$

Dividing Eq. C-20 by G_{xx}^2 and using $G_{vv}/G_{xx} = \left|H_{xy}\right|^2$ gives

$$\mathrm{Var}\left[\left|\hat{H}_{xy}\right|^2\right] \approx \frac{2\left(1-\gamma_{xy}^2\right)\left|H_{xy}\right|^4}{\gamma_{xy}^2 n_d} \ . \tag{C-21}$$

From Bendat and Piersol (1980) the variance of any estimate $\hat{A}$ can be related to the variance of $\hat{A}^2$ as shown below

$$\mathrm{Var}\left[\hat{A}^2\right] = 4A^2 \mathrm{Var}\left[\hat{A}\right] \ . \tag{C-22}$$

Applying this relationship to Eq. C-21 gives

$$\mathrm{Var}\left[\left|\hat{H}_{xy}\right|\right] \approx \frac{\left(1-\gamma_{xy}^2\right)\left|H_{xy}\right|^2}{2\gamma_{xy}^2 n_d} \ . \tag{C-23}$$

Finally the standard deviation for the FRF magnitude becomes

$$\sigma\left(\left|\hat{H}_{xy}\right|\right) \equiv \text{s.d.}\left[\left|\hat{H}_{xy}\right|\right] \approx \frac{\sqrt{1-\gamma_{xy}^2}\left|H_{xy}\right|}{\left|\gamma_{xy}\right|\sqrt{2n_d}} . \tag{C-24}$$

Note that this result approaches zero as γ_{xy}^2 approaches one, independent of the size of n_d, and also approaches zero as n_d becomes large, independent of the size of γ_{xy}^2.

B. Random Error in Phase Factor Estimates

From Figure C-2 it is clear that

$$\tan\left(\phi_{xy}\right) = \frac{Q_{xy}}{C_{xy}} . \tag{C-25}$$

Taking differential increments of both sides gives

$$\Delta\phi_{xy} \sec^2 \phi_{xy} \approx \frac{C_{xy}\Delta Q_{xy} - Q_{xy}\Delta C_{xy}}{C_{xy}^2} \tag{C-26}$$

where from Figure C-2

$$\sec^2 \phi_{xy} = \frac{\left|G_{xy}\right|^2}{C_{xy}^2} . \tag{C-27}$$

Substituting C-27 into C-26 and solving for $\Delta\phi_{xy}$ gives

$$\Delta\phi_{xy} \approx \frac{C_{xy}\Delta Q_{xy} - Q_{xy}\Delta C_{xy}}{\left|G_{xy}\right|^2} . \tag{C-28}$$

A formula for the variance of "raw" estimates $\tilde{\phi}_{xy}$ (expressed in radians) can be derived from Eq. C-28 as follows

$$\begin{aligned} \text{Var}\left[\tilde{\phi}_{xy}\right] &= E\left[\left(\Delta\phi_{xy}\right)^2\right] = \frac{1}{\left|G_{xy}\right|^4} E\left[\left(C_{xy}\Delta Q_{xy} - Q_{xy}\Delta C_{xy}\right)^2\right] \\ &= \frac{1}{\left|G_{xy}\right|^4}\left\{C_{xy}^2 \text{Var}(\tilde{Q}_{xy}) - 2C_{xy}Q_{xy}\text{Cov}(\tilde{C}_{xy}, \tilde{Q}_{xy}) + Q_{xy}^2 \text{Var}(\tilde{C}_{xy})\right\} . \end{aligned} \tag{C-29}$$

This expression can be further simplified by using expressions for the variance and covariance of the terms in C-29 as found in Bendat and Piersol and given below for convenience

$$\begin{aligned}
&\mathrm{Var}\left[\tilde{C}_{xy}\right] = \tfrac{1}{2}\left(G_{xx}G_{yy} + C_{xy}^2 - Q_{xy}^2\right) \\
&\mathrm{Var}\left[\tilde{Q}_{xy}\right] = \tfrac{1}{2}\left(G_{xx}G_{yy} + Q_{xy}^2 - C_{xy}^2\right) \\
&\mathrm{Cov}\left(\tilde{C}_{xy}, \tilde{Q}_{xy}\right) = C_{xy}Q_{xy}
\end{aligned} \tag{C-30}$$

Substituting Eq. C-30 into Eq. C-29 and using $\left|G_{xy}\right|^2 = C_{xy}^2 + Q_{xy}^2$ and using the definition of coherence function (Eq. C-2) gives

$$\mathrm{Var}\left[\tilde{\phi}_{xy}\right] = \frac{1}{\left|G_{xy}\right|^4}\left\{\frac{\left|G_{xy}\right|^2}{2}G_{xx}G_{yy} - \frac{\left|G_{xy}\right|^4}{2}\right\} = \frac{1-\gamma_{xy}^2}{2\gamma_{xy}^2}\,. \tag{C-31}$$

For "smooth" estimates of $\hat{\phi}_{xy}$ from n_d averages, one obtains the standard deviation of the phase estimate

$$\sigma\left(\angle\hat{H}_{xy}\right) \equiv \mathrm{s.d.}\left[\hat{\phi}_{xy}\right] = \frac{\mathrm{s.d.}\left[\tilde{\phi}_{xy}\right]}{n_d} \approx \frac{\sqrt{1-\gamma_{xy}^2}}{\left|\gamma_{xy}\right|\sqrt{2n_d}}\,. \tag{C-32}$$

Note that the standard deviation for the phase factor estimate $\hat{\phi}_{xy}$, measured in radians, is approximately the same as the normalized random error for the gain factor $\left|\hat{H}_{xy}\right|$, that is

$$\mathrm{s.d.}\left[\hat{\phi}_{xy}\right] \approx \varepsilon\left[\left|\hat{H}_{xy}\right|\right] = \frac{\mathrm{s.d.}\left[\left|\hat{H}_{xy}\right|\right]}{\left|H_{xy}\right|} \approx \frac{\sqrt{1-\gamma_{xy}^2}}{\left|\gamma_{xy}\right|\sqrt{2n_d}}\,. \tag{C-33}$$

Another way of showing this result is by looking at a confidence diagram for frequency response function estimates as shown in Figure C3. In this figure, the measured value $\hat{H}$ is shown at the center of the circle with the unknown true value H somewhere inside the circle. When $\varepsilon\left[\left|\hat{H}_{xy}(f)\right|\right]$ is sufficiently small, then the uncertainty $\Delta\hat{\phi}_{xy}(f)$ in radians will satisfy

$$\Delta\hat{\phi}_{xy}(f) \approx \sin\Delta\hat{\phi}_{xy}(f) = \frac{\hat{r}(f)}{\left|\hat{H}_{xy}(f)\right|} \approx \varepsilon\left[\left|\hat{H}_{xy}(f)\right|\right] \tag{C-34}$$

which is identical to the observation made in Eq. C-33.

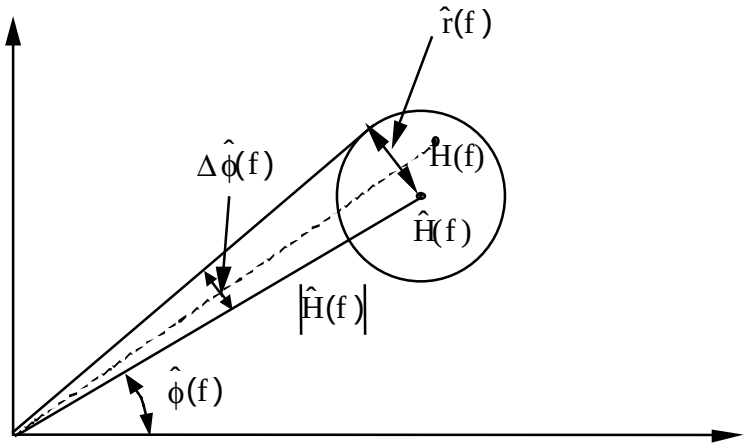

Figure C-3. Confidence diagram for frequency response function estimates.

APPENDIX D:

DIAMOND: A MATLAB TOOLBOX FOR MODAL ANALYSIS AND DAMAGE IDENTIFICATION

This appendix discusses a suite (toolbox) of graphical-interface software algorithms that have been developed to numerically simulate vibration tests and to apply various modal analysis, damage identification, and finite element model refinement techniques to measured or simulated modal vibration data. This toolbox is known as DIAMOND (Damage Identification and MOdal aNalysis of Data), and it was initially developed as a tool to analyze the data from the Alamosa Canyon Bridge tests. DIAMOND is written in MATLAB [MATLAB *Users Manual* (1994)], a numerical matrix math application which is available on all major computer platforms. DIAMOND is unique in three primary ways:

1. DIAMOND contains several of the most widely used modal curve-fitting algorithms. Thus the user may analyze the data using more than one technique and compare the results directly. This modal identification capability is coupled with a numerical test-simulation capability that allows the user to directly explore the effects of various test conditions on the identified modal parameters.

2. The damage identification and finite element model refinement modules are graphically interactive, so the operation is intuitive and the results are displayed visually as well as numerically. This feature allows the user to easily interpret the results in terms of structural damage.

3. DIAMOND has statistical analysis capability built into all three major analysis modules: modal analysis, damage identification, and finite element model refinement. The statistical analysis capability allows the user to determine the magnitude of the uncertainties associated with the results. No other software package for modal analysis or damage identification has this capability.

The development of DIAMOND was motivated primarily by the lack of graphical implementation of modern damage identification and finite element model refinement algorithms. Also, the desire to have a variety of modal curve-fitting techniques available and the capability to generate numerical data with which to compare the results of each technique was a motivating factor. The authors are unaware of any commercial software package that integrates all of these features.

DIAMOND is divided into four primary modules at the top level: numerical vibration test simulator, experimental modal curve fitting and statistical analysis, damage identification, and finite element model refinement. These four modules constitute the primary hierarchy in DIAMOND, as shown in Figure D-1.

In this appendix an overview of DIAMOND is provided, including an outline of each module (except for the numerical test simulator): experimental modal analysis and statistical analysis of modal data, damage identification, and finite element model updating. In each section, a flowchart of the menu structure of DIAMOND is presented.

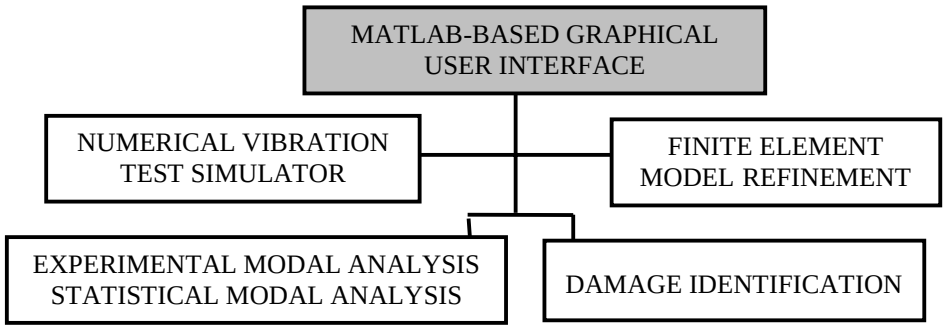

Figure D-1. Flowchart of the top level of DIAMOND.

A. Experimental Modal Analysis / Statistical Analysis of Modal Data

The experimental modal analysis module provides a series of tools for plotting the data in various forms, plotting data indicator functions, defining sensor geometry, performing modal curve fits, and analyzing the results of modal curve fits. Also, it has the ability to analyze the variance of identified modal parameters as a function of the noise in the measurements as defined by the measured coherence function. A flowchart of this module is shown in Figure D-2.

The most important feature of the experimental modal analysis module is the variety of modal parameter identification algorithms which are available. These include:

1. Operating shapes (which is simply “peak picking,” or “slicing” the FRF matrix at a particular frequency bin).

2. Eigensystem Realization Algorithm (ERA), [Juang and Pappa (1985)] which is a low-order time domain modal parameter estimation algorithm.

3. Complex exponential algorithm, which is a high-order time domain modal parameter estimation algorithm. The specific algorithm implemented is the Polyreference Time Domain [Vold, et al. (1982)] approach.

4. Rational Polynomial Curve fit [Richardson and Formenti (1982)], which is a high-order frequency domain technique that uses orthogonal polynomials to estimate the coefficients of a rational polynomial representation of the frequency response function.

5. Nonlinear least squares fit, which uses a Levenberg-Marquardt nonlinear least-squares curve fitting routine [McVerry (1980)] to estimate modal frequencies and modal damping ratios from the unfiltered Fourier spectral responses of a base-excited structure.

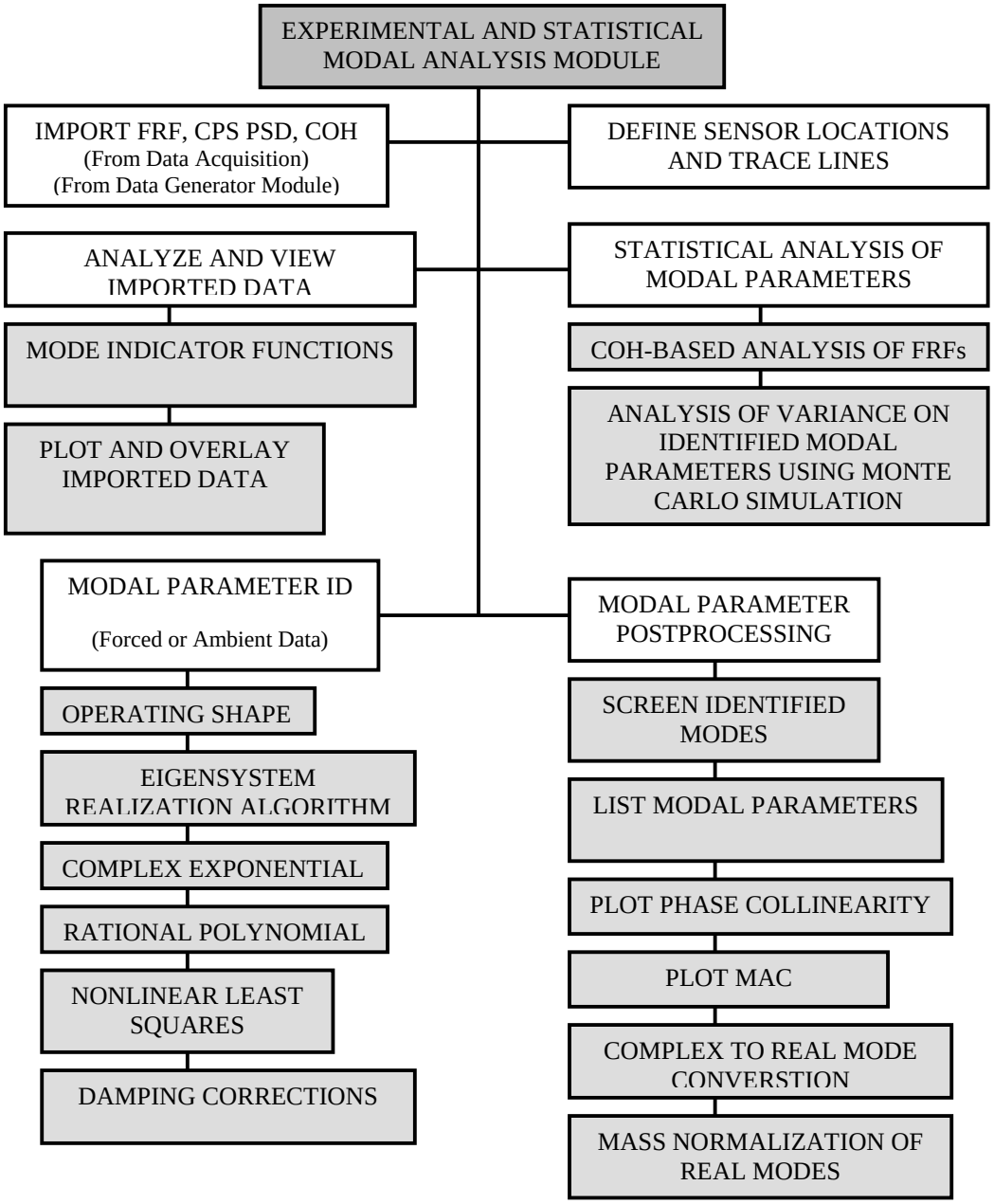

Figure D-2. Flowchart of experimental modal analysis/statistical modal analysis module.

Any of these modal identification algorithms can be implemented in a statistical Monte Carlo [Press (1992)] technique. In such an analysis, a series of perturbed data sets, based on the statistics of the measured FRFs as defined by the measured coherence functions, are generated and propagated through the selected algorithm. The statistics on the results are then used as uncertainty bounds on the identified modal parameters.

B. Damage Identification

The algorithms contained in the damage identification module of DIAMOND can be classified as modal-based, finite element refinement-based, or nonlinear. A flowchart of the damage identification module is shown in Figure D-3.

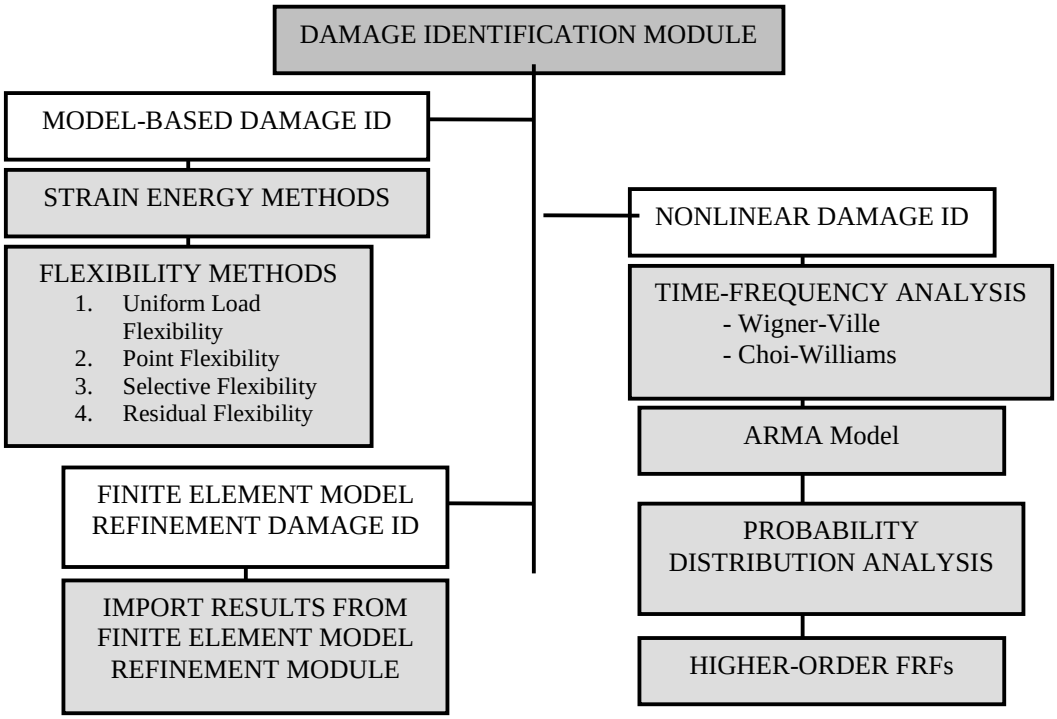

Figure D-3. Flowchart of damage identification module.

The damage identification module presents a number of different algorithms:

1. Strain energy methods are based on the work of Stubbs, Kim and Farrar (1995), Cornwell, Doebling and Farrar (1997), and others. The basic idea of these methods is the division of the structure into a series of beam or plate-like elements, and then the estimation of the strain energy stored in each element both before and after damage. The curvatures (second-derivatives with respect to space) of the mode shapes are used to approximate the strain energy content. A complete discussion of the strain energy method is presented in Appendix E.

2. Flexibility methods all use some measure of the change in the modal flexibility matrix, estimated from the mass-normalized measured mode shapes, [Φ], and modal frequencies squared, [Λ], as

$$[G] \approx [\Phi][\Lambda]^{-1}[\Phi]^{T}. \qquad \text{(D-1)}$$

The modal flexibility matrix is used to estimate the static displacements that the structure would undergo as a result of a specified loading pattern. The uniform load flexibility method [Catbas, et al. (1997)] involves specifying a unit load at all measurement degrees of freedom (DOF), then comparing the change in the resulting displacement pattern before and after damage. The point flexibility method [Robinson, et al. (1996)] specifies the application of a unit load at each measurement DOF one at a time, then looking for a change in the resulting displacements at the same point before and after damage.

The selective flexibility method, which is still under development, uses one of the above two flexibility approaches but filters the modes used to form the flexibility matrix according to their relative statistical uncertainty. The idea of this method is to exclude modes with a high uncertainty from the analysis to avoid biasing the results.

The residual flexibility method [Doebling, Peterson and Alvin (1996)] also uses one of the above two flexibility approaches but includes the estimate of the residual flexibility, which is the contribution to the flexibility matrix from the modes above the bandwidth of interest. The resulting flexibility matrix is a closer approximation to the true static flexibility matrix than is the modal flexibility matrix.

3. Finite element model correlation-based damage identification techniques are based on the comparison of the finite element model correlation results from before damage to those after damage. The correlation techniques are discussed in the next section.

4. Nonlinear damage identification techniques are based on different theories of nonlinear signal processing. They are a widely varying group of methods and are reviewed and discussed in Doebling, et al. (1997).

C. Finite Element Model Refinement

The finite element model refinement module consists of four options: pre-processing for update analysis, optimal matrix updating, sensitivity-based model update, and post-processing of update results. A flowchart of this module is shown in Figure D4.

The preprocessing phase of the model correlation analysis involves the selection of which modal parameters (i.e. modal frequencies and mode shapes) should be used in the correlation, as well as which finite element model parameters should be updated.

The optimal matrix update methods are based on the minimization of the error in the structural eigenproblem using a closed-form, direct solution. The minimum rank perturbation

technique (MRPT) [Zimmerman and Kaouk (1994)] is one such method which produces a minimum-rank perturbation of the structural stiffness, damping, and/or mass matrices reduced to the measurement degrees of freedom. The minimum rank element update (MREU) [Doebling (1996)] is a similar technique which produces perturbations at the elemental, rather than the matrix, level. The Baruch updating technique [Baruch (1982)] minimizes an error function of the eigenequation using a closed-form function of the mass and stiffness matrices.

The sensitivity-based model update methods also seek to minimize the error in the structural eigenequation, but do so using a Newton-Raphson-type technique based on solving for the perturbations such that the gradient of the error function is near zero. Thus these methods require the computation of the sensitivity of the structural eigenproblem to the parameters which are to be updated. The Hemez/Alvin algorithm [Hemez and Farhat (1995), Alvin (1996)] computes the sensitivities at the elemental level, then assembles them to produce the global sensitivity matrices. The Ricles/Kosmatka algorithm [Ricles and Kosmatka (1992)] computes a "hybrid" sensitivity matrix using both analytical and experimental sensitivities.

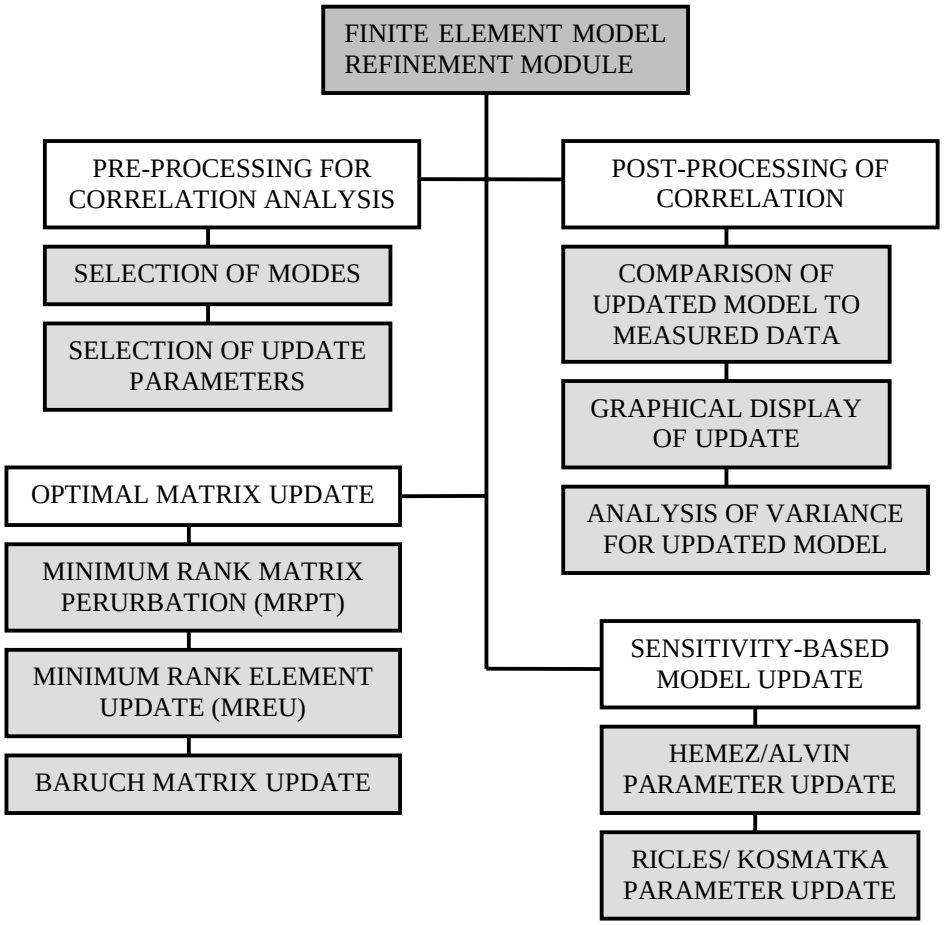

Figure D-4. Flowchart of finite element model refinement module.

APPENDIX E:

THE STRAIN ENERGY DAMAGE DETECTION METHOD

Significant work has been done in the area of detecting damage in structures using changes in the dynamic response of the structure. Because the natural frequencies and mode shapes of a structure are dependent on the mass and stiffness distributions any subsequent changes in them should, theoretically, be reflected in changes in the frequency and mode shapes of the structure. An extensive literature review [Doebling, et al. (1997)] of the state of the art of damage detection and health monitoring from vibration characteristics has recently been published. From this review it is clear that there are a large number of proposed methods of detecting damage from vibration characteristics but, unfortunately, many of these methods require a correlated finite element model and/or mass normalized mode shapes. If the modal properties are obtained using ambient excitation, as would most likely be the case for a remote, automated health monitoring system, then the mode shapes will not be mass normalized. The method discussed in this appendix avoids both of these problems.

In this appendix an extension of a method proposed by Stubbs and Kim (1995) will be presented. This method requires that the mode shapes before and after damage be known, but the modes do not need to be mass normalized and only a few modes are required. The original formulation by Stubbs and Kim was primarily for beam-like structures that are characterized by one-dimensional curvature. The method has been generalized to plate-like structures that are characterized by two-dimensional curvature [Cornwell, Doebling and Farrar (1997)].

The nomenclature used in this appendix is given below.

D	$= Eh^3/12(1-\nu^2)$ = bending stiffness of a plate
EI	Flexural rigidity
F_{ij}	Fractional energy associated with subregion j due to the ith mode
F_{ijk}	Fractional energy associated with subregion jk due to the ith mode
N_d	Number of divisions in beam-like structure
N_x	Number of divisions in the x-direction of a plate-like structure
N_y	Number of divisions in the y-direction of a plate-like structure
U_i	Strain energy associated with the ith mode
U_{ij}	Strain energy associated with subregion j due to the ith mode
U_{ijk}	Strain energy associated with subregion jk due to the ith mode
x, y, z	Translational coordinates
u, v, w	Displacements in x, y and z directions
β_k	Damage index for subregion k
β_{jk}	Damage index for subregion jk
Z_k	Normalized damage index for subregion k
$\bar{\beta}_k$, σ_k	mean and standard deviation of β_k
ψ_i	i^{th} mode shape
( )*	Indicates a quantity calculated using the damaged mode shapes, ψ_i^*

A. Theory

In this section, the derivation of a strain energy damage indicator will be shown for both beam-like and plate-like structures. The derivation for beam-like structures follows that of Stubbs and Kim (1995).

<u>Beam-like structures</u>
The strain energy, U, of a Bernoulli-Euler beam is given by

$$U = \frac{1}{2}\int_0^{\ell} EI\left(\frac{\partial^2 w}{\partial x^2}\right)^2 dx\,. \qquad \text{(E-1)}$$

For a particular mode shape, $\psi_i(x)$, the energy associated with that mode shape is

$$U_i = \frac{1}{2}\int_0^{\ell} EI\left(\frac{\partial^2 \psi_i}{\partial x^2}\right)^2 dx\,. \qquad \text{(E-2)}$$

If the beam is subdivided into N_d divisions as shown in Figure E1, then the energy associated with each sub-region j due to the ith mode is given by

$$U_{ij} = \frac{1}{2}\int_{a_j}^{a_{j+1}} (EI)_j\left(\frac{\partial^2 \psi_i}{\partial x^2}\right)^2 dx\,. \qquad \text{(E-3)}$$

The fractional energy is therefore

$$F_{ij} = \frac{U_{ij}}{U_i} \qquad \text{(E-4)}$$

and

$$\sum_{j=1}^{N_d} F_{ij} = 1\,. \qquad \text{(E-5)}$$

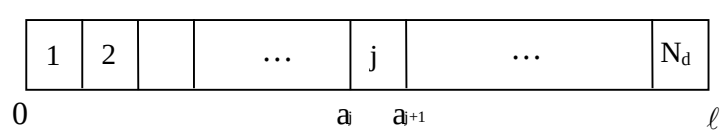

Figure E-1. A schematic illustrating a beam's N_d subdivisions.

Similar quantities can be defined for a damaged structure and are given by Eqs. E-6 to E-9

$$U_i^* = \frac{1}{2}\int_0^{\ell} EI^* \left(\frac{\partial^2 \psi_i^*}{\partial x^2}\right)^2 dx \qquad \text{(E-6)}$$

$$U_{ij}^* = \frac{1}{2}\int_{a_j}^{a_{j+1}} (EI)_j^* \left(\frac{\partial^2 \psi_i^*}{\partial x^2}\right)^2 dx \qquad \text{(E-7)}$$

$$F_{ij}^* = \frac{U_{ij}^*}{U_i^*} \qquad \text{(E-8)}$$

and

$$\sum_{j=1}^{N_d} F_{ij} = \sum_{j=1}^{N_d} F_{ij}^* = 1. \qquad \text{(E-9)}$$

By choosing the subregions to be relatively small, the flexural rigidity for the jth subregion, EI_j is roughly constant and F_{ij}^* becomes

$$F_{ij}^* = \frac{(EI)_j^* \int_{a_j}^{a_{j+1}} \left(\frac{\partial^2 \psi_i^*}{\partial x^2}\right)^2 dx}{U_i^*}. \qquad \text{(E-10)}$$

If we assume that the damage is primarily located at a single subregion then the fractional energy will remain relatively constant in undamaged subregions and $F_{ij}^* = F_{ij}$. For a single damaged location at subregion j = k we find

$$\frac{(EI)_k \int_{a_k}^{a_{k+1}} \left(\frac{\partial^2 \psi_i}{\partial x^2}\right)^2 dx}{U_i} = \frac{(EI)_k^* \int_{a_k}^{a_{k+1}} \left(\frac{\partial^2 \psi_i^*}{\partial x^2}\right)^2 dx}{U_i^*}. \qquad \text{(E-11)}$$

If we assume that EI is essentially constant over the length of the beam for both the undamaged and damaged modes Eq. (E-11) can be rearranged to give an indication of the change in the flexural rigidity of the subregion as shown in Eq. (E-12)

$$\frac{(EI)_k}{(EI)_k^*} = \frac{\int_{a_k}^{a_{k+1}} \left(\frac{\partial^2 \psi_i^*}{\partial x^2}\right)^2 dx \Big/ \int_0^{\ell} \left(\frac{\partial^2 \psi_i^*}{\partial x^2}\right)^2 dx}{\int_{a_k}^{a_{k+1}} \left(\frac{\partial^2 \psi_i}{\partial x^2}\right)^2 dx \Big/ \int_0^{\ell} \left(\frac{\partial^2 \psi_i}{\partial x^2}\right)^2 dx} \equiv \frac{f_{ik}^*}{f_{ik}}. \qquad \text{(E-12)}$$

In order to use all the measured modes, m, in the calculation, the damage index for subregion k is defined to be

$$\beta_k = \frac{\sum_{i=1}^{m} f_{ik}^*}{\sum_{i=1}^{m} f_{ik}}. \qquad \text{(E-13)}$$

One advantage to the formulation shown in Eqs. E-12 and E-13 is that the modes do not need be normalized. Assuming that the collection of the damage indices, β_k, represents a sample population of a normally distributed random variable, a normalized damage index is obtained using Eq. (E-14)

$$Z_k = \frac{\beta_k - \overline{\beta}_k}{\sigma_k} \qquad \text{(E-14)}$$

where $\overline{\beta}_k$ and σ_k represent the mean and standard deviation of the damage indices, respectively. In this paper it will be assumed that normalized damage indices with values greater than two are associated with potential damage locations.

<u>Plate-like structures</u>

The strain energy of a plate is given by Eq. E-15 [Young (1956)].

$$U = \frac{D}{2}\int_0^b\int_0^a \left(\frac{\partial^2 w}{\partial x^2}\right)^2 + \left(\frac{\partial^2 w}{\partial y^2}\right)^2 + 2\nu\left(\frac{\partial^2 w}{\partial x^2}\right)\left(\frac{\partial^2 w}{\partial y^2}\right) + 2(1-\nu)\left(\frac{\partial^2 w}{\partial x \partial y}\right)^2 dxdy. \qquad \text{(E-15)}$$

For a particular mode shape, $\psi_i(x,y)$, the energy associated with that mode shape is

$$U_i = \frac{D}{2}\int_0^b\int_0^a \left(\frac{\partial^2 \psi_i}{\partial x^2}\right)^2 + \left(\frac{\partial^2 \psi_i}{\partial y^2}\right)^2 + 2\nu\left(\frac{\partial^2 \psi_i}{\partial x^2}\right)\left(\frac{\partial^2 \psi_i}{\partial y^2}\right) + 2(1-\nu)\left(\frac{\partial^2 \psi_i}{\partial x \partial y}\right)^2 dxdy. \qquad \text{(E-16)}$$

If the plate is subdivided into N_x subdivisions in the x direction and N_y subdivisions in the y direction as shown in Figure E2 then the energy associated with subregion jk for the ith mode is given by

$$U_{ijk} = \frac{D_{jk}}{2}\int_{b_k}^{b_{k+1}}\int_{a_J}^{a_{j+1}} \left(\frac{\partial^2 \psi_i}{\partial x^2}\right)^2 + \left(\frac{\partial^2 \psi_i}{\partial y^2}\right)^2 + 2\nu\left(\frac{\partial^2 \psi_i}{\partial x^2}\right)\left(\frac{\partial^2 \psi_i}{\partial y^2}\right) + 2(1-\nu)\left(\frac{\partial^2 \psi_i}{\partial x \partial y}\right)^2 dxdy \qquad \text{(E-17)}$$

so

$$U_i = \sum_{k=1}^{N_y}\sum_{j=1}^{N_x} U_{ijk} \qquad \text{(E-18)}$$

and the fractional energy at location jk is defined to be

$$F_{ijk} = \frac{U_{ijk}}{U_i} \tag{E-19}$$

and

$$\sum_{k=1}^{Ny}\sum_{j=1}^{Nx} F_{ijk} = 1. \tag{E-20}$$

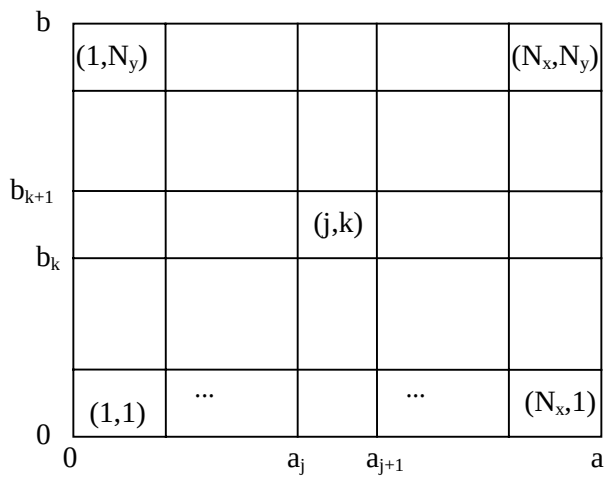

Figure E-2. A schematic illustrating a plate's $N_x \times N_y$ subregions.

Similar expressions can be written using the modes of the damaged structure, ψ_i^*. Using assumptions similar to the ones used for beam-like structures a ratio of parameters can be determined that is indicative of the change of stiffness in the structure as shown in Eqs. E-21 to E-22.

$$\frac{D_{jk}}{D_{jk}^*} = \frac{f_{ijk}^*}{f_{ijk}} \tag{E-21}$$

where

$$f_{ijk} = \frac{\int_{b_k}^{b_{k+1}}\int_{a_J}^{a_{j+1}} \left(\frac{\partial^2\psi_i}{\partial x^2}\right)^2 + \left(\frac{\partial^2\psi_i}{\partial y^2}\right)^2 + 2\nu\left(\frac{\partial^2\psi_i}{\partial x^2}\right)\left(\frac{\partial^2\psi_i}{\partial y^2}\right) + 2(1-\nu)\left(\frac{\partial^2\psi_i}{\partial x\partial y}\right)^2 dxdy}{\int_0^b\int_0^a \left(\frac{\partial^2\psi_i}{\partial x^2}\right)^2 + \left(\frac{\partial^2\psi_i}{\partial y^2}\right)^2 + 2\nu\left(\frac{\partial^2\psi_i}{\partial x^2}\right)\left(\frac{\partial^2\psi_i}{\partial y^2}\right) + 2(1-\nu)\left(\frac{\partial^2\psi_i}{\partial x\partial y}\right)^2 dxdy} \tag{E-22}$$

and an analogous term f_{ijk}^* can be defined using the damaged mode shapes. In order to account for all measured modes, the following formulation for the damage index for subregion jk is used

$$\beta_{jk} = \frac{\sum_{i=1}^{m} f_{ijk}^{*}}{\sum_{i=1}^{m} f_{ijk}} . \qquad \text{(E-23)}$$

Once again a normalized damage index can be found using Eq. (E-14).

B. Application

One of the major difficulties associated with implementing the algorithms discussed in this appendix is the calculation of the derivatives and integrals when the mode shape is known at a relatively small number of discrete locations. In both algorithms additional intermediate points are obtained by curve fitting the data. The derivatives and integrals required by the algorithms are then calculated numerically.

Both algorithms discussed in the theory section can be applied to detect damage in plate-like structures. The algorithm derived assuming plate-like behavior (two-dimensional curvature) can obviously be applied directly. To use the algorithm formulated assuming one-dimensional curvature the structure must be divided into slices and the algorithm needs to be applied to each slice individually. The normalized damage index is then determined using the average and standard deviation of all the damage indices from all the slices. The advantage of this approach is that it is computationally more efficient than the 2-D algorithm. Regardless of the method chosen several additional parameters must be chosen including the number of modes and the number of subdivisions to be used. A comparison of these two strain energy methods on plate-like structures is given in Cornwell, Doebling and Farrar (1997). In this paper the data analyzed was from a finite element model. The strain energy methods were used successfully to identify damage in a beam and plate in Cornwell, et al. (1998).

APPENDIX F:
DATA FILE SUMMARY

This appendix contains a summary of the data files obtained from the Alamosa Canyon Bridge tests that took place in July of 1996 and July of 1997.

Table F-1 Summary of data files from the July 1996 test (ACBT 3)

Filename (No Extension)	Date	Ending Time	Description	Details
dp1	7/30/96	1:44	Recip./Lin. Check	Hammer at DP A (FIG. 33), High Force Level
dp2	7/30/96	2:01	Recip./Lin. Check	Hammer at DP A (FIG. 33), Low Force Level
dp3	7/30/96	2:19	Recip./Lin. Check	Hammer at DP B (FIG. 33), High Force Level
dp4	7/30/96	2:30	Recip./Lin. Check	Hammer at DP B (FIG. 33), Low Force Level
dp5	7/30/96	2:42	Recip./Lin. Check	Hammer at DP B (FIG. 33), High Force Level, DP Accels Switched
sp1_am01	7/31/96	15:45	Ambient Excitation	Sand Trucks? - Ref Channel 2
sp1_am02	7/31/96	15:50	Ambient Excitation	Sand Trucks?
sp1_am03	7/31/96	16:04	Ambient Excitation	Sand Trucks?
sp1_am04	7/31/96	16:12	Ambient Excitation	Sand Trucks?
sp1_am05	7/31/96	16:27	Ambient Excitation	Sand Trucks?
sp1_am06	7/31/96	16:32	Ambient Excitation	Sand Trucks?
sp1_am07	7/31/96	16:40	Ambient Excitation	Sand Trucks?
sp1_am08	8/2/96	16:35	Ambient Excitation	Damage Level 3 - Bad Reference on Channel 2 ?
sp1_am09	8/2/96	20:02	Ambient Excitation	No Damage - Ref. Channel 9
sp1_am10	8/3/96	10:28	Ambient Excitation	Ref. Channel 2
sp1_am11	8/3/96	10:59	Ambient Excitation	Cars Only - Ref. Channel 2
sp1_hm01	7/30/96	4:23	24 Hour Test 1 - Hammer	
sp1_hm02	7/30/96	6:24	24 Hour Test 1 - Hammer	
sp1_hm03	7/30/96	8:14	24 Hour Test 1 - Hammer	
sp1_hm04	7/30/96	10:35		
sp1_hm05	7/30/96	11:48	24 Hour Test 1 - Hammer	Six Cars on Bridge
sp1_hm06	7/30/96	16:41	24 Hour Test 1 - Hammer	
sp1_hm07	7/31/96	9:15	24 Hour Test 2 - Hammer	Moved DAQ Equipment Under Bridge

Continued

Table F-1, continued

Filename (No Extension)	Date	Ending Time	Description	Details
sp1_hm08	7/31/96	11:30	24 Hour Test 2 - Hammer	
sp1_hm09	7/31/96	13:12	24 Hour Test 2 - Hammer	
sp1_hm10	7/31/96	15:13	24 Hour Test 2 - Hammer	
sp1_hm11	7/31/96	17:52	24 Hour Test 2 - Hammer	
sp1_hm12	7/31/96	20:09	24 Hour Test 2 - Hammer	
sp1_hm13	7/31/96	21:20	24 Hour Test 2 - Hammer	
sp1_hm14	7/31/96	23:29	24 Hour Test 2 - Hammer	
sp1_hm15	8/1/96	1:21	24 Hour Test 2 - Hammer	
sp1_hm16	8/1/96	3:19	24 Hour Test 2 - Hammer	
sp1_hm17	8/1/96	5:19	24 Hour Test 2 - Hammer	
sp1_hm18	8/1/96	7:03	24 Hour Test 2 - Hammer	
sp1_hm19	8/1/96	9:22	24 Hour Test 2 - Hammer	
sp1_hm20	8/1/96	9:46	Lateral Hammer Excitation	
sp1_hm21	8/2/96	4:15	Recip./Lin. Check	Hammer at DP A (FIG. 33), Low Force Level
sp1_hm22	8/2/96	4:42	Recip./Lin. Check	Hammer at DP A (FIG. 33), High Force Level
sp1_hm23	8/2/96	5:16	Recip./Lin. Check	Hammer at DP B (FIG. 33), Low Force Level
sp1_hm24	8/2/96	5:40	Recip./Lin. Check	Hammer at DP B (FIG. 33), High Force Level
sp1_hm25	8/2/96	6:12	Recip./Lin. Check	Hammer at DP B (FIG. 33), High Force Level, DP Accels Switched
sp1_hm26	8/2/96	6:46	Damage ID	Undamaged State - Hammer at DP A (FIG. 33)
sp1_hm27	8/2/96	7:57	Damage ID	Damage Level 1 - Hammer at DP A (FIG. 33)

Continued

Table F-1, continued

Filename (No Extension)	Date	Ending Time	Description	Details
sp1_hm28	8/2/96	8:16	Damage ID	Damage Level 1 - Hammer at DP B (FIG. 33)
sp1_hm29	8/2/96	10:28	Damage ID	Damage Level 2 - Hammer at DP B (FIG. 33)
sp1_hm30	8/2/96	10:48	Damage ID	Damage Level 2 - Hammer at DP A (FIG. 33)
sp1_hm31	8/2/96	17:16	Damage ID	Damage Level 3 - Hammer at DP A (FIG. 33)
sp1_hm32	8/2/96	19:05	Damage ID	Restored Undamaged State - 4 Cars on Bridge - Hammer at DP A (FIG. 33)
sp1_hm33	8/3/96	14:46	Multi-Span	Hammer on Span 2 (DP A (FIG. 33))
sp1_hm34	8/3/96	15:16	Multi-Span	Hammer on Span 3 with DP on Span 3 (DP Signal in Question)
sp1_hm35	8/3/96	15:22	Multi-Span	Retake of 5 avgs on Span 3 (for Good DP Signal)
sp1_hm36	8/3/96	15:42	Multi-Span	Hammer on Span 6 with DP on Span 6

Table F- 2 Summary of Data Files from the July 1997 Test (ACBT 4)

Test Name	Brief Description	# of Files	Driving Point (Fig. 33)	Number of Channels	Reference Channel (Fig. 33)	Other comments
time 1	24 hr test	30	A	32	32	Time – 0400
time 2	24 hr test	30	A	32	32	Time – 0600
time 3	24 hr test	30	A	32	32	Time – 0800
time 4	24 hr test	30	A	32	32	Time – 1000
time 5	24 hr test	30	A	32	32	Time – 1200
time 6	24 hr test	30	A	32	32	Time – 1400 Channels 1–8 and 17–24 were switched. They were backwards for tests time 1–time 5.
time 7	24 hr test	30	A	32	32	Time – 1600
time 8	24 hr test	30	A	32	32	Time – 1800
time 9	24 hr test	30	A	32	32	Time – 2000
time 10	24 hr test	30	A	32	32	Time – 2200
time 11	24 hr test	30	A	32	32	Time – 2400
mref2	multiple reference	10	3	32	32	
mref3	multiple reference	10	28	32	32	
mref4	multiple reference	10	11	32	32	
RS1	random 30 lb shaker	10	8	32	32	This data was inaccurate due to a faulty signal from the shaker.
RS2	random 30 lb shaker	10	8	32	32	Ch. 32 was a direct signal from the shaker.
RS3	random 30 lb shaker	10	3	32	32	
RS4	random 30 lb shaker	10	11	32	32	
RS5	random 30 lb shaker	10	28	32	32	
RS6	random 100 lb shaker	10	28	32	32	
RS7	random 100 lb shaker	10	11	32	32	
RS8	random 100 lb shaker	10	8	32	32	
RS9	random 100 lb shaker	10	8	32	32	
A1	ambient test	30	arm	31	8	Excitation source was trucks on adjacent bridge

Continued

Table F-2, continued

Test Name	Brief Description	# of Files	Driving Point (Fig. 33)	Number of Channels	Reference Channel (Fig. 33)	Other comments
Stiff	Stiffness test	30	A	32	32	Steel plate along with 6 C-clamps placed near accelerometer 13
Lat 1	lateral shaker #1	1	28	32	32	10 sets of data were averaged for each lateral shaker case. This data set was thought to be bad because the reference channel was the accelerometer on the shaker which had an unknown calibration factor.
speed 0	lateral shaker #2	1	28	31	8	Pt. 8 was made the reference point and channel 32 is ignored 1 Hz
speed 1	lateral shaker #3	1	28	31	8	speed 1.875 Hz
speed 2	lateral shaker #4	1	28	31	8	speed 2.94 Hz
speed 3	lateral shaker #5	1	28	31	8	speed 3.265 Hz
speed 4	lateral shaker #6	1	28	31	8	speed 5.25 Hz
speed 5	lateral shaker #7	1	28	31	8	speed 5.6875 Hz

REFERENCES

Abdel-Ghaffar, A. M. and G. W. Housner (1978), "Ambient Vibration Tests of a Suspension Bridge," *ASCE Journal of the Engineering Mechanics Division*, **104**, 983–999.

Allemang, R. J. (1995), *Vibrations: Experimental Modal Analysis Course Notes*, UC-SDRL-CN-20-263-663/664, University of Cincinnati.

Alvin, K. F. (1995), "Robust Model Error Localization for Damage Detection and Finite Element Model Update," *Proc. of the Sixth International Conference on Adaptive Structures* (Lancaster, Penn.: Technomic), pp. 305–315.

Alvin, K. F. (1996), "Finite Element Model Update via Bayesian Estimation and Minimization of Dynamic Residuals," *Proc. of the 14th International Modal Analysis Conference*, Dearborn, MI (Bethel, Conn., USA: Society for Experimental Mechanics), pp. 561–567.

Baruch, M. (1982), "Optimal Correction of Mass and Stiffness Matrices Using Measured Modes," *AIAA Journal*, **20** (11), 1623–1626.

Bendat, J. S. and A. G. Piersol (1980), *Engineering Applications of Correlation and Spectral Analysis* (John Wiley & Sons, New York), Chapters 7, 8, and 11.

Catbas, F. N., M. Lenett, D. L. Brown, S. W. Doebling, C. R. Farrar, and A. Turer (1997), "Modal Analysis of Multi-Reference Impact Test Data for Steel Stringer Bridges," *Proc. of the 15th International Modal Analysis Conference*, Orlando, FL, (Bethel, Conn., USA: Society for Experimental Mechanics), pp. 381–391.

Cornwell, P. J., S. W. Doebling and C. R. Farrar (1997), "Application of the Strain Energy Damage Detection Method to Plate-like Structures," *Proc. 15th International Modal Analysis Conference*, Orlando, FL (Bethel, Conn., USA: Society for Experimental Mechanics).

Cornwell, P. J., M. Kam, B. Carlson, B. Hoerst, S. W. Doebling, and C. R. Farrar (1998), "Comparative Study of Vibration-based Damage ID Algorithms," *Proc. of 16th International Modal Analysis Conference*, Santa Barbara, CA, (Bethel, Conn., USA: Society for Experimental Mechanics), pp.1710–1716.

Doebling, S. W. (1996), "Minimum-Rank Optimal Update of Elemental Stiffness Parameters for Structural Damage Identification," *AIAA Journal* **34** (12), 2615–2621.

Doebling, S. W., L. D. Peterson, and K. F. Alvin (1996), "Estimation of Reciprocal Residual Flexibility from Experimental Modal Data," *AIAA Journal* **34** (8), 1678–1685.

Doebling, S. W. and C. R. Farrar (1997) "A Monte Carlo-based Technique for Determination of Statistical Uncertainty on Identified Modal Parameters," Los Alamos National Laboratory document LA-UR-97-1920 (submitted to *Journal of Vibration and Control*).

Doebling, S. W., C. R. Farrar and R. S. Goodman (1997), "Effects of Measurement Statistics on Detection of Damage in the Alamosa Canyon Bridge," *Proceedings of the 15th International Modal Analysis Conference*, Orlando, FL (Bethel, Conn., USA: Society for Experimental Mechanics), pp. 912–929.

Doebling, S. W., C. R. Farrar, M. B. Prime, and D. W. Shevitz (1997), "Damage Identification and Health Monitoring of Structural and Mechanical Systems from Changes in Their Vibration Characteristics: A Literature Review," Los Alamos National Laboratory report LA-13070-MS.

Doebling, S. W. and C. R. Farrar (1998), "Statistical Damage Identification Techniques Applied to the I-40 Bridge Over the Rio Grande River," *Proceedings of the 16th International Modal Analysis Conference*, Santa Barbara, CA. (Bethel, Conn., USA: Society for Experimental Mechanics), pp. 1717–1724.

Doherty, J. E. (1987) "Nondestructive Evaluation," in *Handbook on Experimental Mechanics*, A. S. Kobayashi, Ed. (Society for Experimental Mechanics, Prentice-Hall, Englewood Cliffs, N. J.), Chapter 12.

Efron, B. and R. J, Tibshirani (1993) *An Introduction to the Bootstrap (Monographs on Statistics and Applied Probability, No. 57)* (Chapman & Hall, New York), Chapter 13.

Ewins, D. J. (1985) *Modal Testing: Theory and Practice* (Research Studies Press Ltd., Taunton, Somerset, England).

Farrar, C. R., W. E. Baker, T. M. Bell, K. M. Cone, T. W. Darling, T. A. Duffey, A. Eklund, and A. Migliori (1994), "Dynamic Characterization and Damage Detection in the I-40 Bridge Over the Rio Grande," Los Alamos National Laboratory report LA-12767-MS.

Farrar, C. R. and D. V. Jauregui (1996) "Damage Detection Algorithms Applied to Experimental and Numerical Modal Data From the I-40 Bridge," Los Alamos National Laboratory report LA–13074–MS.

Farrar, C. R. and G. H. James (1997) "System Identification from Ambient Vibration Measurements on Bridges," *J. of Sound and Vibration* **205** (1), 1–18.

Farrar, C. R., S. W. Doebling, P. J. Cornwell, and E. G. Straser (1997) "Variability of Modal Parameters Measured on the Alamosa Canyon Bridge," *Proc. of the 15th International Modal Analysis Conference*, Orlando, FL (Bethel, Conn., USA: Society for Experimental Mechanics), pp. 257–263.

Farrar, C. R., S. W. Doebling and P. J. Cornwell (1998) "A Comparison of Modal Confidence Interval Using the Monte Carlo and Bootstrap Techniques," *Proc. of the 16th International Modal Analysis Conf.*, Santa Barbara, CA (Bethel, Conn., USA: Society for Experimental Mechanics), pp. 936–944.

Freund, J. (1992) *Mathematical Statistics, 5th ed.* (Prentice-Hall, Englewood Cliffs, N.J), p. 462.

Hemez, F. M. and C. Farhat (1995) “Structural Damage Detection via a Finite Element Model Updating Methodology,” *Modal Analysis: The International Journal of Analytical and Experimental Modal Analysis* **10** (3), 152–166.

James, G. H., T. G. Carne, and J. P. Lauffer (1995) “The Natural Excitation Technique (NExT) for Modal Parameter Extraction from Operating Structures,” *The International Journal of Analytical and Experimental Modal Analysis* **10** (4), 260–277.

James, G., R. Mayes, T. Carne, and G. Reese, (1994) “Damage Detection and Health Monitoring of Operational Structures,” *1994 International Mechanical Engineering Congress and Exposition*, Chicago, IL. (American Society of Mechanical Engineers, Aerospace Division, New York: NY).

Jauregui, D. V. and C. R. Farrar, (1996) “Damage Identification Algorithms Applied to Numerical Modal Data from a Bridge,” in *Proc. 14th International Modal Analysis Conference*, (Bethel, Conn., USA: Society for Experimental Mechanics), pp. 119–125.

Jauregui, D. V. and C. R. Farrar (1996) “Comparison of Damage Identification Algorithms on Experimental Modal Data from a Bridge,” in *Proc. 14th International Modal Analysis Conference* (Bethel, Conn., USA: Society for Experimental Mechanics), 1423–1429.

Juang, J. N. and R. S. Pappa, (1985) “An Eigensystem Realization Algorithm for Modal Parameter Identification and Model Reduction,” *Journal of Guidance, Control and Dynamics* **8** (5), 620–627.

Juang. J. N., and R. S. Pappa (1986) “Effects of Noise on Modal Parameters Identified by the Eigensystem Realization Algorithm,” *Journal of Guidance, Control and Dynamics* **9** (3), 294–303.

Juang, J. N. (1987) “Mathematical Correlation of Modal-Parameter-Identification Methods via System Realization Theory,” *International Journal of Analytical and Experimental Modal Analysis* **2** (1).

Kong, F., L. Zhong, and G. Lee (1996) “Responses of a Model Bridge Under Impact and Ambient Excitation,” *Proceedings of the 14th International Modal Analysis Conference*, Detroit, MI. (Bethel, Conn., USA: Society for Experimental Mechanics), pp. 709–716.

Maia, N., and J. Silva, Eds. (1997) *Theoretical and Experimental Modal Analysis* (Research Studies Press Ltd., Taunton, Somerset, England), Chapter 4.

MATLAB, Users Manual, The Mathworks, Inc. (1994).

Mayes, R. (1995) “An Experimental Algorithm for Detecting Damage Applied to the I-40 Bridge over the Rio Grande,” in *Proc. of the 13th International Modal Analysis Conference*, Nashville, TN. (Bethel, Conn., USA: Society for Experimental Mechanics), pp. 219–225.

Mazurek, D. F. (1997) "Modal Sensitivity to Damage in Multigirder Bridges," in *Proc. of 15th International Modal Analysis Conference*, Orlando, FL (Bethel, Conn., USA: Society for Experimental Mechanics), pp. 1892–1898.

McConnell, K. G. (1995) *Vibration Testing: Theory and Practice* (John Wiley and Sons, Inc., New York), Chapter 5.

McLamore, V. R., R. C. Hart and I. R. Stubbs (1971) "Ambient Vibration of Two Suspension Bridges," *Journal of Structural Division, ASCE* **97**, 2567–2582.

McVerry, H. H. (1980) "Structural Identification in the Frequency Domain from Earthquake Records," *Earthquake Engineering and Structural Dynamics* **8**, 161–180.

Pappa, R. S., K. B. Elliott, and A. Schenk (1993) "Consistent-Mode Indicator for the Eigensystem Realization Algorithm," *Journal of Guidance and Control* **16** (5), 852–858 (Sept.-Oct. 1993).

Press, W. H., S. A. Teukolsky, W. T. Vetterling, and B. P. Flannery (1992), *Numerical Recipes in FORTRAN*, 2nd ed. (Cambridge University Press), pp. 605–607, 684–686.

Richardson, M. H., and D. L. Formenti (1982) "Parameter Estimation from Frequency Response Measurements using Rational Fraction Polynomials," *Proceedings of the 1st International Modal Analysis Conference*, Orlando, FL (Bethel, Conn., USA: Society for Experimental Mechanics.), pp. 167–181.

Richardson, M. H., and D. L. Formenti (1982) "Global Curve-Fitting of Frequency Response Measurements using the Rational Fraction Polynomial Method," *Proceedings of the 3rd International Modal Analysis Conference*, Orlando, FL (Bethel, Conn., USA: Society for Experimental Mechanics), pp. 390–397.

Richardson, M. H. (1986) "Global Frequency and Damping Estimates from Frequency Response Measurements," *Proceedings of the 4th International Modal Analysis Conference*, Los Angeles, CA (Bethel, Conn., USA: Society for Experimental Mechanics), pp. 465–470.

Ricles, J. M. and J. B. Kosmatka (1992) "Damage Detection in Elastic Structures Using Vibratory Residual Forces and Weighted Sensitivity," *AIAA Journal* **30**, 2310–2316.

Robinson, N. A., L. D. Peterson, G. H. James, and S. W. Doebling (1996) "Damage Detection in Aircraft Structures Using Dynamically Measured Static Flexibility Matrices," in *Proc. of 14th International Modal Analysis Conference*, Dearborn, MI. (Bethel, Conn., USA: Society for Experimental Mechanics), pp. 857–865.

Simmermacher, T., D. Zimmerman, R. Mayes, G. Reese, and G. James (1995) "The Effects of Finite Element Grid Density on Model Correlation and Damage Detection of a Bridge," *Proceedings of the 1995 AIAA Adaptive Structures Forum*, New Orleans, LA (American Institute of Aeronautics and Astronautics, New York, N.Y.), pp. 2249–22.58.

Simmermacher, T. (1996) "Damage Detection and Model Refinement of Coupled Structural Systems," Ph.D. Dissertation, University of Houston, Houston, TX.

Straser, E. G. (1998) "A Modular, Wireless Damage Monitoring System for Structures," Ph.D. Dissertation, Stanford University.

Structural Measurement Systems, *Modal 3.0 Operating Manual*, San Jose, 1987.

Stubbs, N., J. T. Kim, and C. R. Farrar (1995) "Field Verification of a Nondestructive Damage Localization and Severity Estimation Algorithm," *Proc. 13th International Modal Analysis Conference*, Nashville, TN (Bethel, Conn., USA: Society for Experimental Mechanics), pp. 210–218.

Toksoy, T. and A. E. Aktan (1994) "Bridge-condition Assessment by Modal Flexibility," *Experimental Mechanics* **34**, 271–278.

Vold, H. and G. F. Rocklin (1982) "The Numerical Implementation of a Multi-Input Modal Estimation Method for Mini-Computers," *Proc. 1st International Modal Analysis Conference*, Kissimmee, FL **(**Bethel, Conn., USA: Society for Experimental Mechanics), pp. 542–548.

Vold, H., J. Kundrat, T. Rocklin, R. Russell (1982) "A Multi-Input Modal Estimation Algorithm for Mini-Computers," *SAE Transactions* **91** (1), 815–821.

White, K. R., J. Minor, and K. N. Derucher (1992) *Bridge Maintenance, Inspection and Evaluation* (Marcel Dekker, New York).

Young, D. (1956) "Vibration of Rectangular Plates by the Ritz Method," *Journal of Applied Mechanics*, December, 448–453.

Zimmerman, D. C. and M. Kaouk, (1994) "Structural Damage Detection Using a Minimum Rank Update Theory," *Journal of Vibration and Acoustics* **116**, 222–230.

Zimmerman, D. C., T. Simmermacher, and M. Kaouk (1995) "Model Correlation and System Health Monitoring Using Frequency Domain Measurement," *Proceedings AIAA/ASME Adaptive Structure Forum*, New Orleans, LA (American Institute of Aeronautics and Astronautics, New York, NY.), pp. 3318–3326.

DISTRIBUTION

Masato Abe
University of Tokyo
Dept. of Civil Engineering
Hongo 7-3-1, Bunkyo-ku
Tokyo 113-8656
Japan

Emin Aktan
Drexel University
3201 Arch Street, Suite 240
Philadelphia, PA 19104

Sreenivas Alampalli
New York Dept. of Transportation
1220 Washington Ave.
Albany, NY 12232

Ken Alvin
Sandia National Laboratories
M/S 0439
Albuquerque, NM 87185-5800

Grahem C. Archer
School of Civil Engineering
1284 Civil Engineering Building
Purdue University
West Lafayette, IN 47907-1284

Alejandro Asfura
EQE, Inc.
44 Montgomery St., Suite 3200
San Francisco, CA 94104

Bill Baker
Los Alamos National Laboratory
ESA-EA, MS P946
P.O. Box 1663
Los Alamos, NM 87545

Doo Byong Bae
Dept. of Civil and Environmental Eng.
Kookmin University
861-1 Chongnung-dong Songbuk-gu
Seoul,136-702, Korea

Luciana Barroso
CE/TTI Building, Room 705-L
Department of Civil Engineering
Texas A&M University
College Station, TX 77845

Jim Beck
Applied Mechanics and Civil Engineering
Caltech 104-44
Pasadena, CA 91125

Mrinmay Biswas
Duke University
Dept. of Civil Engineering
Durham, NC 27706

Christian Boller
Daimler Chrysler Aerospace
Munich, D-81663
Germany

Rune Brinker
Department of Building Technology and
Structural Engineering
Aalborg University
Sohngaardsholmsvej 57, DK-9000
Aalborg, Denmark

Janice Brandon
University of South Hampton
Dept. of Ship Science
South Hampton SO17 1BJ
UK

James M. W. Brownjohn
Nanyang Technological University
School of Civil and Structural Engineering
Nanyang Avenue, Singapore 639798

Bob Burick
Granite Construction Co.
Heavy Construction Division
Box 50024
Watsonville, CA 95077-5024

Thomas Burton
Dept. of Mech. Engineering
Texas Tech Univeristy
Lubbock, TX 79409-1021

R. Cantieni
Uberlandstrasse 129
Dubendorf, CH-8600 Switzerland

Eric Canuteson
Kinemetrics Inc.
222 Vista Ave.
Pasadena, CA 91107

Tom Carne
Dept. 2741
Sandia National Laboratory
Albuquerque, NM 87185-5800

Peter Cawley
Dept. of Mechanical Engineering
Imperial College
Exhibition Rd
London, SW7 2BX
UK

Fu-Kuo Chang
Dept. of Aeronautics and Astronautics
Stanford University
Stanford, CA 94305

Sung-Pil Chang
Dept. of Civil Engineering
Seoul National University
Shilimdong, Kwanaku,
Seoul, Korea 151-742

Tse-Yung Chang
Hong Kong University of Science and Technology
Civil Engineering
Clear Water Bay
Kowloon, Hong Kong

Steve Chase
Federal Highway Administration
6300 Georgetown Pike
McLean, VA 22101-2296

Franklin Cheng
University of Missouri Rolla
Dept. of Civil Eng.
Rolla, MO 65401

Eu Kyeung Cho
Hyundai Engineering & Construction Co. Ltd.
San1-1, Mabuk-Ri, Goosung-Myun,Yongin-Si
Kyunggi-Do, Korea, 449-910

Chang Keun Choi
Dep. of Civil Engineering
Korean Institute of Advanced Science and Technology
373-1, Kusong-dong, Yusong-gu,
Taejon, Korea, 305-701

Ken Chong
National Science Foundation
4201 Wilson Blvd., Rm. 545
Arlington, VA 22230

Anil K. Chopra
Earthquake Engineering Research Center
University of California
1301 South 46th St.
Richmond, CA 94804

Lowell Cogburn
Assocation of American Railroads
P.O. Box 11130
Pueblo, CO 81001

Jerry Conner
Room 1-290
Massachusetts Institute of Technology
77 Massachusetts Avenue
Cambridge, MA 02139

Joel Conte
Dept. of Civil and Environmental Engineering
5731 G Boelter Hall
UCLA
Box 951593
Los Angeles, CA 90095-1593

Roy R. Craig, Jr.
University of Texas at Austin
Aerospace Engineering and Engineering
Mechanics Dept., Mail Code C0600
Austin, TX 78712-1085.

Barry Davidson
Compusoft Engineering Ltd.
PO Box 9493
Newmarket, Auckland
New Zealand

Shirley Dyke
Washington University
One Brookings Hall 1130
St. Louis, MO 63130

Dave Ewins
Imperial College
Mechanical Engineering Dept.
Exhibition Road
London SW7 2BX
UK

Gregory L. Fenves
Department of Civil and Environmental
Engineering, MC 1710
University of California
Berkeley, CA 94720-1710

M. Ferner
Anlauf Ingenicur—Consulting GMBH
Posttach 101259
D-69002 Heidelberg, Germany

Mike Friswell
Dept. of Mechanical Engineering
University of Wales, Swansea
Singleton Park
Swansea, SA2 8PP
UK

Claus-Peter Fritzen
Institute of Mechanics and Automatic
Control
University of Siegen
Paul-Bonatz-Str. 9-11
D-57068 Siegen
Germany

Gongkang Fu
New York State Dept. of Transportation
1220 Washington Ave.
Albany, NY 12232

Chris Gannon
Penguin Engineering Ltd
PO Box 33 093
Petone
New Zealand

Ephrahim Garcia
DARPA
Dense Science Office
3701 N. Fairfax Dr.
Arlington, VA 22203-1714

Luigi Garibaldi
Dipartimento di Meccanica
Politecnico di Torino
Corso Duca degli Abruzzi, 24
10129 Torino
Italy

Lothar Gaul
Institut A fur Mechanik
Universitat Stuttgart
Pfaffenwaldring 9
70550 Stuttgart
Germany

Michael Grygier
NASA Johnson Space Center
ES43
Houston, TX 77058

Alfredo Guemes
UPM
ETSI Aeronautics
Madrid, 28016
Spain

Joe Hammond
Institute of Sound and Vibration Research
University of South Hampton
SO17 1BJ
South Hampton, UK

Kurt S. Hansen
Dept. of Energy Engineering
Technical University of Denmark
Building 404, DTU
DK 2800 Lyngby
Denmark

Nicholas Haritos
Dept. of Civil and Environment Eng.
University of Melbourne
Parkville, Victoria 3052
Australia

Phil Hashimoto
EQE Engineering, Inc.
Lakeshore Towers
18101 Von Karman Ave., Suite 400
Irvine, CA 92715

Dan Inman
Virginia Polytechnic Institute of State Univ.
310 New Engineering Building
Mail code 0261
Blacksburg, Va 24061-0219

Jim Johnson
EQE, Inc.
44 Montgomery St., Suite 3200
San Francisco, CA 94104

Daniel C. Kammer
University of Wisconsin-Madison
Dept. of Engr. Mechanics and Astronautics
3352 Engr. Hall, 1415 Johnson Drive
Madison, WI 53706

Tom Kashanganki
University of Maryland
SMART Materials and Structures Res. Center
College Park, MD 20742

Robert Kennedy
18971 Villa Terrace
Yorba Linda, CA 92686

Klaus Kerkhoff
Staatliche Materialprufungsanstalt
Universitat Stuttgart
D-70569 Stuttgart (Vailhingen)
Germany

Magdi Khalifa
University of Nebraska Lincoln
Civil Engineering Department
W348 Nebraska Hall
Lincoln, NE 68588-0531

Chul Young Kim
Dept. of Civil & Environmental Engineering
Myong Ji University
San 38-2, Nam-dong, Yongin-si
Kyunggi-do, 449-728, Korea

Hyoung-Man Kim
McDonnell Douglas Aerospace
M/S: MDC-2-3353
13100 Space Center Blvd
Houston, TX 77059

Jae Kwan Kim
Dept. of Civil Engineering
Seoul National University
Shilimdong, Kwanaku,
Seoul, Korea 151-742

Nam Sik Kim
Hyundai Engineering & Construction Co. Ltd.
San1-1, Mabuk-Ri, Goosung-Myun,Yongin-Si
Kyunggi-Do, Korea, 449-910

Anne Kiremidjian
Stanford University
Department of Engineering
Terman Engineering Center 238
Stanford, CA 94305-4020

Poul Henning Kirkegaard
Department of Building Technology and
Structural Engineering
Aalborg University
Sohngaardsholmsvej 57, DK-9000
Aalborg, Denmark

Hyun Moo Koh
Dept. of Civil Engineering
Seoul National University
Shilimdong, Kwanaku,
Seoul, Korea 151-742

Richard Kohoutek
University of Wollongong
Dept. of Civil and Mining Engineering
Northfields Avenue
Wollongong 2522, Australia

John Kosmatka
University of California
Department of AMES
San Diego, CA 92093-0085

Christian Kot
Argonne National Laboratory
9700 South Cass Ave. RE/331
Argonne, IL 60439-4817

Everett Y. Kuo
Ford Research Laboratory
P.O. Box 2053/MD2122
Dearborn, MI 48121

Kincho Law
Dept. of Civil Engineering
Stanford University
Stanford, CA 94305-4020

George Lee
Multidisciplinary Center for Earthquake
Engineering Research
SUNY at Buffalo
Red Jacket Quadrangle
Buffalo, NY 14261-0025

H. S. Lew
NIST
Bldg. 226 , Rm B168
Gaithersburg, MD 20899

Brett Lewis
APTEK, Inc.
1257 Lake Plaza Dr.
Colorado Springs, CO 80906

Zhong Liang
University of Buffalo
Dept. of Mechanical and Aerospace Eng.
141 Ketter Hall
Buffalo, NY 14260

Nick Lieven
Dept. of Aerospacce Engineering
University of Bristol, Queen’s Bldg.
Bristol, BS8 1TR, UK

Tae W. Lim
University of Kansas
Dept. of Aerospace Engineering
2004 Learned Hall
Lawrence, KS 66045

Michael Link
Universitat Gesamthochschule Kassal
Fachbereich 14
Bauingenienurwesen, Fachgebiet
Leichtbau
Monchebergstr. 7
D-34109 Kassal
Germany

Shih-Chi Liu
National Science Foundation
4201 Wilson Blvd.
Arlington, VA 22230

Richard Livingston
Federal Highway Administration
6300 Georgretown Pike, HRD1-12
McLean, Va 22101

Nuno Maia
IDME/IST
Av. Rovisco Pais
1096 Lisboa Codex
Portugal

Dave Martinez
Sandia National Laboratories
M/S 0439
Albuquerque, NM 87185-5800

Sami Masri
University of Southern California
Department of Civil Engineering
MC 2531
Los Angeles, CA 90089-2531

Randy Mayes
Sandia National Laboratories
MS0557
PO Box 5800
Albuquerque, NM 87185

David McCallen
Center for Complex Distributed Systems
Lawrence Livermore National Laboratory
Livermore, CA 94550

Ken McConnell
Iowa State University
3017 Black Eng. Bldg.
Ames, Iowa 50011

Akira Mita
Shimizu Corporation
3-4-17 Etchujima, Koto-ku
Tokyo, 135-8530
Japan

Jack Moehle
University of California
Department of Civil Engineering
775 Davis Hall
Berkeley, CA 94720

Julio M. Montalvao e Silva
IDME/IST
Av. Rovisco Pais
1096 Lisboa Codex
Portugal

Denby Morrison
Shell E&P Technology Company
Ocean R&D, Bellarie Technology Center
P.O. Box 481
Houston, TX 7700

Peter Moss
University of Canterbury
Department of Civil Engineering
Private Bag 4800
Christchurch, New Zealand

John Mottershead
Dept. of Engineering
Brownlow Hill
University of Liverpool
Liverpool, L69 3GH
UK

Robert Murray
Lawrence Livermore National Laboratory
P.O. Box 808, L-197
Livermore, CA 94550

H.G. Natke
Universtat Hannover
Applestrabe 9A
D-30167 Hannover
Germany

Robert Nigbor
Department of Civil Engineering
University of Southern California
Los Angeles, CA 90089-2531

Ozden O. Ochoa
Offshore Technology Research Center
1200 Mariner Dr.
Texas A&M University
College Station, TX 77845

Roberto Osegueda
The University of Texas at El Paso
Department of Civil Engineering
El Paso, TX 79912

Richard Pappa
NASA Langley Research Center
MS 230
Hampton, VA 23681

Gerard Pardoen
University of California-Irvine
101 ICEF-Civil Eng.
Irvine, CA 92717

K. C. Park
Center for Aerospace Structures
University of Colorado, Boulder
Campus Box 429
Boulder, CO 80309-0429

Bruno Piombo
Departimento di Meccanica
Politecnico di Torino
Corso Duca degli Abruzzi, 24
I - 10129 Torino, Italy

Lee Peterson
Center for Aerospace Structures
University of Colorado, Boulder
Campus Box 429
Boulder, CO 80309-0429

Darryll J. Pines
Dept. of Aerospace Engineering
Room 3154 Engineering Classroom Bldg
University of Maryland
College Park, MD 20742

Bob Randall
School of Mechanical/Manufacturing Engineering
University of New South Wales
Sydney 2052, Australia

John Reed
Jack Benjamin & Associates
Mountain Bay Plaza
444 Castro St. Suite 501
Mountain View, CA 94041

Mark Richardson
Vibrant Technology, Inc.
18141 Main Street
Jamestown, CA 95327

Jim Ricles
Lehigh University
Department of Civil Engineering
117 ATLSS Drive, H Building
Bethlehem, PA 18015-4729

David Robert
Litton Laser Systems / CLS Operations
5 Jeffrey Drive
South Windsor, CT 06074

John Ruminer
Los Alamos National Laboratory
DDESA, MS P945
P.O. Box 1663
Los Alamos, NM 87545

Romualdo Ruotolo
Dip. Ingegneria Aeronautica e Spaziale
Politecnico di Torino
10100 Torino
Italy

Anders Rytter
RAMBOLL
Kjaerulfsgade 2
DK-9400 Norresundby
Denmark

Erdal Safak
U.S. Geological Survey
DFC, Box 25046, MS.966
Denver, CO 80225

M. Saiidi
College of Engineering
Department of Civil Eng./258
Reno, NV 89557-0152

Masoud Sanayei
Tufts University
Dept. of Civil and Env. Engineering
Lexington, MA 02173

Jose Maria Campos dos Santos
UNICAMP
Caixa Postal 6122
13083-970 Campinas, SP
Brazil

Paul Sas
Katholieke Universiteit Leuven
Mechanical Engineering Dept.
Celestijnenlaan 300B
B-3001 Herverlee
Belgium

John F. Schultze
Mechanical Engineering and Engineering Mechanics Dept.
815 R. L. Smith ME-EM Building
1400 Townsend Dr.
Houghton, MI 49931-1295

Bob Shumway
Division of Statistics
Univ. of California, Davis
Davis, CA 95616

Suzanne Smith
University of Kentucky
Department of Engineering Mechanics
467 Anderson Hall
Lexington, KY 40506-0046

Cecily Sobey
Earthquake Engineering Research Center Library
Gift & Exchange Dept.
University of California/RFS 453
1306 South 46th Street
Richmond, CA 94804-4698

Norris Stubbs
Texas A&M University
Department of Civil Engineering
Mechanics & Materials Center
College Station, TX 77843-3136

Fred Tasker
Dept. of Mechanical Engineering
University of Maryland Baltimore County
Baltimore, MD 21228-5398

Mike Todd
Naval Research Laboratory
Optical Sciences Division
Code 5673
4555 Overlook Ave. SW
Washington D.C. 20375

Pavel Trivailo
RMIT University
226 Lorimer St.
Fishermen's Bend 3207 Victoria
GPO Box 2476V
Melbourne 3001 Victoria Australia

Geoff Tomlinson
The University of Sheffield
Department of Mechanical and Process Engineering
PO Box 600
Mappin St
Sheffield S1 4DU
UK

Ward Turner
Exxon Production Research Company
P.O. Box 2189
Houston, TX 77252

Herman Van Der Auweraer
LMS International
Interleuvenlaan 68
B-3001 Leuven, Heverlee
Belgium

C. E. Ventura
The University of British Columbia
Dept. of Civil Engineering
2324 Main Mall
Vancouver, B.C.
Canada, V6T 1Z4

Sara Wadia-Fascetti
Northeastern University
Dept. of Civil Engineering
443 Snell Engineering Center
Boston, MA 02115

Gunnar Wang
Norwegian Defense Research Est.
P.O. Box 25
N-2007 Kjeller, Norway

Ming Wang
Dept. of Civil and Material Engineering (M/C 246)
College of Engineering
842 West Taylor St.
Chicago, Illinois 60607-7023

Lloyd Welker, Jr.
Ohio Department of Transportation
25 South Front Street
Columbus, OH 43216-0899

Robert West, Jr.
Virginia Polytechnic Institute of State Univ.
Structural Imaging and Modal Analysis Lab.
Mechanical Engineering Department
Blacksburg, VA 24061-0238

Ed White
Boeing
P.O. Box 516
St. Louis, MO 63166

Ken White
Dept. of Civil, Agricultural, and Geological Eng.
Box 30001/Dept. 3CE
Las Cruces, NM 88003-0001

Al Wicks
Mechanical Engineering Department
Virginia Polytechnic Institute of State Univ.
Blacksburg, VA 24061-0238

P. Winney
P&P Engineering
Consultant Engineers
P.O.Box 36
Billingshurst, West Sussex RH14 OYG

Felix S. Wong
Weidlinger Associates
4410 El Camino Real, Suite 110
Los Altos, CA 94022-1049

Shi-Chang Wooh
Room 1-272
Massachusetts Institute of Technology
77 Massachusetts Avenue
Cambridge, MA 02139

Keith Worden
The University of Sheffield
Department of Mechanical and Process Engineering
PO Box 600
Mappin St
Sheffield, S1 3JD
UK

J. T. P. Yao
Dept. of Civil Engineering
Texas A&M University
College Station, TX 77843-3136

Chung-Bang Yun
Dep. of Civil Engineering
Korean Institute of Advanced Science and Technology
373-1, Kusong-dong, Yusong-gu,
Taejon ,KOREA, 305-701

Bill Young
W. P. Young Construction, Inc.
426 Lincoln Centre Drive
Foster City, CA 94404-1127

Dave Zimmerman
University of Houston
Department of Mechanical Engineering
Houston, TX 77204-4792

This report has been reproduced directly from the best available copy. It is available electronically on the Web (http://www.doe.gov/bridge).

Copies are available for sale to U.S. Department of Energy employees and contractors from—

Office of Scientific and Technical Information
P.O. Box 62
Oak Ridge, TN 37831
(423) 576-8401

Copies are available for sale to the public from—

National Technical Information Service
U.S. Department of Commerce
5285 Port Royal Road
Springfield, VA 22616
(800) 553-6847

Los Alamos
NATIONAL LABORATORY
Los Alamos, New Mexico 87545